# Acoustic Classification of Buried Objects with Mobile Sonar Platforms

by

Joseph R. Edwards

M.S. Mechanical Engineering, 1996
B.S. Mechanical Engineering, 1994
Virginia Polytechnic Institute & State University

Submitted to the Department of Ocean Engineering
in partial fulfillment of the requirements for the degree of

Doctor of Philosophy in Ocean Engineering

at the

MASSACHUSETTS INSTITUTE OF TECHNOLOGY

June 2006

Author ..........................................................
Department of Ocean Engineering
February 15, 2006

Certified by ..........................................................
Henrik Schmidt
Professor of Mechanical Engineering
Thesis Supervisor

Accepted by ..........................................................
Lallit Anand
Chairman, Department Committee on Graduate Students

# Acoustic Classification of Buried Objects with Mobile Sonar Platforms

by

Joseph R. Edwards

Submitted to the Department of Ocean Engineering
on February 15, 2006, in partial fulfillment of the
requirements for the degree of
Doctor of Philosophy in Ocean Engineering

## Abstract

In this thesis, the use of highly mobile sonar platforms is investigated for the purpose of acoustically classifying compact objects on or below the seabed. The extension of existing strategies, including synthetic aperture sonar and conventional imaging, are explored within the context of the buried object problem. In particular, the need to employ low frequencies for seabed penetration is shown to have a significant impact both due to the relative length of the characteristic scattering mechanisms and due to the interface effects on the target scattering. New sonar strategies are also shown that exploit incoherent wide apertures that are created by multiple sonar platforms. For example, target shape can be inverted by mapping the scattered field from the target with a team of receiver vehicles. A single sonar–adaptive sonar platform is shown to have the ability to perform hunting and classification tasks more efficiently than its pre–programmed counterpart. While the monostatic sonar platform is often dominated by the source component, the bistatic or passive receiver platform behavior is controlled by the target response. The sonar–adaptive platform trajectory, however, can result in the platform finishing its classification effort out of position to complete further tasks. Within the context of a larger mission, the use of predetermined adaptive behaviors is shown to provide improved detection and classification performance while minimizing the risk to the overall mission. Finally, it is shown that multiple sonar–adaptive platforms can be used to create new sonar strategies for hunting and classifying objects by shape and content. The ability to sample the scattered field from the target across a wide variety of positions allows an analysis of the aspect–dependent behavior of the target. The aspect–dependence of the specular returns indicate the shape of the target, while the secondary returns from an elastic target are also strongly aspect–dependent. These features are exploited for improved classification performance in the buried object hunting mission.

Thesis Supervisor: Henrik Schmidt
Title: Professor of Mechanical Engineering

# Acknowledgments

As is the case for all theses, this work was the product of the efforts of a large number of people. My intention in including people in this acknowledgment list is to give credit to those who supported me in all of the many ways necessary for the successful completion of this thesis.

I would of course first like to thank my advisor, Professor Henrik Schmidt for providing me with the opportunity to tackle an interesting, relevant and challenging area of research, and for exhibiting a great deal of patience as I wrestled with these new problems. As anyone who has worked with Henrik knows, he is very energetic and has a particular talent for dreaming up extremely challenging problems for his students. The GOATS program and datasets are certainly no exception to this, and it has been a pleasure to be a part of this effort.

I would also like to thank my committee member, Professor John Leonard, for his advocacy of my work as well as for the inspiration to move toward simpler and more mobile sonar sensor processing methods. I believe that we will all be living his vision of the future — a lot sooner than most people think.

My third committee member, Arthur Baggeroer, provided balance to this set. His intimate first–hand knowledge of signal processing history as it relates to operational sonar systems provided an invaluable resource for grounding my work in the historical context.

During my time in the Ocean Acoustics Group at MIT, I overlapped with a number of interesting characters, who will undoubtedly be leaders in this field and others in the years ahead. Included in this list are Te-Chih Liu, Purnima Ratilal, Luiz Souza, Michele Zanolin, Sunwoong Lee, Josh Wilson, Yi-san Lai, Andrew Poulsen, Ding Wang, Dee Symonds, Ioannis Bertsatos, Don Eickstedt and Irena Veljkovic. Don't forget me when you're famous.

While I have remained fairly insulated for the duration of this work, I am now emerging from my shell to find the world a different place than I left it. Fortunately, my old friends and family provide signposts for me. My parents, Charles and Jean

Edwards, have both retired during my time here, and have resettled in a location that I haven't seen. My brother, Andrew Edwards, has taken his PhD in a field that I don't understand and is making things that I don't understand either in another place I haven't seen. In any case, they have been (for the most part) patient and understanding of the fog I have been living in for the last several years. Justin Nave has gone from my college roommate to a married, expectant father, and from mathematician to sonar "expert" and coding guru. I'm excited that we will be able to now focus on realizing some of the work that we have been doing in the last few years, and, more importantly, being successful — our way. I'd also like to thank Denise (Sergi) Nave for marrying him without changing him (yet!). I'd like to thank Tim Conway for keeping me in touch with the goings–on in technology and cable TV, and for keeping a couch open for me when I have been down in DC.

Finally, to my wife, Monica Montanari, *cominciamo la nostra vita!* It's time to dream big things, and make them happen. You have tolerated innumerable nights and weekends of work, and now they are over. You have also made an even bigger sacrifice, moving from your beloved Italy to be with me (and Kitty). This is a moment of great possibilities, and it's your turn to choose, so choose wisely. *Ti amo, Mia!!!*

# Contents

# List of Figures

# List of Tables

# Part I

# Mobile Sonar Systems in the Littoral Ocean

# Chapter 1

# Introduction

Since the 1970s, the use of robotic vehicles for undersea applications has been an active area of research, primarily spurred by the inability of the U.S. Navy to effectively locate sunken submarines and ordnance in the deep ocean [85]. International and industrial acceptance of the underwater robotics vision came in the late 1980s and early 1990s [84, 81, 31]. Unmanned underwater vehicles (UUVs) have since become an important asset in undersea research and operations, and are becoming more entrenched every year in military, commercial, archaeological and oceanographic missions. The UUVs provide increased mobility over towed systems or remotely operated vehicles (ROVs), and they eliminate the historically problematic tether from the system [85]. They can also access areas denied to surface ships and towed systems due to their relatively small size. The small size and lack of surface presence of the UUVs also provide a measure of stealth for military operations.

The term UUV is used to indicate that there is no human on board the vehicle, but it does not indicate that the humans have ceded control or decision–making powers over to the vehicle. In this limited mission the UUVs have proven to be capable and successful in a wide variety of uses. However for many long–term missions it would be preferable if the vehicle could perform its mission unmanned, unsupervised and with minimized energy and time requirements. The prior instructions to the vehicle in these long–term missions would not include point–by–point instructions of where to go but rather a more general instruction such as to monitor an area or sweep for mines or other objects within an area. To achieve this capability level, the vehicle must actively adapt its behavior based upon *in situ* measurements made by on–board sensors in such a way that it enhances the ability of the UUV to meet the mission requirements. Such a transformation of mission leads to an autonomous underwater vehicle (AUV), which the vehicles are called in this thesis, both due to the nature of this thesis and because the AUV moniker has been traditionally used at MIT [52].

## 1.1 General Overview

This thesis covers the topic of exploiting the mobility of AUVs to improve the object detection and classification performance of the on-board sonar systems. Such a general problem is, of course, more than can be addressed in a single thesis. In order to reduce the scope of the problem somewhat, much of the work in this thesis is designed to parallel the standard littoral mine countermeasures (MCM) problem. Particular aspects of the littoral MCM scenario that influence the thesis problem formulation include:

1. the type of target
2. the need to consider that targets may be buried beneath the seabed
3. the influence of sub- vs. super-critical seabed incidence
4. operating frequency
5. operating range
6. seabed types - ripple fields, etc.

It is also noted that the term AUV corresponds to a wide class of vehicles that are designed for a wide variety of tasks, including beach/near–beach crawlers [23], surface vessels [45] and the more common freely swimming vessels such as the Battlespace Preparation AUV (BPAUV) of Bluefin Robotics or the REMUS of Hydroid, Inc. The freely swimming type of AUV is the only one considered in this thesis. The analysis is


(a) (b)

Figure 1-1: Images of MIT–owned Bluefin Odyssey 21 AUVs in action at the GOATS 2002 experiment.

based upon the Bluefin Odyssey–class vehicles that are owned and operated by MIT in the GOATS experiment series. These AUVs are approximately 2 meters long and have robust and stable control over a planned mission path. The vehicles can be seen being deployed and surfacing in Fig. 1-1 (a) and (b), respectively.

Even prior to the consideration of AUV mobility, littoral MCM remains a daunting challenge to state-of-the-art sonar systems. The most effective mine-clearing systems can be classified into three types: biological methods (e.g. trained dolphins), sonar methods or brute force methods (helicopter-pulled sleds). The first two methods are relevant to this thesis, whereas the brute force mine neutralization will be set aside. In effect, the current work seeks to utilize the mobility of the AUV to allow the sonar-based methods to mimic the relevant capabilities of the biological assets, and then to explore possible advantages that the AUVs may have over these biological assets.

## 1.2 Mine Countermeasures

Although this thesis is written strictly from an academic perspective, it is instructive to understand the prominence of the MCM problem in the naval world. The first shot fired in the undersea mine battlefield came during the American Revolutionary War in 1777, when David Bushnell, ordered by George Washington, floated kegs of gunpowder in the Delaware River near a fleet of British ships in an unsuccessful attempt to destroy them. The American Civil War (1861–1865) was the first conflict in which naval mines were used extensively by both sides, and by this time they were extremely effective [89]. After their success in the late 19th century, mines continued to progress technologically through the first and second World Wars, and on through today. The high degree of efficacy while using crude technology make these offensive and defensive weapons of choice for militaries around the world. Mine warfare is also popular among underdeveloped countries and paramilitary groups interested in asymmetric warfare. Far from being a tactic of the past, the use of mines has been steadily increasing even within the past decade [29]. Two US naval ships were damaged during the Gulf War of 1991 despite advanced MCM capabilities, encouraging many foreign governments to form or improve their mine capabilities, as well as terrorists to exploit similar tactics. For example, the terrorist bombing of the USS Cole [63] was a variation on the generally unsuccessful drifting mine, simply steered by a willing crew in order to improve its effectiveness.

Once sea mines proved to be effective, mine countermeasures were introduced in an attempt to remove the threat, and the race was on. The technology moved from floating passive mines to remotely controlled mines to active ship hunting mines. The countermeasures moved from lookout crew members to sonars, electromagnetic sensors, and tow sleds from helicopters, among others. Effective mine countermeasures pushed the mine layers into counter-countermeasures, and so on. The general consensus is that mine layers have maintained the advantage [29], which is supported by the fact that mines have caused more damage to US Naval ships in recent years than any other single weapon system [79]. Recent advancements employing robotic and biological assets have begun to even the playing field [68], of course with the likely outcome being that the mine layers currently or in the near future will employ the same technologies to reclaim the advantage. It is in the utilization of these robotic assets that this thesis finds its inspiration.

Technological assets, networking and systems integration are among the asymmetric assets of developed nations [16, 48], and this work investigates some aspects of exploiting these technologies for defensive purposes. The use of robotic systems can reduce the threat to soldiers or more expensive assets, and at the same time provide better MCM performance in some cases. The first deployments of AUV–borne MCM systems have already been launched and received their first wartime trials, on a limited but apparently promising basis [68].

A last note on mines before turning attention to the academic problem at hand. Although fixed sea mines remain largely an asset for organized militaries, there is natural comparison to be drawn between sea mines and land mines in at least one respect: that the end of hostilities does not end the mine threat. Mines can remain active for decades after placement [64]. This longevity also points to a need for humanitarian demining efforts as well as tactical military MCM.

## 1.3 Acoustics Perspective

Within this thesis, the object hunting/classification sensor of choice is active sonar. Such a choice clearly leads to an acoustic propagation and scattering problem, complicated by the planned or unplanned robotic motions of the mobile sonar platform as well as uncertainties in environmental parameters and the lack of *a priori* knowledge of the target. From an acoustics point of view, each ping of the active sonar is not remarkable in itself, resulting in an acoustic time series that looks much the same as it would from any sonar system of similar frequency spread, acoustic power and other characteristics. The only noticeable influences of the mobile platform may be in a Doppler spread (although the AUV platforms typically move slowly), and in vehicle self–noise.

### 1.3.1 Propagation

The acoustic field in the very shallow water (VSW) environment is characterized by a complex combination of multipath arrivals, interface waves and spatially varying seabeds - all further complicated by tidal effects, as well as the diurnal and seasonal variations of the sound speed profile. Existing current and tidal prediction models can at best provide rough estimates of the local acoustic propagation environment. As such, perfect knowledge of the environment, including water depth, local sound speed and sediment properties cannot be assumed known *a priori*. For short–range sonar systems, the ray path propagation methods are appropriate, as there are relatively few multipath arrivals. The primary multipath is the reflection off of the sea surface. This short–range propagation regime is used in this thesis, in order to simplify the analysis of the the acoustic features of interest for the original work. Full spectral integral and normal modes formulations of the synthetic aperture are presented in Chapter 2, as the basis of a signal model that can be applied when the propagation is guided. Tidal variations, etc. are not considered at all in this work.

### 1.3.2 Seabed Scattering

The first acoustical topic of interest is the interaction between the insonifying signal and the seabed. In this regard there are two interesting features. First is that the deterministic result of sub–critical vs. super–critical insonification. The effect of the critical angle can be dramatic with respect to the sonar detection and classification performance for buried objects. The second seabed–interaction feature is the effect of surficial and sub–bottom roughness on the scattered field. The roughness parameters affect the expected signal–to–noise ratio of the returned signal as well as the coherence of the reverberation field. The coherence of the reverberation field is shown to have a significant effect both on the formation of a synthetic aperture as well as the capability of the synthetic aperture to cancel the reverberation noise.

### 1.3.3 Target Scattering

A further acoustic interest in this thesis is the behavior of insonified elastic targets. At high frequencies that are typically used for imaging ($ka \gg 1$), target response is generally flat in the backscattered direction. There is little information to be gained from the target other than the geometric response. Two methods for extracting more information from the target are investigated in this thesis, exploiting the mobility of the sonar platforms. First, if the sonar frequency is lowered to the mid–frequency regime, i.e. for $1 < ka < 10$, then the target response becomes non–specular. The entire target is entrained in the wavelength of the pulse, rather than just a superficial bounce off of the target surface. The resulting target behavior provides clues that may be exploited for classification. The second source of additional target information comes from the bi–static reception of the target scattered field. Even at high frequency, the target has a radiated beampattern that indicates its size and shape.

In searching the literature for the acoustic scattering of elastic targets, there are two common applications that have faced similar problems to that of the mine hunter. There is a clear comparison to be drawn between anti–submarine warfare (ASW) efforts and mine hunting. Also, fish classification by swim bladder response provides some similarities. Both fields have led to research on scattering from canonical shapes [4, 27], slender bodies [55] and elastic targets [86] for both monostatic and bistatic sonar systems. For spherical and spheroidal objects, there is simply a frequency (or $ka$) scaling to be made for direct comparisons. However, there are a wide range of known shapes of mines, along with a likely wider range of unknown shapes, and so the mine classification problem is more general in this respect.

### 1.3.4 Vehicle Effects

The acoustic effects of the AUV itself depends largely upon the AUV and the deployment of the acoustic sensors that it carries. While the particulars of the acoustic effects of the vehicle are mentioned only in passing in this thesis, it is important to outline those effects that should be considered when deploying a real system. The AUV impacts the received signal both passively and actively, from an acoustics point of view. Passive effects are distortion of the received signal due to the insertion of the AUV, while the active effects are contributions to the acoustic field from the self–noise acoustic signature and active transponders in the vehicle.

The passive acoustic effects arise from vehicle motions and nearfield scattering and diffraction caused by the vehicle body. In survey missions such as those considered in this thesis, the AUV typically moves at 3 knots or less, resulting in a very small

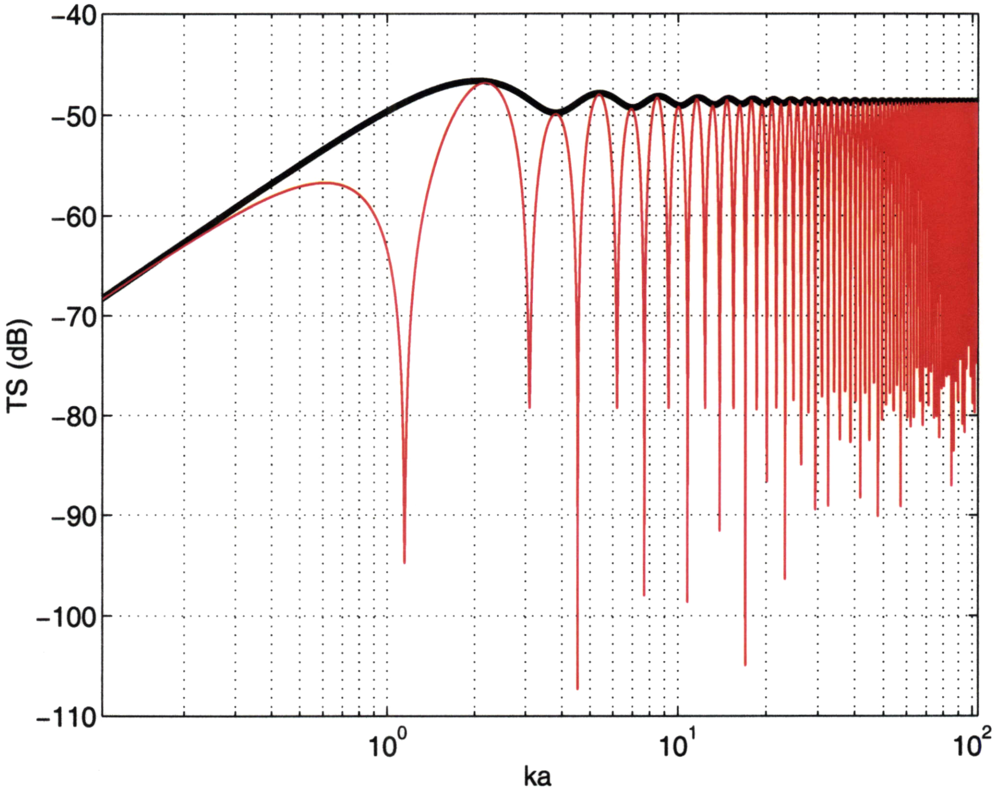

Figure 1-2: Target strength of a weakly scattering sphere for ka between 0.1 and 100.

Doppler effect that is often negligible on a ping–to–ping basis. Considering that the AUV is a body carrying sensors very near (or on) its surface, the returned signal also undergoes the equivalent of the head related transfer function (HRTF) experienced by humans [9, 13]. It is assumed in this work that the HRTF of the particular AUV/sonar system combination are well–known and taken into account in the pre–processing of any received data, and as such the effect of the HRTF is negligible.

At the current stage of AUV development, active AUV self–noise can vary dramatically between system models, and even between different vehicles of the same model. This personalized signature effect can be expected to persist over time, much like the personalized acoustic signatures of submarines have persisted despite the relative maturity of the submarine industry. In general, the AUV self–noise of particular systems has been shown to be reducible to a level that allows sensitive passive measurements for localization [21] or characterization of hydroacoustic noise [87]. In addition to noise emanating from the motion and propulsion of the vehicle, other

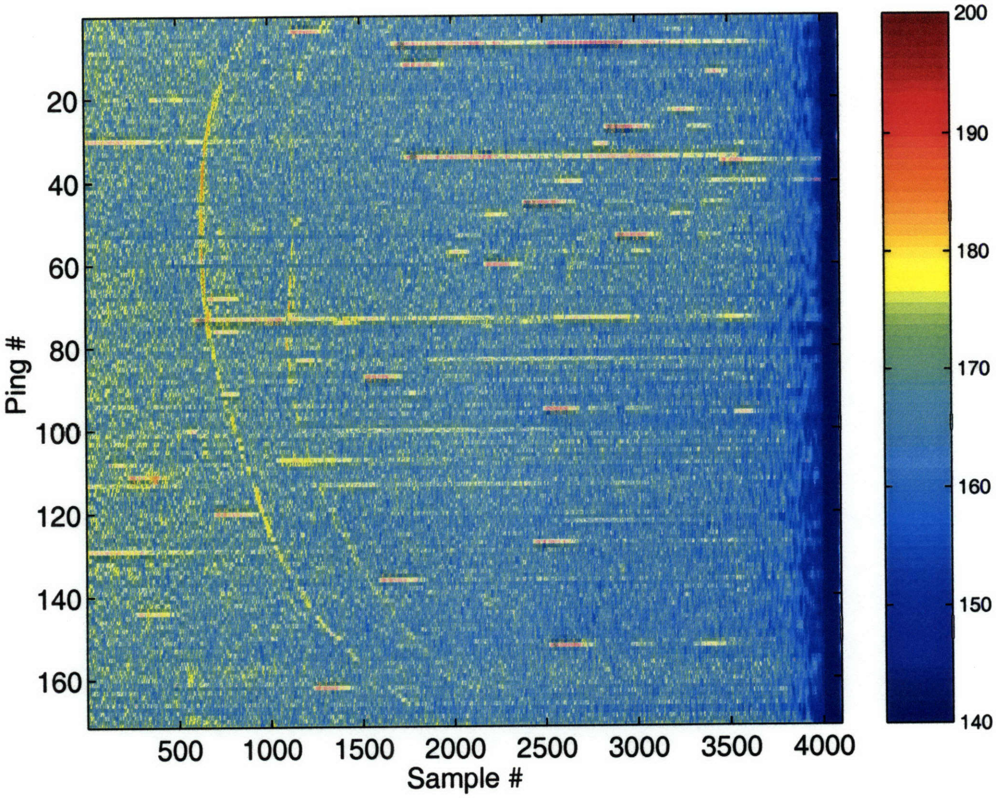

Figure 1-3: Sonar data received during the GOATS 2002 experiment. Note the strong signals that are a result of the acoustic modem and navigational tones.

acoustic transponders are generally carried on board, including navigation and communications equipment. In some cases, the bandwidths of one or more devices may overlap with the object–hunting sonar band, resulting in cross–talk between sensors. An example of the sonar affecting the navigation sensors has been shown by Newman [54], and an example of the reverse is shown 1-3, where the acoustic modem can be seen to be interfering with the sonar receptions in the GOATS 2002 experiment.

## 1.4 Signal Processing Perspective

Signal processing algorithms have been developed over the last several decades to obtain optimal performance given the sonar design. In addition to the fixed algorithms, signal processing *adaptivity* provides a capability to suppress noise and interferers that cannot be foreseen prior to sensor deployment. The advent of AUVs, however, has dramatically increased the possibilities of sonar design, requiring greater flexibility from the signal processing algorithms. In particular, geometric deformability and multi–static approaches are envisioned to optimally achieve an objective or set of objectives within a mission. This exploitation of vehicle mobility and cooperation can lead to a shift in paradigm, from deploying a sonar system to gather a specific type of information to deploying a group of sensors to accomplish a mission.

Several signal processing techniques are required in the hunting and classifying of objects with moving sonar platforms — including noise characterization and suppression, signal detection, spectral analysis, beamforming and tracking. All of these techniques can be applied either on a ping–by–ping basis or over an extended aperture composed of a series of pings. Additionally, a distinction must be drawn between monostatic and bi–static sonar configurations.

On a ping–by–ping basis, the applicable signal processing algorithms are well–known, due to several decades of research in radar, seismic and acoustic signal processing [6]. There is a natural advantage to single–ping processing, which is that the relative positions of the physically connected sensors are known. The interest in single–ping processing in this thesis is not to develop new algorithms for better extracting spectral or wavenumber information from the receptions, but rather to apply existing algorithms to meet the demands of the buried object classification problem.

For multi–ping processing, the history and applications are much more limited. Although synthetic aperture radar (SAR) [17] has been around for half a century, the sonar equivalent, synthetic aperture sonar (SAS) has developed much more slowly. The slow development has largely been a result of the inability to compensate for sonar platform motions. These small platform motions result in a degradation of the coherence between multiple pings, creating a data association problem for the SAS. As recently as 1998, there were only five systems worldwide that were known to be seaworthy [28]. Unsupervised and real–time SAS processing was first demonstrated on a limited basis in 1996 [3]. In this unsupervised SAS, the vehicle continuously takes imagery data during its mission and coherently combines a scrolling series of pings to generate a scrolling image much like a side scan system.

In this thesis, unsupervised multi–ping processing is moved forward from unsupervised SAS in three ways. First, the displaced phase center antenna (DPCA) motion compensation technique applied in unsupervised SAS processing is generalized from a strictly monostatic technique to a bi–static technique, under certain conditions. This extension is described in detail in Sec. 3.5.1. A second extension to unsupervised SAS is the adjustment of the DPCA motion compensation for lower frequency processing, as discussed in Sec. 3.1.4. Finally, the unsupervised SAS processing is used as an autonomous classification tool rather than as a mission definition. This general concept pervades the thesis, and as such is not limited to a single section or two. In the unsupervised SAS case, the application of this concept means that the AUV detects a target, and then uses SAS to image locally around the target to achieve sufficient resolution to see the physical shape of the target. So rather than being a fixed SAS processor, the sonar system maintains its full capability and flexibility. There are several specific reasons that make such an approach desirable, as will become clear in later sections. An intuitive way to describe the motivation for maintaining flexibility in a more general sense is to consider that the formation of images from data is a transformation of the measurement from time domain to a chosen set of pixels. This transformation *necessarily* causes a loss of information, leading to a suboptimal detection capability. In the localized imaging upon detection method, the detector can be optimized, while the imager is used for its specialty, which is to determine the shape of the object. The limitation in scope of the imaging can also reduce the computational burden on the vehicle as well as the communications burden over the acoustic channel.

## 1.5 Robotics Perspective

From the standpoint of pure robotics, the robot nearly always has its own sensor that utilizes range–only (sonar), angle–only (video) or range–and–angle (laser) measurements to navigate through the world. An extensive amount of research has been applied to this problem and a fair amount of success enjoyed. Robots are used to accomplish many and varied objectives, even in a single mission. In this thesis, it is attempted to apply some of the basic robotic solutions to the problem of buried mine–hunting, where the sonar has limited range and angular resolution at a given ping, and the acoustic environment is challenging. While in some sections the link will be made between the robotics literature and the current work, the mobility of the AUV will often be taken for granted to achieve the desired goal of acoustic classification of targets.

In contrast to the signal processing case, *adaptivity* in robotics refers to capability of the robot to move itself to an advantageous position for accomplishing its mission, noting that this position can not be foreseen prior to deployment. In the course of this thesis, these two forms of adaptive behavior will be denoted as *robotic adaptivity* and *signal processing adaptivity.* A simple illustration of the difference between the two forms is shown in Fig. 1-4. In this figure, the left panel (a) shows the antenna steering itself to find the target of interest, while the right panel (b) shows the antenna repositioning itself to better detect the target of interest. Both methods can be effective, and each has its advantages and disadvantages. Signal processing adaptivity has the advantage that there have been a large number of research projects and practical implementations in order to create robust algorithms for a wide variety of applications. In addition, the fact that the antenna itself is rigidly or nearly rigidly connected contributes to a stable sonar platform for processing. The disadvantage is primarily that the initial deployment is everything, meaning that the prior selection of sensor position or trajectory strictly determines whether a target will be detectable. It can be seen that robotic adaptivity complements signal processing adaptivity in these terms, as the advantages and disadvantages are reversed. Robotic adaptivity allows the sensor to further investigate potential sites of interest near the pre–planned trajectory, reducing the risk of missing a target. Fig. 1-5 shows the antenna moving to a preferred look angle on an aspect–dependent target. This type of detection enhancement cannot be achieved through signal processing adaptivity. On the other hand, the uncertainty of vehicle position creates a problem with coherently combining multiple pings.

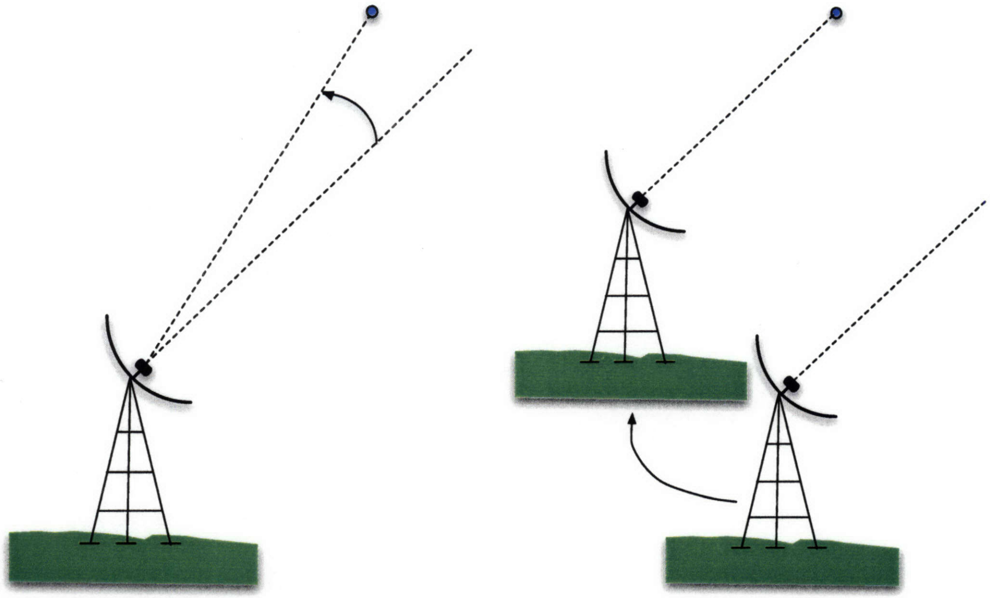

(a) (b)

Figure 1-4: Signal processing vs. robotic adaptivity. On the left panel, the receiver steers itself using signal processing adaptivity to enhance target detection capability. On the right panel, the receiver physically moves itself (robotic adaptivity) to achieve a better view of the target.

## 1.6 An Autonomous Systems World View

Although the three perspectives outlined above were presented separately, there is significant overlap between these classical fields of study. In general, signal processing is a means to an end in both acoustics and robotics, but the end goal is different for these two fields. For mobile sonar platforms as used in this thesis, there are a variety of ways in which the acoustics, signal processing and robotic motion interact, as outlined in this section. The distinction to be made is how each of the three are influenced by the others. The term *static system* is used to refer to a sonar or robotic system in which the behavior of the system is determined prior to the mission. A *dynamic system* is one in which the results during the mission can influence the remainder of the mission.

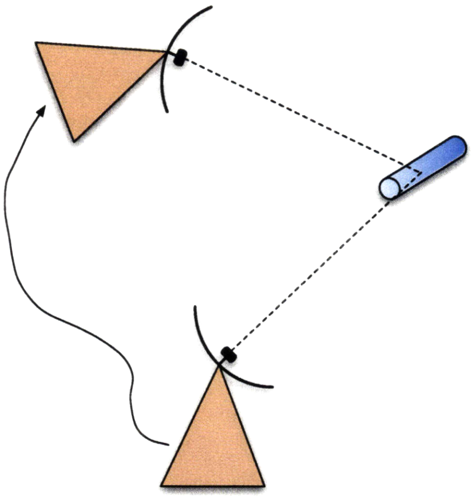

Figure 1-5: Robotic adaptive behavior to select an advantageous point of view on a target.

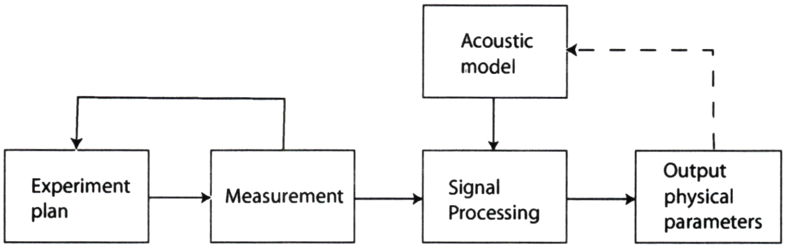

Figure 1-6: Block diagram of a statically interacting signal processing and acoustic system. When the dashed line link from the output physical parameters and the acoustic model is included, the interaction is dynamic.

### 1.6.1 Acoustics and Signal Processing

Acoustics and signal processing are intimately connected to one another. When using an acoustic measurement to infer properties of the surrounding environment, acoustic propagation and scattering physics are the means of understanding the link between the measurement and the properties of interest, and signal processing is the means for transforming the measurement into the best estimate of the properties of interest. The same relationship holds in any remote sensing field, except that the propagation physics varies to suit the problem, from acoustics (e.g. ultrasound) to electromagnetic (e.g., radar) to seismics (e.g. earthquake monitoring).

### Static Interaction

Acoustics and signal processing typically interact in an open–loop format as shown in Fig. 1-6, where some environmental or object parameter is desired from acoustic measurements. An experimental plan is devised, and a series of measurements are performed to meet the plan. Each measurement is processed to obtain the desired physical parameters, taking into account the acoustic propagation model of the local area. In a static case, the best estimates of the parameters are made based upon the best available knowledge of the propagation environment. The dashed line representing the link between the acoustic model and the output parameters does not exist in the static case. An advanced form of static interaction is matched field processing (MFP) [7] and its variants [35], in which the environmental model is also adjusted to create a combined best estimate of the desired parameters and the environmental model.

### Dynamic Interaction

For a long–term acoustic monitoring system, the acoustic propagation paths vary over time and so the propagation model should evolve to match the altered environment. One way to achieve proper environmental matching is to have independent observers or ocean models to update environmental parameters. In a slowly varying (with respect to sonar snapshot or ping rates) environment, however, a self–contained dynamic system can accomplish similar results without the intervention of an independent observer. Again referring to Fig. 1-6, the dashed line is now a firm link between the output parameters and the acoustic model. The returns over time are adjusted as they evolve, and the acoustic model is enhanced through MFP or a linearized model to improve the sonar performance. In this case there is a forward prediction for desired acoustical parameters combined with an acoustic inversion for the nominally known parameters.

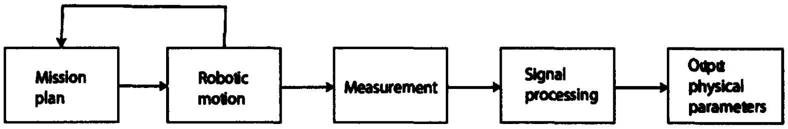

Figure 1-7: Robotic mission from the view of the inert sonar payload (static case).

### 1.6.2 Robotics and Signal Processing

Robots also rely on signal processing in order to transform their sensor measurements into a perception of the environment around them. This perception confers to the robot a measure of whether it is meeting its mission goals, e.g. following its prescribed track, and allows the robot to perform safety maneuvers, such as obstacle avoidance. An AUV carrying an active sonar does not necessarily have to use that sonar as a sensor, but instead may consider the sonar an inert payload. It is this distinction that separates static from dynamic robotic–signal processing interactions, and Part II from Part III in this thesis.

#### Static Interaction

From the point of view of the inert payload, the robotic mission appears as in the system diagram of Fig. 1-7. The mission plan is set, and the robot follows the mission to the best of its abilities using the relevant sensors. The inert sensor goes along for the ride, taking measurements of the environment that are transformed into physical parameters of interest.

#### Dynamic Interaction

In a dynamic system, the robotic motion is allowed to vary based upon its perception of the environment. In this case, the sensor system and the robotic motions collaborate to achieve a mission. Prominent examples of the robots with dynamic interaction range from simple depth abort on AUVs to human–interactive museum tour robots [80, 57]. For the sonar payload, this dynamic interaction is as displayed in Fig. 1-8. In this case the output of the interpreted sensor measurements is fed into the mission plan, which now must contain a decision process to adjust the mission based upon

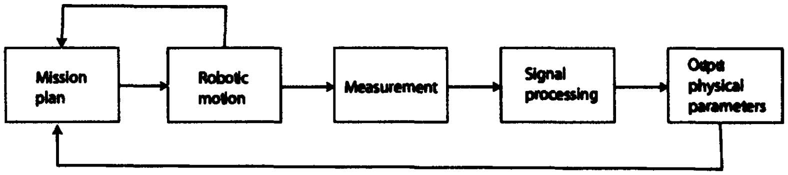

Figure 1-8: Robotic mission from the view of the sonar in the dynamic case.

the sensor output.

### 1.6.3 Acoustics, Robotics and Signal Processing for Remote Sensing

At the heart of this thesis is a remote sensing problem, with a particular style of acoustic environment, robot type and signal processing goal. There are three principal types of missions encompassed in this view, depending on the autonomy of the vehicle. *Unmanned* missions consist of the vehicle following a set of pre-defined steps and returning to base. In a *dynamic autonomous* mission, on the other hand, the vehicle is given freedom to alter the mission to meet the mission goals, while being limited by rigidity in the environmental modeling. Finally a *self-reliant* mission enables the vehicle to adjust its perception of the world as it sees it while altering the mission to achieve the mission goals.

#### Unmanned Remote Sensing

The primary focus of this thesis is to address the sonar issues facing a moving system of sources and receivers in the littoral ocean. The first goal of such analysis is to human users to make sense of the inherently complex data sets that are produced by such systems. A later goal is to enable autonomous systems to handle the deforming geometry and varying content of these acoustic measurements without human intervention. One form of unmanned remote sensing that has been practiced extensively in military, commercial and research operations is imaging or inversion from a towed array or towfish [43]. The limitation of towed systems is that they are of limited mobility. More mobile systems are also of concern in this thesis.

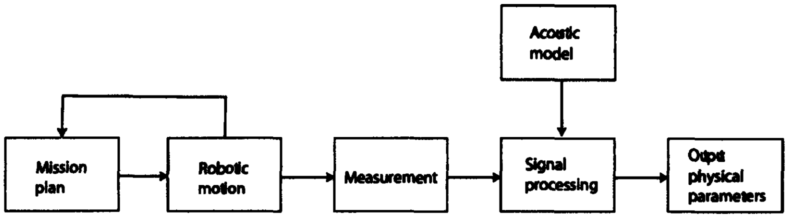

Figure 1-9: An unmanned remote sensing mission.

The unmanned remote sensing mission is shown in Fig. 1-9. This type of mission is identical to the static robotics–signal processing mission of Sec. 1-7, except that the signal processing is informed by an acoustic model. The active sonar is treated by the robot as a passenger.

### Dynamic Autonomous Remote Sensing

Autonomy begins when the vehicle is permitted to alter its mission based upon what its sensors measure. A small degree of autonomy is required for safety reasons on any mission. For example, the vehicle may abort the mission if it senses that it is too close to the bottom. Of concern in this thesis is the subset of dynamic autonomy that is sonar–adaptive. That is, the sonar mission is altered due to the output from the sonar sensor for the purpose of accomplishing the mission goal. The mission goal in this case is related to determine the existence of objects in or on the seabed and to classify them. For autonomous remote sensing, there are several competing mission goals. A general system diagram of an autonomous remote sensing system is shown in Fig. 1-10. In this case, the acoustic physics is used to inform both the signal processing and the robotic motion of the vehicle. In other words, the sonar receptions have some degree of navigational control over the vehicle. Autonomous systems allow vehicles to actively hunt for objects alone or in teams.

In this thesis, the target classification aspects of autonomous remote sensing are investigated strictly from a sonar point of view as represented in Fig. 1-10, neglecting the various other tasks that the vehicle must accomplish simultaneously. The multi–tasking requirements and control requirements are an active field of study for AUVs and manned systems [11, 12]. The dynamic autonomous remote sensing mission is

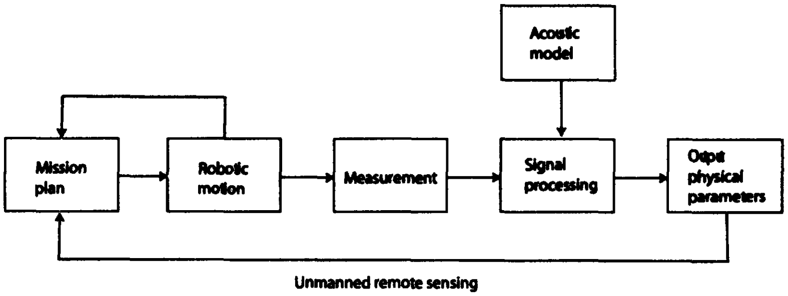

Figure 1-10: An autonomous remote sensing mission.

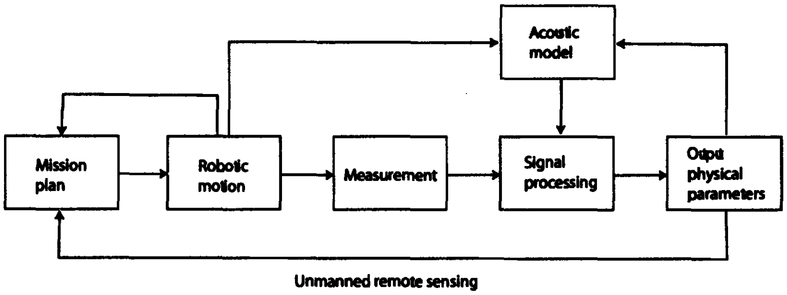

Figure 1-11: A self–reliant autonomous remote sensing mission.

identical to the dynamic robotics–signal processing mission, except that the signal processing is specifically informed by an acoustic model.

### Self–reliant Autonomous Remote Sensing

In the long view, a *self–reliant* remote sensing model is required for robust long–term missions. A system diagram for the self–reliant remote sensing model is shown in Fig. 1-11. In this model, the robotics, acoustics and signal processing are fully integrated, collaborating rather than using one to instruct the other. The major difference in the self–reliant system is that along with the mission plan, the robots world view is allowed to change during the course of the mission. In terms of the acoustic object classification problem, the world view of the robot consists of its acoustic model of the environment and prospective scatterers.

## 1.7 Organization of the Thesis

Arriving at the destination of multiple self–reliant remote sensing vehicles working cooperatively is clearly a long–term endeavor. This thesis seeks to provide several discrete contributions along this path. It is divided into three major parts: the first part, "Mobile Sonar Systems in the Littoral Ocean", provides an overview of the impact of the free mobility on the expected returns of the sonar system and the implications to the signal processing algorithms. Chapter 2 presents the expected sonar signals received by a moving active sonar platform in spectral integral and normal modes forms, as well as the specific simplifications that can be made given particular platform movements.

The second part of the thesis, "Target Classification with Passively Mobile Sonar Platforms", discusses approaches to target classification when the AUV happens to pass near a target along its pre–defined path. Chapter 3 describes the extension of SAS motion compensation to bi–static sonar systems and bottom–penetrating sonars. In Chapter 4, the imaging and detection applications are discussed in terms of the AUV mission. Finally, target classification is addressed in Chapter 5.

The third part of this thesis, "Target Classification with Actively Mobile Sonar Platforms", addresses dynamic autonomous remote sensing in terms of sonar–adaptive behavior to assist in object classification.

# Chapter 2

# Theoretical Development - Mobile Sonar

Freely moving sonar platforms evoke a sense of unlimited possibility and untapped potential. Given the ability to take any set of sonar measurements to accomplish the mission — be it navigation, object detection, object classification or environmental assessment — what should one choose? The challenge becomes even more demanding in a temporally varying medium such as the littoral ocean. One first must select tools to work with that are consistent and applicable to all situations. In this chapter, the sonar signal models for mobile sonars are developed such that they may be applied to selected missions and platform trajectories.

This thesis concerns itself with the classification of fixed targets, and as such the moving source and moving receiver are the variables of primary interest. Because all source and receiver motions may be modeled locally as constant heading, constant velocity, the linearly moving platform assumptions are also important. Also, due to clutter and signal interference problems, it may often be useful to have a stationary or distant, slowly moving source while analyzing the scattered field with local, highly mobile receivers. In these scenarios, the fixed source problem also becomes applicable. Of course, a fundamental basis upon which to compare all mobile sonar results is the classical SAR/SAS, and this is where the presented signal models will begin.

## 2.1 Sonar Signal Model - Classical SAR/SAS

The radar literature is replete with ray-path formulations for the two-way propagation from a moving source/receiver unit to a fixed target in a free or half-space medium. The formulation will begin by following along these lines. Further theory will then be developed that are applicable to the sonar scenario, namely wavenumber integral and modal formulations for waveguide propagation.

The traditional SAR signal model contains a number of assumptions, including the following:

1. High frequency, ray path propagation.
2. Free space boundary conditions.
3. Monostatic source/receiver.
4. Single element linear source/receiver unit.
5. Linear source/receiver motion.
6. Constant velocity source/receiver motion.

Under this set of constraints, the received SAR signal from a target is characterized by a linear Doppler chirp, which fits into an elegant chirp compression signal processing algorithm. When employed with a linear chirp signal, the result is a signal processing algorithm that is efficient and symmetrical, applying chirp compression in both time and space to arrive at the image. By varying the length of the apparent aperture with range and moving the center of the aperture with aspect, the resolution of the pixels are made uniform in both image dimensions. A heuristic approach to the demonstrate the linear spatial chirp is presented, following Kovaly [41]. Consider the source/receiver unit moving past the target at velocity $v_p$. Defining a time $t_{CPA}$ at which the unit makes its closest point of approach (CPA), and defining the range at the CPA to be R, the range to target at a given time $t$ is given by

$$R(t) = \sqrt{R^2 + v_p^2(t - t_{CPA})^2} = R\sqrt{1 + \frac{v_p^2}{R^2}(t - t_{CPA})^2}$$

Then by assuming the range is much greater than the horizontal offset of the target along the synthetic aperture,

$$R(t) \approx R\left(1 + \frac{v_p^2}{2R^2}(t - t_{CPA})^2\right) = R + \frac{v_p^2}{2R}(t - t_{CPA})^2$$

From the two–way ray path assumption, the received signal $\psi(t)$ is proportional to the complex exponential

$$\psi(t) \propto \exp\left\{\jmath(\omega t - 2k_0 R(t))\right\}$$

where $k_0$ is the medium wavenumber. Given that the phase shift from the two–way ray path propagation is $\omega t - 2k_0 R(t)$, the instantaneous frequency can be determined from the time rate of change of the phase, i.e.

$$\frac{\partial \phi}{\partial t} = \frac{\partial}{\partial t}\left[\omega t - 2k_0 R(t)\right] = \omega - 2k_0 \frac{\partial R(t)}{\partial t} \approx \omega - \frac{4\pi}{\lambda}\frac{v_p^2(t - t_{CPA})}{R}$$

which indicates that the frequency shift is linear with time. The apparent Doppler shift along the source/receiver trajectory is then approximately

$$f_D = \frac{1}{2\pi}\left[-\frac{4\pi}{\lambda}\frac{v_p^2(t - t_{CPA})}{R}\right] = -\frac{2v_p^2}{\lambda R}(t - t_{CPA}) \qquad (2.1)$$

subject to the limitations of the approximations listed above, and those used in the approximation of the range.

A further result of classical SAR is that the image resolution is independent of range and azimuth. The azimuth independence arises from the shifting of the synthetic aperture phase center with azimuth such that it is centered on each row of pixels. The range independence arises from the single linear source/receiver element assumption and is heuristically argued as follows, and as illustrated in Fig. 2-1. Given that the source aperture is of length $L_p$ and it is linear, the null–to–null source beamwidth is $2\lambda/L_p$ radians. At an arbitrary range $R$, the illuminated region is of

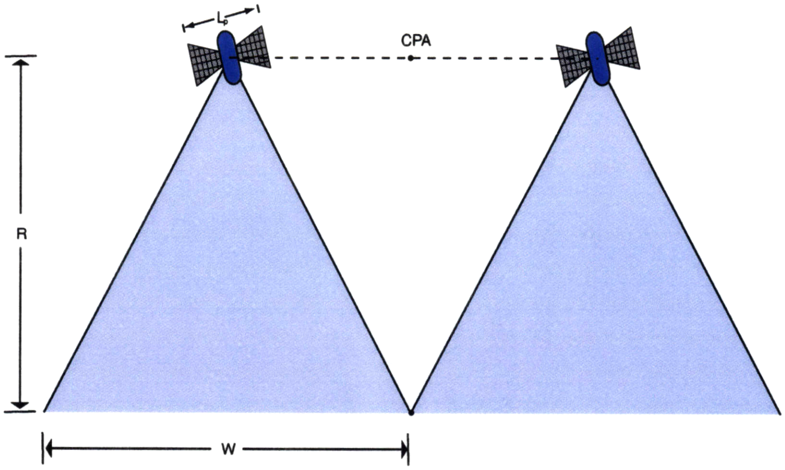

Figure 2-1: Canonical synthetic aperture radar.

width $W = 2R\lambda/L_p$, which can be seen as the maximum synthetic aperture length available for a point target at that range. The null–to–null angular resolution of a synthetic aperture of length $W$ is $2\lambda/W$ radians, and the spatial resolution at range $R$ is then $2R\lambda/W = L_p$, the length of the physical aperture. Notice that the resulting spatial resolution is independent of range, as advertised.

This section has highlighted two of the salient features of traditional SAR/SAS – linear spatial Doppler shifts and range–independent resolution. The remainder of this chapter focuses on the generalized formulation of the signal receptions by mobile sonar platforms. While the clean results of SAR do not necessarily hold for the generally mobile sonars, the classical SAR results described in this section are a useful baseline for comparison with the more general mobile sonar system.

## 2.2 Sonar Receptions in a Waveguide

The first issue to be dealt with is apparent Doppler shift of the mobile sonar. In contrast to the SAR described in Sec. 2.1, the Doppler shifts will not necessarily be linear, due to both the generalization of platform motion to non–linear trajectories and the effect of the waveguide on propagation. In the littoral environment, waveguide effects inevitably come into play. The resulting Doppler–like phenomenon is that there are multiple phase shifts for multiple propagation paths, and these shifts are not reciprocal when the source and receiver are physically separated. In this section, the sonar receptions at a single ping will first be written, and then the evolution of the Doppler shift over canonical trajectories will be investigated. The mathematical representation of the sonar receptions can be written in integral, modal, parabolic or ray forms. In this thesis, the parabolic equation method is ignored due to the phase errors inherent in the parabolic approximation. The one-way modal formulation of the transmission between a moving source and a moving receiver has appeared in various forms since the 1970s [30, 32, 24]. The one-way spectral integral formulation for a moving source and receiver in a waveguide is detailed by Schmidt and Kuperman [70], and has been recently extended to include the two-way propagation and scattering from a target by Lai and Makris [42]. The modal formulation of object scattering in the waveguide was famously completed by Ingenito [36], and was also extended to moving entities in the Lai and Makris paper [42].

### 2.2.1 Spectral Integral Model

The spectral integral solution has the advantage of being more accurate than the normal mode solution, at the cost of computational efficiency. Since this formulation includes all of the physical mechanisms, including evenescent and boundary waves, it makes sense to start with its derivation and then to proceed to make the assumptions necessary to improve computational efficiency, finally arriving at the normal modes model in the following section. As reported by Schmidt and Kuperman [70] Eq.(16), the one–way signal from a source to a moving receiver is given by

$$\psi\left(\vec{r_0} + \vec{v}_r t, z_r, \omega\right) = \frac{1}{2\pi} \int d^2\vec{k}_r \exp\left\{\jmath \vec{k}_r \cdot \vec{r_0}\right\} S\left(\Omega_k\right) G_\omega\left(\vec{k}_r, z_r, \omega + \vec{k}_r \cdot \vec{v}_r\right) \qquad (2.2)$$

where the $\vec{k}_r$ is the horizontal wavenumber, $\vec{r_0}$ is the vector connecting source and receiver, $S(\omega)$ is the source spectrum, $\Omega_k = \omega - \vec{k}_r \cdot (\vec{v}_s - \vec{v}_r)$ is the Doppler–shifted radian frequency and $G_\omega(\vec{k}_r, z, \omega)$ is the waveguide Green's function. It is worth noting here that Eq. (2.2) is written in terms of the received frequency $\omega$, and the source is evaluated at the frequency $\omega - \vec{k}_r \cdot (\vec{v}_s - \vec{v}_r)$. The common interpretation of the Doppler shift is the other way around — it is the frequency shift at the receiver from that which is output at the source. As such, the Doppler shift is $\omega_D = \vec{k}_r \cdot (\vec{v}_s - \vec{v}_r)$. The representation of the signal in in terms of the receiver frequency is useful for computational reasons.

For reference, consider the classical SAR/SAS Doppler shift described in Sec. 2.1. For one–way transmission to a fixed receiver ($\vec{v}_r = \vec{0}$) in the far field, the Doppler shift $f_D$ is seen to be approximately equal to the classical SAR/SAS Doppler as follows:

$$f_D = -\frac{1}{2\pi}\vec{k}_r \cdot \vec{v}_r = -\frac{1}{\lambda}v_p \cos\theta = -\frac{1}{\lambda}v_p \frac{v_p(t - t_{CPA})}{\sqrt{R^2 + v_p^2(t - t_{CPA})^2}} \approx -\frac{v_p^2(t - t_{CPA})}{\lambda R}$$

so as expected the Doppler shift arises from the rate of change of the range between source and receiver (or target). The two–way transmission from a monstatic sonar to a fixed target will result a doubling of the above Doppler shift, arriving at the exact expression as in Eq. (2.1).

In order to translate this result into a two–way reception for the mobile sonar platform, first consider the second part of the signal transmission path (target to receiver). The model for this part of the signal path is as in Eq. (2.2), but the target acts as the source, so $\Omega_k = \omega - \vec{k}_r \cdot (\vec{v}_t - \vec{v}_r)$. The source term $S(\Omega_k)$ is then the result of the source–to–target propagation, and the target scatterer serves as a coupling mechanism. The resulting two–way propagation reception for a general moving sonar in a depth–dependent waveguide is

$$\begin{aligned}
\psi\left(\vec{r}_0 + \vec{v}_r t,\ z_r, \omega; \vec{r}\,'_0 + \vec{v}_t t, z_t, \Omega_k\right) = \\
& \frac{1}{(2\pi)^2}\int d^2\vec{k}_r \exp\left\{\jmath\vec{k}_r \cdot \vec{r}_0\right\} G_\omega\left(\vec{k}_r, z_r, \omega + \vec{k}_r \cdot \vec{v}_r\right) \\
& \times \int d^2\vec{k}'_r \Gamma(\vec{k}_r, \alpha, \vec{k}'_r, \alpha'; \Omega_k) \exp\left\{\jmath\vec{k}'_r \cdot \vec{r}\,'_0\right\} S(\Omega'_k) G_\omega\left(\vec{k}'_r, z_t, \Omega_k + \vec{k}'_r \cdot \vec{v}_t\right)
\end{aligned} \tag{2.3}$$

where $\Gamma(\vec{k}_r, \alpha, \vec{k}'_r, \alpha'; \Omega_k)$ is the target scattering function, the new doubly Doppler-shifted frequency $\Omega'_k$ is given by

$$\Omega'_k = \Omega_k - \vec{k}'_r \cdot (\vec{v}_s - \vec{v}_t) = \omega - \vec{k}_r \cdot (\vec{v}_t - \vec{v}_r) - \vec{k}'_r \cdot (\vec{v}_s - \vec{v}_t)$$

and the terms with a prime ($\prime$) marker indicate the source to target segment of the propagation path, e.g. $r'_0$ is the distance from source to target. First, consider the Doppler shifts as they appear in Eq. (2.3). The Green's function at each $\vec{k}'_r$ is in the source–to–target segment is scattered into a continuum of shifted frequencies. The Green's function shape limits the extent of the wavenumber support, and the double integral acts as a type of outer product of the shifted Green's functions. Eq. (2.3) represents the most general case of a moving source, moving target and moving receiver in depth–dependent waveguide. This equation forms the basis upon which some basic assumptions will be made for specific cases of interest.

For convenience, the one–dimensional integral equivalents of the above equations will be employed in this thesis. The assumption that must hold is that the motion of the source, receiver and target must be small relative to the ranges of propagation during the signal transmission, scattering and reception. In effect, each propagation path must be appear to be a 2–D propagation path. Following from Schmidt and Kuperman Eq. (18), the one–way transmission is

$$\psi\left(\vec{r_0} + \vec{v}_r t, z_r, \omega\right) = \frac{1}{2} \int_{-\infty}^{\infty} dk_r k_r H_0^{(1)}(k_r r_0) S\left(\Omega_k\right) G_\omega\left(k_r, z_r, \omega + k_r(\hat{r_0} \cdot \vec{v}_r)\right) \qquad (2.4)$$

where the Doppler–shifted frequency $\Omega_k$ is now expressed $\Omega_k = \omega - k_r \hat{r}_0 \cdot (\vec{v}_t - \vec{v}_r)$, and $H_0^{(1)}(kr)$ is the zeroth order Hankel function of the first kind. For future reference, the large argument asymptote [2] of the Hankel function will be used extensively for high frequency or long range ($kr \gg 1$) cases:

$$H_0^{(1)}(kr) \approx \sqrt{\frac{2}{\pi kr}} \exp\left\{-\jmath\pi/4\right\} \exp\left\{\jmath kr\right\} \qquad (2.5)$$

Following the same argument as above, where the source–to–target transmission plus the target scattering is used as $S(\Omega_k)$, the two–way transmission can be expressed as follows:

$$\begin{aligned}\psi\left(\vec{r_0} + \vec{v}_r t,\; z_r, \omega; \vec{r_0'} + \vec{v}_t t, z_t, \Omega_k\right) &= \frac{1}{4}\int_{-\infty}^{\infty} dk_r H_0^{(1)}(k_r r_0) G_\omega\left(k_r, z_r, \omega + k_r(\hat{r}_0 \cdot \vec{v}_r)\right) \\ &\times \int_{-\infty}^{\infty} dk_r' \Gamma(k_r, \alpha, k_r', \alpha'; \Omega_k) H_0^{(1)}(k_r' r_0') S(\Omega_k') G_\omega\left(k_r', z_t, \Omega_k + k_r'(\hat{r}_0' \cdot \vec{v}_t)\right)\end{aligned} \tag{2.6}$$

where $\Gamma(\vec{k_r}, \vec{k_r'}; \Omega_k)$ is the target scattering function, the Doppler–shifted frequency $\Omega_k'$ is given by

$$\Omega_k' = \Omega_k - k_r'\hat{r}_0' \cdot (\vec{v}_s - \vec{v}_t) = \omega - k_r\hat{r}_0 \cdot (\vec{v}_t - \vec{v}_r) - k_r'\hat{r}_0' \cdot (\vec{v}_s - \vec{v}_t)$$

Eq. (2.6) holds for a sonar reception from an arbitrary source position to an arbitrary target position to an arbitrary receiver position, where all three elements may be moving in the x–y plane. Further assumptions are that the source, receiver and target are compact, and that the received signal is of a single frequency. Note again that the Doppler shifts are not reciprocal as they are in free space.

Finally for high frequency and/or long range, the approximation in (2.5) can be applied to simplify (2.6):

$$\begin{aligned}\psi\left(\vec{r_0} + \vec{v}_r t,\; z_r, \omega; \vec{r_0'} + \vec{v}_t t, z_t, \Omega_k\right) &= \\ &\frac{-\jmath}{2\pi\sqrt{r_0 r_0'}} \int_{-\infty}^{\infty} dk_r \frac{\exp\{\jmath k_r r_0\}}{\sqrt{k_r}} G_\omega\left(k_r, z_r, \omega + k_r(\hat{r}_0 \cdot \vec{v}_r)\right) \\ &\times \int_{-\infty}^{\infty} dk_r' \Gamma(k_r, \alpha, k_r', \alpha'; \Omega_k) \frac{\exp\{\jmath k_r' r_0'\}}{\sqrt{k_r'}} S(\Omega_k') G_\omega\left(k_r', z_t, \Omega_k + k_r'(\hat{r}_0' \cdot \vec{v}_t)\right)\end{aligned} \tag{2.7}$$

So there are three fundamental wavenumber integral expressions for the sonar reception at a given frequency, as represented by Eqs. (2.3), (2.6), and (2.7). In the following, the three representations will be simplified as appropriate by applying constraints for varying sonar conditions.

## Fixed Target

The first simplification of the general wavenumber integral forms is due to the assumption that the target is not moving. In this thesis, the target of interest is at all times assumed to be stationary. So applying this assumption by assigning $\vec{v}_t = \vec{0}$, Eq. (2.3) has some subtle changes:

$$\begin{aligned}\psi\left(\vec{r_0} + \vec{v}_r t, z_r, \omega; \vec{r}_0', z_t, \Omega_k\right) = \frac{1}{(2\pi)^2} \int d^2\vec{k}_r \exp\left\{\jmath \vec{k}_r \cdot \vec{r_0}\right\} G_\omega\left(\vec{k}_r, z_r, \omega + \vec{k}_r \cdot \vec{v}_r\right) \\ \times \int d^2\vec{k}_r' \Gamma(\vec{k}_r, \vec{k}_r'; \Omega_k) \exp\left\{\jmath \vec{k}_r' \cdot \vec{r}_0'\right\} S(\Omega_k') G_\omega\left(\vec{k}_r', z_t, \Omega_k\right)\end{aligned}$$

where now the Doppler–shifted frequencies are

$$\begin{aligned}\Omega_k &= \omega + \vec{k}_r \cdot \vec{v}_r \\ \Omega_k' = \Omega_k - \vec{k}_r' \cdot \vec{v}_s &= \omega + \vec{k}_r \cdot \vec{v}_r - \vec{k}_r' \cdot \vec{v}_s\end{aligned}$$

The above equations include fully bistatic sonar geometries, with arbitrary motion of source and receiver. Note that the frequency term in the Green's function is now equal to the Doppler–shifted frequency $\Omega_k$, resulting in the following form:

$$\begin{aligned}\psi\left(\vec{r_0} + \vec{v}_r t, z_r, \omega; \vec{r}_0', z_t, \Omega_k\right) = \frac{1}{(2\pi)^2} \int d^2\vec{k}_r \exp\left\{\jmath \vec{k}_r \cdot \vec{r_0}\right\} G_\omega\left(\vec{k}_r, z_r, \Omega_k\right) \\ \times \int d^2\vec{k}_r' \Gamma(\vec{k}_r, \vec{k}_r'; \Omega_k) \exp\left\{\jmath \vec{k}_r' \cdot \vec{r}_0'\right\} S(\Omega_k') G_\omega\left(\vec{k}_r', z_t, \Omega_k\right) \qquad (2.8)\end{aligned}$$

In this form, it can be seen that the Green's functions are evaluated at the same frequency for both legs of the propagation path.

Applying the Hankel transform approximation to reduce the order of the integrals, the fully bistatic reception with a fixed target becomes:

$$\begin{aligned}\psi\left(\vec{r_0}+\vec{v}_r t, z_r, \omega; \vec{r'_0}, z_t, \Omega_k\right) &= \frac{1}{4}\int_{-\infty}^{\infty} dk_r H_0^{(1)}(k_r r_0) G_\omega\left(k_r, z_r, \Omega_k\right) \\ &\times \int_{-\infty}^{\infty} dk'_r \Gamma(k_r, \alpha, k'_r, \alpha'; \Omega_k) H_0^{(1)}(k'_r r'_0) S(\Omega'_k) G_\omega\left(k'_r, z_t, \Omega_k\right) \qquad (2.9)\end{aligned}$$

where the Doppler–shifted frequencies $\Omega_k$ and $\Omega'_k$ are given by

$$\begin{aligned}\Omega_k &= \omega + k_r \hat{r}_0 \cdot \vec{v}_r \\ \Omega'_k = \Omega_k - k'_r \hat{r}'_0 \cdot \vec{v}_s &= \omega + k_r \hat{r}_0 \cdot \vec{v}_r - k'_r \hat{r}'_0 \cdot \vec{v}_s\end{aligned}$$

Finally, to provide the fixed–target equivalent of Eq. (2.7), the large argument asymptote of the Hankel function is employed to get:

$$\begin{aligned}\psi\left(\vec{r_0}+\vec{v}_r t, z_r, \omega; \vec{r'_0}, z_t, \Omega_k\right) &= \frac{-\jmath}{2\pi\sqrt{r_0 r'_0}}\int_{-\infty}^{\infty} dk_r \frac{\exp\{\jmath k_r r_0\}}{\sqrt{k_r}} G_\omega\left(k_r, z_r, \Omega_k\right) \\ &\times \int_{-\infty}^{\infty} dk'_r \Gamma(k_r, \alpha, k'_r, \alpha'; \Omega_k) \frac{\exp\{\jmath k'_r r'_0\}}{\sqrt{k'_r}} S(\Omega'_k) G_\omega\left(k'_r, z_t, \Omega_k\right) \quad (2.10)\end{aligned}$$

### Monostatic Sonar

From Eqs. (2.8)– (2.10), it is possible to reduce the problem to special cases that are of interest in this thesis. A commonly used sonar would employ a source and receiver on the same mobile platform, resulting in a monostatic sonar system. In virtually any detection/classification deployment, the source—bearing vehicle is likely to be used as a monostatic sonar system due to the relative convenience of analyzing the returns with a well–controlled . In the case of a monostatic system, $\vec{v}_s = \vec{v}_r$ and $\vec{r}_0 = -\vec{r}'_0$ and the spectral integral formulation appears as

$$\begin{aligned}\psi\left(\vec{r_0}+\vec{v}t, z_r, \omega; \vec{r_0}, z_t, \Omega_k\right) = \frac{1}{(2\pi)^2}\int d^2\vec{k_r}\exp\left\{\jmath\vec{k_r}\cdot\vec{r_0}\right\}G_\omega\left(\vec{k_r}, z_r, \Omega_k\right)\\ \times\int d^2\vec{k_r'}\Gamma(\vec{k_r}, \vec{k_r'}; \Omega_k)\exp\left\{-\jmath\vec{k_r'}\cdot\vec{r_0}\right\}S(\Omega_k')G_{\Omega_k}\left(\vec{k_r'}, z_t, \Omega_k\right)\end{aligned} \tag{2.11}$$

where the Doppler–shifted frequencies reduce to

$$\begin{aligned}\Omega_k &= \omega + \vec{k_r}\cdot\vec{v}\\ \Omega_k' = \Omega_k - \vec{k_r'}\cdot\vec{v} &= \omega + (\vec{k_r}-\vec{k_r'})\cdot\vec{v}\end{aligned}$$

Note that the wavenumber vectors for the monostatic case are in opposite directions, i.e. $\vec{k_r}$ points from the AUV to the target while $\vec{k_r'}$ points from the target to the AUV. So for corresponding waves, the dot products with the wavenumbers will sum in $\Omega_k'$. This summation is consistent with the doubled Doppler shifts from the classical SAR case, as well as with the intuitive argument that if the source/receiver is moving toward the target, both the source motion and the receiver motion serve to cause "up" Doppler shifts.

To make the 1-D monostatic result, the Hankel transform approximation is applied again. The resulting signal return is:

$$\begin{aligned}\psi\left(\vec{r}+\vec{v}t, z_r, \omega; \vec{r}, z_t, \Omega_k\right) = \frac{1}{4}\int_{-\infty}^{\infty} dk_r k_r H_0^{(1)}(k_r r)G_\omega\left(k_r, z_r, \Omega_k\right)\\ \times\int_{-\infty}^{\infty} dk_r' k_r' H_0^{(1)}(k_r' r)\Gamma(k_r, \alpha, k_r', \alpha'; \Omega_k)S(\Omega_k')G_\omega\left(k_r', z_t, \Omega_k\right)\end{aligned} \tag{2.12}$$

where now the Doppler–shifted frequencies are

$$\begin{aligned}\Omega_k &= \omega + k_r(\hat{r}\cdot\vec{v})\\ \Omega_k' = \Omega_k - k_r'(-\hat{r})\cdot\vec{v} &= \omega + (k_r + k_r')(\hat{r}\cdot\vec{v})\end{aligned}$$

Note that the wavenumber summation has become explicit in the form of $\Omega'_k$. This result arises from the fact that the pointer from source to target is the opposite direction of the pointer from target to receiver, i.e. $\hat{r}_0 = -\hat{r}'_0$, for the monostatic case.

Finally, to provide the monostatic version of Eq. (2.10), the large argument asymptote of the Hankel function is employed to get:

$$\begin{aligned}\psi\left(\vec{r}+\vec{v}_r t, z_r, \omega; \vec{r}, z_t, \Omega_k\right) &= \frac{-\jmath}{2\pi r}\int_{-\infty}^{\infty} dk_r \frac{\exp\{\jmath k_r r\}}{\sqrt{k_r}} G_\omega\left(k_r, z_r, \Omega_k\right) \\ &\times \int_{-\infty}^{\infty} dk'_r \Gamma(k_r, \alpha, k'_r, \alpha'; \Omega_k) \frac{\exp\{\jmath k'_r r\}}{\sqrt{k'_r}} S(\Omega'_k) G_\omega\left(k'_r, z_t, \Omega_k\right)\end{aligned} \qquad (2.13)$$

### Monostatic Linear SAS

The most extensively studied signal return over the trajectory of a mobile sonar or radar system is that of a linearly moving monostatic sonar/radar. This type of mobile sonar/radar system forms the basis of SAS/SAR theory, as was briefly outlined in Sec. 2.1. It is natural to presume that space–borne satellites, airborne radar aircraft, and undersea towfish move linearly over the extent of the aperture, although automated phase corrections are often necessary to enforce this condition. In this section, the highly practical linear, constant velocity, monostatic sonar system signal returns are developed for the waveguide. If the monostatic system moves with constant velocity $v_p$ past a target at a standoff range of $R$, then the propagating phase term $\vec{k}_r \cdot \vec{r}_0$ may be simplified, as shown in Cartesian coordinates for convenience:

$$\vec{k}_r \cdot \vec{r}_0 = \langle k_x, k_y \rangle \cdot \langle v_p(t - t_{CPA}), R \rangle = k_x v_p (t - t_{CPA}) + k_y R$$

Similarly, the normal velocity term $\vec{k}_r \cdot \vec{v}$ that creates the Doppler shifts is reduced to

$$\vec{k}_r \cdot \vec{v}_0 = \langle k_x, k_y \rangle \cdot \langle v_p, 0 \rangle = k_x v_p$$

Then by expanding the two–dimensional integrals in Cartesian coordinates, the spectral integral formulation of the monostatic synthetic aperture sonar receptions becomes:

$$
\begin{aligned}
&\psi\left(\vec{r}_0 + \vec{v}t,\ z_r, \omega; \vec{r}_0, z_t, \Omega_k\right) = \\
&\qquad \frac{1}{(2\pi)^2} \int\!\!\int dk_x dk_y \exp\left\{\jmath(k_x v_p(t - t_{CPA}) + k_y R)\right\} G_\omega\left(\vec{k}_r, z_r, \Omega_k\right) \\
&\qquad \times \int\!\!\int dk'_x dk'_y k'_r \Gamma(\vec{k}_r, \vec{k}'_r; \Omega_k) \exp\left\{\jmath(k'_x v_p(t - t_{CPA}) + k'_y R)\right\} \\
&\qquad \times S(\Omega'_k) G_\omega\left(\vec{k}'_r, z_t, \Omega_k\right) \qquad (2.14)
\end{aligned}
$$

where now the Doppler–shifted frequencies are

$$
\begin{aligned}
\Omega_k &= \omega + \vec{k}_r \cdot \vec{v} = \omega + k_x v_p \\
\Omega'_k = \Omega_k - \vec{k}'_r \cdot \vec{v} &= \omega + (\vec{k}_r - \vec{k}'_r) \cdot \vec{v} = \omega + (k_x + k'_x) v_p
\end{aligned}
$$

Further simplification can be made by reducing the order of the integrals to one dimension. With the Hankel transform approximation, the signal is assumed to travel along a single direction, say $\hat{r}$. It is therefore convenient to rotate the coordinates and express the dot product terms like this:

$$
\begin{aligned}
\vec{k}_r \cdot \vec{r}_0 = k_r r_0 &\approx k_r R \left(1 + \frac{v_p^2 (t - t_{CPA})^2}{2R^2}\right) \\
\vec{k}_r \cdot \vec{v} = \langle k_r, 0\rangle \cdot \langle v_p \hat{r} \cdot \hat{x}, v_p \hat{\theta} \cdot \hat{x}\rangle &\approx \frac{v_p^2 (t - t_{CPA})}{R}
\end{aligned}
$$

Applying the Hankel transform approximation, with the above dot products, resultrs in the following 1-D integral formula for monostatic linear SAS in the waveguide:

$$\begin{aligned}
&\psi\left(\vec{r_0}+\vec{v}t,\ z_r,\omega;\vec{r_0},z_t,\Omega_k\right)= \\
&\qquad \frac{1}{(2\pi)^2}\int dk_r H_0^{(1)}\left(k_r\left\{R+\frac{v_p^2(t-t_{CPA})^2}{2R}\right\}\right)G_\omega\left(k_r,z_r,\Omega_k\right) \\
&\qquad \times\int dk_r'\Gamma(k_r,\alpha,k_r',\alpha';\Omega_k)H_0^{(1)}\left(k_r'\left\{R+\frac{v_p^2(t-t_{CPA})^2}{2R}\right\}\right) \\
&\qquad \times S(\Omega_k')G_{\Omega_k}\left(k_r',z_t,\Omega_k\right) \qquad (2.15)
\end{aligned}$$

where now the Doppler–shifted frequencies are

$$\Omega_k=\omega+k_r\frac{v_p^2(t-t_{CPA})}{R}$$

$$\Omega_k'=\Omega_k+k_r\hat{r_0}\cdot\vec{v}-k_r'(-\hat{r_0})\cdot\vec{v}=\omega+(k_r+k_r')\frac{v_p^2(t-t_{CPA})}{R}$$

Note that the instantaneous Doppler can be seen to be directly analogous to the heuristic argument in Sec. 2.1. In free space, there is a single ray connecting the source to target, and the propagating wavenumber is fixed, $k_r=k_r'=2\pi/\lambda$. Plugging these values into the above Doppler–shifted frequencies, the Doppler shifts for free–space SAS/SAR are realized:

$$f_D=\frac{1}{2\pi}\left(\omega-\Omega_k\right)=-\frac{1}{2\pi}\frac{2\pi}{\lambda}\frac{v_p^2(t-t_{CPA})}{R}=-\frac{v_p^2(t-t_{CPA})}{\lambda R}$$

for one–way propagation and

$$f_D=\frac{1}{2\pi}\left(\omega-\Omega_k'\right)=-\frac{1}{2\pi}\left(\frac{2\pi}{\lambda}+\frac{2\pi}{\lambda}\right)\frac{v_p^2(t-t_{CPA})}{R}=-\frac{2v_p^2(t-t_{CPA})}{\lambda R}$$

for round–trip monostatic SAS.

Similarly, the apparent Doppler in the propagation term appears:

$$f_D = -\frac{1}{2\pi}\frac{\partial}{\partial t}\left[k_r\left(R + \frac{v_p^2(t - t_{CPA})^2}{2R}\right)\right] = -\frac{v_p^2(t - t_{CPA})}{\lambda R}$$

for one–way and

$$f_D = -\frac{1}{2\pi}\frac{\partial}{\partial t}\left[k_r\left(R + \frac{v_p^2(t - t_{CPA})^2}{2R}\right) + k_r'\left(R + \frac{v_p^2(t - t_{CPA})^2}{2R}\right)\right] = -\frac{2v_p^2(t - t_{CPA})}{\lambda R}$$

for two–way propagation.

Finally, the linear, monostatic SAS version of Eq. (2.13) is written using the far–field ($kr \gg 1$) approximation:

$$\begin{aligned} \psi\left(\vec{r} + \vec{v}_r t, z_r, \omega; \vec{r}, z_t, \Omega_k\right) &= \frac{-\jmath}{2\pi r}\int_{-\infty}^{\infty} dk_r \frac{\exp\{\jmath k_r r\}}{\sqrt{k_r}} G_\omega\left(k_r, z_r, \Omega_k\right) \\ &\times \int_{-\infty}^{\infty} dk_r' \Gamma(k_r, \alpha, k_r', \alpha'; \Omega_k) \frac{\exp\{\jmath k_r' r\}}{\sqrt{k_r'}} S(\Omega_k') G_\omega\left(k_r', z_t, \Omega_k\right) \end{aligned} \tag{2.16}$$

where

$$r = R + \frac{v_p^2(t - t_{CPA})^2}{2R}$$

### Fixed Source, Bistatic Linear SAS

In several cases of interest, the sonar source is stationary or nearly stationary while the receiver moves. For example, if the source is far away from the target while the receiver is near the target. The range approximation is applied in this case only to the target–to–receiver path, i.e. the second integral. In the spectral integral formulation, the bistatic sonar reception becomes:

$$
\begin{aligned}
&\psi\left(\vec{r_0} + \vec{v}t,\ z_r, \omega; \vec{r_0}, z_t, \Omega_k\right) = \\
&\qquad \frac{1}{(2\pi)^2} \int\!\!\int dk_x dk_y \exp\left\{\jmath(k_x v_p(t - t_{CPA}) + k_y R)\right\} G_\omega\left(\vec{k_r}, z_r, \Omega_k\right) \\
&\qquad \times \int d^2\vec{k}'_r \Gamma(\vec{k_r}, \vec{k}'_r; \Omega_k) \exp\left\{\jmath \vec{k}'_r \cdot \vec{r_s}\right\} S(\Omega'_k) G_{\Omega_k}\left(\vec{k}'_r, z_t, \Omega_k\right)
\end{aligned}
\tag{2.17}
$$

where $\vec{r_s}$ is the fixed range vector from source to target. The Doppler–shifted frequencies are now

$$
\begin{aligned}
\Omega_k = \omega + \vec{k_r} \cdot \vec{v} \approx \omega + k_r \frac{v_p^2(t - t_{CPA})}{R} \\
\Omega'_k = \Omega_k
\end{aligned}
$$

The Hankel transform approximation can be made again to provide a more computationally efficient, 1-D integral formulation. In the fixed source, bistatic linear SAS receiver, the Hankel transform representation appears as:

$$
\begin{aligned}
&\psi\left(\vec{r_0} + \vec{v}t,\ z_r, \omega; \vec{r_0}, z_t, \Omega_k\right) = \\
&\qquad \frac{1}{4} \int dk_r k_r H_0^{(1)}(k_r \left(R + \frac{v_p^2(t - t_{CPA})^2}{2R}\right)) G_\omega\left(k_r, z_r, \Omega_k\right) \\
&\qquad \times \int dk'_r k'_r \Gamma(k_r, \alpha, k'_r, \alpha'; \Omega_k) H_0^{(1)}(k'_r R_s) S(\Omega'_k) G_{\Omega_k}\left(k'_r, z_t, \Omega_k\right)
\end{aligned}
\tag{2.18}
$$

where $R_s$ is the fixed distance from source to target. The Doppler–shifted frequencies are now

$$
\begin{aligned}
\Omega_k = \omega + k_r \frac{v_p^2(t - t_{CPA})}{R} \\
\Omega'_k = \Omega_k
\end{aligned}
$$

Finally, the long–range, high $kr$ result is realized through the application of the large–argument asymptote of the Hankel transform, arriving with the bistatic equivalent of Eq. (2.16) — the fixed source, bistatic linearly moving receiver result:

$$\begin{aligned}\psi\left(\vec{r}+\vec{v}_r t, z_r, \omega; \vec{r}, z_t, \Omega_k\right) &= \frac{-\jmath}{2\pi\sqrt{rR_s}} \int_{-\infty}^{\infty} dk_r \frac{\exp\left\{\jmath k_r r\right\}}{\sqrt{k_r}} G_\omega\left(k_r, z_r, \Omega_k\right) \\ &\times \int_{-\infty}^{\infty} dk'_r \Gamma(k_r, \alpha, k'_r, \alpha'; \Omega_k) \frac{\exp\left\{\jmath k'_r r\right\}}{\sqrt{k'_r}} S(\Omega'_k) G_\omega\left(k'_r, z_t, \Omega_k\right) \qquad (2.19)\end{aligned}$$

where

$$r = R + \frac{v_p^2 (t - t_{CPA})^2}{2R}$$

This concludes the relevant spectral integral models that are applied in this thesis. Further canonical models can be derived through a similar approach, including circular SAS or other regular trajectories. The following section will demonstrate the normal modes formulation of all of the above sonar deployments.

### 2.2.2 Normal Modes Model

To arrive at the normal modes respresentation of the signal, the Green's function of the spectral integral model is replaced by

$$G(\vec{k}_r, z; \omega) \approx \frac{1}{2\pi\rho(z_s)} \sum_{n=0}^{\infty} \frac{\Psi_n(z)\Psi_n(z_s)}{k_r^2 - k_n^2} \qquad (2.20)$$

where $k_n$ and $\Psi_n$ are the associated modal wavenumbers (eigenvalues) and mode shapes (eigenvectors) of the depth–separated wave equation [70]. The $\omega$ influence, which is subject to Doppler shift, is contained in the wave equation, so the eigenvalues and eigenvectors are shifted appropriately. In this formulation, the mode shapes are assumed constant due to the relatively small Doppler shifts, so the effect of the Doppler shift resides solely in the modal wavenumbers $k_n$. Assuming the shift to be small, the wavenumber is expanded using a first–order Taylor expansion. The

Doppler shifted Green's function is then

$$G(\vec{k}_r, z; \omega + \vec{k}_r \cdot \vec{v}_r) \approx \frac{1}{2\pi\rho(z_s)} \sum_{n=0}^{\infty} \frac{\Psi_n(z)\Psi_n(z_s)}{k_r^2 - \left[k_n(1 + \hat{r}_0 \cdot \vec{v}_r \, \frac{\partial k_n}{\partial \omega}\big|_\omega\right]^2} \tag{2.21}$$

For one-way transmission, Eq. (2.21) can be inserted into (2.2) to produce the one-way normal mode Doppler shifted result consistent with [70] Eq. (22):

$$\psi\left(\vec{r}_0 + \vec{v}_r t, z_r, \omega\right) \approx \frac{\jmath}{4\rho(z_s)} \sum_{n=0}^{\infty} S\left(\Omega_n\right) \Psi_n(z_r)\Psi_n(z_s) H_0^{(1)}\left(k_n r_0 (1 + \hat{r}_0 \cdot \vec{v}_r \left.\frac{\partial k_n}{\partial \omega}\right|_\omega\right) \tag{2.22}$$

where

$$\Omega_n = \omega - k_n \hat{r}_0 \cdot (\vec{v}_s - \vec{v}_r)$$

and noting that the group speed of each mode $v_{g,n}$ is given by:

$$v_{g,n} = \frac{\partial \omega}{\partial k_n}$$

so the Doppler shift is a function of the ratio of the platform velocity to the group speed of each mode. In contrast, the free-space Doppler shift is a ratio of the platform velocity to the material compressional wavespeed. The Doppler shift term in the Hankel function argument comes from an approximate first-order Taylor expansion of the modal wavenumber $k_n$:

$$\begin{aligned} k_n\big|_{\omega + k_n(\vec{v}_r \cdot \hat{r}_0)} &\approx k_n\big|_\omega + \left.\frac{\partial k_n}{\partial \omega}\right|_\omega (\omega + k_n(\vec{v}_r \cdot \hat{r}) - \omega) \\ &= k_n + k_n(\vec{v}_r \cdot \hat{r}_0) \left.\frac{\partial k_n}{\partial \omega}\right|_\omega \\ &= k_n \left[1 + \hat{r}_0 \cdot \vec{v}_r \left.\frac{\partial k_n}{\partial \omega}\right|_\omega\right] \end{aligned}$$

Applying the large-argument asymptotic expression for the Hankel function provides the long-range (or high frequency) version of Eq. (2.22):

$$
\begin{aligned}
\psi\left(\vec{r_0}+\vec{v}_r t,\ \ z_r,\omega\right) &\approx \\
&\approx \frac{\jmath \exp\left\{-\jmath\frac{\pi}{4}\right\}}{\rho(z_s)\sqrt{8\pi r_0}} \sum_{n=0}^{\infty} S\left(\Omega_n\right)\Psi_n(z_r)\Psi_n(z_s) \frac{\exp\left\{\jmath k_n r_0 (1+\hat{r}_0\cdot\vec{v}_r\ \frac{\partial k_n}{\partial\omega})\big|_\omega\right\}}{\sqrt{k_n(1+\hat{r}_0\cdot\vec{v}_r\ \frac{\partial k_n}{\partial\omega}\big|_\omega)}} \\
&\approx \frac{\exp\left\{\jmath\frac{\pi}{4}\right\}}{\rho(z_s)\sqrt{8\pi r_0}} \sum_{n=0}^{\infty} S\left(\Omega_n\right)\Psi_n(z_r)\Psi_n(z_s) \frac{\exp\left\{\jmath k_n r_0 (1+\hat{r}_0\cdot\vec{v}_r\ \frac{\partial k_n}{\partial\omega})\big|_\omega\right\}}{\sqrt{k_n}}
\end{aligned}
\tag{2.23}
$$

The two–way transmission can then be derived following the same argument reported in Sec. 2.2.1. Namely, that the one–way equation, Eq. (2.22), is considered for the target–to–receiver segment, and the source–to–target signal is included in the source term, with the target scattering function providing a link between the two segments. Also following the same notation as in the spectral integral formulations, the normal modes formulation for the two–way propagation with general (horizontally) moving source, target and receiver is expressed:

$$
\begin{aligned}
\psi\left(\vec{r}_0+\vec{v}_r t,\ \ z_r,\omega;\vec{r}\,'_0+\vec{v}_t t, z_t\right) &\approx \frac{-1}{16\rho(z_s)\rho(z_t)} \\
&\times \sum_{n=0}^{\infty}\Psi_n(z_t)\Psi_n(z_r)H_0^{(1)}\left(k_n\left\{1+\hat{r}_0\cdot\vec{v}_r\ \frac{\partial k_n}{\partial\omega}\bigg|_\omega\right\}\right) \\
&\times \sum_{m=0}^{\infty}\Gamma(k_n,k_m;\Omega_n)S\left(\Omega_{mn}\right)\Psi_m(z_s)\Psi_m(z_t) \\
&\times H_0^{(1)}\left(k_m\left[1+\left\{\hat{r}'_0\cdot\vec{v}_t+\frac{k_n}{k_m}(\hat{r}_0\cdot\vec{v}_r)\right\}\frac{\partial k_m}{\partial\omega}\bigg|_\omega\right]\right)
\end{aligned}
\tag{2.24}
$$

where

$$
\Omega_n = \omega - k_n\hat{r}_0\cdot(\vec{v}_t-\vec{v}_r)
$$

$$
\Omega_{mn} = \Omega_n - k_m\hat{r}'_0\cdot(\vec{v}_s-\vec{v}_t)
$$

Note that the argument of the second Hankel function (that of the source–to–target summation) is derived similarly to the one–way method, via a first–order Taylor expansion. The term finishes with a computationally problematic interlocution of terms from both summations:

$$\begin{aligned}
k_m\Big|_{\omega+k_n(\vec{v}_r\cdot\hat{r}_0)+k_m(\vec{v}_t\cdot\hat{r}'_0)} &\approx k_m\Big|_\omega + \left.\frac{\partial k_m}{\partial\omega}\right|_\omega \{\omega + k_n(\vec{v}_r\cdot\hat{r}) + k_m(\vec{v}_t\cdot\hat{r}'_0) - \omega\} \\
&= k_m + [k_n(\vec{v}_r\cdot\hat{r}_0) + k_m(\vec{v}_t\cdot\hat{r}'_0)]\left.\frac{\partial k_m}{\partial\omega}\right|_\omega \\
&= k_m\left[1 + \left\{\frac{k_n}{k_m}(\hat{r}_0\cdot\vec{v}_r) + \vec{v}_t\cdot\hat{r}'_0\right\}\left.\frac{\partial k_n}{\partial\omega}\right|_\omega\right]
\end{aligned}$$

which renders the summations inseparable. This term goes identically to zero only when the normal component of the receiver velocity goes to zero, which is contrary to the concept of roving receivers espoused in this thesis. It is, however, possible to choose a representative $k_n$ for expedience in separating the summations.

The mode shapes $\Psi_m$ should be evaluated at the Doppler–shifted frequency $\Omega_k$, but the assumption has been made that the mode shapes remain constant over the relatively small Doppler shifts. The Doppler shifts remain in the highly sensitive phase terms in the propagation. Considering the Doppler shifts, note that each shift $m$ scatters into all outgoing modes $n$. Since there are an infinite number of discrete modes, the result is a countably infinite number of Doppler shifts. If the analysis is limited to $N$ propagating modes, then there are $N^2$ Doppler–shifted signal returns.

For long-range or high frequency transmission, the large–argument asymptote of the Hankel function is inserted in Eq. (2.24) to get:

$$\begin{aligned}\psi\left(\vec{r}_0+\vec{v}_r t,\ z_r,\omega;\vec{r}\,'_0+\vec{v}_t t,z_t\right) &\approx \frac{\jmath}{8\pi\rho(z_s)\rho(z_t)\sqrt{r_0 r'_0}} \\ &\times\sum_{n=0}^{\infty}\Psi_n(z_t)\Psi_n(z_r)\frac{\exp\left[\jmath k_n r_0\left\{1+\hat{r}_0\cdot\vec{v}_r\ \tfrac{\partial k_n}{\partial\omega}\big|_\omega\right\}\right]}{\sqrt{k_n}} \\ &\times\sum_{m=0}^{\infty}\Psi_m(z_s)\Psi_m(z_t)\frac{\exp\left[\jmath k_m r'_0\left[1+\left\{\hat{r}'_0\cdot\vec{v}_t+\tfrac{k_n}{k_m}(\hat{r}_0\cdot\vec{v}_r)\right\}\ \tfrac{\partial k_m}{\partial\omega}\big|_\omega\right]\right]}{\sqrt{k_m}} \\ &\times\Gamma(k_n,k_m;\Omega_n)S\left(\Omega_{mn}\right) \qquad (2.25)\end{aligned}$$

### Fixed Target

In the case of the fixed target, as is assumed throughout this thesis, $\vec{v}_t=\vec{0}$ and the Doppler shifts in the Hankel (Green's) functions take a similar form. For the fixed target:

$$\begin{aligned}\psi\left(\vec{r}_0+\vec{v}_r t,\ z_r,\omega;\vec{r}\,'_0,z_t\right) &\approx \frac{-1}{16\rho(z_s)\rho(z_t)} \\ &\times\sum_{n=0}^{\infty}\Psi_n(z_t)\Psi_n(z_r)H_0^{(1)}\left(k_n r_0\left\{1+\hat{r}_0\cdot\vec{v}_r\ \frac{\partial k_n}{\partial\omega}\bigg|_\omega\right\}\right) \\ &\times\sum_{m=0}^{\infty}\Psi_m(z_s)\Psi_m(z_t)H_0^{(1)}\left(k_m r'_0\left[1+\frac{k_n}{k_m}(\hat{r}_0\cdot\vec{v}_r)\ \frac{\partial k_m}{\partial\omega}\bigg|_\omega\right]\right) \\ &\times\Gamma(k_n,k_m;\Omega_n)S\left(\Omega_{mn}\right) \qquad (2.26)\end{aligned}$$

where

$$\Omega_n=\omega+k_n\hat{r}_0\cdot\vec{v}_r$$

$$\Omega_{mn}=\Omega_n-k_m\hat{r}'_0\cdot\vec{v}_s$$

Note that the fixed target representation is consistent with that of the spectral integrals in that the depth–dependent Green's functions take the same form, but evaluated at different wavenumbers and different depths. Roughly speaking,

$$\begin{aligned}
G_\omega\left(k_n, z_r, \Omega_n\right) &\sim \Psi(z_r) H_0^{(1)}\left(k_n r_0 + k_n r_0 (\hat{r}_0 \cdot \vec{v}_r) \left.\frac{\partial k_n}{\partial \omega}\right|_\omega\right) \\
G_\omega\left(k_m, z_t, \Omega_n\right) &\sim \Psi(z_t) H_0^{(1)}\left(k_m r_0 + k_n r_0 (\hat{r}_0 \cdot \vec{v}_r) \left.\frac{\partial k_m}{\partial \omega}\right|_\omega\right)
\end{aligned}$$

In the high frequency regime ($kr \gg 1$), the fixed target signal model for bistatic, moving source and moving receiver is as follows:

$$\begin{aligned}
\psi\left(\vec{r}_0 + \vec{v}_r t,\ z_r, \omega; \vec{r}_0', z_t\right) \approx{} & \frac{\jmath}{8\pi \rho(z_s) \rho(z_t) \sqrt{r_0 r_0'}} \\
& \times \sum_{n=0}^{\infty} \Psi_n(z_t) \Psi_n(z_r) \frac{\exp\left[\jmath k_n r_0 \left\{1 + \hat{r}_0 \cdot \vec{v}_r \left.\frac{\partial k_n}{\partial \omega}\right|_\omega\right\}\right]}{\sqrt{k_n}} \\
& \times \sum_{m=0}^{\infty} \Psi_m(z_s) \Psi_m(z_t) \frac{\exp\left[\jmath k_m r_0' \left[1 + \frac{k_n}{k_m} (\hat{r}_0 \cdot \vec{v}_r) \left.\frac{\partial k_m}{\partial \omega}\right|_\omega\right]\right]}{\sqrt{k_m}} \\
& \times \Gamma(k_n, k_m; \Omega_n) S\left(\Omega_{mn}\right) \qquad (2.27)
\end{aligned}$$

### Monostatic Sonar

For a monostatic mobile sonar, the ranges $r_0 = r_0' = r$ and the velocities $\vec{v}_r = \vec{v}_s = \vec{v}$ of the source and receiver are equal. The direction of the range pointers are opposite in sign, i.e. $\hat{r}_0 = -\hat{r}_0' = \hat{r}$. Applying these assumptions, the modal formulation of a monostatic sonar system is given by:

$$\begin{aligned}
\psi\left(\vec{r} + \vec{v} t,\ z_r, \omega; \vec{r}, z_t\right) \approx{} & \frac{-1}{16 \rho(z_s) \rho(z_t)} \sum_{n=0}^{\infty} \Psi_n(z_t) \Psi_n(z_r) H_0^{(1)}\left(k_n r \left\{1 + \hat{r} \cdot \vec{v} \left.\frac{\partial k_n}{\partial \omega}\right|_\omega\right\}\right) \\
& \times \sum_{m=0}^{\infty} \Psi_m(z_s) \Psi_m(z_t) H_0^{(1)}\left(k_m r \left[1 + \frac{k_n}{k_m} (\hat{r} \cdot \vec{v}) \left.\frac{\partial k_m}{\partial \omega}\right|_\omega\right]\right) \\
& \times \Gamma(k_n, k_m; \Omega_n) S\left(\Omega_{mn}\right) \qquad (2.28)
\end{aligned}$$

where

$$\Omega_n = \omega + k_n \hat{r} \cdot \vec{v}$$
$$\Omega_{mn} = \Omega_n - k_m(-\hat{r}) \cdot \vec{v} = \omega + (k_n + k_m)\hat{r} \cdot \vec{v}$$

In the high frequency regime ($kr \gg 1$), the fixed target signal model for a monostatic sonar platform is as follows:

$$\begin{aligned} \psi\left(\vec{r}+\vec{v}t,\ z_r,\omega;\vec{r},z_t\right) \approx {} & \frac{\jmath}{8\pi\rho(z_s)\rho(z_t)r}\sum_{n=0}^{\infty}\Psi_n(z_t)\Psi_n(z_r)\frac{\exp\left[\jmath k_n r\left\{1+\hat{r}\cdot\vec{v}\ \frac{\partial k_n}{\partial\omega}\Big|_{\omega}\right\}\right]}{\sqrt{k_n}} \\ & \times\sum_{m=0}^{\infty}\Psi_m(z_s)\Psi_m(z_t)\frac{\exp\left[\jmath k_m r\left[1+\frac{k_n}{k_m}(\hat{r}\cdot\vec{v})\ \frac{\partial k_m}{\partial\omega}\Big|_{\omega}\right]\right]}{\sqrt{k_m}}\Gamma(k_n,k_m;\Omega_n)S\left(\Omega_{mn}\right) \end{aligned} \tag{2.29}$$

### Monostatic Linear SAS

For a monostatic linear synthetic aperture format, the receptions of the mobile sonar platform can be derived in normal modes following the same argument as in section 2.2.1. Starting with the relevant approximations of the range to target:

$$r \approx R + \frac{v_p^2(t-t_{CPA})^2}{2R} \tag{2.30}$$

and

$$\hat{r}\cdot\vec{v} = \frac{\langle R, v_p(t-t_{CPA})\rangle}{\sqrt{R^2+v_p^2(t-t_{CPA})^2}}\cdot\langle 0, v_p\rangle = \frac{v_p^2(t-t_{CPA})}{\sqrt{R^2+v_p^2(t-t_{CPA})^2}} \approx \frac{v_p^2(t-t_{CPA})}{R}$$

Then the sonar receptions can be written as follows:

$$
\begin{aligned}
\psi\left(\vec{r}+\vec{v}t,\ z_r,\omega;\vec{r},z_t\right) \approx\ & \frac{-1}{16\rho(z_s)\rho(z_t)} \\
& \times \sum_{n=0}^{\infty} \Psi_n(z_t)\Psi_n(z_r) H_0^{(1)}\left(k_n r\left\{1+\frac{v_p^2(t-t_{CPA})}{R}\left.\frac{\partial k_n}{\partial\omega}\right|_{\omega}\right\}\right) \\
& \times \sum_{m=0}^{\infty} \Psi_m(z_s)\Psi_m(z_t) H_0^{(1)}\left(k_m r\left[1+\frac{k_n}{k_m}\frac{v_p^2(t-t_{CPA})}{R}\left.\frac{\partial k_m}{\partial\omega}\right|_{\omega}\right]\right) \\
& \times \Gamma(k_n,k_m;\Omega_n)S\left(\Omega_{mn}\right) \qquad (2.31)
\end{aligned}
$$

where

$$
\begin{aligned}
\Omega_n &= \omega + k_n\frac{v_p^2(t-t_{CPA})}{R} \\
\Omega_{mn} &= \Omega_n - k_m(-\hat{r})\cdot\vec{v} = \omega + (k_n+k_m)\frac{v_p^2(t-t_{CPA})}{R}
\end{aligned}
$$

In the high frequency regime ($kr \gg 1$), the fixed target signal model for a monostatic linear SAS sonar platform is as follows:

$$
\begin{aligned}
\psi\left(\vec{r}+\vec{v}t,\ z_r,\omega;\vec{r},z_t\right) \approx\ & \frac{\jmath}{8\pi\rho(z_s)\rho(z_t)r} \\
& \times \sum_{n=0}^{\infty} \Psi_n(z_t)\Psi_n(z_r)\frac{\exp\left[\jmath k_n r\left\{1+\frac{v_p^2(t-t_{CPA})}{R}\left.\frac{\partial k_n}{\partial\omega}\right|_{\omega}\right\}\right]}{\sqrt{k_n}} \\
& \times \sum_{m=0}^{\infty} \Psi_m(z_s)\Psi_m(z_t)\frac{\exp\left[\jmath k_m r\left\{1+\frac{k_n}{k_m}\frac{v_p^2(t-t_{CPA})}{R}\left.\frac{\partial k_m}{\partial\omega}\right|_{\omega}\right\}\right]}{\sqrt{k_m}} \\
& \times \Gamma(k_n,k_m;\Omega_n)S\left(\Omega_{mn}\right) \qquad (2.32)
\end{aligned}
$$

### Bistatic, Fixed Source

For a bistatic mobile sonar with a stationary source, $\vec{v}_s = \vec{0}$:

$$\begin{aligned}\psi\left(\vec{r}_0+\vec{v}_r t,\ z_r,\omega;\vec{r}^{\,\prime}_0,z_t\right) \approx{}& \frac{-1}{16\rho(z_s)\rho(z_t)} \\ &\times \sum_{n=0}^{\infty}\Psi_n(z_t)\Psi_n(z_r)H_0^{(1)}\left(k_n r_0\left\{1+\hat{r}_0\cdot\vec{v}_r\left.\frac{\partial k_n}{\partial\omega}\right|_{\omega}\right\}\right) \\ &\times S\left(\Omega_n\right)\sum_{m=0}^{\infty}\Psi_m(z_s)\Psi_m(z_t)H_0^{(1)}\left(k_m r_0'\left[1+\frac{k_n}{k_m}(\hat{r}_0\cdot\vec{v}_r)\left.\frac{\partial k_m}{\partial\omega}\right|_{\omega}\right]\right) \\ &\times \Gamma(k_n,k_m;\Omega_n) \qquad (2.33)\end{aligned}$$

where

$$\Omega_n = \omega + k_n\hat{r}_0\cdot\vec{v}_r$$
$$\Omega_{mn} = \Omega_n$$

and the only difference from the bistatic, fixed target case is that the source amplitude no longer depends upon the incoming mode number $m$. This independence is computationally convenient as it allows the $S(\omega)$ term to be pulled out of the second summation. Of course, for a band–limited impulse source, the same could be done if the source signal is selected to be a band–limited impulse.

In the high frequency regime ($kr \gg 1$), the fixed target signal model for bistatic, moving source and moving receiver is as follows:

$$\begin{aligned}\psi\left(\vec{r}_0+\vec{v}_r t,\ z_r,\omega;\vec{r}^{\,\prime}_0,z_t\right) \approx{}& \frac{\jmath}{8\pi\rho(z_s)\rho(z_t)\sqrt{r_0 r_0'}} \\ &\times \sum_{n=0}^{\infty}\Psi_n(z_t)\Psi_n(z_r)\frac{\exp\left[\jmath k_n r_0\left\{1+\hat{r}_0\cdot\vec{v}_r\left.\frac{\partial k_n}{\partial\omega}\right|_{\omega}\right\}\right]}{\sqrt{k_n}} \\ &\times S\left(\Omega_n\right)\sum_{m=0}^{\infty}\Psi_m(z_s)\Psi_m(z_t)\frac{\exp\left[\jmath k_m r_0'\left[1+\frac{k_n}{k_m}(\hat{r}_0\cdot\vec{v}_r)\left.\frac{\partial k_m}{\partial\omega}\right|_{\omega}\right]\right]}{\sqrt{k_m}} \\ &\times \Gamma(k_n,k_m;\Omega_n) \qquad (2.34)\end{aligned}$$

### Bistatic, Fixed Source, Linear SAS

Further constraining the bistatic, fixed source case to the linear receiver SAS problem provides some further simplification. As mentioned previously, the stationary or apparently stationary source problem is of interest in the multi–vehicle deployment scheme. Also considering that the receiver can be assumed to be moving linearly at least over a short period of time, the bistatic, fixed source, linear SAS scenario becomes an important canonical case. Then the sonar receptions can be written as follows:

$$\begin{aligned} \psi\left(\vec{r}_0 + \vec{v}_r t,\ z_r, \omega; \vec{r}_0', z_t\right) \approx & \frac{-1}{16\rho(z_s)\rho(z_t)} \\ & \times \sum_{n=0}^{\infty} \Psi_n(z_t)\Psi_n(z_r) H_0^{(1)}\left(k_n r_0 \left\{1 + \hat{r}_0 \cdot \vec{v}_r \left.\frac{\partial k_n}{\partial \omega}\right|_{\omega}\right\}\right) \\ & \times S\left(\Omega_n\right) \sum_{m=0}^{\infty} \Psi_m(z_s)\Psi_m(z_t) H_0^{(1)}\left(k_m r_0' \left[1 + \frac{k_n}{k_m}(\hat{r}_0 \cdot \vec{v}_r) \left.\frac{\partial k_m}{\partial \omega}\right|_{\omega}\right]\right) \\ & \times \Gamma(k_n, k_m; \Omega_n) \end{aligned} \tag{2.35}$$

where

$$\Omega_n = \omega + k_n \hat{r}_0 \cdot \vec{v}_r$$

$$\Omega_{mn} = \Omega_n$$

In the high frequency regime ($kr \gg 1$), the fixed target signal model for a bistatic linear SAS sonar platform is as follows:

$$\begin{aligned}\psi\left(\vec{r}+\vec{v}t,\ z_r,\omega;\vec{r},z_t\right) \approx{}& \frac{\jmath}{8\pi\rho(z_s)\rho(z_t)r} \\ &\times\sum_{n=0}^{\infty}\Psi_n(z_t)\Psi_n(z_r)\frac{\exp\left[\jmath k_n r\left\{1+\frac{v_p^2(t-t_{CPA})}{R}\ \frac{\partial k_n}{\partial\omega}\Big|_{\omega}\right\}\right]}{\sqrt{k_n}} \\ &\times S\left(\Omega_n\right)\sum_{m=0}^{\infty}\Psi_m(z_s)\Psi_m(z_t)\frac{\exp\left[\jmath k_m R_s\left\{1+\frac{k_n}{k_m}\frac{v_p^2(t-t_{CPA})}{R}\ \frac{\partial k_m}{\partial\omega}\Big|_{\omega}\right\}\right]}{\sqrt{k_m}} \\ &\times\Gamma(k_n,k_m;\Omega_n) \qquad (2.36)\end{aligned}$$

where $R_s$ is the fixed range from source to target, and the distance from target to receiver is given by Eq. (2.30).

# Part II

# Target Classification with Passively Mobile Sonar Platforms

# Chapter 3

# Synthetic Aperture Sonar with Mobile Sonar Platforms in the Littoral Ocean

An obvious place to start venturing into the world of arbitrarily moving platforms is to constrain vehicle motion to nearly straight lines and apply well–worn and established methods of signal processing and analysis. Synthetic aperture sonar for imaging is the most clear example of exploiting the moving sonar for some sonar advantage, in this case azimuthal resolution. With the mobile sonar platforms, there are some small steps away from traditional monostatic SAS, including bistatic SAS, for which it is possible to apply many of the lessons learned in SAS development. However, monostatic SAS has some way to go to become generally and robustly applicable for a roving sonar system.

The mobile monostatic sonar design has some advantages for analytical results. The most powerful advantage is the large body of literature that is readily available on closely related subjects. Towed sonar arrays and radar satellites are examples of moving platforms that tolerate slight deviations from a linear or orbital path. Large deviations and unplanned paths are covered more thoroughly in the robotics literature, in which robots carrying video, laser or sonar sensors attempt to accurately navigate themselves in an unknown environment. In this chapter, the work in these fields is leveraged and adapted to fit the mobile monostatic sonar system that is to be employed in this thesis.

## 3.1 Motion Compensation

A fundamental characteristic of highly mobile sonar systems is that they are relatively small. Sonar–bearing research AUVs are typically about 1–3 $m$ [20] in length. The physical receiver aperture is limited by the length of the AUV, which in turn limits the resolution of the physical aperture. In order to enhance the resolution of the sonar system, multiple pings can be coherently summed to give a longer apparent receiver aperture using a synthetic aperture approach. In sonar systems, the difficult part of synthetic aperture formation is typically the navigation uncertainty. Sub–wavelength accuracy is required for coherent integration along the platform trajectory, and typical navigation systems are not accurate to sub–wavelength accuracy for the imaging sonars. Typical navigation errors for long baseline systems are on the order of 1 $m$ absolute [50], while even high–end inertial navigation systems (INS), which have the additional problem of being expensive and large [44], have navigational drift on the order of $10°/hr$ [25]. Kalman filters are used to fuse a number of sensors for improved stable navigation, but typical errors remain measured in meters [26] rather than fractions of a wavelength. There has been, to date, one attempt to employ an INS system directly into SAS processing, and it required a worldwide search for a customized INS system that met the required specifications [34].

This section examines a commonly used micronavigation technique for SAS imaging based on the seabed reverberation. The implications of seabed properties, bi–static sonars, and lower sonar frequencies such as those used for buried mine hunting are investigated within this micronavigation context. Finally, the relationship between micronavigation accuracy and sonar performance is investigated.

### 3.1.1 Displaced Phase Center Antenna (DPCA)

The displaced phase center antenna (DPCA) method is commonly applied in SAS systems for sub–wavelength relative navigation. For a given source/receiver pair, the displaced phase center corresponds to the point at which a true monostatic source/receiver unit would be to result in the same signal paths. Under the assumptions of being in the far field, and with a uniform sound velocity profile, the phase center is identically the geometric mean position between the source and receiver. The idea behind the DPCA micronavigation is to cross–correlate returns from consecutive pings and employ the overlapping segment of the array for motion compensation. A thorough development of this theory for monostatic linear, planar and volumetric sonars is provided by Doisy [19], while performance bounds for linear arrays have been addressed by authors at NATO SACLANTCEN [60, 10]. Although the relative error is small on a ping–to–ping basis, the error is cumulative over the formed synthetic aperture, so it must be extremely small from one ping to the next in order to provide a coherent aperture for imaging.

A simple description of the DPCA follows in order to form a basis and a lead–in to some original work of this thesis. The linear array is used for convenience, as illustrated in Fig. 3-1. In this figure, a discrete linear array is shown at two consecutive pings. Between pings, the array has translated, swayed and yawed. At the center of the array is a source, shown in red. The displaced phase centers are shown as gray dots, and are located at the midpoint between the source and each receiver element. They are slightly offset in the diagram for visibility. Note that the resulting DPCA is half the length of the original array, and the sensor spacing is $\Delta x/2$. Assuming the array moves slowly enough with respect to the ping interval $\tau_p$, there is an overlapping segment of the two consecutive DPCAs. The overlapping segment is required for micronavigation, leading to the restriction on platform speed $v_p$.

$$v_p \leq \frac{N\Delta_x}{2\tau_p} \tag{3.1}$$

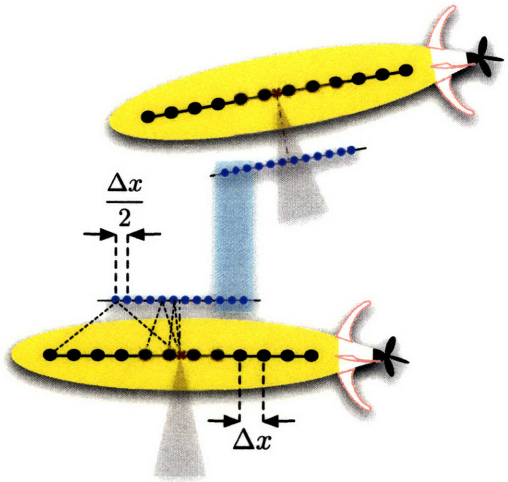

Figure 3-1: Displaced phase center antenna concept.

where $N$ is the number of sensors in the physical aperture. Essentially this means that the monostatic mobile sonar platform is limited to move at a rate that is less than one–half the length of the physical aperture per ping interval. This limitation in turn constrains the maximum range of the sonar.

### 3.1.2 DPCA Approach to Micronavigation

Sub–wavelength phase compensation, or micronavigation, is accomplished by exploiting the overlapping segment of DPCAs of consecutive pings. For a monostatic mobile sonar, the trajectory is assumed to follow nearly a straight line, with some small deviation in the off–track directions and angles, as well as some deviation from the nominal translational (along–track) speed. The along–track speed and the cross–track offset (sway) and angle (yaw) are estimated through a series of cross–correlation operations on the overlapping segment of the DPCAs of consecutive pings. The monostatic micronavigation concept is shown in Fig. 3-2. As in Fig. 3-1, the array translates, sways and yaws between pings, and contains a source, shown in red, in the center of the array. The DPCAs are formed as the geometrical mean of the source and each receiver element, and are plotted in gray at a slightly offset position for visibility. The blue target is an example of a scatterer in the insonified field of view of the

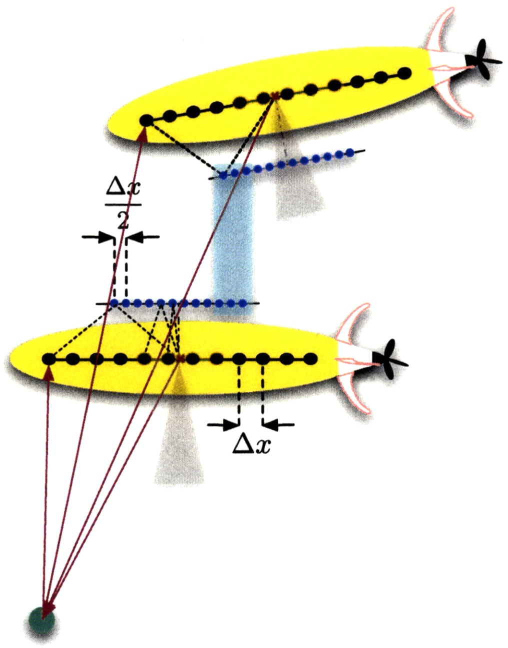

Figure 3-2: Displaced phase center antenna micronavigation with a monostatic sonar.

monostatic sonar for both pings, and the round–trip paths of the acoustic signals are shown for the central elements in the overlapped segment of the DPCAs. Note that these round–trip paths are very nearly the same, except that they are in reverse directions. If the platform translates exactly $2\Delta x$ during the ping interval, without swaying or yawing, then the received signal from the blue target will be exactly the same at the corresponding (and collocated) DPCA elements due to reciprocity. Any deviation from this special case will result in a loss of direct reciprocity, but the micronavigation can still be achieved under the assumption that the received signal of two nearest–neighbor DPCA elements are highly correlated. Similarly, the more widely spaced DPCA elements must be less correlated in order to provide a unique and reliable micronavigation capability.

The along–track speed ($v_n$) is given by the spatial location of maximum correlation, averaged over the overlapped segment:

$$\widehat{v_n} = \frac{\chi}{\Delta t} \tag{3.2}$$

while the sway ($\gamma$) and yaw ($\psi$) are jointly estimated from the temporal correlation delay vector $\vec{D}$ along the overlapped segment:

$$\widehat{\gamma} + \widehat{\psi}\vec{x} = \frac{c}{2}\vec{D} \tag{3.3}$$

In the above equations, $\chi$ is the spatial separation of the most highly correlated sensors, as measured in the local coordinates, $\Delta t$ is the ping interval, $\vec{x}$ is the position along the physical aperture in local coordinates, and $c$ is the speed of sound.

Although the DPCA method has been applied with success in a number of applications, its robustness and frequency range of effective operation are restricted by the inherent assumptions. The assumption that the seabed is a diffuse scatterer is applicable only for flat seabeds insonified by a wide–angle, very high frequency (multiple 10s of kHz) source. Also the sway estimate for the linear array is biased and requires a very high signal to noise ratio to be accurate.

### 3.1.3 Relationship to Tracking and Navigation

The DPCA micronavigation technique can be seen as a statistical tracking and navigation problem. When tracking a single coherent target with an active sonar or radar system, the range to target is obtained at each ping, and the trajectory of the target and/or receiver is estimated through either Doppler shift or return moveout over multiple pings. In the case of the fixed target as in this thesis, the receiver trajectory can be built around the target, which will be the focus of a later chapter (Chapter 6), but the absolute trajectory requires some additional assumptions or constraints. The typical constraints are usually wrapped in the Kalman or $\alpha$–$\beta$ filter [72] to provide a converging solution. If there are at least three coherent fixed targets, the navigation problem is sufficiently constrained to yield a determined system that can be solved with a non–linear least squares approach. This case is exploited in the long baseline (LBL) and other similar beacon–based navigation systems.

In the case of DPCA navigation, there are many targets that are not resolvable by the sonar system. So rather than separating the targets and tracking them individually, the correlation coefficient is used as a "score" of the consistency between returns. As in the case of the LBL system, the DPCA method requires a large aperture of the scatterers to achieve a high resolution navigation performance.

### 3.1.4 Correlation of Seabed Returns, and Its Relation to Micronavigation

While a significant amount of effort has been directed toward measuring the monostatic signal statistics, relatively little thought has been given to the spatial correlation of signals backscattering from the seabed. One such study was made by Tang [77], in which the correlation was derived for rough seabed with an underlying random sub–bottom that has a differing length scale. This sub-bottom inclusion becomes a concern for lower–frequency systems, particularly systems that are intended to search for buried objects.

A significant conclusion made by Tang is that the correlation of the seabed scattering is limited by the controlling correlation length scale of the seabed. Specifically, Tang made the hypothesis that at a particular cut–off frequency, the spatial correlation of the received field ceases to shrink with increasing frequency, and at that point (or above) the spatial correlation of the controlling scatterers is imprinted in the received correlation [76]. Considering that seabed correlation scales are generally on the order of 10 cm, while the sub–bottom correlation scales are generally on the order of 1 m, there is a big difference between the scattering from a high–frequency imaging sonar and from a bottom–penetrating sonar.

To see the relationship between correlation length and micronavigation performance, consider the cross–correlation between a single DPCA element at ping $p$ with the full DPCA array at ping $p + 1$. The micronavigation relies on the ability to accurately estimate the peak in the spatial correlation function. The spatial cross–correlation function is sampled at the sensor spacing $\Delta x$. A spatial correlation length of less than $\Delta x$ may therefore be missed entirely in the output, assuming that the vehicle controls are more coarse than that. In the other extreme, a spatial correlation

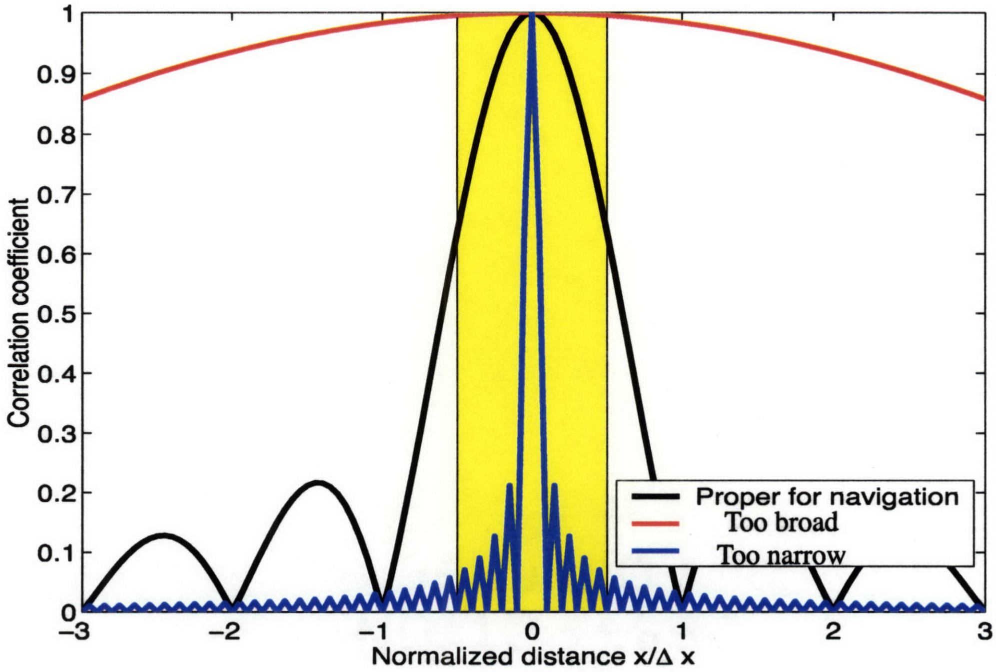

Figure 3-3: Spatial correlation vs. sensor separation. The yellow box indicates the navigation uncertainty due to sensor separation, corresponding to $\pm\Delta x$. The black line corresponds to a measured spatial correlation length of roughly $\Delta x$, which provides information for more precise navigation while precluding the possibility of missing the correlation peak. The limiting cases are shown in blue (high probability to miss peak) and red (no useful navigation information).

length of many times $\Delta x$ does not provide sufficient resolution to provide meaningful navigation information. A convenient balance occurs when the measured spatial correlation is on the order of the sensor spacing. All of these cases are illustrated in Fig. 3-3.

Note that a special case of the broadly correlated return is that of the strong, coherent return from a compact target. In this case, given an assumption about the motion of the target (i.e. stationary), navigation can be effectively performed using the target as a basis. This navigation aid is a result of the fact that the compact target comes from a consistent point in space from which at least the range can be estimated. A non–compact target such as the seabed, on the other hand, does not provide a stable range reference as so is not a navigation aid.

## 3.2 Spatial Correlation of the Received Fields

Having introduced the concepts of relative navigation based upon the spatial correlation of the received field, and the qualitative effects of various degrees of correlation upon these navigation results, attention is now turned toward understanding the physical nature of the received field statistics. The cause of the spatial correlation (or decorrelation) of the coherent projected field as it is received on the mobile sonar platform is the rough seabed. Therefore if the seabed roughness statistics can be related to the received field statistics, then the received correlation may be predictable from physical parameters.

### 3.2.1 Interface Roughness

As detailed by Doisy [19], it is possible to exploit the Van Cittert–Zernike theorem of optics when the seabed consists of uncorrelated scatterers. Simply stated, the Van Cittert–Zernike theorem relates the spatial coherence of the received field to the Fourier transform of the incoherent source. In the active sonar situation, the source is coherent, impinging on an incoherent surface which in turn re–radiates the acoustic energy as an incoherent source.

The cross–correlation function of two points in the receiver plane is given by [14]:

$$J_{P_1P_2}(t) = \int_\sigma \frac{I(S,t)}{R_1R_2} e^{j\frac{2\pi f_0}{c}(R_1-R_2)} dS \tag{3.4}$$

where $I(S,t)$ is the illuminated intensity on the incoherent scatter, and $R_1$ and $R_2$ are the distances from each point on the incoherent scatterer to points $P_1$ and $P_2$, respectively.

In order to relate the received correlation length to the source signal, consider the following heuristic argument. A linear source of dimension $L_s$ transmits a signal that scatters from an incoherent seabed at range $R$. The null–to–null beamwidth of the transmitter is $\frac{2\lambda}{L_p}$, resulting in an insonified patch of width $\frac{2\lambda R}{L_p}$. Treating the insonified patch as a re–radiating incoherent source, and assuming it is uniformly illuminated for convenience, the coherence function back at the source position is the

Fourier transform of the patch illumination. The null–to–null width of the transform is then $\frac{L_p}{R}$, resulting in a null–to–null coherence of $L_p$ back at the source. Considering that a linear source can be no less than $\lambda/2$ in length, the minimum coherence length is $\lambda/2$. Recall from the previous section that such a spatial correlation length places the system in the region in which precise navigation is possible.

Although the analogy between the active sonar reception and the Van Cittert–Zernike radiator holds in the abstract sense, it is oversimplified in terms of seabed roughness statistics and reflection character. The proper handling of the reflection coefficient of the medium within the rough interface scattering framework has been adequately addressed in the literature [8, 76, 82]. The seabed roughness statistics, however, remain an open debate [37]. Following Bass and Fuks [8] as did Tang in his thesis [77], the correlation length of the scattering from a randomly rough interface can be expressed as [8]

$$C_s(\vec{R}_1, \vec{R}_2) = \frac{\sigma_s^2}{4\pi^2} \int\int d^2\vec{\kappa}\, |f(\vec{\kappa})|^2\, S_s(\vec{\kappa} - \vec{k}_r) e^{\jmath(\vec{\kappa}\cdot\vec{R} + \kappa_z \Delta Z)} \tag{3.5}$$

where $\sigma_s$ is the rms interface height, $f(\vec{\kappa})$ is a complicated term that defines the strength of the scattering taking into account the boundary conditions and the incident plane wave angle, $S_s(\vec{\kappa})$ is the wavenumber spectrum of the interface height, $\vec{k}_r$ is the horizontal component of the incident wavenumber, $\vec{R}$ is the horizontal distance between receivers and $\Delta Z$ is the vertical distance between receivers.

At a given receiver height, the correlation function is again a Fourier transform. In this case it is the transform of the product of the mysterious function $f(\vec{\kappa})$ and the scattering function of the seabed. If it is assumed that the reflection coefficient is equal to $-1$, which is consistent with either a pressure–release boundary or a low grazing angle source, then some interesting features of the spatial correlation field can be seen by following Brekhovskikh [15]. Using the expression of $f(\vec{\kappa})$ given by Tang, and inserting the reflection coefficient of $V_0 = -1$ along with $\rho_2 = 0$, the strength function simplifies to

$$f(\vec{\kappa}) = -k_{z0} \tag{3.6}$$

and the correlation of the received field to

$$C_s(\vec{R}_1, \vec{R}_2) = \frac{\sigma_s^2}{4\pi^2} k_{z0}^2 \int\int d^2\vec{\kappa} S_s(\vec{\kappa} - \vec{k}_r) e^{\jmath(\vec{\kappa}\cdot\vec{R} + \kappa_z \Delta Z)} \tag{3.7}$$

For $\Delta Z = 0$, Eq. (3.7) becomes a Fourier transform of the scattering function. Assuming that the seabed consists of uncorrelated scatterers as in the Van Cittert–Zernike approach, and that the scattered field only consists of propagating waves (the farfield assumption), the received field is a bandlimited sinc function with a null–to–null bandwidth of $\lambda$, so the correlation length is seen to be proportional to the wavelength. For the vertical correlation function ($\left|\vec{R}\right| = 0$), Brekhovskikh has shown that the correlation length of the received field is proportional to $\lambda$, as well.

Note that the "proportional to $\lambda$" effect is in reality a reflection of the source length, with respect to wavelength. If the projector insonifies a full 180° region, then the received backscattering covers the full propagating wavenumber spectrum, $[-2\pi/\lambda, 2\pi/\lambda]$. If the projector insonifies a lesser angular extent then the received wavenumber limits are reduced as well. Assuming a linear source, the beamwidth of the source is directly related to the source length. A further consideration that arises as a result of the projector beamwidth is that of anisotropic roughness. If the projector has a 180° beam, then the horizontal arrival angles on the seabed cover all angles. If the seabed is anisotropic then the projection of the wavenumber spectrum varies with incident angle and therefore cannot be represented as a fixed correlation length over the insonified region. Instead, the wavenumber limits in the analysis must correspond to the component of the correlation length at each propagation direction.

In the case of large–scale scattering, which is defined by the length of the seabed correlation becoming larger than the incident wavelength, the correlation function changes. For horizontal correlation, Eq. (3.7) is the Fourier transform of the seabed power spectrum, which is simply the correlation function of the seabed. This result means that that the measured correlation length is constant with respect to frequency, so long as the large–scale assumption holds. The vertical correlation component, on the other hand, is again not a Fourier transform and so it must be integrated. For a pressure–release surface, Brekhovskikh has shown that the vertical correlation length is proportional to $k_r \ell_0^2$, which is larger than the seabed correlation length $\ell_0$ due to the large–scale scattering assumption ($\ell_0 > \lambda$).

### 3.2.2 Ripple Fields

The sandy seabeds that are common in near–shore locations throughout the world are often covered with ripple fields, as a result of periodic natural processes. The power spectrum of the ripple fields can be modeled as the interface roughness placed on a carrier frequency that corresponds to the characteristic wavenumber of the ripples. This representation of the ripple field power spectrum is supported by experimental evidence, for example by Piper [62]. Applying this model to a ripple field of characteristic wavenumber $\vec{\kappa}_r$ results in a slightly modified form of the received correlation field:

$$C_s(\vec{R}_1, \vec{R}_2) = \frac{\sigma_s^2}{4\pi^2} \int\int d^2\vec{\kappa} \, |f(\vec{\kappa})|^2 \, S_s(\vec{\kappa} + \vec{\kappa}_r - \vec{k}_r) e^{\jmath(\vec{\kappa}\cdot\vec{R} + \kappa_z \Delta Z)} \tag{3.8}$$

The shift in the seabed scattering function creates an interesting dynamic in the received field correlation. When there were no ripple fields, the default analysis (assuming the power spectra are constant within the correlation length) indicates that whichever correlation length is longer controls the field. In the case of the ripple fields, both correlation lengths may come into play. To see this, consider a ripple field of wavenumber $\kappa_r$ and uniformly distributed interface roughness of correlation length $\ell_0$. The power spectrum of the seabed is then assumed constant over the interval $[k_r - \pi/\ell_0, k_r + \pi/\ell_0]$. The wavenumber spectrum of a wide–angle source is approximated as a constant over the interval $[-2\pi/\lambda, 2\pi/\lambda]$. If the seabed correlation length is longer than the wavelength ($\ell_0 < \lambda$), but $\kappa_r + \pi/\ell_0 < 2\pi/\lambda$, then the supported wavenumber regime, $[k_r - \pi/\ell_0, 2\pi/\lambda]$, contains all three length scales. Similarly, in the case of small scale random roughness, i.e. $\lambda > \ell_0$, the situation may arise in which the left side of the shifted spectrum, $\kappa_r - \pi/\ell_0$, enters the sonic cone. The resulting wavenumber support is again $[\kappa_r - \pi/\ell_0, 2\pi/\lambda]$. Note that both of these situations require that the characteristic lengths be fairly close.

In reality, the scattering from ripple fields is more complicated due to the inherent anisotropy. Assuming that the source insonifies a wide swath, the ripple field is interrogated at a variety of angles with respect to its dominant direction. In keeping with the 180° theoretical projector of the examples ($\lambda/2$ source), the field arriving at the receiver scatters from the ripple field over the full complement of angles. Thus in the analysis above the value $\kappa_r$ is not a constant but rather varies with the incident wavenumber [71].

### 3.2.3 Subbottom Volumetric Inhomogeneities

Following Tang Eq.(69) [76], the balance between the central wavelength of the signal and the correlation length of the seabed can be understood in a similar manner. Repeating his equation,

$$C_v(\vec{R}_1, \vec{R}_2) = z_0 \left(\frac{\sigma k_2^2}{2\pi}\right)^2 \int dz' \int\int d^2\vec{\kappa}\, |P(z')|^2\, S(\vec{\kappa}-\vec{\kappa}_0) g(\kappa, z_1, z') g^*(\kappa, z_2, z') e^{\jmath\vec{\kappa}\cdot(\vec{r}_1-\vec{r}_2)} \tag{3.9}$$

For a pair of receivers nearly collocated, the Green's functions are identical, resulting in a simplified form,

$$C_v(\vec{R}_1, \vec{R}_2) = z_0 \left(\frac{\sigma k_2^2}{2\pi}\right)^2 \int dz'\, |P(z')|^2 \int\int d^2\vec{\kappa} S(\vec{\kappa} - \vec{\kappa}_0)\, |g(\kappa, z, z')|^2\, e^{\jmath\vec{\kappa}\cdot(\vec{r}_1-\vec{r}_2)} \tag{3.10}$$

From this form of the correlation function, it can be seen that the wavenumber integral is a two–dimensional Fourier transform of the product of the squared Green's function and the power spectrum of the seabed. The spatial correlation length of the received field will then be approximately the reciprocal of the wavenumber bandwidth of this product. Consider a case in which the wavenumber support of the Green's function is much larger than that of the seabed. In such a situation, the correlation function becomes the Fourier transform of the seabed power spectrum, and the received field has a correlation length equal to the seabed correlation length. In the opposite extreme, an uncorrelated seabed has infinite wavenumber support, which results in the received correlation function being expressed as the Fourier transform of the magnitude–squared Green's function. The wavenumber support of the Green's function can be seen using the same heuristic argument used in the discussion of the Van Cittert–Zernike theorem. The Green's functions applied connect the illuminated region to the receiver elements, which are very near the source. Each path is the reverse direction from the source to the scatterer. So the wavenumber support of the returning Green's function is equal to that of the outgoing Green's function. A point source would result in complete wavenumber support, so the correlation length of the seabed would always control the received field in the waveguide. Considering the limitation of a linear source, the minimum correlation length of the received field is $\lambda/2$, as argued in the Van Cittert–Zernike approach.

## 3.3 Micronavigation Performance Analysis

### 3.3.1 Cramér–Rao Lower Bounds on the Velocity Estimate

The accuracy of a correlation–based navigator relies on the ability to estimate the location of the correlation peak from measured data. To surmise the quality of the estimations, the performance bound results from estimation of time delay can be applied to the spatial and the temporal correlations. The Cramér–Rao lower bound (CRLB) of the temporal delay estimation can be expressed as [65, 83]:

$$\sigma_D \geq \left(\frac{3}{8\pi^2 T}\right)^{\frac{1}{2}} \frac{1}{\sqrt{SNR}} \frac{1}{\sqrt{f_2^3 - f_1^3}} \tag{3.11}$$

where $T$ corresponds to the length of the signal, $SNR$ is the signal to noise ratio, and $f_2$ and $f_1$ correspond to the frequency limits of the signal. In spatial domain, $T$ will be written as $\chi$ and $f$ written as $k$ to indicate spatial aperture and wavenumber, respectively. The CRLB is then

$$\sigma_D \geq \left(\frac{3}{8\pi^2\chi}\right)^{\frac{1}{2}} \frac{1}{\sqrt{SNR}} \frac{1}{\sqrt{k_2^3 - k_1^3}} \tag{3.12}$$

In order to achieve a tight bound, the signal to noise ratio term is given in terms of the amplitude ratio $\rho = \langle S^2 \rangle / \langle N^2 \rangle$ as [69]:

$$SNR = \left[\frac{2}{\rho} + \frac{1}{\rho^2}\right]^{-1}$$

This form of the signal to noise ratio encompasses the high– and low–SNR limits reported by Quazi, namely that the CRLB varies as $SNR^{-1}$ at low values of $\rho$ and varies as $1/\sqrt{SNR}$ at large values of $\rho$.

### Small–scale Roughness

Following the small roughness correlation argument ($\lambda \gg \ell_0$), the wavenumber support is on the interval $[0, 2\pi/\lambda]$. The resulting CRLB for peak position estimation is

$$\sigma_D \geq \left(\frac{3}{8\pi^2\chi}\right)^{\frac{1}{2}} \frac{1}{\sqrt{SNR}} \left(\frac{\lambda}{2\pi}\right)^{\frac{3}{2}} \tag{3.13}$$

Then noting that the useful aperture of the cross–correlation estimation is only when the correlation coefficient is relatively high, and recalling that the correlation falls to zero at $\pm\lambda/2$, an approximate aperture length can be given by $\lambda/2$. The CRLB then appears to be linearly related to wavelength:

$$\sigma_D \geq \left(\frac{3}{8\pi^5}\right)^{\frac{1}{2}} \frac{1}{\sqrt{SNR}} \frac{\lambda}{2} \tag{3.14}$$

This CRLB represents the minimum variance unbiased estimator performance possible for the Van Cittert–Zernike theorem approach.

### Large–scale Roughness

When the roughness is large in horizontal scale, as defined by $\ell_0 \gg \lambda$, then the correlation length of the seabed dominates. The correlated seabed strongly prefers to scatter over a finite bandwidth, as the wavenumber support rolls off for $k > 2\pi/\ell_0$. Applying this wavenumber support to the CRLB results in an estimation performance that is independent of wavelength:

$$\sigma_D \geq \left(\frac{3}{8\pi^2\chi}\right)^{\frac{1}{2}} \frac{1}{\sqrt{SNR}} \left(\frac{\ell_0}{2\pi}\right)^{\frac{3}{2}} \tag{3.15}$$

Again, the usable aperture for peak estimation is limited to approximately half of the null–to–null bandwidth of the correlation function. In the large–scale roughness case, this null–to–null bandwidth is given by $\ell_0$, resulting in a useful aperture of $\ell_0/2$. The CRLB is then

$$\sigma_D \geq \left(\frac{3}{8\pi^5}\right)^{\frac{1}{2}} \frac{1}{\sqrt{SNR}} \frac{\ell_0}{2} \tag{3.16}$$

### Ripple Fields

The power spectrum of a ripple field can be seen to be that of the smaller–scale roughness placed on a carrier wavenumber that correponds to the ripple spacing. The component of the ripple field along the direction of the receiver aperture is denoted by $k_{\rho,\|} = \vec{k}_\rho \cdot \vec{\chi}$. The wavenumber support then is on the interval $[k_{\rho,\|} - \pi/\ell_0, k_{\rho,\|} + \pi/\ell_0]$. Applying these wavenumber bounds to the original expression for the CRLB in Eq. (3.12), the CRLB in the ripple field is derived:

$$\sigma_D \geq \left(\frac{1}{8\pi^2\chi}\right)^{\frac{1}{2}} \frac{1}{\sqrt{SNR}} \sqrt{\frac{\ell_0}{2\pi}\frac{\lambda_r}{2\pi}} \sqrt{\frac{1}{1 + \frac{1}{12}\frac{\lambda_r^2}{\ell_0^2}}} \tag{3.17}$$

Now assuming that the ripple field carrier wavenumber does not move the incoming field far away from broadside to the receiver aperture, the useful aperture is again $\ell_0/2$, resulting in a CRLB of:

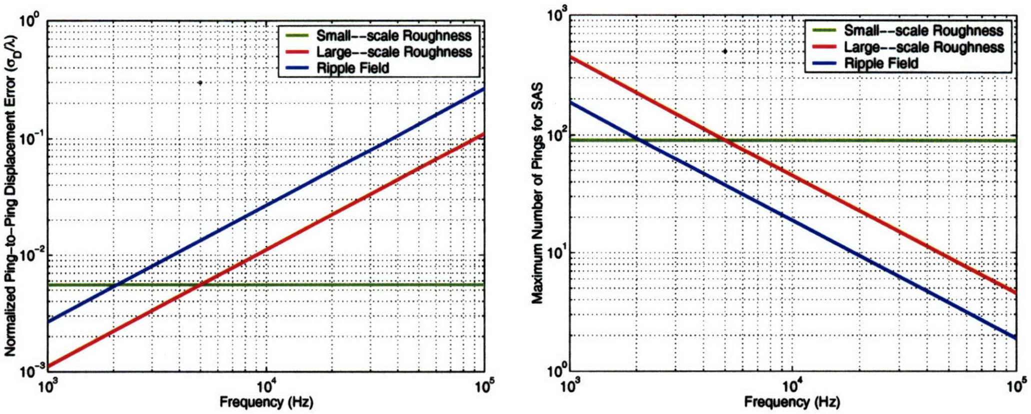

(a) (b)

Figure 3-4: CRLB of the sway estimate for an example case. On the left, the per–ping error in the estimate normalized by the wavelength is shown. On the right is the estimated number of pings before the micronavigation error becomes too high for SAS generation.

$$\sigma_D \geq \left(\frac{1}{8\pi^5}\right)^{\frac{1}{2}} \frac{1}{\sqrt{SNR}} \frac{\lambda_r}{2} \sqrt{\frac{1}{1+\frac{1}{12}\frac{\lambda_r^2}{\ell_0^2}}} \tag{3.18}$$

The operational consequences of the seabed roughness are indicated in Fig. 3-4. On the left plot, the expected micronavigation error from ping to ping is shown as a function of frequency. The values are normalized by the wavelength. Note that the Van Cittert–Zernike approach leads to a uniform error as a percentage of wavelength. The crossover between the correlated seabed and the uncorrelated seabed occurs when the wavelength reaches one–half the trasmitted wavelength. In the right side of the figure is the number of pings that may be processed before the accumulated micronavigation error becomes a significant fraction of the wavelength.

### 3.3.2 Cramér–Rao Lower Bounds on the Sway and Yaw Estimates

The sway and yaw estimates are formed by estimating the time delay at which the correlation peak occurs in the velocity estimate. The velocity estimation error is therefore tied into the sway and yaw estimates, however slightly. Considering first the sway and yaw estimates individually, following Pinto et al. [60], the CRLBs are easily derived. Rewriting the conjoined sway and yaw estimates shown in Eq. (3.3) in discrete form, and solving for the delay $D$ at each DPCA sensor $i$:

$$D_i(\gamma, \psi) = \frac{2\gamma}{c} + \psi\frac{2d_i}{c} \tag{3.19}$$

where $d_i$ is the position of DPCA sensor $i$, relative to the DPCA phase center. Although there is some uncertainty in the location of the DPCA phase center, the effect of shifting the axis to the phase center creates a convenient result in the CRLB cross–terms. It is assumed that the velocity estimate is accurate enough to allow this shift. The Fisher information matrix of the sway and yaw estimates is then given by:

$$\mathcal{F} = \begin{bmatrix} -\langle\frac{\partial^2\mathcal{L}}{\partial\gamma^2}\rangle & -\langle\frac{\partial^2\mathcal{L}}{\partial\gamma\partial\psi}\rangle \\ -\langle\frac{\partial^2\mathcal{L}}{\partial\psi\partial\gamma}\rangle & -\langle\frac{\partial^2\mathcal{L}}{\partial\psi^2}\rangle \end{bmatrix} \tag{3.20}$$

where $\mathcal{L}$ is the log–likelihood function of the delay vector $\vec{D}$. Assuming that the delay errors are independent, $\mathcal{L}$ can be expressed as the summation of the individual delay log–likelihood functions $\mathcal{L}_{\infty}$:

$$\mathcal{L}_N(\gamma, \psi) = \sum_{i=1}^{N} \mathcal{L}_1\{D_i(\gamma, \psi)\} \tag{3.21}$$

The four elements of the Fisher information matrix can be directly determined using the derivative chain rule:

$$\begin{aligned} -\langle\frac{\partial^2\mathcal{L}_N}{\partial\gamma^2}\rangle &= -\langle\frac{\partial^2\mathcal{L}_N}{\partial D_i^2}\left(\frac{\partial D_i}{\partial\gamma}\right)^2 + \frac{\partial\mathcal{L}_N}{\partial D_i}\frac{\partial^2 D_i}{\partial\gamma^2}\rangle = -\frac{4}{c^2}N\langle\frac{\partial^2\mathcal{L}_1}{\partial D_i^2}\rangle \\ -\langle\frac{\partial^2\mathcal{L}_N}{\partial\gamma\partial\psi}\rangle &= -\langle\frac{\partial^2\mathcal{L}_N}{\partial D_i^2}\frac{\partial D_i}{\partial\psi}\frac{\partial D_i}{\partial\gamma} + \frac{\partial\mathcal{L}_N}{\partial D_i}\frac{\partial^2 D_i}{\partial\gamma\partial\psi}\rangle = -\frac{4}{c^2}\langle\frac{\partial^2\mathcal{L}_1}{\partial D_i^2}\rangle\sum_{i=1}^{N} d_i \\ -\langle\frac{\partial^2\mathcal{L}_N}{\partial\psi^2}\rangle &= -\langle\frac{\partial^2\mathcal{L}_N}{\partial D_i^2}\left(\frac{\partial D_i}{\partial\psi}\right)^2 + \frac{\partial\mathcal{L}_N}{\partial D_i}\frac{\partial^2 D_i}{\partial\psi^2}\rangle = -\frac{4}{c^2}\langle\frac{\partial^2\mathcal{L}_1}{\partial D_i^2}\rangle\sum_{i=1}^{N} d_i^2 \end{aligned} \tag{3.22}$$

Assuming that the displaced phase centers are uniformly spaced by $\frac{\Delta x}{2}$ and that the axis has been centered at the phase center of the DPCA, the summations over $d_i$ can be reduced to:

$$\begin{aligned} \sum_{i=1}^{N} d_i &= 0 \\ \sum_{i=1}^{N} d_i^2 &= \frac{N(N^2-1)}{48}\Delta x \end{aligned} \tag{3.23}$$

The Fisher information matrix has now been established in terms of the single time delay estimation bound. Utilizing the time delay result given in Eq. (3.11), and assuming that the frequency band is $f_0 \pm B/2$, the single element delay vector is given by:

$$-\langle \frac{\partial^2 \mathcal{L}_1\{D_i(\gamma,\psi)\}}{\partial D_i^2} \rangle = \frac{1}{\sigma_D^2} = 8\pi^2 BT(SNR) f_0^2 \left(1 + \frac{1}{12}\frac{B^2}{f_0^2}\right) \tag{3.24}$$

The joint CRLB is given by the inverse of the Fisher information matrix:

$$\sigma_N^2 \geq \begin{bmatrix} \frac{32}{c^2} N\pi^2 BT(SNR) f_0^2 \left(1 + \frac{1}{12}\frac{B^2}{f_0^2}\right) & 0 \\ 0 & \frac{8}{c^2}\frac{N(N^2-1)}{12}\pi^2 BT(SNR) f_0^2 \left(1 + \frac{1}{12}\frac{B^2}{f_0^2}\right) \end{bmatrix}^{-1} \tag{3.25}$$

## 3.4 Practical Application of the Limited Correlation

When considering the move toward autonomous, moving sonar platforms, it is important to take into account the point of view of the platforms in question. The emphasis of a mission is shifted toward real–time decision making with the best information available. With this in mind, consider the relation between seabed correlation length and navigation accuracy that has been made in the analysis in Sec. 3.1.

1. The loss or gain of coherence of the scattered field at the receiver limits the accuracy of the micronavigation technique.
2. When signals are uncorrelated, the DPCA micronavigation fails.
3. When the correlation becomes more spatially protracted, the micronavigation performance slowly degrades.

This relationship can have a significant impact on the performance of a synthetic aperture or other multi–ping integrated sonar system. An obvious problem is that the correlation length of the seabed is generally not known, nor is it a readily measurable quantity for a mobile sonar platform. For bistatic moving sonars, a number of factors come into play in determining the effective correlation length seen at the receiver, including:

1. Correlation length of the seabed interface.
2. Correlation length of the subbottom scatterers.
3. Anisotropy of the scatterers.
4. The relative weightings between the surface scattering and the subbottom scattering.
5. Incoming and outgoing angles relative to the relevant scatterers.

In order to sort out these factors prior to the mission, an extremely accurate survey would be required. Furthermore, the positions (and angles) of the source and receiver would have to be precisely known to the receiver. Assuming that neither of these conditions is satisfied in most missions, the knowledge of the relationship between seabed correlation lengths and micronavigation accuracy may appear to be fruitless.

In fact, it is more enlightening for practical reasons to consider the link between the physical phenomena and the micronavigation as shown in Fig. 3-5. In this schematic diagram, it is emphasized that the measured quantity is the correlation length at the receiver. The correlation length at the receiver is determined by the physical scattering, and it in turn determines the maximum synthetic aperture length. The important link for micronavigation is simply the correlation length at the receiver to the navigation accuracy. The physical inversion problem is secondary. In complex sonar configurations, it is extremely difficult to sort out the physical scattering mechanisms that generate the received field, so the link to the physical phenomena can be ignored. In favorable conditions, e.g. monostatic high–frequency sonar, the inversion for physical parameters is easily made, and from multiple aspects a more comprehensive model can be formed. It is expected that in a practical mission, there will be a high–frequency, monostatic component to the mission, due to the relative ease of use.

## 3.5 DPCA with a Swordfish–style GOATS Array

In the GOATS experiments, a swordfish–style receiver array is attached to the front end of the monostatic AUV while the source is located in the center section of the AUV. The effect of this separation between the source and receiver is that the reciprocal measurements applied in the standard DPCA micronavigation method are not available. The swordfish–style array DPCA is illustrated in Fig. 3-6 for a monostatic AUV–borne sonar system. Note that there is overlap in the DPCA apertures from ping–to–ping, but that these overlapped phase centers are not due to reciprocal measurements. The equivalency of the measurements then relies upon the monostatic–to–bistatic equivalency theorem (MBET).

To support the analysis above, consider the vehicle, moving at a platform speed of $v_p$ and a ping interval of $\tau_p$. The offset between the source and the phase center of the array is $x_o$, and the source position at ping $p$ is $x_{s,p}$. The position of each receiver element is measured with respect to the receiver phase center and is denoted by $\xi$. It is assumed that a pair of sensors have displaced phase centers that align across pings $p$ and $p+1$, and these are measured at local positions $\xi_p$ and $\xi_{p+1}$. The along–track positions of the displaced phase centers are then equated:

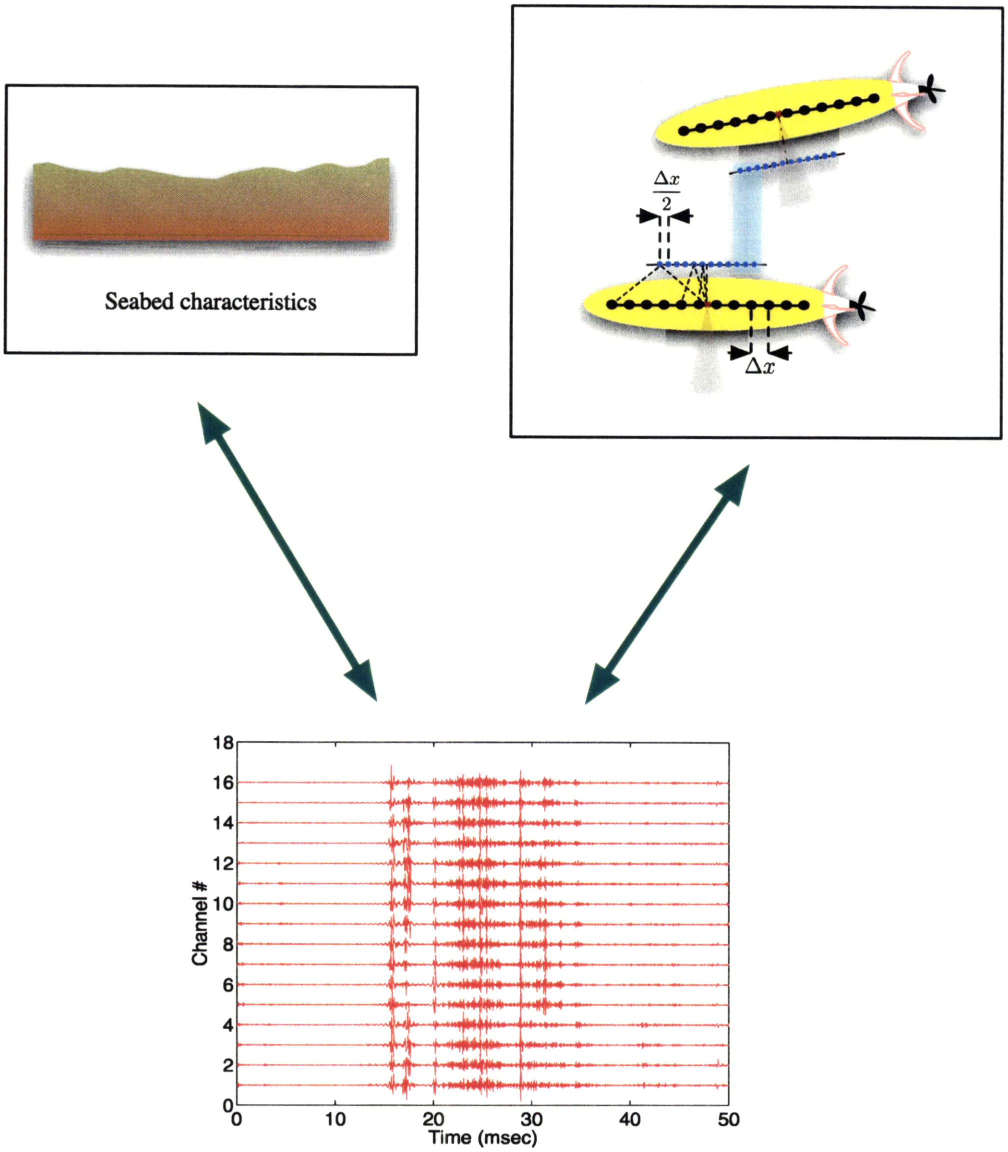

Figure 3-5: Illustration of the relationship between the physical characteristics of the seabed, the received field and the micronavigation capability.

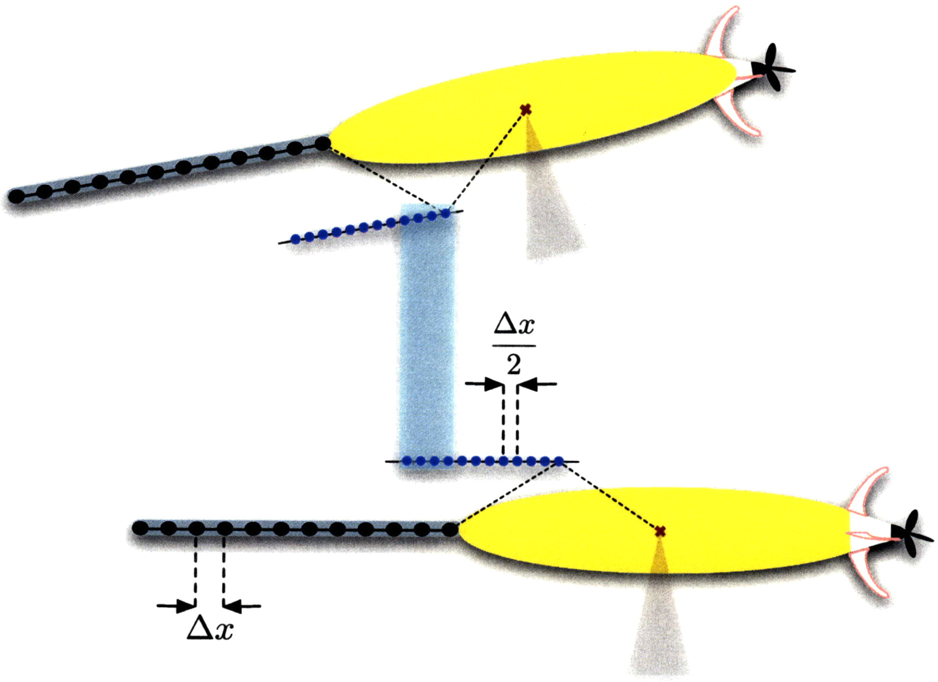

Figure 3-6: Displaced phase center antenna micronavigation with the swordfish–style array.

$$\frac{x_{s,p} + (x_{s,p} + x_o + \xi_p)}{2} = \frac{x_{s,p} + v_p\tau_p + (x_{s,p} + v_p\tau_p + x_o + \xi_p)}{2}$$
$$\frac{\xi_p}{2} = v_p\tau_p + \frac{\xi_{p+1}}{2} \tag{3.26}$$

The limit at which there is overlap in the DPCA is when the frontmost element at ping $p$ aligns with the rearmost element at ping $p+1$. At this limit, the platform velocity is limited by:

$$v_p \leq \frac{(\xi_{max} - \xi_{min})}{2\tau_p} \tag{3.27}$$

which can be seen to be identical to the limit in the true monostatic DPCA given in Eq. (3.1) by choosing $\xi_{max}$ and $\xi_{min}$ to equal $\pm\frac{N\Delta x}{2}$. Although the platform speed limit is the same, the mechanism by which the reverberation returns may be correlated is different. It is clear that there will not be reciprocal paths, as can be shown by equating the position of the source at ping $p$ to the position of the receiver element at ping $p+1$.

$$\begin{aligned} x_{s,p} &= x_{s,p} + v_p\tau_p + x_o + \xi_{p+1} \\ -\xi_{p+1} &= v_p\tau_p + x_o \end{aligned} \tag{3.28}$$

So for any positive velocity $v_p > 0$, the corresponding receiver position must lag the receiver phase center by more than $x_o$. This requirement indicates that the source must be embedded within the aperture of the receiver in order to achieve reciprocal returns.

Having established the requirements on the overlapped DPCAs, the issue of whether the MBET results in a correlated signal return is addressed. Beginning with intuition, it is immediately clear that in the general case, the paths to scatterers are not the same, and the received fields will therefore not be well–correlated. What is not clear, and must be gleaned from the equations, is how poorly correlated, and in what conditions the correlation level improves. The expected result is a new constraint on the vehicle motion that is a function of platform motion and the extent to which the source and receiver are separated.

Considering the formulation of the two–point cross–correlation for the rough interface given in Eq. (3.5), it is apparent that the source does not come into play. This insensitivity to source position is not an oversight, but rather a result of the far–field assumption. The far–field assumption at the receiver is well–defined in the context of the formulation, but the source was merely considered to be a plane wave propagating in free space. The implication is that the phase front is linear at all points on the interface. Given that the source is generally directional, the region in which the phase front must be linear is reduced to the insonified beamwidth. In consideration of the analysis in Section 3.2, the range of linear phase front can be further restricted to the

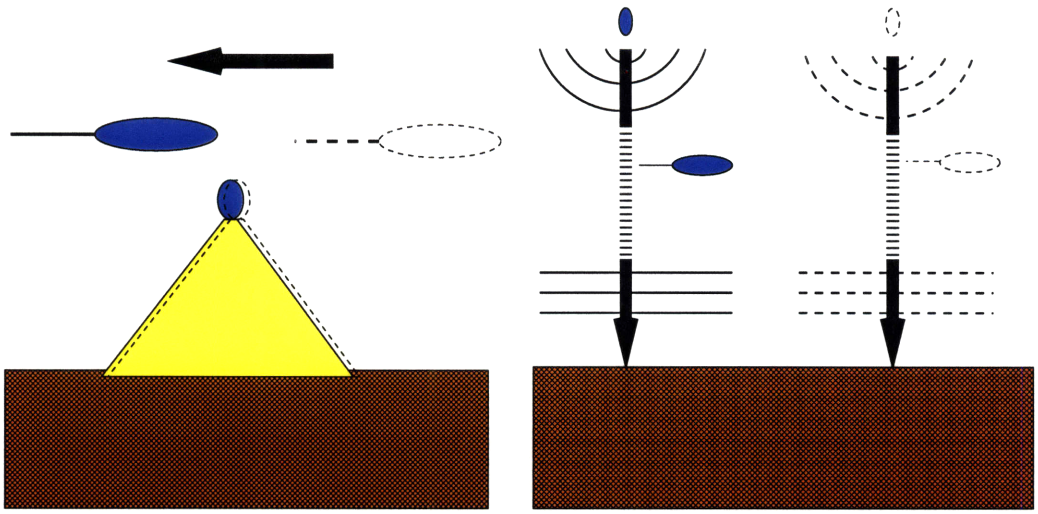

(a) Stationary source.

(b) Remote source.

Figure 3-7: Two cases of an apparently stationary source. On the left, the source moves so slowly that the phase at the boundary is nearly unchanged. On the right, the source is so far away that the wavefront curvature is negligible.

area over which the rough interface has wavenumber support.

In the case of the monostatic moving sonar platform with separated source and receiver, the condition that controls the source–to–interface segment is that the relative phases at which the source signals impinge upon each scatterer must be approximately the same for the two pings. This situation can occur in two ways, as illustrated in Fig. 3-7. The first mechanism is if the source signal has moved a small enough distance that it has little effect on the insonifying field. The second case is when the source is so far away that the wavefront curvature is virtually eliminated by the time it reaches the interface. Both of these cases have practical implications in the case of the GOATS–style moving sonar platform.

### 3.5.1 Bistatic Extension of the DPCA

#### The Stationary Source Problem

The simplest abstraction from the monostatic geometry is the case of a stationary source and a moving receiver. This scenario is illustrated in Fig. 3-8. With such a

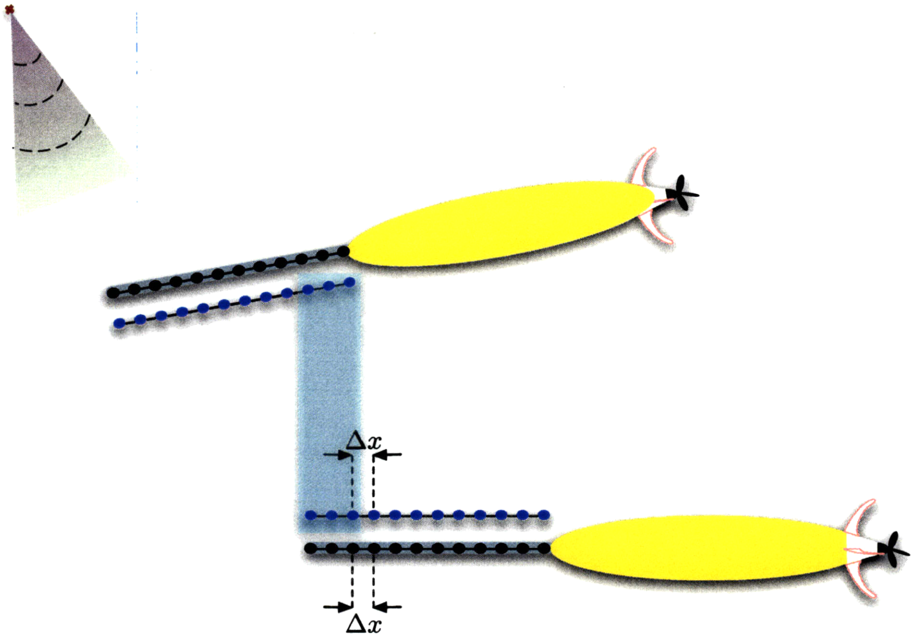

Figure 3-8: Displaced phase center antenna concept for the bistatic, fixed–source geometry.

configuration, the overlap of the physical array is the redundant measurement. No reciprocity or MBET is necessary for relating the correlated signals. This type of system corresponds to synthesizing a large array to sample a static scattered field. The receiver in this scenario can move a maximum of the receiver length $L$ per interping interval, as opposed to the $L/2$ limit imposed by traditional SAS. Aside from these differences, the micronavigation follows as in the monostatic scenario. We first consider a single element at ping $n$, which is matched with an element of ping $n+1$ located at a distance of $\vec{dx} = \Delta v_{n+1}\widehat{a}_{v,n} + \Delta s_{n+1}\widehat{a}_{s,n} + \Delta p_{n+1}\widehat{a}_{p,n}$, where the axes are the local coordinate system of the receiver at ping $n$. Then the one-way range from the center of the insonified patch to the receiver at ping $n$ is approximately:

$$R_{n+1} \approx R_n + \Delta s_{n+1} + \frac{1}{2}\frac{(\Delta v_{n+1})^2 + (\Delta p_{n+1})^2}{R_1 + \Delta s_{n+1}} \tag{3.29}$$

For slant-range imaging operations, the time of arrival difference is assumed to be $\Delta s$, which means that the last term in Eq. (3.29) becomes the error in the slant-range position estimate. The positional error could become significant with this assumption, but the phase error of the signals remains small near the center of the insonified patch. However, for general bistatic and particularly for multi-platform operations, true navigation is desired rather than phase compensation. Some improvement on the physical location estimate of the receiver can be achieved through the use of the Eq. (3.29) and the amplitude of the maximum correlation coefficient. Noting that the error term on $\Delta s$ is quadratic, it appears that the best slant-range position estimate for a linear array is the tangent of the estimated sway curve along the array. The along-track motion is well-estimated by a properly sampled array, so $\Delta v$ will be small. The pitch motion, $\Delta p$, can then be estimated through the value of the maximum correlation coefficient, given that the correlation length of the seabed is on the order of the interelement separation.

### The Moving Source Problem

When the source is moving, the overlapping section of the random surface is insonified from a different angle at each ping. Because the random surface is a *realization* of its statistical distribution, the statistics of the surface may not directly indicate the statistics of the measured field. The reciprocity of the correlated receptions are exploited in monostatic SAS to avoid this difficulty, but such measurements are unavailable in general bistatic operations. However, the broadband nature of typical sonar systems provides the opportunity to average over independent frequency bins to create an ensemble measure of the received signal, which has been shown in radar applications to effectively enhance the stability of the scattered field [88] and elicit the ensemble characteristic known (for a 1-D surface) as the "memory line" [51]. The memory line can in turn be used to provide the consistent basis for micronavigation. The 1-D memory line analysis predicts that the best correlated returns will occur at points described by:

$$\cos\theta_i^{(n)} - \cos\theta_i^{(n+1)} = \cos\theta_r^{(n)} - \cos\theta_r^{(n+1)} \tag{3.30}$$

where the angles $\theta$ are grazing angles, the subscripts refer to i)ncident or r)eceived, and the superscripts refer to the ping number. With this basis, the motion compensation follows as in the monostatic case. The platform velocity limitation is equivalent to that of the monostatic case as well, except that it corresponds to one–half the physical aperture length *plus the source motion.*

Basic examples of the moving source problem include the fast monostatic platform and the swordfish array problem. In the fast monostatic problem, the vehicle motion exceeds the speed limit for deterministic correlation between pings. The statistical characteristics of the correlation will hold given translational invariance of the seabed, and the platform motion can be compensated on this basis. For the swordfish array, as used in the GOATS series of experiments, there is no nonzero platform velocity that will provide reciprocal or redundant measurements, and the user must then resort to the statistical correlations in this geometry as well.

### The Remote Source Problem

The stochastic equivalent to the stationary source problem is the remote source problem. In this case, the moving acoustic source is located far from the area of interest such that its apparent motion is negligible. In this case, the spatial correlation holds in a statistical sense rather than in a deterministic sense, because the acoustic scattering paths are not identical from ping to ping. The additional difficulty that may arise in the remote source case is fluctuation in the propagation paths.

### Micronavigation for Multi–static Operations

The use of strong correlations in reverberation for navigation purposes is in contrast to the desire to reduce the noise in the combined signal or image. If the vehicle attempts to closely follow a trajectory for which the reverberation is strongly correlated, then the reverberation signal will sum nearly coherently just as the target will. One concept of operations to mitigate this effect is to utilize a multi–static system to combine a navigation capability with a reverberation suppression. For minimal complexity, consider a pair of monostatic vehicles. Each vehicle may use its own return for fine navigation and imaging results, while using the signal return from the other platform for reverberation suppression. In order to accomplish this to best effect, the separation between the vehicles should be such that the respective angles fall far from the memory line. An unlimited number of extensions to this concept can be imagined, with a common basis of the systems that each receiver vehicle uses one source as a navigation tool and another for reverberation suppression.

### 3.5.2 Vehicle Navigation in the GOATS'98 Experiment

Navigation of the AUVs is perhaps the most critical limiting factor for precise imaging in the GOATS scenario. There are two methods of navigation used by the AUV, which can be classified by scale. The *global* navigation is performed by AUVs using a variety of systems, such as inertial navigation systems (INS), Doppler-Velocity Logs (DVL), or an acoustic system such as the LBL system used in GOATS'98, all in combination with GPS while surfaced. The *local* navigation is accomplished by a self-navigation process based on the acoustic data, and both methods come into play in the processing decision.

The global fix navigation is the more straightforward consideration of the two. Between the 7 second acoustic acquisition periods, the LBL network provides a global position estimate with estimated error bounds. However, the current technology, and likely the technology for some time to come, does not allow a global position estimate accuracy on the order of the acoustic wavelength needed for acoustic array processing. Consequently, the use of LBL navigation is limited to anchoring the image in space, and coherent processing based on global navigation alone is not considered here.

The local navigation, often termed "micro-navigation", provides a much finer position estimate. However, the micro-navigation provides only relative positions, and as such the positional uncertainty increases with time. It is clear that the error will, at some point, reach a level such that coherent processing can no longer be implemented in a robust manner. In this case, it makes sense to micro-navigate until the error reaches the order of the LBL network, thus maximizing the amount of acoustic data, and then initiate an LBL cycle. The full micro-navigated array can then be segmented into coherent parts.

Sonar self-navigation techniques generally rely on the coherence (or lack thereof) of the return from the insonified patch, and fall into two categories: *target*-based and *reverberation*-based navigation. Target-based navigation relies on the availability of a strong, well-placed target (or targets) and large, high-resolution apertures. Neither of these requirements are in place for general AUV applications.

Reverberation-based navigation instead relies on having a large number of independent scatterers of roughly equal magnitude to generate a signal return that is nearly uncorrelated in space. The self-navigation technique used in the current work is based on the DPCA approach commonly used for monostatic SAS. This method has been shown to compensate for positional errors and array calibration errors simultaneously [10].

### The DPCA Method

In the traditional DPCA approach, the displaced phase centers of the quasi-monostatic array are located midway between the source and receiver. Each displaced phase center behaves as a single purely monostatic source/receiver element. If the platform, which includes source and receiver in the monostatic case, moves less than 1/2 of the physical receiver aperture length between ping receptions, then there will be overlap between the received signals. This region of overlap is then used to determine the trajectory of the vehicle to sub-wavelength accuracy.

For general bistatic sonar, the displaced phase center approach is invalid, because the displaced phase center cannot be considered a single purely monostatic source/receiver element. The representation of the displaced phase centers as monostatic elements arises from Crispin's monostatic to bistatic equivalence theorem (MBET) approximation, which states [38] that the bistatic scattering cross section $\sigma_B$ is the monostatic scattering cross section $\sigma_M$ evaluated at half the bistatic look angle $\beta$, i.e.

$$\sigma_B(\theta, f) = \sigma_M(\theta = \frac{\beta}{2}, f) \tag{3.31}$$

This theorem is valid for simple objects with a bistatic look angle ($\beta$) less than $10^o$, which may be violated by general bistatic sonar.

However, with restricted source motion, the technique is easily extended. With the stationary source in the GOATS'98 experiment, the *actual* receiver positions can be used in the place of the displaced phase centers. An overlap in the physical receiver aperture corresponds to an overlap in the data. The platform velocity can then be as high as a full physical receiver aperture length between ping receptions. With this modification, the along-track motion estimate is the same as in the monostatic case. Cross-track motions will vary from the monostatic case, as they will generally be functions of the bistatic reflection and the receiver angle.

*Along-track Micro-navigation*

The simplest micro-navigation method is the estimation of platform velocity. Its original formulation was for the purpose of estimation of ship speed [18]. The nominal platform velocity $v_{p,nom}$ and the pulse repetition period $\tau_{PRP}$ are chosen such that there is significant overlap of the physical receiver aperture between consecutive receptions. Then the sensors at which there is a maximum correlation between the reverberation returns indicate the platform velocity. For a linear array:

$$v_p \approx \frac{\Delta x}{\tau_{PRP}} \tag{3.32}$$

where $\Delta x$ corresponds to the distance along the physical array between the sensors with maximum correlation across the consecutive pings. This estimate can be considered a 1-D navigation, as it estimates only the along-track translation of the sonar platform.

*Cross-track Micro-navigation*

Cross-track micro-navigation encompasses the remaining two dimensions of platform motion, including translation and rotation in both planes. Most common micro-navigation methods in SAS imaging restrict the motion estimate to the slant-range plane, referring to the projected translations and rotations as sway and yaw, respectively. Theoretical studies have have shown that effective 2-D micro-navigation with the DPCA method requires phase difference estimation within a small fraction of the characteristic wavelength [60]. In particular, the fact that the yaw estimate is dependent on the individual sway estimates causes a high error variance, and a bias in the resulting micro-navigation. Despite this high sensitivity, the 2-D micro-navigation technique has been proven effective in at-sea experiments with towfish [61].

Sway estimation can normally be extracted from the velocity estimate with minimal computational cost. In the monostatic case, it is simply the time lag of the maximum correlation coefficient between consecutive pings multiplied by the medium wave speed. The hardware at the time of the GOATS'98 experiment did not provide a reliable source trigger synchronization with the data acquisition system, so the sway estimate was not possible.

### *Patch Coherence and Vehicle Navigation*

The coherence of the insonified patch returns can be seen as a measurement of the radiated power spectrum at a given angle [58] . The angle of arrival can affect the ability of the AUV to navigate based on the patch returns. For example, if the patch is at end–fire, the signals arriving on the AUV array will be nearly perfectly correlated. The AUV maintains a receiving angle with the patch within a range of ±60° to avoid this problem. The maximum correlation coefficient between patch returns on the physical aperture is shown in the upper frame of Fig. 3-9, for the same pass as in the above section. The patch correlation coefficients show that the returns are correlated significantly over 2 to 3 sensor spacings, corresponding to a seabed correlation length of approximately 40 cm [77].

The lower frame shows the vehicle velocity estimate for the same pass of the target field, calculated with Eq. 3.32. The nominal AUV velocity is 1 m/s, and it can be seen that the velocity estimate indicates that the vehicle was slowing from a higher speed down to the nominal velocity. This was in fact the case, as this pass is the first pass of the run, and the AUV was slowing from its approach speed down to its mapping speed.

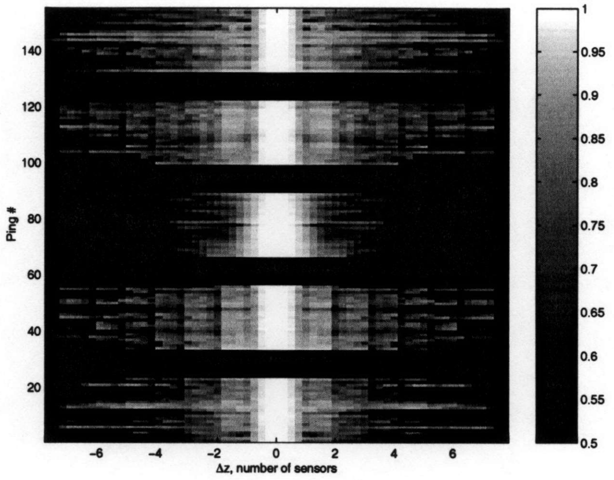

(a) Maximum correlation coefficient.

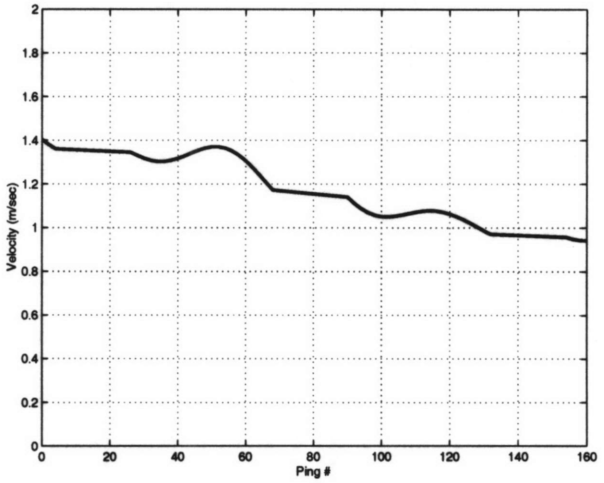

(b) Vehicle velocity estimate.

Figure 3-9: Vehicle velocity estimates during the GOATS'98 experiment. Top: Maximum correlation coefficient between the patch returns measured by sensors on the physical aperture, pass 23-27. The blank sections are during the LBL cycle. Bottom: The corresponding vehicle velocity estimate.

## 3.6 Beampattern Analysis

A traditional way to analyze the performance of an array is through the beampattern. For limited cases, an analogous measure is possible for the synthesized array. Consider the SAS imaging sonar – the array moves in a nearly straight line and the synthetic aperture is essentially a line array. For this case the analogy is clear. In addition, the DPCA micronavigation requirement of maximum vehicle velocity is also seen as the limit for suppressing sidelobes. In this section, the synthetic array performance is followed for nearly linear AUV motion. Implications of limited and controlled maneuverability, navigation uncertainty and vehicle speed are addressed in the context of beampattern analysis.

### 3.6.1 Traditional SAS with the DPCA

SAS imaging is typically performed using towfish or AUVs moving in a straight line. The idea is to increase the length of the aperture coherently through multi–ping integration. As was mentioned in section 3.1, the key lies in the ability to compensate for the platform motion. The DPCA approach to platform motion compensation imposes a speed limit on the vehicle, as was shown in Eq. (3.1). The DPCA for the consecutive pings at this maximum velocity is shown in Fig. Note that the requirement that there be overlap in consecutive DPCAs means that there is no discontinuity in the synthetic aperture. Assuming the physical aperture is sufficiently sampled to avoid grating lobes (i.e. $\Delta x \leq \lambda/4$), it is clear that the synthetic array will also not contain grating lobes, as the sensor spacing on the physical aperture ($\Delta x$) represents the maximum sensor spacing in the synthetic aperture. An insight into the array performance if the AUV exceeds this speed limit can be more clearly demonstrated through beampatterns.

In synthetic aperture radar (SAR), the source and receiver are a single element (antenna). Due to the restrictions imposed by the sound speed relative to the platform speed, this is not a feasible design for a SAS system. Typically, the sonar source is a single element, but the receiver is an array. When considering the beampattern of the SAS system, it must be taken into account that the source moves as well as the receiver. There are two ways to view this motion: one is to consider the DPCAs themelves with each element representing a point source/receiver, and the second is to consider the source forming a synthetic array as well as the receiver forming a synthetic array. In the DPCA view, it is necessary to reduce the phase shifts by a factor of two to preserve the accurate resolution. The second view will be followed in this section because it provides more insight into the array performance, especially regarding the inclusion of source beampatterns.

### Physical Aperture Response

The sonar system to be considered consists of a compact, broad beam source accompanied by a linear receiver array that extends only a few ($< 10$) wavelengths. The 180° field of view of the receiver can then be divided into several resolution bins with a plane wave beamformer, forming the basis of all coherent processing in this thesis. A sketch of this division is shown in Fig. 3-10. Considering the source to be of length $L_s$ and a receiver aperture of length $L_r$, and assuming uniform weighting of both source and receiver aperture, the two–way beampattern of the physical aperture (PA) on a given ping is:

$$\begin{aligned}\Upsilon_{PA}(\omega, k_z) &= \frac{1}{L_r L_s}\int dz \int dz' e^{-jk_z z} e^{-jk_z z'} \\ &= sinc\left[\frac{L_s}{2}k_z\right] sinc\left[\frac{L_r}{2}k_z\right] \\ &= \Upsilon_r(\omega, k_z)\Upsilon_s(\omega, k_z) \qquad (3.33)\end{aligned}$$

Both the source and receiver were assumed to be continuous in the above equation, which is equivalent to the assumption that the source and receiver are sampled at more than the Nyquist rate, i.e. $\Delta x \leq \lambda/2$. The source is assumed to be mechanically and electronically fixed, but the receiver aperture can be electronically steered to angle $\theta_T$, where $k_{z_T} = k_0 \sin\theta_T$. The steered physical aperture response is then:

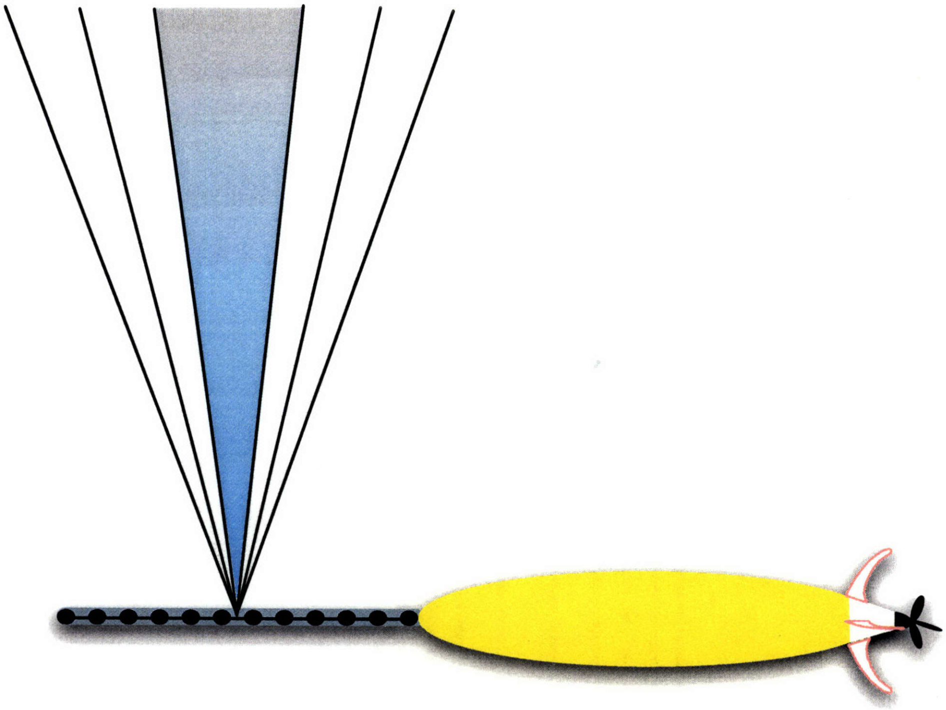

Figure 3-10: Beamforming on the physical aperture.

$$\Upsilon_{PA}(\omega, k_z; k_{z_T}) = sinc\left[\frac{L_s}{2}k_z\right] sinc\left[\frac{L_r}{2}(k_z - k_{z_T})\right] = \Upsilon_r(\omega, k_z; k_{z_T})\Upsilon_s(\omega, k_z) \quad (3.34)$$

Illustrative examples of the beampatterns of Eqs. (3.33) and (3.34) are shown in Fig. 3-11. In both panels, the source length $L_s$ is one wavelength while the receiver length $L_r$ is three wavelengths. The left panel shows the source, receiver and combined source/receiver beampattern at broadside, while the right panel shows the same result while steered to 60°, or 30° from broadside. From the figure it can be seen that the unsteered source can have a significant impact on the two–way beampattern as the target moves away from broadside. The impact of the source provides the first clue that the monostatic SAS could benefit from source steering (spotlight mode) either by mechanically or electronically, or through the alternative means that is of central importance to this thesis — sonar platform mobility.

Note that the beampatterns are a result of the assumption that the target is in

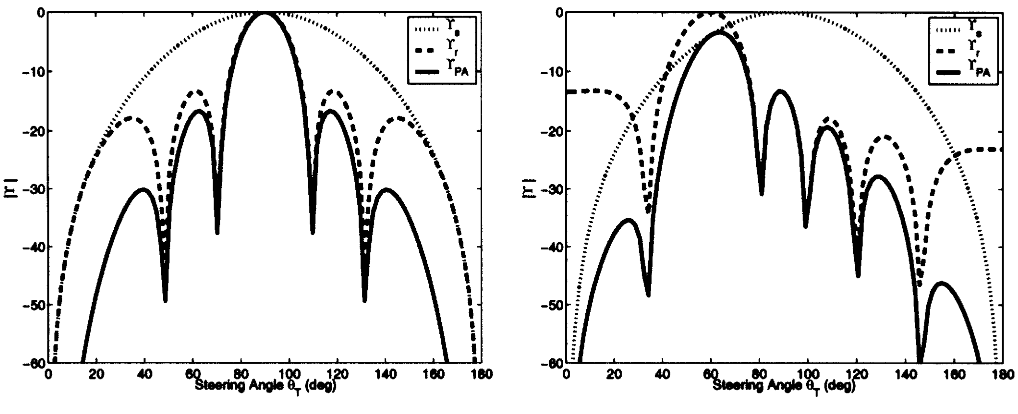

(a) Broadside beampatterns.

(b) Steered to 60°.

Figure 3-11: Source, receiver, and combined physical aperture beampatterns for a source of length $\lambda$ and a receiver of length $3\lambda$.

the far–field of the physical aperture, i.e.

$$R \geq \frac{L_r^2}{\lambda}$$

which is a reasonable assumption because if it were not the case then there would be little need for a synthetic aperture. If the equality condition is met, then the along–track resolution of the physical aperture at range $R$ is equal to the length of the aperture, compared to the theoretical maximum (and practically unattainable) resolution of $\lambda/2$. This formulation characterizes the fundamental response of the physical aperture, which is the building block of the synthetic aperture.

In the mobile sonar platform case, the synthetic aperture can be built in several ways, as shown in Fig. 3-12. The difference between these integration methods lies in the combination of the physical aperture beamformer over the multiple pings. In the leftmost plot, the SAS is shown as an extended linear array. This approach allows the AUV to have increased azimuthal resolution without range information. The center plot illustrates the response of this method to a compact target. The target remains in the mainlobe of the receiver over a certain number of pings, which is consistent with the SAR formulation developed previously. On the right, the SAS formation useful for imagery and target tracking is illustrated. This plot illustrates the sweeping of the

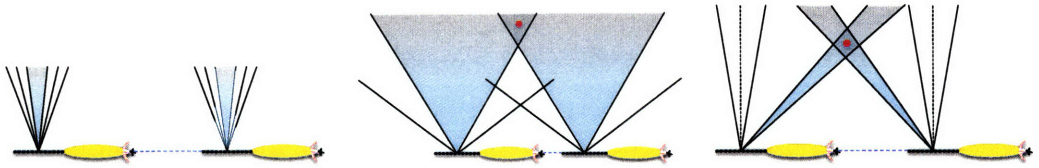

(a) (b) (c)

Figure 3-12: Formation of the synthetic aperture over the platform trajectory. (a) Unfocused, plane–wave beamforming over the synthetic aperture. (b) Unfocused, plane–wave SAS beamforming of a compact target (shown in red) (c) Focused SAS beamforming of a target, where the physical aperture steering angle changes with aspect to the target.

beam–steered angle to follow the target as the AUV passes. If the sweep is performed to a pre–determined grid, then the result is SAS imagery. If, on the other hand, the sweep is adaptive to a detected target (feature–based), then the result is target tracking.

### Synthetic Aperture Response

To get the SAS beampattern, the physical aperture can be considered as individual receiver elements of beampattern $\Upsilon_{PA}$ spaced by the interping spacing $v_r \Delta t$. First consider the far–field. Note that in the far–field, the source motion is irrelevant, due to the angle–only paradigm. So the beampattern is simply the convolution of the pulse train with the source/receiver beampattern.

$$\Upsilon^{far}_{SAS}(\omega, k_z) = \sum_{n=0}^{N_p-1} e^{-jk_z z_n} \Upsilon_{PA} = \frac{sinc\left[\frac{N_p}{2}\Delta z k_z\right]}{sinc\left[\frac{1}{2}\Delta z k_z\right]} \Upsilon_{PA}(\omega, k_z)$$

where $z_n$ are the positions of the AUV at each ping,

$$z_n = -\frac{N_p + 2n - 1}{2} \Delta z$$

and $\Delta z = v_r \Delta t$. Again with steering, the receiver terms only are steered, such that

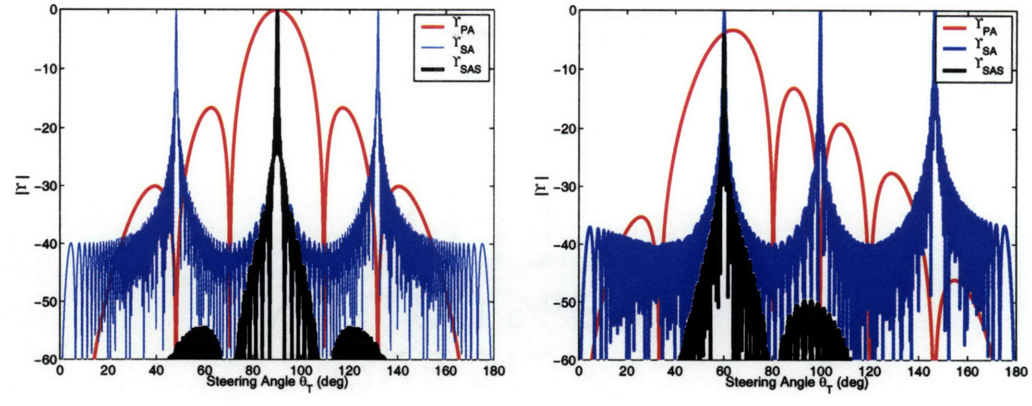

(a) Broadside beampatterns.

(b) Steered to 60°.

Figure 3-13: Source, receiver, and combined synthetic aperture beampatterns for a source of length $\lambda$ and a receiver of length $3\lambda$, and a synthetic aperture generated from 100 consecutive pings spaced by $L_r/2\ m$.

$$\Upsilon_{SAS}^{far}(\omega, k_z; k_{z_T}) = \sum_{n=0}^{N_p-1} e^{-j(k_z-k_{z_T})z_n}\Upsilon_{PA} = \frac{sinc\left[\frac{N_p}{2}\Delta z(k_z - k_{z_T})\right]}{sinc\left[\frac{1}{2}\Delta z(k_z - k_{z_T})\right]}\Upsilon_{PA}(\omega, k_z; k_{z_T})$$

The far–field SAS beampatterns are illustrated in Fig. 3-13. In the example shown the source and receiver are 1 and 3 wavelengths long, respectively, resulting in a physical aperture exactly the same as in Fig. 3-11. The synthetic aperture is generated by assuming the AUV moves at exactly the speed limit, one–half the length of the receiver aperture per ping interval. In both the steered and unsteered cases it can be seen that the aliasing lobes are perfectly cancelled due to their exact placement in the nulls of the physical aperture.

In practice, the far–field assumption is typically not applicable to the synthetic aperture, as is indicated by the desire to create pixellated images rather than beam–time sweeps. In order to incorporate the near–field effect of the synthetic aperture, the two–way travel to a fixed point in space (a pixel) is considered. The effect is that there is a doubling of the phase shift at each ping in the synthetic aperture, as has been described variously as an effective doubling of the aperture length [67] and, as can be seen in the DPCA, a halving of the physical aperture length. The DPCA view requires that the frequency be doubled to compensate [10], which leads to a confusing picture of the problem. Following the former approach, the SAS beampattern is given by

$$\Upsilon^{near}_{SAS}(\omega, k_z) = \sum_{n=0}^{N_p-1} e^{-j2k_z z_n} \Upsilon_{PA} = \frac{sinc\left[N_p \Delta z k_z\right]}{sinc\left[\Delta z k_z\right]} \Upsilon_{PA}$$

The SAS aperture at the central frequency over $N_p$ pings is therefore:

$$\Upsilon^{near}_{SAS}(\omega, k_z) = \frac{sinc\left[N_p v_r \Delta t k_z\right]}{sinc\left[v_r \Delta t k_z\right]} sinc\left[\frac{L_s}{2} k_z\right] sinc\left[\frac{L_r}{2} k_z\right] \tag{3.35}$$

where the physical source and receiver apertures are assumed to be continuous and uniformly shaded. The first term is the synthetic aperture beampattern and the last two terms are the physical aperture. The physical aperture beampattern serves as shading over the visible region $-k_0 < k_z < k_0$, where the mainlobe null–to–null width is

$$\Delta\phi^r_{N-N} = 2\sin^{-1}\frac{\lambda}{L_r}$$

The synthetic aperture beampattern, on the other hand, has a very narrow main lobe with closely spaced aliasing lobes. The numerator controls the SAS resolution, with the null–to–null resolution being

$$\Delta\phi^r_{N-N} = 2\sin^{-1}\frac{\lambda}{2N_p v_r \Delta t}$$

and the demoninator controls the locations of the aliasing lobes, which are located at

$$\Delta\phi^a_{N-N} = 2\sin^{-1}\frac{\lambda}{2v_r \Delta t}$$

Again, if the SAS array is steered, then receiver elements are shifted to the desired

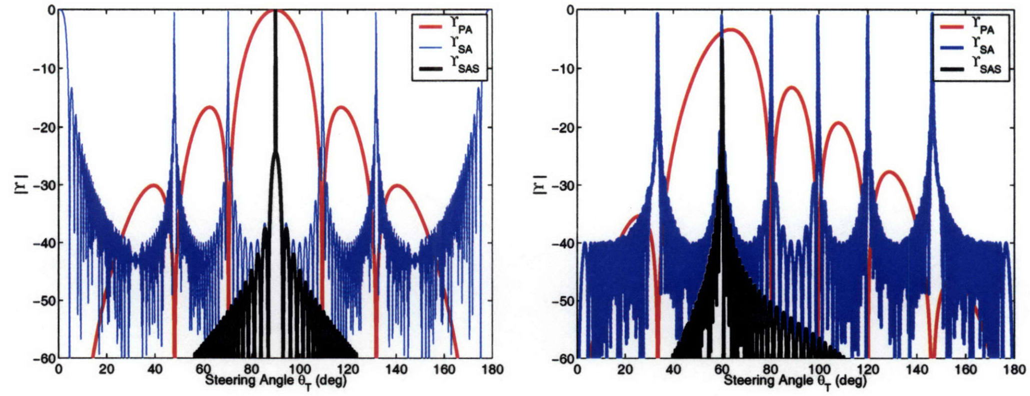

(a) Broadside beampatterns.

(b) Steered to 60°.

Figure 3-14: Source, receiver, and combined synthetic aperture beampatterns for a source of length $\lambda$ and a receiver of length $3\lambda$, and a synthetic aperture generated from 100 consecutive pings spaced by $L_r/2\ m$.

angle $k_{z_T}$, and the resulting beampattern is

$$\Upsilon_{SAS}^{near}(\omega, k_z; k_{z_T}) = \frac{sinc\left[N_p v_r \Delta t(k_z - k_{z_T})\right]}{sinc\left[v_r \Delta t(k_z - k_{z_T})\right]} sinc\left[\frac{L_s}{2} k_z\right] sinc\left[\frac{L_r}{2}(k_z - k_{z_T})\right] \quad (3.36)$$

The near–field SAS beampatterns are illustrated in Fig. 3-14. In the example shown the source and receiver are 1 and 3 wavelengths long, respectively, resulting in a physical aperture exactly the same as in Fig. 3-11. The synthetic aperture is generated by assuming the AUV moves at exactly the speed limit, one–half the length of the receiver aperture per ping interval. In both the steered and unsteered cases it can be seen that the aliasing lobes are perfectly cancelled due to their exact placement in the nulls of the physical aperture. However, the inclusion of the source motion (near–field effect) has moved the cancellation into the first null of the physcial aperture rather than the second. Any further separation between the synthetic array elements will cause the aliasing lobes to enter the main lobe of the combined system. Thus the speed limit for DPCA micronavigation is also the speed limit for keeping grating lobes out of the main lobe of the SAS.

If the vehicle moves at exactly the SAS speed limit (i.e. $v_r\Delta t = L_r/2$), the beampattern reduces to:

$$\Upsilon_{SAS}(\omega, k_z) = sinc\left[\frac{N_p L_r}{2} k_z\right] sinc\left[\frac{L_s}{2} k_z\right] \tag{3.37}$$

Note that the grating lobes are precisely cancelled at this speed, and the beampattern becomes the product of the source beampattern and the synthetic aperture beampattern. If the AUV moves more slowly than the maximum speed, the aliasing term remains in the beampattern formula, but the first aliasing lobe lies outside of the main lobe of the synthetic aperture, and is therefore all aliasing lobes are significantly attenuated. If, on the other hand, the vehicle moves faster than the speed limit, then the aliasing lobes move into the main lobe of the physical aperture.

All of the preceding analysis presumes that the target lies at precisely the same angle from the moving sonar platform over the entire course of insonification. This assumption is clearly inapplicable to imaging sonars that aim to achieve very high resolution. In most applications, then, it is more appropriate to follow a more general, ping–wise formulation of the SAS system. Leaving in place for now the quasi–linear motion of the platform, the imaging SAS system is represented as follows

$$\Upsilon_{image}^{near}(\omega, k_z) = \sum_{n=0}^{N_p-1} e^{-j2(k_z - k_{zT}^{(n)})z_n} \Upsilon_{PA}(\omega, k_z; k_{zT}^{(n)})$$

Although the system as described in Eq. (3.6.1) is a more accurate representation of the imaging sonar, the performance is somewhat more difficult to assess. In the following sections, the range resolution is introduced and ambiguity surfaces are used as the primary tool for analysis.

### The Effect of Broadband Sources

Since the lower frequency systems used for buried object hunting are generally required to be broadband to achieve sufficient range resolution, it is important to consider the influence of these broadband sources. The effect of frequency bandwidth on a remote sensing application in general is to create range resolution. The range and bearing resolutions are then orthogonal and create a resolution cell as shown in Fig. 3-15. When placed in a mobile mine–hunting system, however, the effects of the

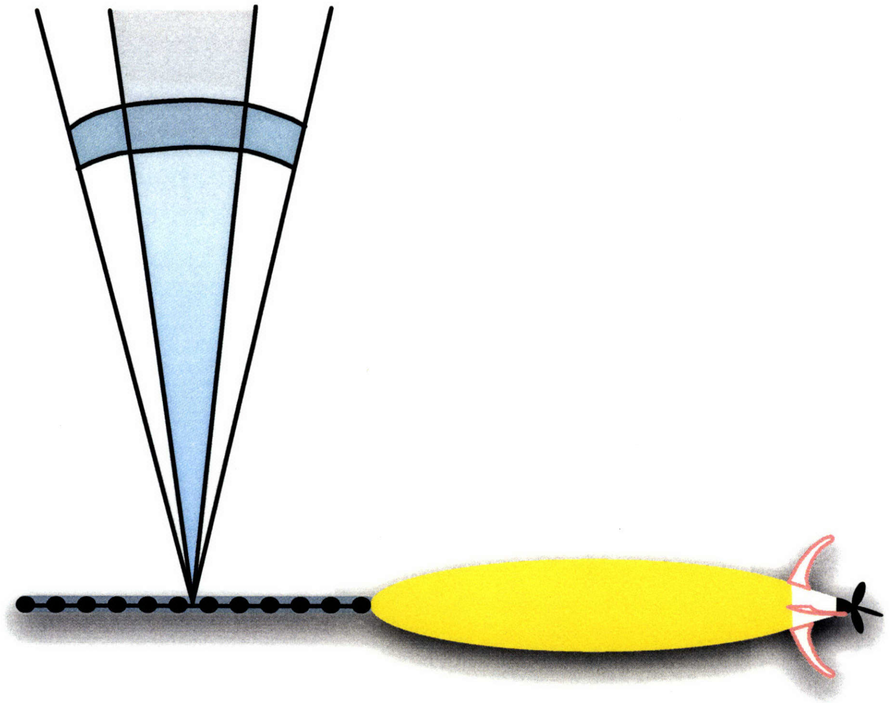

Figure 3-15: Resolution of the physical aperture with a bandlimited source. The angular resolution is set by the length of the aperture, while the temporal (range) resolution is set by the bandwidth. The resolution cell is the overlapping region, shown in gray.

range and bearing resolution may not be orthogonal, due to the wide aperture of the SAS relative to the target range. The combined effect of the broadband system is:

$$\Upsilon_{SAS}(\omega, k_z) = \frac{sinc\left[\frac{N_p}{2} v_r \Delta t k_z\right]}{sinc\left[\frac{1}{2} v_r \Delta t k_z\right]} sinc\left[\frac{L_s}{2} k_z\right] sinc\left[\frac{L_r}{4} k_z\right] sinc\left[\pi B \left(t - \frac{2R}{c_0}\right)\right] \tag{3.38}$$

The effect of this frequency bandwidth is that it allows some range resolution where the null–to–null range resolution is

$$\Delta R = \frac{2}{B}$$

Upon inclusion of range resolution, the beampattern approach is more appropri-

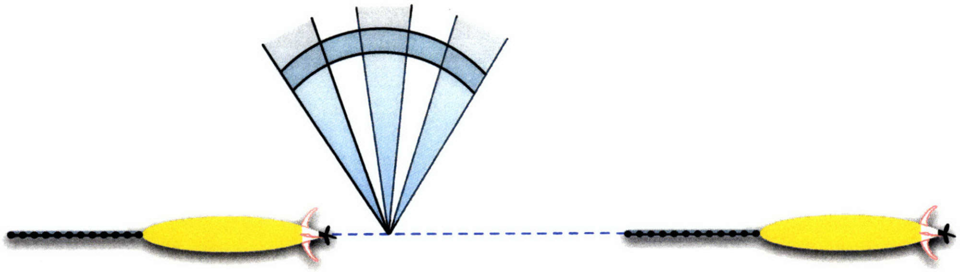

Figure 3-16: Resolution of the unfocused synthetic aperture with a bandlimited source. The angular resolution is set by the length of the synthetic aperture, while the temporal (range) resolution is set by the source bandwidth. Angular aliasing lobes may appear, as shown in the figure, if the synthetic aperture is undersampled. The resulting ambiguous resolution cells are shown in gray.

ately considered as a range–azimuth ambiguity surface, and the aliasing lobes become aliasing spots. As the AUV moves past a target of interest, the direct return from the target remains at the same apparent location — assuming there is adequate navigation — while the aliasing spots move according to range and viewing aspect fluctuations. An example of this in the unfocused SAS application is shown in Fig. 3-16. In this example, the vehicle is exceeding the SAS speed limit, so aliasing occurs in the angular domain. When combined with a broadband source, the aliased result is reduced to ambiguous resolution cells, resulting in a pincushion–type resolution plot reminiscent of range–Doppler abiguity plots in radar. In both the near–field and far–field SAS cases described in the previous section, the aliasing spots do not move sufficiently to ameliorate the aliasing effect.

### Combined Range and Azimuthal Resolution in the SAS

In the beampattern analogy, the range resolution and azimuthal resolution are orthogonal. In practice, the SAS extends over a wide angle about the target, causing the azimuthal and range resolution to co–mingle, particularly at the edges of the SAS. An example of this effect, in the focused SAS application, is illustrated in Fig. 3-17. At the target location, the range–azimuth cells form a cross, mixing the range and azimuth directions with respect to the synthetic aperture. With an appropriate

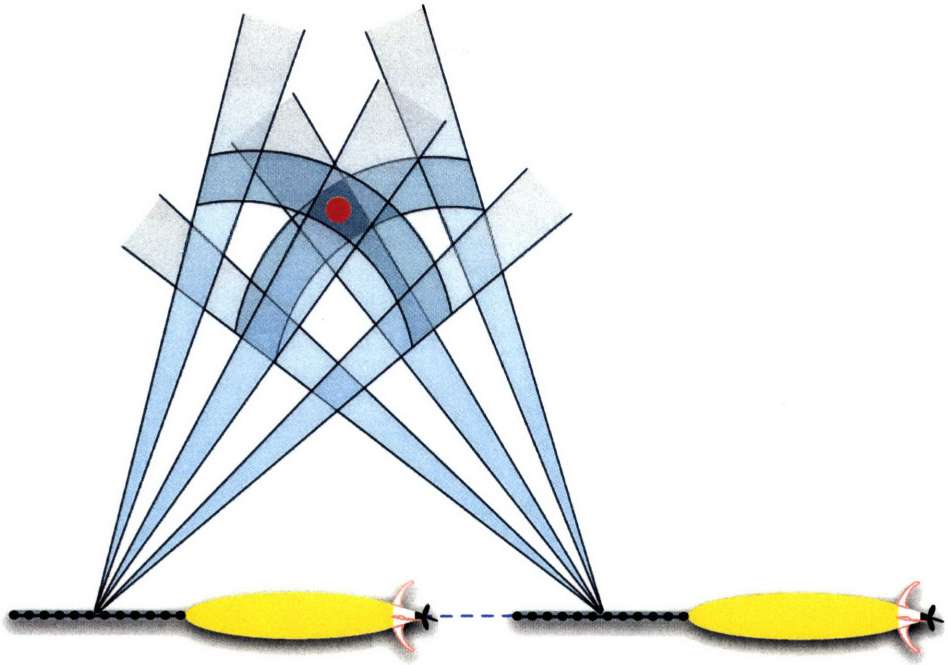

Figure 3-17: Resolution of the focused synthetic aperture imaging sonar with a bandlimited source. The angular resolution is set by the length of the synthetic aperture, while the temporal (range) resolution is set by the source bandwidth. Angular aliasing lobes may appear, as shown in the figure, if the synthetic aperture is undersampled. Over a sufficient aperture, the variation in steering angle smears the aliasing lobes, leaving a an unambiguous resolution cell, shown in gray.

choice of platform motion, the combination of these two types of resolution can be used to mitigate some of the aliasing concerns from the strict beampattern analogy. The combination arises from the varying steering angle over the synthetic aperture:

$$\begin{aligned}\Upsilon^{near}_{SAS}(\omega, k_z) =& \frac{sinc\left[N_p v_r \Delta t k_z\right]}{sinc\left[v_r \Delta t k_z\right]} sinc\left[\frac{L_s}{2} k_z\right] \\ & \times sinc\left[\frac{L_r}{2} k_z\right] sinc\left[\pi B \left(t - \frac{2R}{c_0}\right)\right] \end{aligned} \tag{3.39}$$

The ambiguity function illustrates the combined range and azimuthal performance of the sonar. In order to generate an ambiguity surface, a hypothetical target must be established. The ambiguity surface is then the cross–correlation of the actual return from the target with the beam response of the SAS.

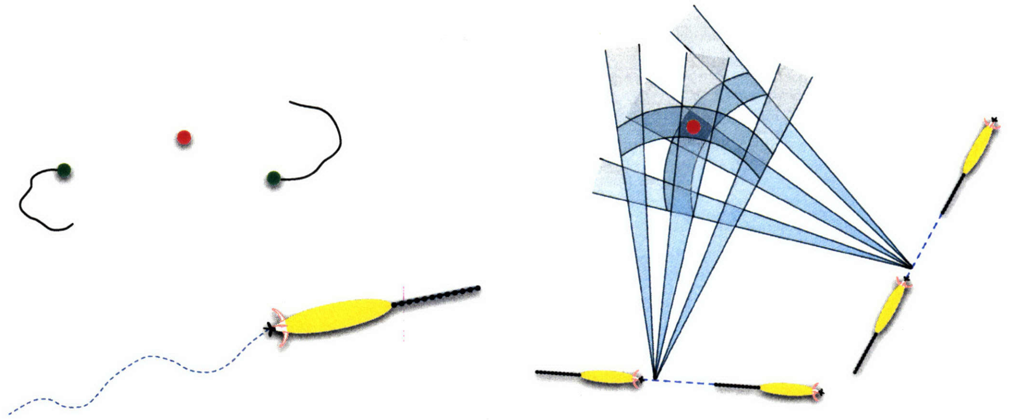

(a) (b)

Figure 3-18: Moveout of the aliasing lobes due to platform mobility. As the vehicle moves past the target (in red), the target position remains the same while the apparent aliasing lobes (shown in green) sweep a trajectory that depends on the vehicle motion. (b) Illustration of the ability to smear aliasing lobes through aggressive platform motion. The vehicle makes a nearly 90° turn to separate the aliasing lobe and isolate the target.

Strategies for detecting or removing aliasing through platform motion are shown in Fig. 3-18. In Fig. 3-18 (a), the moveout of the aliased targets is shown as the AUV passes the true target during the course of its pre–planned mission. In Fig. 3-18 (b), the SAS outputs of two vehicle passes at sharply different angles are combined. The target then stands 3 dB above the aliased lobes. These strategies and others will be explored later in this thesis to provide an increased area search rate for mobile sonar platforms.

# Chapter 4

# Target Detection and Imaging

In the littoral ocean, targets of interest may be few and far between, and may in addition be obscured by reverberation levels. There may also be spurious noise caused by local biologics or shipping. A target is then detected if it is a consistent anomaly above the background noise. If the target is small, soft, buried or stealthy, then the signal–to–noise ratio of the target may be insufficient for detection from a single sonar reception. However, the inherent uncertainty in undersea navigation makes the coherent association of sonar data between multiple receptions challenging. In addition, associating simultaneous receptions from multiple sonar platforms is challenging due to the severely limited communication rates.

## 4.1 Single Ping Methods

In a given ping, the geometry of the sonar is fixed. For this reason, classical signal processing methods are directly applicable to each reception. Optimal signal detection generally require a model of the signal and a model of the noise. Given an active sonar system, the model of the signal is readily available as a replica of the transmitted pulse. The noise, on the other hand, is not as easy to model. It is determined by the material properties and roughness statistics of the corresponding resolution cell, as well as the sonar geometry.

The advantage of a single ping process is clear. As described extensively in the previous section, combining signals from multiple pings is difficult even in the case of monostatic platforms moving in a quasi–linear trajectory. When the source and receiver are in different locations and traveling different directions, the process becomes even more challenging.

### 4.1.1 Monostatic Single Ping Methods

A monostatic sonar system with a receiver array provides both angular and temporal resolution. Therefore the obvious choices are to detect an object in some combination of time–frequency, wavenumber–beam domain. For detection of frequency–dependent characteristics such as elastic returns or buried objects it may be beneficial to make the detection in frequency domain. For broadband returns like specular bounces from proud targets, time domain may be the more appropriate choice.

As an example of the monostatic single ping analysis, consider a pass made over a target field in the GOATS'98 experiment, as shown in Appendix A. Although the experiment was bistatic, the data selected is when the vehicle passes near the fixed transmitter, resulting in a series of nearly monostatic measurements. In Fig. 4-1, the beam–frequency and beam–time response on the physical aperture is shown on a ping–by–ping basis as the AUV passes near the three 1–m diameter, air–filled steel spheres. The two leftmost columns show the half–buried sphere, the central columns show the flush–buried sphere and the two rightmost columns show the fully buried sphere. As expected, the proud sphere is detectable on a ping–by–ping basis, and can be readily tracked as the AUV passes the target field, although the angular resolution of the physical aperture is not great. The buried targets, on the other hand, are not detected from the single ping results. The insonification angle of the flush–buried target is sub–critical, approximately 20°, compared with the 24° critical angle. The insonification angle of the deeply buried target is very close to the critical angle.

In Fig. 4-2, the same processing is shown for a pass over the target field when the source is at a super–critical angle for both buried targets. There are two structural differences between the previous case and this one: first, there are less pings because the ping repetition rate was slower for the second mission, and second, the vehicle pass is from one side of the target just to the source–target axis, whereas the previous data selection was nearly centered on the source–target axis. The latter difference is a consequence of where the vehicle happened to be when the navigation cycle began. It can be seen that the target scattering energy is greater in the super–critical case, but the targets are still difficult to distinguish in beam–time space.

In order to detect more obscure targets such as the buried spheres, it is necessary to form a synthesized aperture to improve the target SNR. In Figs. 4-3 and 4-4, the resulting beam–frequency and beam–time plots are shown when integrating sets of four ping receptions. Over four pings the aperture length is extended by about a factor of two, while the lateral vehicle motion is small enough that the micronavigation is not critical.

The maximum length of consecutive pings available in the GOATS'98 experiment was a seven second time window. The rsulting synthetic aperture is approximately 7 meters in length, which is a nearly tenfold increase over the physical aperture. In the sub–critical case, corresponding to Fig. 4-5, the seven second window contained 23 pings. In the super–critical case, corresponding to Fig. 4-6, the seven second window contained 17 pings. The supercritical insonification provides stronger target receptions for the buried targets, while the proud target receptions are nearly equal for the two cases.

### 4.1.2 Bistatic

Bistatic target detection from mobile sonar platforms is more complicated both operationally and in terms of the signal processing. Operationally, it is not easy for one vehicle to be aware of the current position and state of another vehicle. Communications between AUVs is not reliably established in most cases. In terms of signal processing, the loss of relative positioning as well as possibly the time trigger of the source makes the localization of the target more difficult. In addition, in some configurations, the receiver can be blinded by the source direct blast or specular bounce from the interfaces. There are, however, operational advantages to bistatic configurations if they can be well–controlled. Some such configurations are included

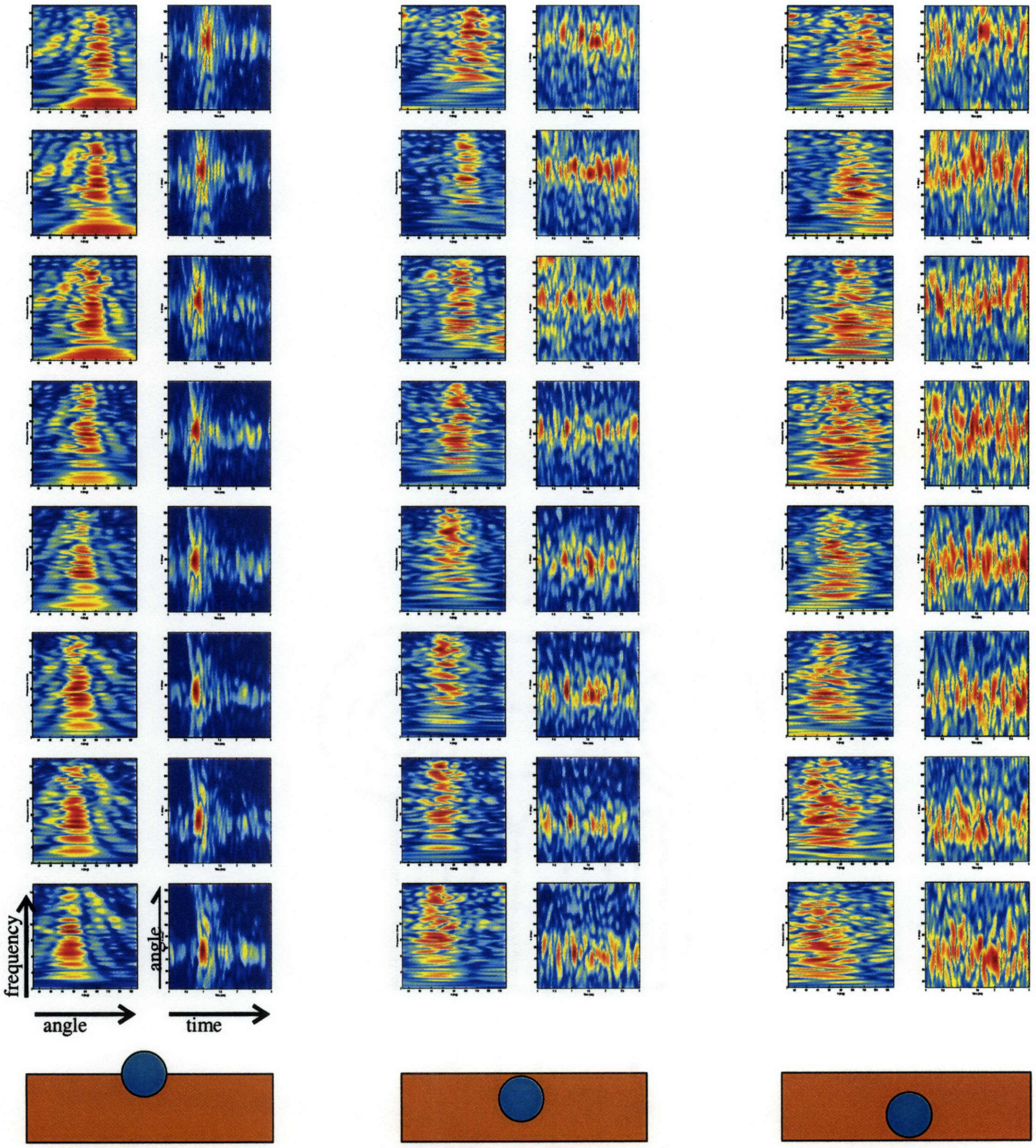

Figure 4-1: Beam angle vs. frequency and beam angle vs. time as the AUV passes half–buried (left), flush–buried (center) and 1–m deep buried spheres (right). The source is below the critical angle for the buried targets. Each row corresponds to a single reception along the receiver array.

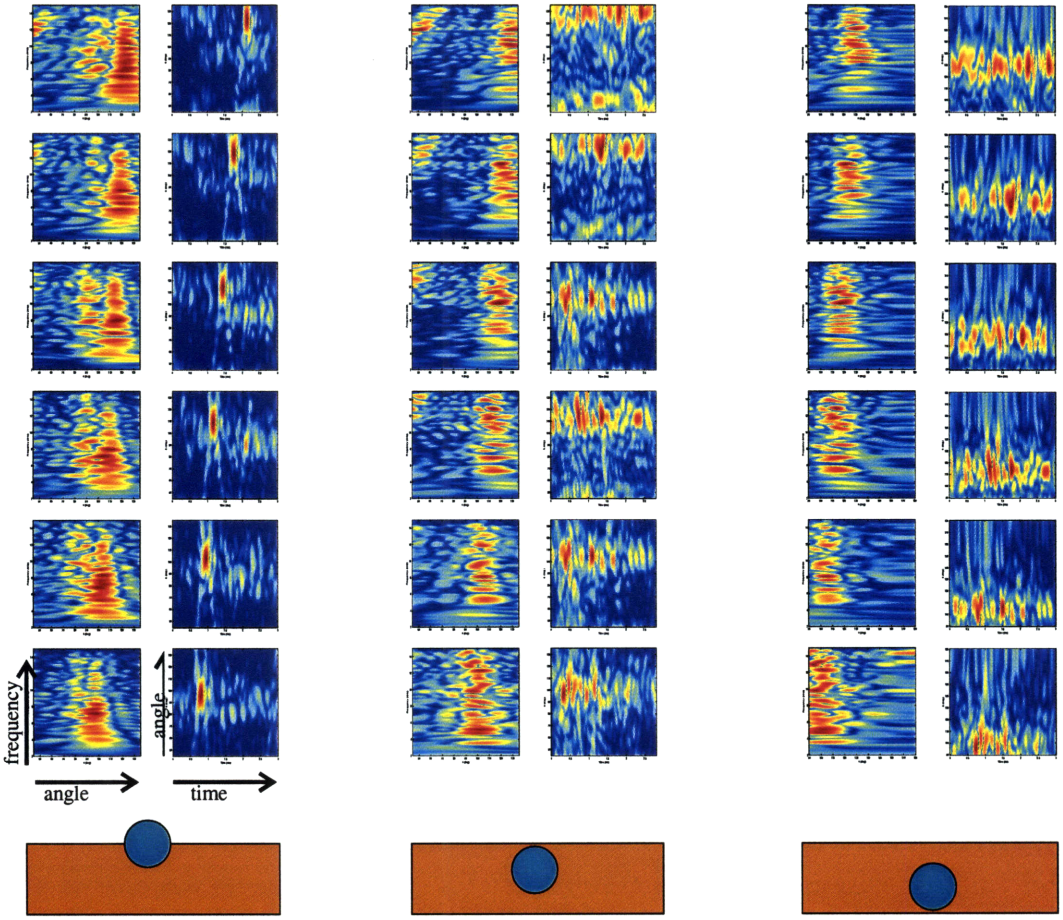

Figure 4-2: Beam angle vs. frequency and beam angle vs. time as the AUV passes half–buried (left), flush–buried (center) and 1–m deep buried spheres (right). The source is above the critical angle for the buried targets. Each row corresponds to a single reception along the receiver array.

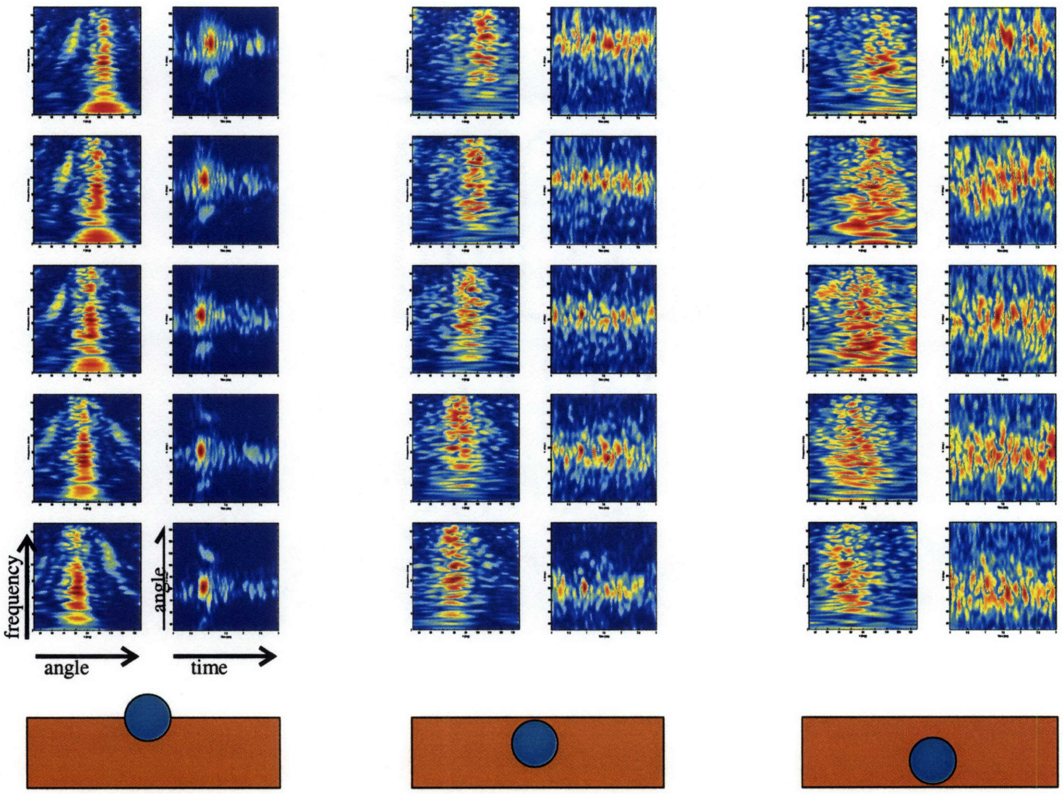

Figure 4-3: Beam angle vs. frequency and beam angle vs. time as the AUV passes half–buried (left), flush–buried (center) and 1–m deep buried spheres (right). The source is below the critical angle for the buried targets. Each row corresponds to a 4–ping synthetic aperture.

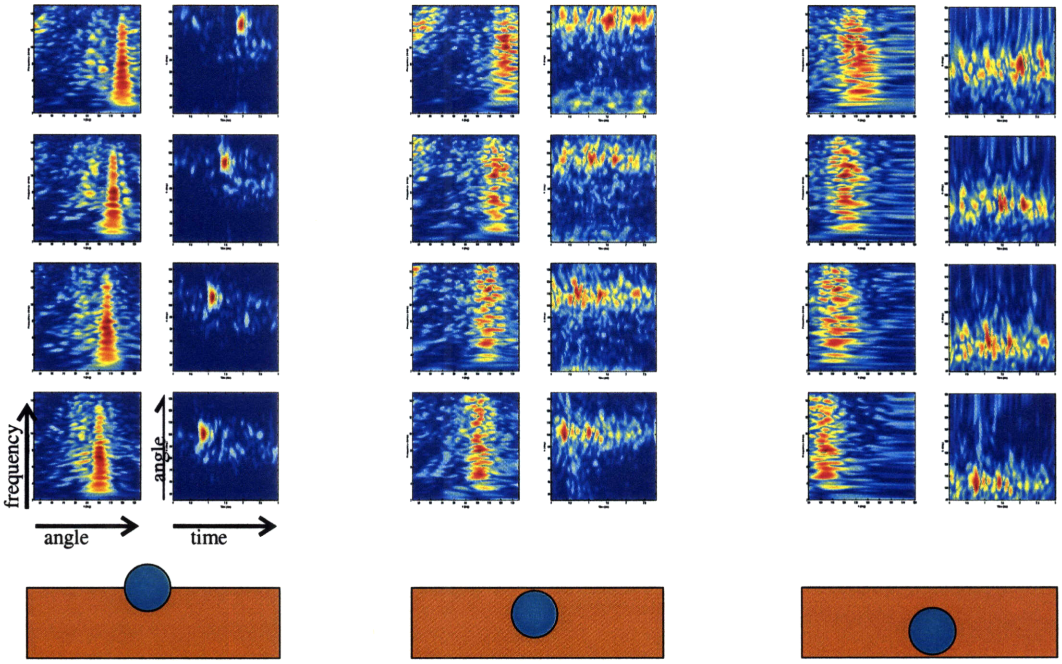

Figure 4-4: Beam angle vs. frequency and beam angle vs. time as the AUV passes half–buried (left), flush–buried (center) and 1–m deep buried spheres (right). The source is above the critical angle for the buried targets. Each row corresponds to a 4–ping synthetic aperture.

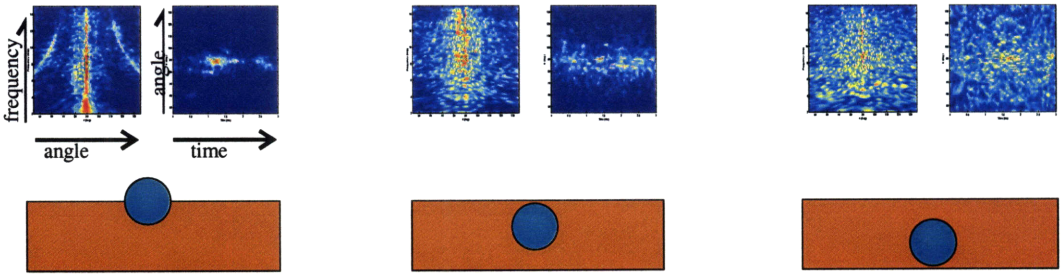

Figure 4-5: Beam angle vs. frequency and beam angle vs. time as the AUV passes half–buried (left), flush–buried (center) and 1–m deep buried spheres (right). The source is below the critical angle for the buried targets. Each plot corresponds to a 23–ping synthetic aperture.

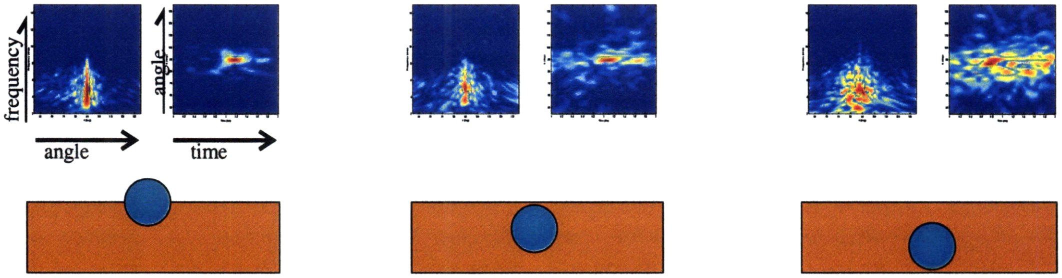

Figure 4-6: Beam angle vs. frequency and beam angle vs. time as the AUV passes half–buried (left), flush–buried (center) and 1–m deep buried spheres (right). The source is above the critical angle for the buried targets. Each plot corresponds to a 23–ping synthetic aperture.

here.

Consider a crawling vehicle, attached to a surface buoy by a tether. The surface buoy provides accurate position coordinates through GPS, and the time trigger of the source is passed through the tether for a precise synchronization between the source and receiver. This configuration removes some of the challenges to the purely bistatic operations by allowing automatic time synchronization and navigation with fixed relative geometry. Fig. 4-7 shows the pre–planned trajectory and the maximum range–corrected measured signal amplitude along that trajectory. In this case, a 2–m long cylinder lies in the target field and the vehicle passes near it. As can be seen in the plot on the right, a spike in the measured amplitude occurs when the vehicle passes the broad side of the target. This spike in measured amplitude indicates a target, and the vehicle could take action based on this result.

Another preferred bistatic scenario is that of the remote source. This configuration is practical, because AUV–borne sources, tend to be wide–beam sources, and the entire water column is lit up when they fire. The wide–beam nature of the sources is a simple result of the low frequency required for sub–bottom penetration combined with the dimensions of the AUV platform that must carry it. An example of the remote source scenario is shown in Fig. 4-8. The setup is almost the same as in the previous example, except that the source remains fixed at the bottom of the plot. The trajectory shown is for the receiver only. The amplitude plot is similar, although the lobe of the target scattering is somewhat wider and has higher sidelobes.

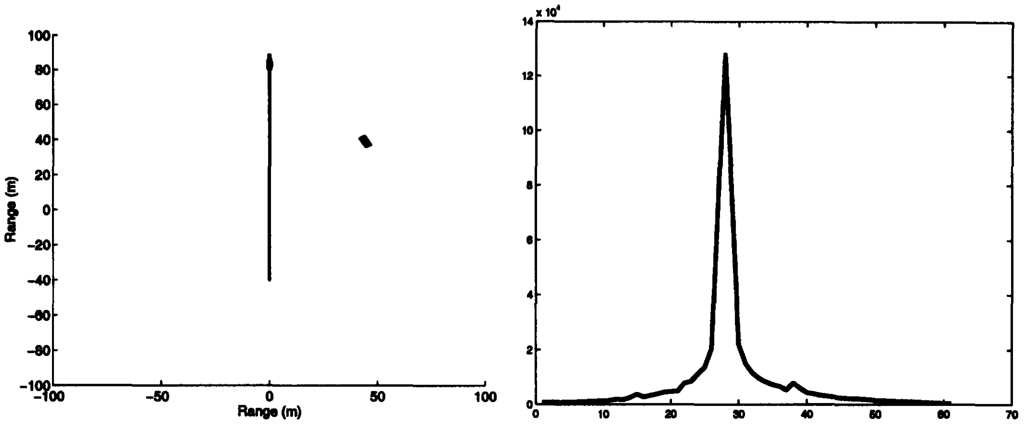

(a) Vehicle trajectory.

(b) Amplitude of the target return.

Figure 4-7: Target detection with a tethered vehicle. The source is at the surface of the water column, while the receiver is on a vehicle at depth.

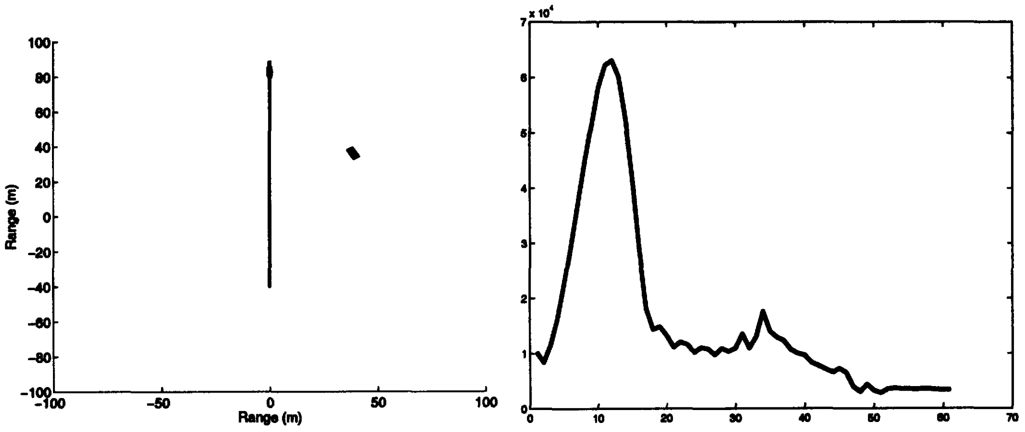

(a) Receiver trajectory.

(b) Amplitude of the target return.

Figure 4-8: Target detection with a remote source. The source is positioned at (0,-100), and the receiver vehicle drives toward and past the target.

## 4.2 Multi-ping/Integral Methods

Given the challenging SNR for many situations encountered by mobile sonar platforms, the integration of multiple pings is often necessary for the detection of targets. The desirable wide–angle source serves to further increase the noise level, exacerbating the SNR problem. Weaker signals, such as specular returns from buried targets, or elastic returns, are even more challenging to detect. In addition to the detection problem, there is the suppression of false alarms. Glints from seabed features or spurious noises in the ocean caused by biological sources can occasionally be detected on a given ping, and eliminated as a compact stationary target through the processing of successive pings.

For moving sonar platforms, the coherent integration of multiple pings is extremely challenging. Independent navigation is rarely of sub–wavelength accuracy, and the platform motion is typically significant in both along–track and cross–track directions. As illustrated in Chapter 3, the motion compensation problem has been addressed for limited applications through a great deal of prior research in SAS. Thus, SAS provides a strong candidate starting point for multi–ping integration with mobile sonar platforms.

### 4.2.1 Synthetic Aperture Sonar (SAS)

Synthetic aperture sonar (SAS) is the sonar equivalent of the synthetic aperture radar (SAR) algorithm that was first presented in the 1950s. It is desirable for human–reviewed applications because it transforms the time series data into a format that is consistent with the experience of the user, i.e. a high resolution image. A standard way to classify targets is to create a maximum resolution image and then classify based upon the image. This methodology drives the desire to maximize frequency and/or aperture in pursuit of the highest possible image resolution. However, as will be shown in this thesis, significant information can be lost in the process.

### Coherent and Incoherent SAS

For the maximization of signal to noise ratio (SNR) and resolution of the synthetic aperture, coherent processing is obviously desirable. Incoherent signal processing is generally only used when environmental parameters disallow confidence in coherent processing. In the GOATS scenario, there are several reasons that a reduction in SNR and resolution may be accepted in favor of an incoherent approach. However, coherent processing should be used as much as possible while maintaining a robust and computationally efficient system. Accuracy, simplicity and robustness must all be considered in the AUV application. With these in mind, some of the significant factors contributing to the coherent vs. incoherent processing decision are outlined in this section.

In considering buried or elastic targets (or in this case both), there will be returns that are delayed or advanced relative to the assumed straight ray propagation through a water medium. These returns will tend to sum out as noise in near–field processing. However, they also contain information about a relevant target, so eliminating them through beamforming will result in a loss of information useful for both detection and classification. This information loss could be inconsequential if the target is easily detectable, or it could be extremely significant, as in cases where the direct return either does not exist or is masked by a stronger scatterer. Incorporating an unknown seabed and unknown elastic returns coherently would require iterating over possible medium properties, as in matched field processing [7] , or over the depth dimension, as in seismic migration [75]. An incoherent approach may allow robust imaging over the medium with small changes in the propagation paths, caused either by elastic delays or medium sound velocity changes. Coherent processing begins to degrade detection capability of delayed returns once the aperture reaches a length at which range information cannot be ignored. As such, a likely choice would be to limit the coherent processing to plane-wave beamforming.

Several other sources of received signal incoherence have not been investigated in this work. Temporal and spatial non-stationarity effects are neglected, as the VSW waveguide is assumed to be well mixed and the ranges involved are very short, on the order of 10 *m*. The loss of coherence due to the cumulative micro-navigation error is not quantitatively considered due to hardware limitations at the time of the experiment, although it may be of significant magnitude.

One extreme of the imaging algorithm is to bypass the coherent processing block altogether and incoherently sum all of the channels in the synthetic aperture. The image value at pixel $j$ can be expressed in this case as:

$$K_j = \sum_{n=0}^{N-1} R^H_{nj}(t)\,|e_n(t)|^2 \tag{4.1}$$

where N is the number of elements in the SAS, $R_{nj}$ is the signal replica for element $n$ and $e_n(t)$ is the measured echo return at element $n$. In this case a signal replica is produced for each element and the matched filter outputs are summed incoherently.

The use of the surface-reflected multipath return in the incoherent processing generates image side-lobes of $-3\ dB$, which can allow a strong scatterer to mask other targets. Due to the circular ambiguity of each sensor, a very long aperture is needed to localize a target. This method was applied to the 7 *m* synthetic aperture, and the resulting image can be seen in upper left of Fig. 4-9 .

In this figure, it can be seen that the half-buried sphere is clearly detected. However, the sphere image has two significant side-lobes in range, one ofwhich masks the image of the flush-buried sphere, S2. This is a major limitation of the incoherent matched filter approach. The simplest, although not necessarily the most robust, way around this is to simply remove bright scatterers from the data. The upper right image is created by time-gating to remove the returns from S3. Once S3 is removed from the data, S2 can be seen in the image much more clearly than it can be seen in the physical aperture data, although it appears to be located further from the receiver than expected.

The lower images show the other extreme in the imaging algorithm, which is to use all of the information possible for coherent imaging. In this case, the image value at pixel $j$ is given by:

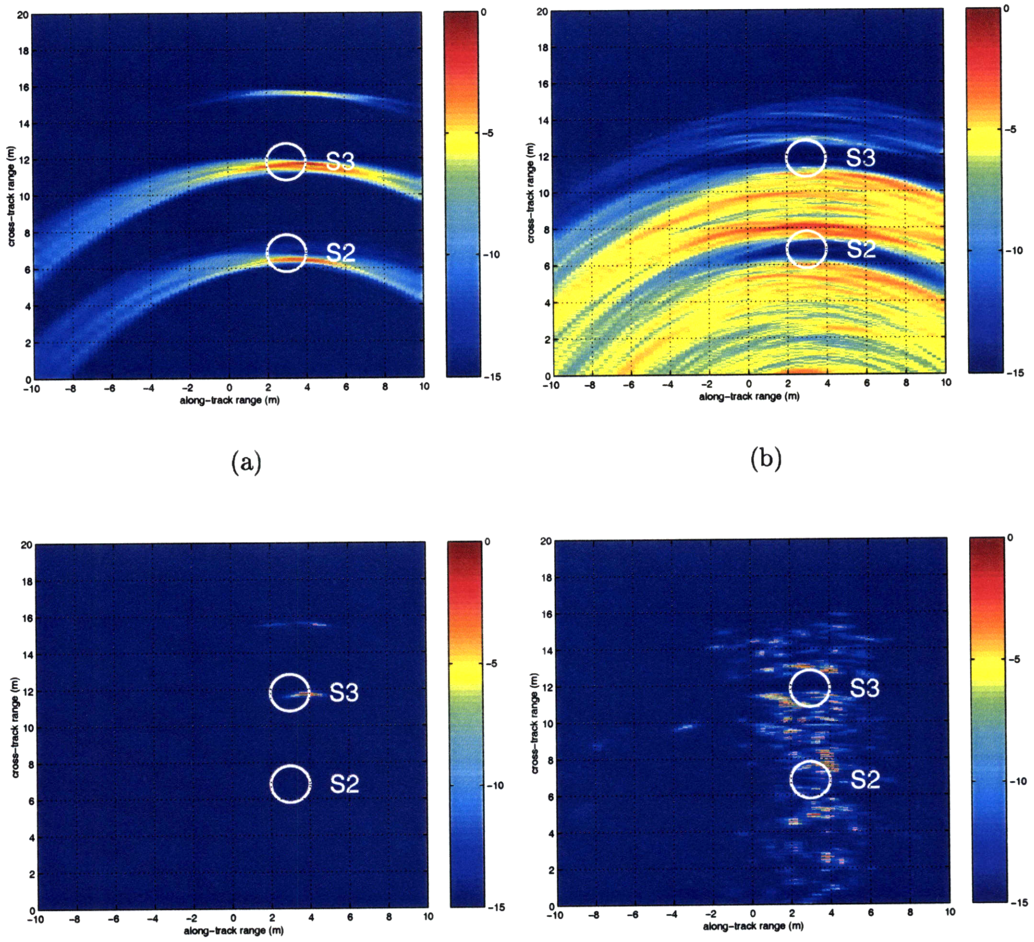

(a) (b)

(c) (d)

Figure 4-9: Extremes of the imaging process, file 25. The SAS extends from the origin to $x \approx 6.7\ m$ along the x-axis. (a) Fully incoherent image. (b) Fully incoherent image with the half-buried sphere time-gated out. (c) Fully coherent image. (d) Fully coherent image with the half-buried sphere time-gated out.

$$K_j = R_{0j}^H(t)\left|\sum_{n=0}^{N-1} e_n(t-\tau_{nj})\right|^2 \tag{4.2}$$

where $R_{0j}$ is the signal replica at the SAS phase center, N is the total number of elements in the SAS, and $\tau_{nj}$ is the time delay of the return on element $n$ from pixel $j$ relative to the return at the phase center. In this case echoes are delayed by the proper amount to focus on the given pixel, and then the inner product is taken with a single incoherent matched filter at the SAS phase center to extract the image value. The coherent processing is performed in time domain due to the broadband nature of the signal.

The synthesized array then is focused in range and azimuth, so the accuracy of the data alignment becomes more important. The inclusion of range information causes returns that do not fit the standard imaging model to destructively interfere, as is illustrated in the images. The return from the buried target, S2, appears to be a mode of the sphere, which is delayed and therefore not properly focused in the image. The direct return is not apparent, and in fact may not exist due to the evanescent insonification. Although the target can still be seen in the image, the detection capability is slightly degraded by focused coherent processing. While fully coherent processing would seem to be the optimal way to extract the most information from the SAS, it is more sensitive to geometrical or data alignment uncertainties than is incoherent processing.

### Coherent-Incoherent SAS Compromise

In the case of the GOATS'98 dataset, there is no way to know the cumulative navigation error along the synthetic aperture, due to the hardware limitations mentioned previously. In future work, the navigation error will be quantifiable, and it will be possible to balance the micro-navigation error with the length of coherent aperture. Here, the length of the synthetic aperture segment for coherent processing is chosen based on other concerns. With the mixed processing, the image value at pixel $j$ is given by:

$$K_j = \sum_{m=0}^{M-1} R_{mj}^{H}(t) \left| \sum_{n=0}^{N_m-1} e_n(t - \tau_{nj}) \right|^2 \tag{4.3}$$

where $M$ is the number of coherent processing blocks and $N_m$ is the number of elements in block $m$. The elements within the coherent block are delayed and summed to focus on the given pixel, and then the inner product is taken with a matched filter evaluated at the phase center of the block. This process is repeated for the $M$ blocks, and the results are summed incoherently. The block length can be decided based on the desired balance between coherent and incoherent processing.

### 4.2.2 Simulation

Using the MIT-MCM package (see Appendix B), synthetic experiments are performed to evaluate potential target detection and classification methods. The synthetic datasets are of sufficient quality to allow end–to–end simulation data acquisition and signal processing, including synthetic aperture imagery. The most noticeable difference between experimental SAS images and those created with the simulation is the lack of a shadow region in the simulation. As a first example, consider the target field shown in Fig. 4-10. The three proud targets are two water filled 2–m long, 0.5–m radius steel cylinders and a rigid sphere of radius 0.25 m. The monostatic AUV makes two passes: one to the left of the target field, and one to the right of the target field. The results are compared at 30 kHz and 5 kHz center frequency.

In the first simulation, the central frequency of the sonar is 30 kHz, which is somewhat higher than that used in other parts of this thesis for buried target detection. The vehicle traverses a 20–m long path and the synthetic aperture is built over this entire trajectory. The resulting SAS images are shown in Fig. 4-11. The top pair of images are the images created by the two passes, while the third image is a summation of the two images. It can be seen from all three images that the target are readily discerned above the reverberation and a human end–user could easily determine which target is a sphere and which is a cylinder. Further, one could imagine an automatic sphere/cylinder classifier determining which target was which shape. The obvious

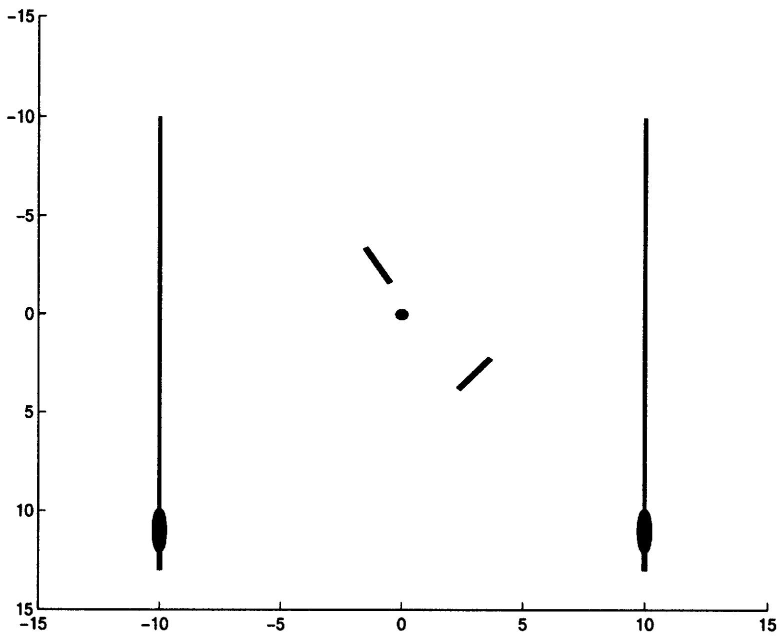

Figure 4-10: Two passes of AUV over target field, used in SAS simulation. The three targets are a 0.25–m radius sphere and two 2–m long, 0.1–m radius cylinders.

advantage to higher frequency operations is that the detail of the imagery will be finer and image–based classification techniques more easily applied. The drawbacks are the minimal seabed penetration and minimal excitement of target resonances.

At 5 kHz, the targets are also well–resolved, as shown in Fig. 4-12. For a given aperture length, however, fewer receiver elements are required. The fundamental difference between the higher–frequency case and the lower–frequency images can be seen in the images of the elastic cylinders. The 5 kHz images have ghosts on the far side of the cylinder from the sonar platform. It is also notable that the back–scattered reverberation is lower in the 5 kHz case.

A comparison of the raw data further bears out these differences. Waterfall plots of the trajectory to the right of the target field, shown in Fig. 4-13, indicate that prior to the target returns, the reverberation is slightly lower, while the post–target arrivals are higher in level. This indicates that the difference is related to the target return. As would be expected, the lower frequency source elicits more of an elastic response from the target by entraining the whole target on impact.

Now consider the results when one of the targets is buried. The simulation was

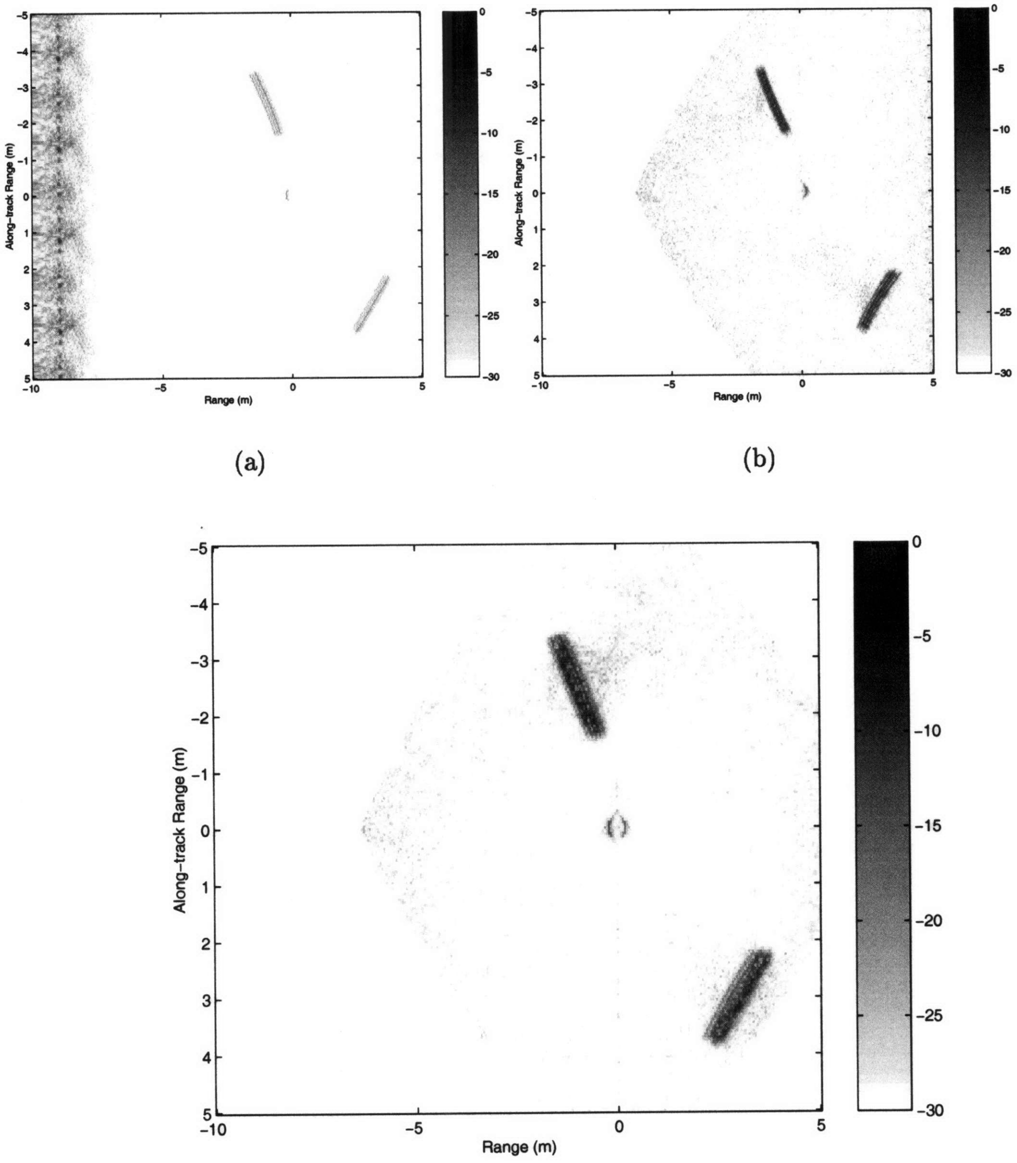

(a)

(b)

(c)

Figure 4-11: SAS imagery from the simulated mission, at 30 kHz. All targets are proud. On the top row are the passes to the left and right of the target field. The bottom plot is the fused image.

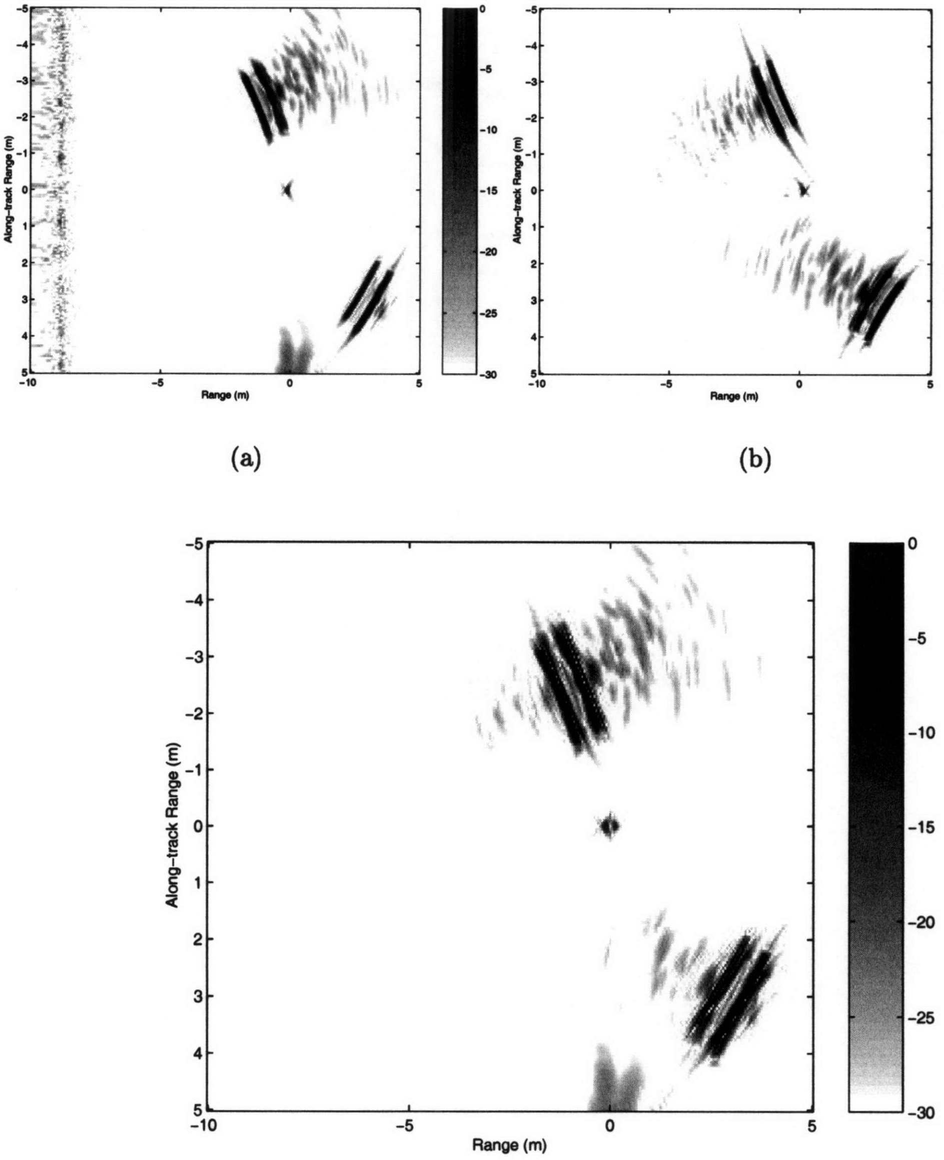

(a)

(b)

(c)

Figure 4-12: SAS imagery from the simulated mission, at 5 kHz. All targets are proud. On the top row are the passes to the left and right of the target field. The bottom plot is the fused image.

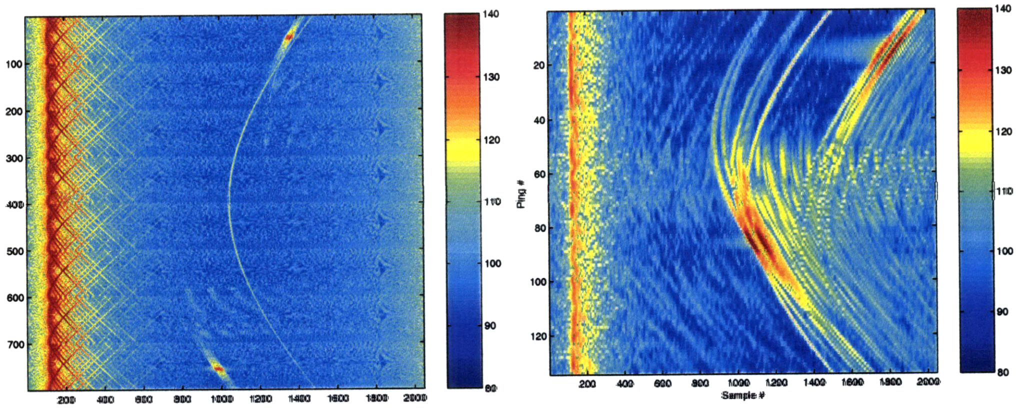

(a) 30 kHz.

(b) 5 kHz.

Figure 4-13: Time history of the receptions made by the receiver platform as it passes the target field.

executed again, with the cylinder in the bottom right corner buried just below the seabed. At 30 kHz, the imagery shown in Fig. 4-14 shows that the buried cylinder is not detectable. The 5 kHz run, on the other hand, creates a weak image of the buried cylinder, as shown in Fig. 4-15. Even in the 5 kHz case, however, the shape of the target is not as clearly visible. Note also that the 5 kHz image shows some elastic response of the target that could be used for classification.

### Image Quality

As detailed in Chapter 3, the quality of SAS imagery is directly related to the ability to combine data along the synthesized aperture. The integration of data is in turn related to the seabed roughness statistics in the case of DPCA micronavigation. In order to study the degradation of the image quality resulting from varying seabed conditions, the simulated SAS runs were performed with seabed correlation lengths ranging from 0 to 2 m. A quality factor is introduced to determine the target contrast to background:

$$Q = \frac{\sum I^2(x_t, y_t)}{\sum I^2(x_i, y_i)} \tag{4.4}$$

where the summation index $t$ covers only the detected target boundaries and the

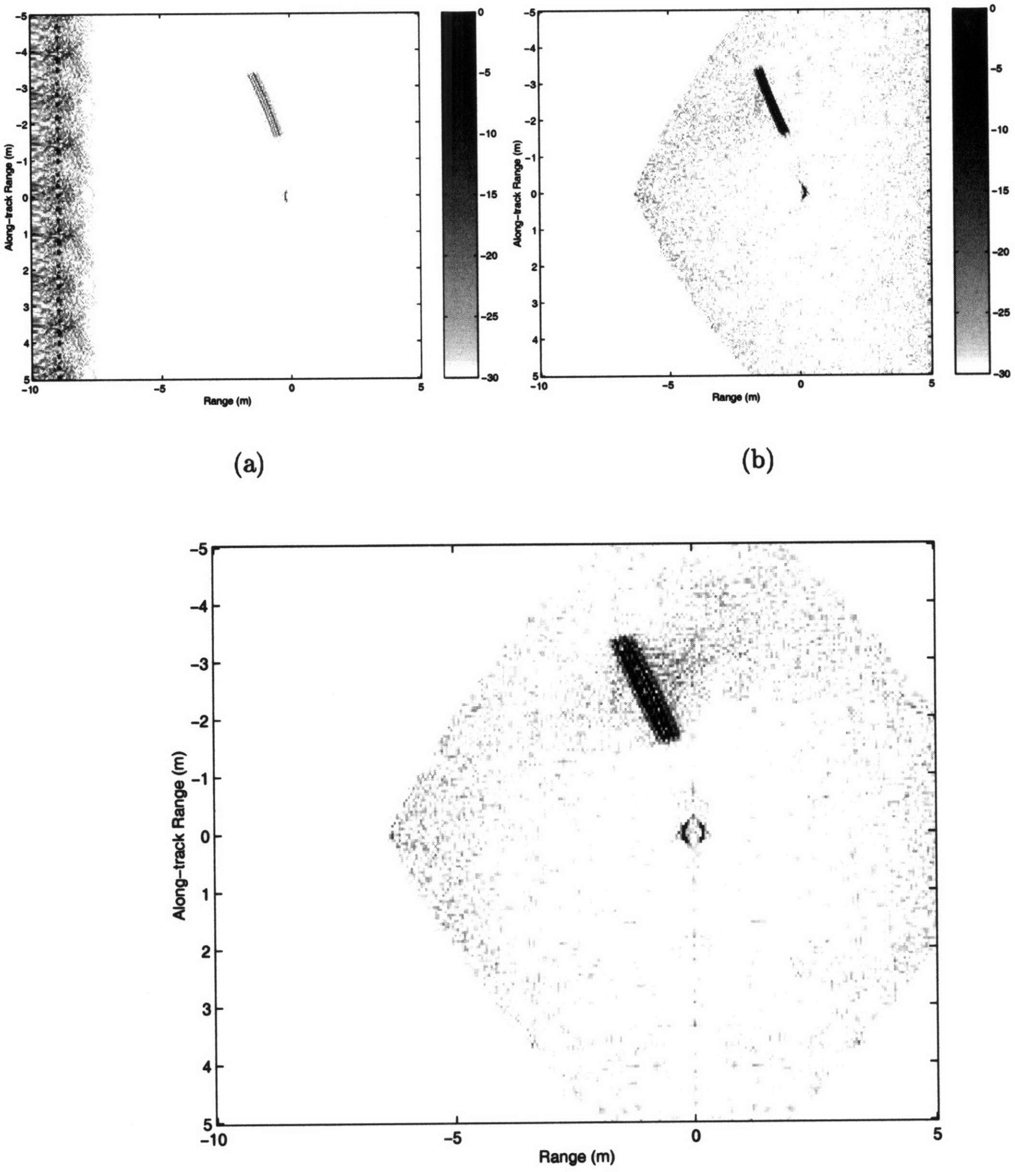

(a)

(b)

(c)

Figure 4-14: SAS imagery from the simulated mission with a buried cylinder, at 30 kHz. On the top row are the passes to the left and right of the target field. The bottom plot is the fused image.

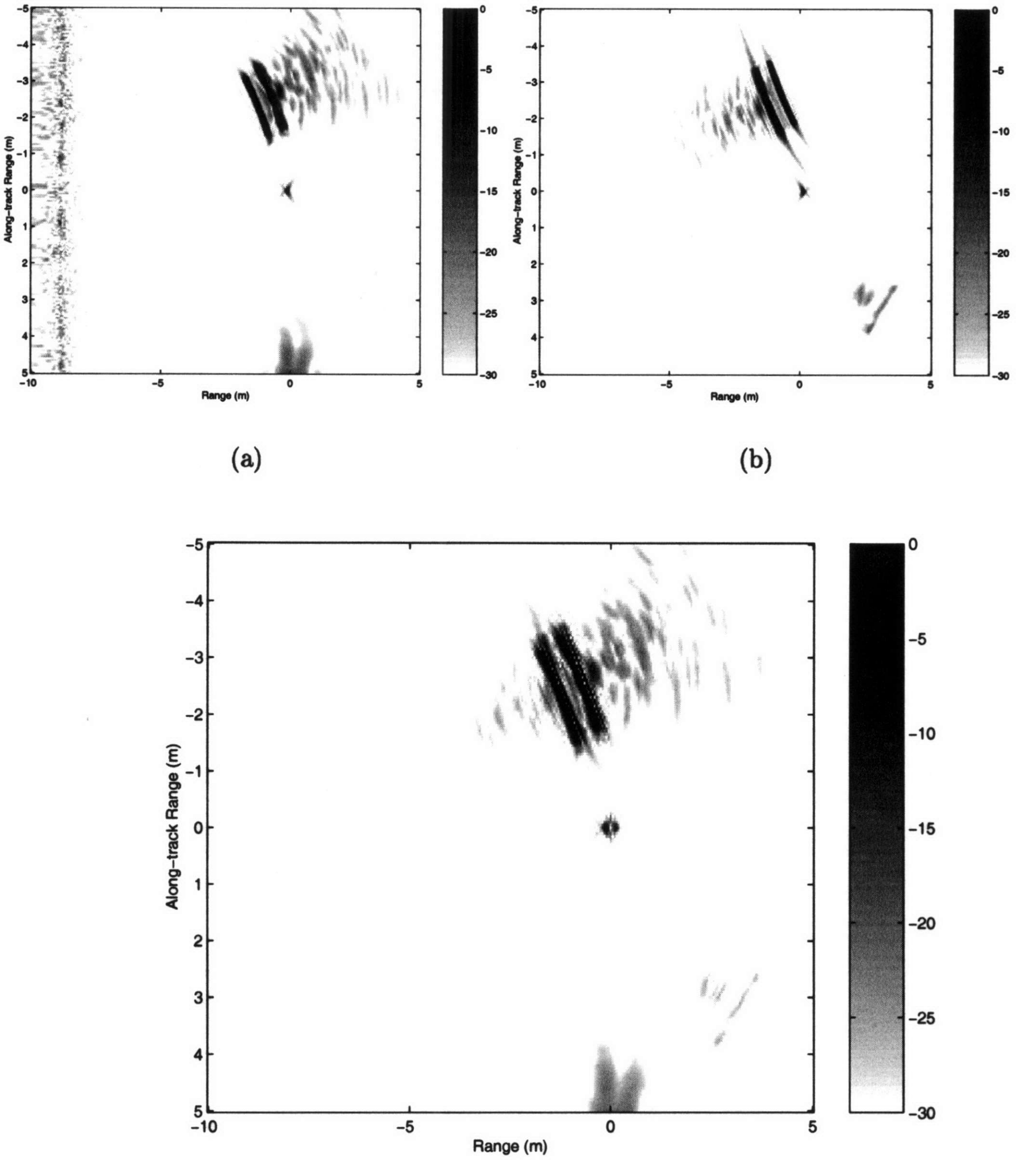

(a) (b)

(c)

Figure 4-15: SAS imagery from the simulated mission with a buried cylinder, at 5 kHz. On the top row are the passes to the left and right of the target field. The bottom plot is the fused image.

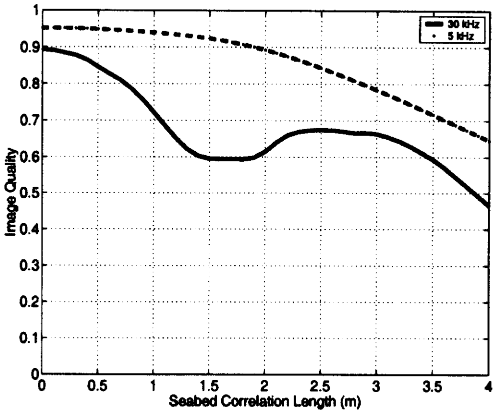

Figure 4-16: Image quality factor as a function of seabed correlation length, for the low frequency and high frequency SAS imagery.

summation index $i$ covers the entire image. The value of $Q$ therefore ranges from 0 to 1. This quality factor is shown for both the 30 kHz and 5 kHz SAS imagery in Fig. 4-16. Note that the high frequency SAS degrades more quickly than does the lower frequency SAS. Note that the absolute quality factors are not directly comparable, however, and is only the result of one particular objective test.

### 4.2.3 Experiment–GOATS'98

In this section, SAS results from the bistatic imaging phase of the GOATS'98 experiment will be presented. The sonar source was mounted on a fixed tower during the experiment while a roving AUV traversed the target field with a linear receiver array mounted on its nose. The target field contained proud and buried targets. A more detailed description of the experiment is given in Appendix A.

A natural balance between coherent and incoherent SAS to be applied in the GOATS case is to coherently process the receptions along the physical aperture, since the relative sensor position error is small and known. The physical aperture can be steered toward each pixel, then the steered physical aperture returns can be summed incoherently with the multipath arrival. This process minimizes the effect of the micro-navigation error. The images created with this method are shown in the upper half of Fig. 4-17. When compared to Fig. 4-9, these images show that the angular resolution is significantly improved, and the buried target is slightly more readily detectable.

Although the cross-track motion in the current data set is unknown, the micronavigation proved to be fairly accurate based on the coherent imaging results. Because of the apparent accuracy in the synthesized array positions, it is not necessary to limit the coherent processing to only the physical array. Another reasonable balance can be met by choosing the aperture length such that it is maximized within the constraint that plane-wave beamforming can be applied. The maximum length of the array with this criterion is about 2.4 $m$, or a 5–ping aperture. Using exclusively plane wave processing reduces the computation requirement and eliminates the problem of defocusing returns that arrive later or earlier than expected. This choice of aperture results in the images shown in the lower half of the figure. In this case, both of the insonified targets can be seen. The incoherent matched-filtering side-lobes remain a problem, but this method appears to be optimal for creating an accurate image.

### Subcritical Insonification

Subcritical insonification geometries are important because they allow the sonar to operate at a high area coverage rate. Fig. 4-18 shows the imaging performance of the AUV in such a configuration. The source insonifies the flush-buried sphere (S2) at 18.7°, which is well below the critical grazing angle of 24°. The 1 m deep sphere (S1) is insonified at very close to the critical angle, 22.7°. The receiver is above critical. The TOPAS is focused on S3, and its main lobe footprint includes both S2 and S3. However, the sidelobes of the source appear to insonify S1 sufficiently that it is detectible in some of the images, perticularly the focused and low frequency images. In fact, S2 is the least well-imaged target, although its elastic responses are clear in the high frequency images, particularly using incoherent SAS (part (c)). This is an indication of a strong coupling between the evanescent field and the elastic response of the target. The fact that the incoherent SAS provides the best detection of the elastic response is not surprising, because there is a range mismatch in the coherent SAS due to the delay of the elastic response. The proud sphere, S3, is clearly imaged in all cases, as expected. It also exhibits some elastic reponse, which also is best seen

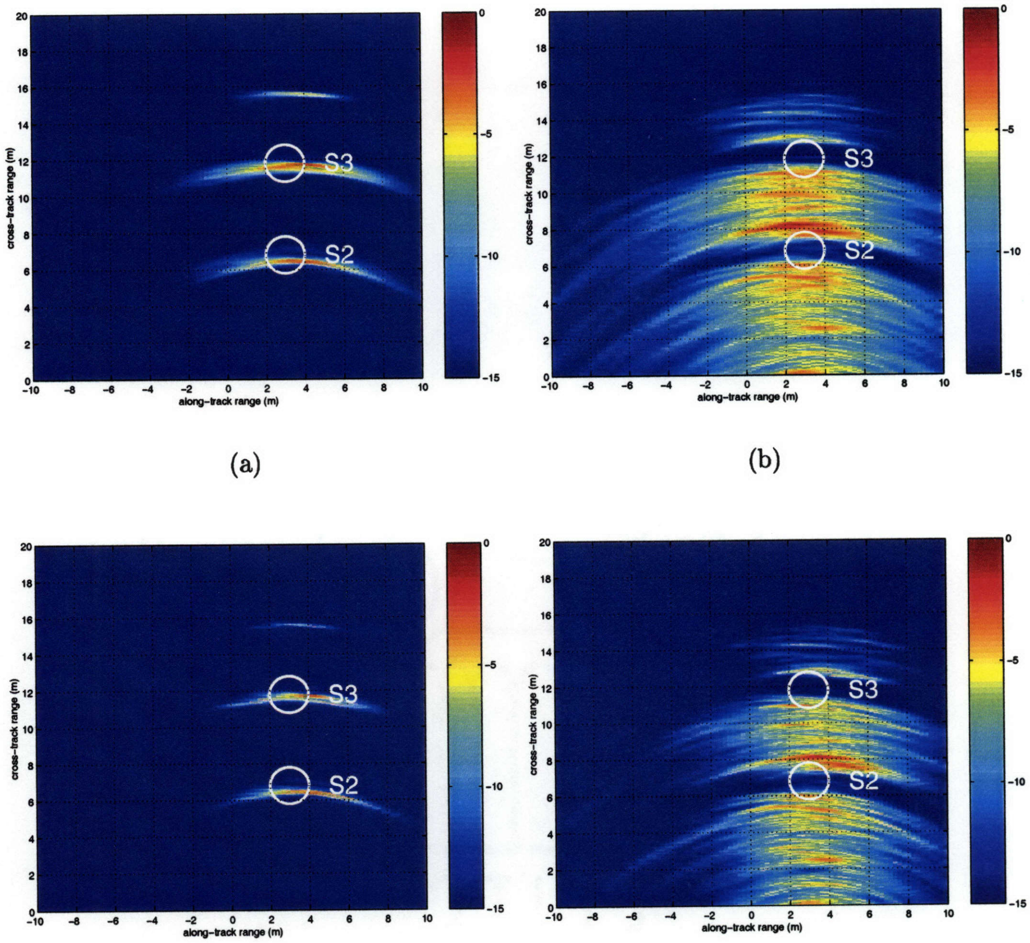

(a)

(b)

(c)

(d)

Figure 4-17: Balancing coherent and incoherent processing, run 25. The SAS extends from the origin to $x \approx 6.7\ m$ along the x-axis. (a) Plane wave beamforming on the physical apertures. (b) Same as (a), with S3 time-gated out. (c) Plane wave beamforming on 5-ping apertures. (d) Same as (c), with S3 time-gated out.

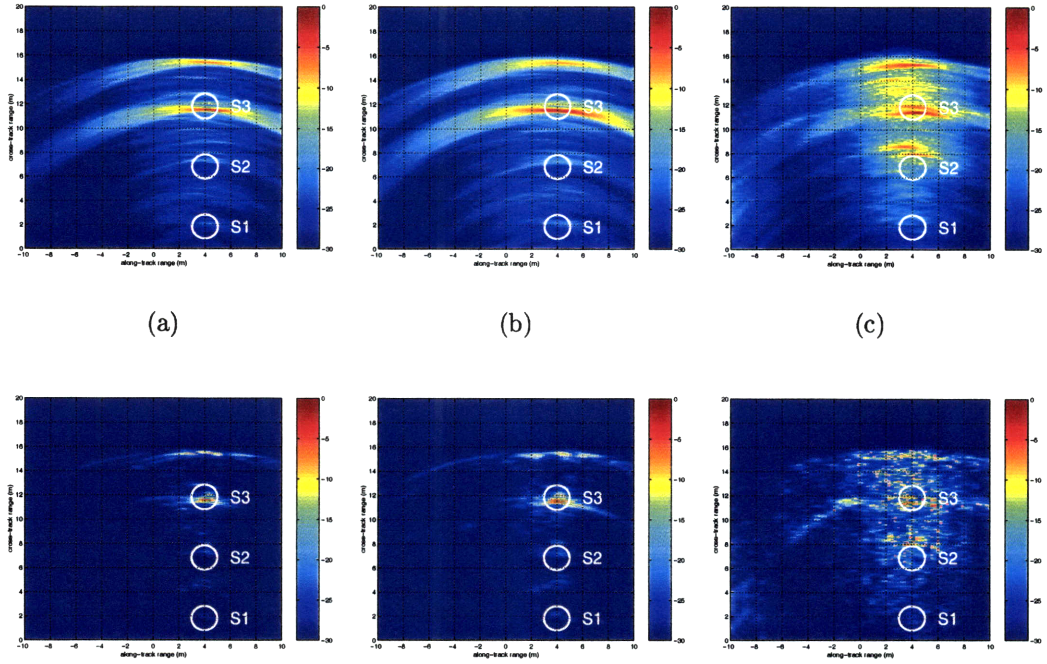

(a) (b) (c)

(d) (e) (f)

Figure 4-18: Synthetic aperture images, data file x9814501_025. Both buried targets are insonified at or below critical grazing - 22.7° (S1), 18.7° (S2). The SAS extends from the origin to $x \approx 6.7\ m$ along the x-axis. (a) Incoherent SAS, 2-15 kHz. (b) Incoherent SAS, 2-5 kHz. (c) Incoherent SAS, 10-15 kHz. (d) Coherent SAS, 2-15 kHz. (e) Coherent SAS, 2-5 kHz. (f) Coherent SAS, 10-15 kHz.

in the high frequency, incoherent SAS.

### Supercritical Insonification

Supercritical insonification geometries limit the area coverage rate, but they are still important because they provide maximum seabed penetration. Fig. 4-19 shows the imaging performance of the AUV in the supercritical configuration. The source insonifies the flush-buried sphere (S2) near the critical angle, 24.4°. The 1 m deep sphere (S1) is insonified at well above the critical angle, 30.5°. The TOPAS is focused on S2, and its main lobe footprint includes all three spheres. In this case, all three spheres are detected in with both incoherent and coherent SAS, particularly at low frequency. There appear to be detectible elastic returns of all three spheres only in

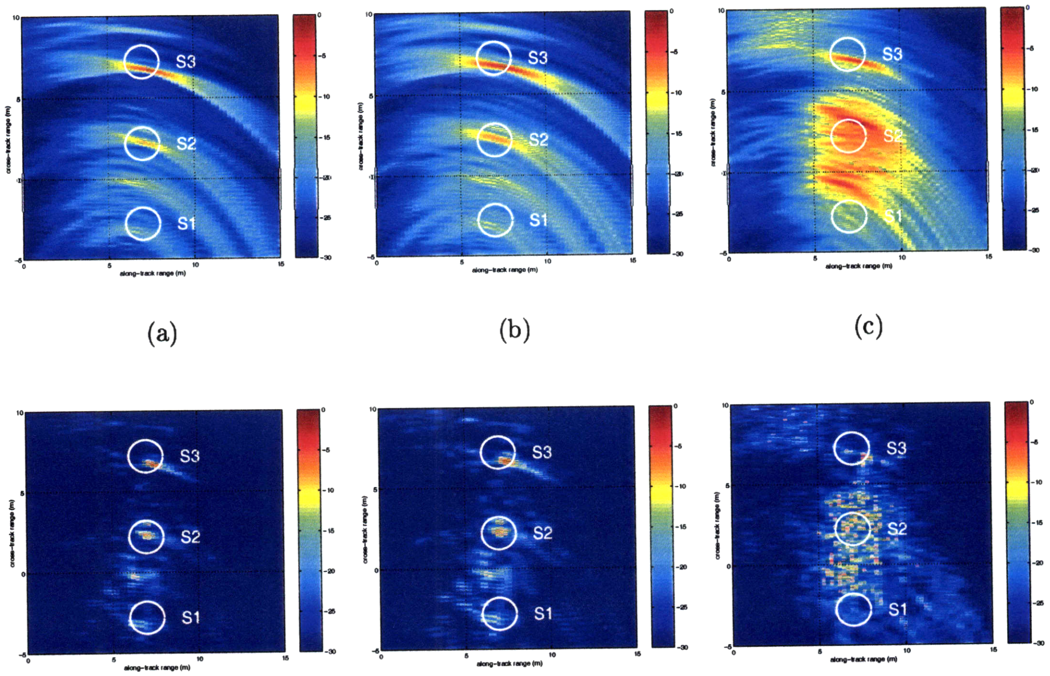

(a) (b) (c)

(d) (e) (f)

Figure 4-19: Synthetic aperture images, data file x9814601_025. Both buried targets are insonified at supercritical grazing - 30.5° (S1), 24.4° (S2). The SAS extends from the origin to $x \approx 6.7\ m$ along the x-axis. (a) Incoherent SAS, 2-15 kHz. (b) Incoherent SAS, 2-5 kHz. (c) Incoherent SAS, 10-15 kHz. (d) Coherent SAS, 2-15 kHz. (e) Coherent SAS, 2-5 kHz. (f) Coherent SAS, 10-15 kHz.

the low frequency incoherent SAS images. The clutter in the high frequency images covers the elastic arrivals. There also appears to be a foreign buried object between S1 and S2, as it is clearly seen in the focused low frequency images, (c) and (d). This object was not well detected in the previous case because it was out of the main lobe footprint and below critical insonification.

### Signal Characterization

In analyzing the GOATS'98 experimental data, a simple linear system model is used to represent the signal path. Thus, the received signal is modeled in time domain as a convolution of the input signal with a series of filters, including the medium impulse response, the target response, and the transmitter and receiver beampatterns. In the monostatic case, an echo return can then be written as [33]

$$e_i(t) = \sum_{j=1}^{J} s(t) * h(t, \tau_{ij}) * a_j(t, \theta_{ij}) * b_p(t, \theta_{ij}) * b_h(t, \theta_{ij}) \tag{4.5}$$

where $s(t)$ is the source signal, $h(t, \tau_{ij})$ is the impulse response of the time-invariant medium, $a_j(t, \theta_{ij})$ is the impulse response of scatterer $j$, $b_p(t, \theta_{ij})$ is the level of the projector beampattern in the direction of scatterer $j$, and $b_h(t, \theta_{ij})$ is the level of the receiver beampattern in the direction of scatterer $j$.

In the GOATS'98 scenario, the receiver is not at the source position, and the bistatic response of the target must therefore be considered. Analysis of the resulting signal return is greatly complicated by this fact. The source angle remains the same, but there is now a receiver angle that is not in the same plane as the receiver in general. With these considerations, the linear system model of the received signal then becomes

$$\begin{gathered} e_i(t) = \sum_{j=1}^{J} s(t) * h\left(t, \tau_{ij}\right) * a_j(t, \theta_{ij}^{(r)}, \phi_{ij}^{(r)}; \theta_{ij}^{(s)}) * \\ b_p(t, \theta_{ij}^{(s)}) * b_h(t, \theta_{ij}^{(r)}) \end{gathered} \tag{4.6}$$

where the superscripts $(r)$ and $(s)$ correspond to the receiver and the source, respectively.

For imaging purposes, the echo return will be assumed to be the result of a simple environmental model that includes only a direct and a surface-reflected return from each scatterer. Within this model, several assumptions will be applied, as listed below:

- Only the scatterers in the main lobe of the projector contribute, i.e., $b_p(t, \theta_{ij}^{(r)}) \approx 1$.
- The scatterers do not fluctuate with time, due to the stationary projector.
- The sea surface behaves as a pressure-release plane boundary.
- The bistatic scattering strengths of the direct and surface-reflected returns are approximately equal for each scatterer.

These assumptions can be used to recast the echo return model into the following form:

$$\begin{aligned} e_i(t) \approx s(t) \sum_{j=1}^{J} \frac{\mu_j(\theta_{ij}^{(r)}, \phi_{ij}^{(r)}; \theta_{ij}^{(s)})}{r_{ij}^{(p-t)}(\theta_{ij}^{(s)})^{\prime}} * \\ \left\{ \frac{\delta\left(t - \tau_{ij}^{dir}\right)}{r_{ij}^{(t-r)}(\theta_{ij}^{(r)}, \phi_{ij}^{(r)})} - \frac{\delta\left(t - \tau_{ij}^{SR}\right)}{r_{ij}^{(t-s)} r_{ij}^{(s-r)}} \right\} \end{aligned} \tag{4.7}$$

where $\mu_j$ is the scattering strength of scatterer j, $\tau_{ij}^{dir}$ and $\tau_{ij}^{SR}$ indicate the time delays of the direct and surface-reflected returns, and the projector to target scatterer, target scatterer to receiver, target scatterer to sea surface, and sea surface to receiver straight line distances are indicated by $r_{ij}^{(p-t)}$, $r_{ij}^{(t-r)}$, $r_{ij}^{(t-s)}$ and $r_{ij}^{(s-r)}$, respectively.

From this point, the generation of the image data is straightforward. Given the receiver position $i$, the receiver is focused on a patch centered on the desired scatterer $j$. The receiver beampattern is then approximately unity in the region of the scatterer. The scattering coefficient is then extracted by a matched filtering process, using the environmental model to form the matching filter. This extraction is implemented as an inner product between the measured signal and the return replica $R(t)$:

$$\mu_j\left(\theta_{ij}^{(r)}, \phi_{ij}^{(r)}; \theta_{ij}^{(s)}\right) \approx R_j^H(t) e_i(t) \tag{4.8}$$

Finally, if the array aperture spans an angular region over which the bistatic scattering strength is nearly constant, the result is equivalent to the canonical monostatic image, except that the image is evaluated at some fixed bistatic angle.

### *The Bistatic Effect*

Classical imaging is optimized for detection, and it averages out any frequency or angular diversity in the data [33] . Monostatic SAS will generally provide a better imaging performance, but this property is not useful in cases where the image resolution is insufficient for classification. Detection without classification results in unacceptably high false alarm rates in sonar mine hunting applications.

The bistatic nature of the GOATS geometry is in some ways inconsistent with the

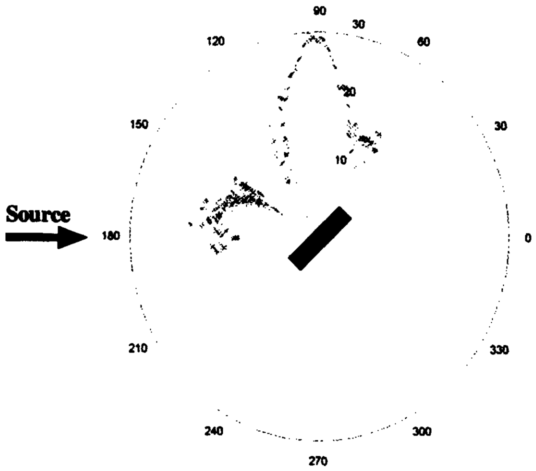

Figure 4-20: Scattered field of the flush-buried cylinder measured by the HLA. The backscattered signal is 10 – 15 *dB* less than that scattered near 90°. The distinctive shape of the scattered field can also be used as a clue for classification.

concept of imaging. Bistatic measurements are spread over a range of bistatic angles, and as such the removal of the propagation effects leaves a scattering strength that is a function of receiver position, i.e., the image is created using an inconsistent basis. However, it is precisely this property that may give the bi- and multi-static configurations their potential for concurrent detection and classification. The SAS platform motion techniques remain very important to preserve coherence of the bistatic data, but alternative processing techniques are required to preserve the data diversity that is critical for classification.

Spectral and angular diversity for classification purposes have not yet been fully exploited, but the preliminary analysis provides evidence that each of these and their combination can provide important classification clues. For example, a fixed horizonal line array (HLA) was also used in the GOATS'98 experiment to measure the scattered field from the targets. The strongly aspect-dependent field of the cylinder C2 under sub-critical insonification, as measured by the HLA, is shown in Fig. 4-20 . Such aspect-dependence provides a basis for interest in bistatic classification.

**GOATS'98 Synthetic Aperture Processing**

### *Surface Reflection Coherence*

In a multipath environment, it is often possible to use known coherent returns as an imaging aid. In the GOATS'98 scenario, multipath arrivals resulting from the sea surface reflection are known to exist, but the extent to which they are coherent with the direct arrivals is unknown. The most simplistic model of the sea surface is as a flat pressure-release boundary that reflects the incident wave 180° out of phase. However, waves and other disturbances at the ocean surface will cause a degradation in the coherence and arrival time of the surface-reflected returns. It is therefore useful to investigate the coherence of the surface-reflected returns to determine whether they can be used in a coherent or incoherent processor. Otherwise, these returns become strictly noise.

Fig. 4-21 illustrates the stability of the surface-reflected return from the half-buried sphere during one full pass of the AUV, which includes 115 pings over 50 seconds. The upper frame a shows the correlation coefficient between the direct and the surface-reflected returns. The correlation is consistently around -0.7, a fairly high magnitude, and the sign is as expected for a pressure-release boundary. The center frame shows the peak sound pressure difference between the two returns. The two are consistently within 3 $dB$ of each other, which indicates that the assumptions made about the bistatic return will be valid. It is not surprising that the bistatic angle between the returns does not have a significant impact on the reflection coefficient for the spherical target. The lower frame shows the time difference between the two returns (in samples). This difference appears to be fairly smooth, in spite of the fact that the time of arrival of the surface reflection is very sensitive to several uncertain parameters, such as the proximity of the AUV, source and target, the uncertainty in the receiver position, and the bistatic nature of the problem. The oscillation of the times of arrival corresponds to a peak to peak wave height of only 35 cm, but this is enough to preclude coherent inclusion of the surface-reflected return without more advanced processing techniques than are presented here.

### *Target Detection and Imaging*

The data were first aligned using a linear motion assumption, i.e., using the 1-D

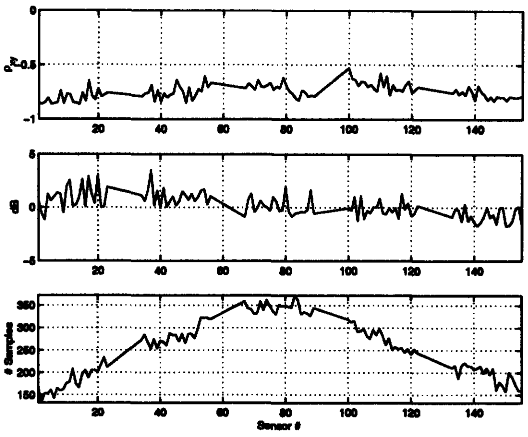

Figure 4-21: Relationship between the surface reflected return and the direct return from S3, pass 23-27. The pass limits correspond to the numbers in Fig. 5. The upper frame is the correlation coefficient, the center frame is the dB difference in the peak amplitudes, and the lower frame is the lag (in samples) between the returns.

micro-navigation technique described above. This process resulted in a straight linear synthetic array. Due to hardware limitations in the GOATS'98 experiment, the time of the source trigger then had to be determined by a least squares fit of the hyperbolic return times of a known strong scatterer in the data.

Once the synthetic aperture data is assimilated and aligned, the imaging process is an inversion to calculate the reflection coefficient at a given pixel $j$. The general form of the algorithm that is used for the GOATS'98 data is shown schematically in Fig. 4-22 . The aligned synthetic aperture data at all sensor positions $\vec{x}_a$ are divided spatially into blocks that are passed into a coherent processor or beamformer. The coherent processor effectively reduces the number of elements to be passed through the incoherent processor by replacing each block with a single beamformed response at each block phase center, which are located at points $\vec{x}_p$. The squared amplitude of the output of the coherent processor is then passed through an incoherent matched filter, where the matched filter for receiver element $i$ is denoted as $R_{ij}(t)$ and is derived from the signal model in Eq. 4.7 , i.e.,

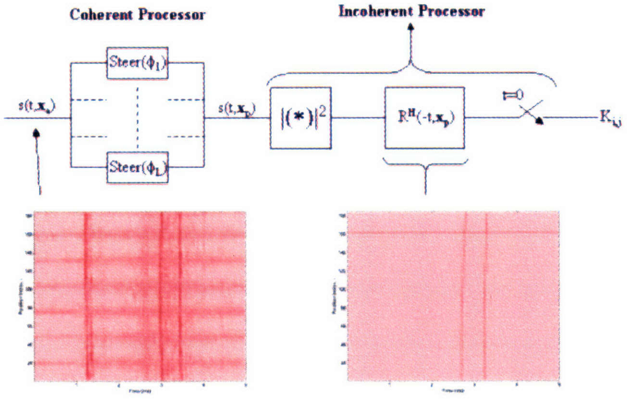

Figure 4-22: Schematic diagram of the image generation algorithm. The aligned synthetic aperture data $s(t, \vec{x}_a)$ are split into spatial blocks. The data in each block are then coherently focused on the current pixel $(i, j)$. The output of the coherent processor, $s(t, \vec{x}_p)$, is the collection of the steered time series, one for each coherent block. This output is then passed to an incoherent matched filtering process. The matched filter, $R^H(-t, \vec{x}_p)$, is the expected direct reflection plus surface bounce from the current pixel. The output of the incoherent processor is the image intensity at the given pixel, $K_{i,j}$.

$$R_{ij}(t) = \left| \frac{s(t)}{r_{ij}^{(p-t)}(\theta_{ij}^{(s)})} * \left\{ \frac{\delta\left(t - \tau_{ij}^{dir}\right)}{r_{ij}^{(t-r)}(\theta_{ij}^{(r)}, \phi_{ij}^{(r)})} - \frac{\delta\left(t - \tau_{ij}^{SR}\right)}{r_{ij}^{(t-s)} r_{ij}^{(s-r)}} \right\} \right| \tag{4.9}$$

where the time delays and ranges are calculated for each position $\vec{x}_p$. The result of the imaging algorithm will in general be an average of the reflection coefficient over the range of bistatic angles included in the synthetic aperture. For a consistent basis of comparison, all images shown are from a single 7-second data file, which includes 23 pings. The file corresponds to the line from '25' to '26' in Fig. A-4 . The insonification grazing angle is subcritical (18.7°) and the receiver grazing angle is supercritical (35°).

## 4.3 Detection, Classification and Localization Sonar

The new description of the moving sonar platform as an integrated detection, classification and localization (DCL) sonar requires the platform to automate target decisions. In the simplest case, the DCL steps are separate, sequential steps, kicking off with the target detection on a per–ping basis. The classification and localization steps follow as needed. In this section, a means for automating target detection in an unknown environment is presented.

### 4.3.1 Characterizing the Reverberation Signal

Setting a detection threshold for a prospective target requires some assumption about the underlying noise content. In the littoral ocean, the reverberation statistics are highly dependent upon the local area. A further complication is that the reverberation is multiplicative noise. In this section, a simple method for data–dependent thresholding is pursued following the generalized likelihood ratio test (GLRT) model. The GLRT relies upon a dual hypothesis model, which are generally described in this work as follows:

$$\begin{aligned} \mathcal{H}_0 &: s(t) = w(t) \\ \mathcal{H}_1 &: s(t) = r(t)w(t) \end{aligned} \tag{4.10}$$

In the above equation, $\mathcal{H}_0$ corresponds to the ***null hypothesis*** (no target) while $\mathcal{H}_1$ corresponds to the ***alternative hypothesis*** (target present). The time series $s(t)$ is the measured signal, while $w(t)$ is the underlying noise and $r(t)$ is the target return signal. In order to establish the probability of a correct detection, some knowledge (or assumptions) must be applied to establish the statistical properties of $w(t)$. In keeping with the Van Cittert–Zernike view of the reverberation, as detailed by Doisy, it can be appropriate to assume the reverberation at a given range cell is Gaussian distributed. This Gaussianity is achieved through the application of the Central Limit

Theorem to the large number of independent scatterers at a given range. Naturally the wider azimuthal coverage of the source signal, the closer the Gaussian hypothesis fits.

### 4.3.2 Energy Detector with Adaptive Thresholding

A common method for detecting a target in noise is through an energy detector. In this approach, the time series in both the null and alternative hypotheses correspond to the signal envelopes of the measurement time series. Upon taking the signal envelope, the hypotheses can be expressed in terms of the Rice distribution. The Gaussian–distributed time series value that is derived from the Van Cittert–Zernike theorem becomes a Rayleigh–distributed envelope. For strong coherent targets, the signal envelope in the alternative hypothesis becomes Gaussian centered at some signal strength $\sigma_c$. The transition between these can be expressed in terms of the coherent to incoherent signal strength ratio in the Rice distribution [73].

Note that the use of a simple energy detector requires the hypothesis test to be made within each resolution cell of the receiver. In the case of an omnidirectional hydrophone these resolution cells correspond to various ranges. A beamformed receiver has angular and range resolution cells. As the resolution cells shrink, however, the Rayleigh reverberation assumption shifts toward the Gaussian. In any case, the statistical properties of the noise must be established separately for each resolution cell.

The detection threshold is then set by the desired probability of false alarm ($P_F$). In either case, the $P_F$ is expressed as the integral of the tail of the noise probability distribution:

$$P_F = \int_{\gamma}^{\infty} p_{s_{ij}|H}\left(s_{ij}|H_0\right) \tag{4.11}$$

If the reverberation is Rayleigh distributed, then $P_F$ is directly integrable:

$$P_F = \int_{\gamma}^{\infty} \frac{x}{\sigma^2} e^{-\frac{x^2}{2\sigma^2}} = e^{-\frac{\gamma^2}{2\sigma^2}} \tag{4.12}$$

In the Gaussian case, $P_F$ is represented in terms of the error function:

$$P_F = \int_{\gamma}^{\infty} \frac{1}{\sqrt{2\pi\sigma}} e^{-\frac{(x-\mu)^2}{2\sigma}} = \frac{1}{2} erfc\left(\frac{\gamma - \mu}{\sqrt{2}\sigma_{ij}}\right) \tag{4.13}$$

One way to view the target in terms of the Rice distribution is as the source of coherent energy. Thus, the alternative hypothesis pushes the received signal distribution toward the Gaussian distribution. If the target is much louder than the local reverberation level, then the distribution in that resolution cell will be Gaussian. If it is equivalent to the level of one or a few small seabed scatterers, then the effect of the target presence is merely a shift in the variance of the Rayleigh distribution. In the general case, however, the distribution will transition from an intermediate Rician form to another intermediate Rician form.

However the target–present distribution may assert itself, the detection threshold is determined by the distribution in the null case. The related detection performance can then be computed numerically using the Rice distribution assumption. The receiver performance in terms of the Rice distribution are shown in Fig. 4-23. In the left plot, the receiver operator characteristic (ROC) curves are shown for various levels of SRR. The false alarm rate is set assuming a Rayleigh distribution (Rice with zero coherent energy), and the probability of detection is then computed by numerically integrating the Rice pdf:

$$w_R(s) = \frac{2s(1+\nu)}{\sigma_T} e^{-\frac{(1+\nu)s^2+\nu\sigma_T}{\sigma_T}} I_0\left(\frac{2s\sqrt{\nu(1+\nu)}}{\sqrt{\sigma_T}}\right) \tag{4.14}$$

In Eq. (4.14), $\nu$ represents the coherent to incoherent signal energy ratio, and $\sigma_T$ represents the total signal energy. The integration must then be performed individually for each SRR, because the total signal energy changes as a function of coherent energy.

The GLRT is then expressed in terms of the as–yet–undetermined threshold $\gamma$:

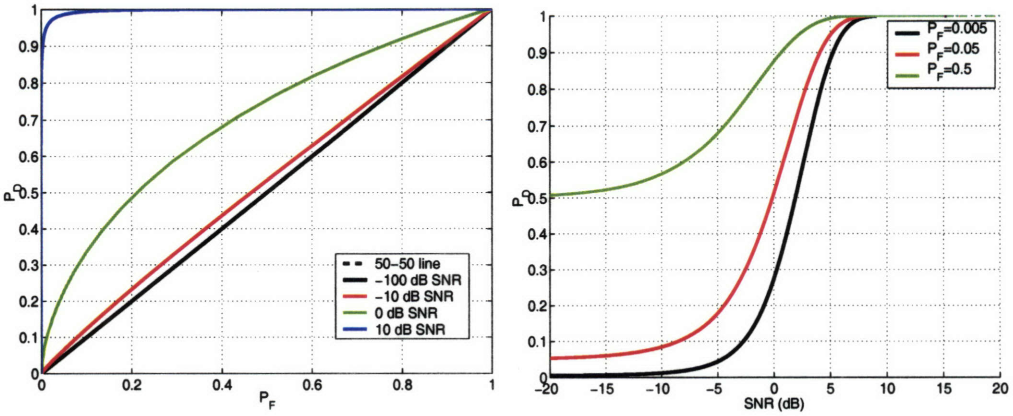

(a) Receiver operator characteristic curve.

(b) Probability of detection as a function of SRR.

Figure 4-23: Detection performance derived from the Rice distribution.

$$\mathcal{L}_G : \frac{p_{s_{ij}|H}\left(s_{ij}|H_1\right)}{p_{s_{ij}|H}\left(s_{ij}|H_0\right)} \underset{H_0}{\overset{H_1}{\gtrless}} \gamma \tag{4.15}$$

In the general mine–hunting problem, there is no way to reliably determine the target amplitude $r_{ij}$ prior to the mission. So it would seem that the GLRT may not be appropriate. Furthermore, the performance statistic of the second kind ($P_D$) cannot be computed, so the receiver operating characteristic (ROC) curve is not established. Fortunately, this difficulty can be resolved using the Wald test or the Rao test for unknown amplitude. In the case of Gaussian noise as presented here, these tests both reduce to the GLRT [40] with the mean term $r_{ij}$ replaced by its maximum likelihood estimate $E[r_{ij}] = E[s_{ij}] = \overline{s}_{ij}$. This approach is equivalent to declaring that the probability of detection is solely dependent upon the probability of false alarm ($P_D = f(P_F)$), since the degrees of freedom were reduced by one by assuming no probability of missing a target. The problem then simplifies to identifying the $\sigma_{ij}$. This task is momentarily put aside to consider the GLRT under this assumption. The likelihood ratio is then written as:

$$\mathcal{L}_G : \frac{p_{\bar{s}_{ij}|H}\left(\bar{s}_{ij}|H_1\right)}{p_{\bar{s}_{ij}|H}\left(\bar{s}_{ij}|H_0\right)} \underset{H_0}{\overset{H_1}{\gtrless}} \gamma \tag{4.16}$$

Considering that the probability of detection is based upon an estimated parameter, and moreover a parameter that is unlikely to be well estimated, the figure of merit for sonar–adaptive behavior will be the probability of false alarm, $P_F$. An accurate estimation of the probability of detection depends upon a high SNR measurement of the target strength, which requires either a loud target or a large number of independent measurements of the target, both of which are inconsistent with the general mobile sonar target mine hunting problem.

### 4.3.3 Setting the Detector Performance

A common way to set the threshold in these situations is to choose a constant false alarm rate (CFAR) condition. Upon estimating the local reverberation statistics within each resolution cell, the ROC curves are examined to determine the $P_D$ for the prescribed $P_F$. However, the mine hunting problem leads one to think in the reverse, because detections are so important. In this way of thinking, the probability of detection is paramount, while the probability of false alarm should be minimized.

If the performance of the detector is unsuitable on a ping–by–ping basis, then a multiping detector can be applied. The effect of the multiping detector is to increase the SRR by a factor of $P$, the number of pings included in the detection. This factor is an approximation that assumes coherent summation of the target signal and incoherent summation of the reverberation signal.

### 4.3.4 Automated Detection Examples

Examples of the adaptive detection are shown in Figs. 4-24 and 4-25. These figures parallel Figs. 4-7 and 4-8, except that the target in question is now a sphere, and the plots on the right are no longer amplitude but probability of detection. As the vehicle

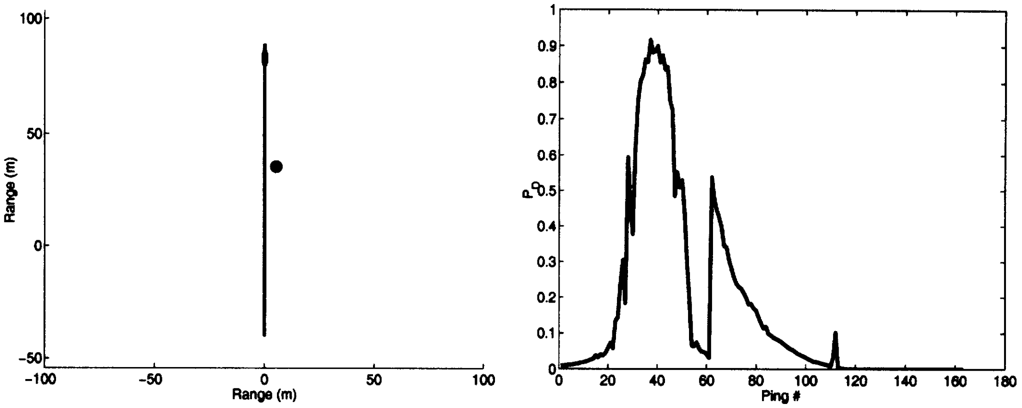

(a) Vehicle trajectory.

(b) Target detection statistic.

Figure 4-24: Target detection with a tethered vehicle. The source is at the surface of the water column, while the receiver is on a vehicle at depth. On the left is the path of the vehicle. On the right is the detection statistic at the given ping.

approaches the target but prior to detecting any target, the range–dependent reverberation amplitude is estimated and smoothed. At each ping, the amplitude within each range bin is compared with the reverberation estimate to estimate the probability of false alarm. The probability of false alarm is set at 0.05 based on the Rayleigh assumption, and the probability of detection is derived from the corresponding ROC curves.

In the crawling vehicle example (Fig. 4-24), the sonar geometry is fixed, so the reverberation threshold only needs to be set for a single ping as long as the seabed remains similar. In general, the reverberation threshold may need to be reset when the heading of the vehicle changes as well. As can be seen from the plot on the right, the probability of detection increases from zero up to nearly one and back down again as the vehicle passes the target. Even in simulation the difficulty in smoothing the reverberation returns can be seen.

In the remote source example (Fig. 4-25), the establishment of a reverberation threshold is more challenging. In this case it is an iterative process. The range–dependent reverberation amplitude estimate is determined at the first ping and then assumed to be consistent at the next ping. The second ping is then screened for

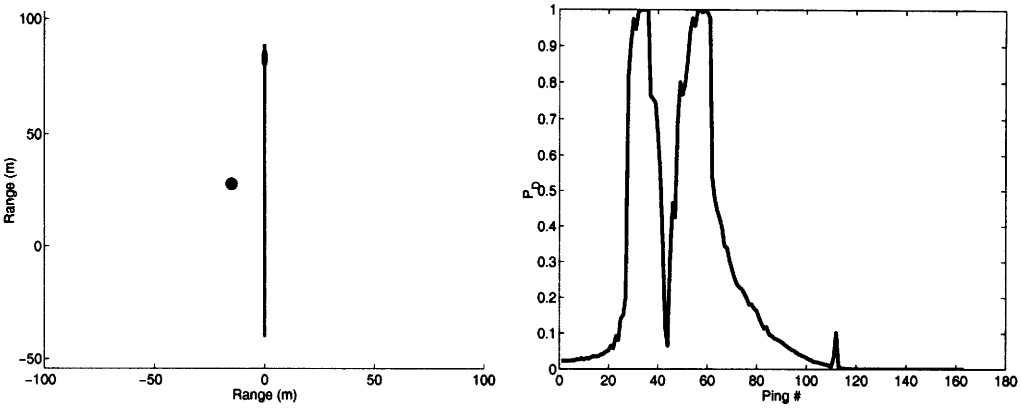

(a) Receiver trajectory.

(b) Target detection statistic.

Figure 4-25: Target detection with a remote source. The source is positioned at (0,-50), and the receiver vehicle drives toward and past the target.

targets above a certain threshold, and if there are none, the reverberation estimate is replaced. If there is a target detected, then the range cells at which the target was detected is not recomputed in the reverberation estimate. In this way, the detection prediction and the reverberation estimate work together over a bistatic mission.

# Chapter 5

# Target Classification

One of the most powerful capabilities of mobile sonar platforms is to combine the detection and classification steps in a mine–hunting mission. This process is known generally as concurrent detection and classification (CDAC), although that term implies simultaneous detection and classification. In the view of mobile sonar systems, *concurrent* is interpreted to mean "within a single mission." The vehicle first detects a target, then focuses its signal processing or mobility toward determining the nature of the target. In this chapter, candidate signal processing methods are investigated that could be implemented by a mobile, deformable sonar system for the purpose of target classification. Target classification approaches generally follow one of two approaches: either to find the one property that separates the targets of interest and measure it precisely, or to collect as much information as possible about the targets and apply that diversity of information to separate them. An example of the former is classification through high–resolution imagery. The latter method typically is realized through pattern recognition or data fusion methods.

In the general mobile sonar problem, little is known about the candidate targets or false alarms prior to launch, and unknown target types are always a possibility. Further, the *a priori* unknown target aspect and sonar geometry make the required databases prohibitively large. The classification system must therefore focus on properties that distinguish a target of interest from one that may not be of interest.

The approach taken in this work is to parameterize characteristics of the target in a manner that is largely independent of the sonar geometry and is robust to navigation error. The bases selected for classification are shape and spectral characteristics. Different approaches are shown depending upon whether the system is monostatic or bistatic. Shape can be classified by either extraction from an image or by inversion of the target scattered field. Spectral characteristics are investigated locally. This distinction is critical: the local nature of the spectral characteristics indicates that the sonar geometry must be nearly replicated for re–acquisition, while the shape can be rotated from any view angle for fairly compact targets.

## 5.1 Spectral Methods

Classifying the composition of the target in littoral minehunting essentially consists of discriminating between man–made objects (possibly mines) and natural objects (probably rocks). Man–made objects are likely to contain characteristic dimensions and nonhomogeneous composition, while rocks are typically homogeneous in nature. The characteristics of man–made objects give rise to resonant responses from the targets, which are typically of low amplitude and do not constructively sum over a spatial aperture. In addition, the resonant behavior of the target is not necessarily directed back at the source, but rather in a direction that is characteristic of the target. The adaptability of the AUV sonar platform allows the vehicles to search for advantageous sonar geometries to detect these elastic target responses. Figure 5-1 shows a simple comparison of the received field from (a) experimental and (b) simulated resonant targets to the pure reverberation field in terms of power spectral density (PSD). In both results, the source insonifies a buried 1 m diameter sphere at subcritical grazing while the receiver remains within the supercritical cone in which the target reradiation is strongest and the reverberation is relatively low. Although the overall signal power is low, the low frequency resonances are easily detectable over the reverberation. In fact, the reverberation tends to decrease with decreasing frequency, while target resonances tend to be stronger at lower frequency. This simple spectral analysis illustrates the possibility of detecting elastic returns from

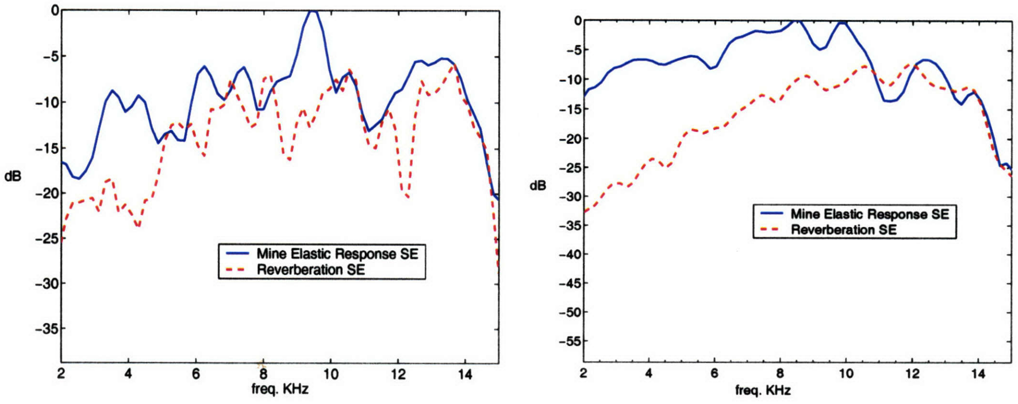

(a) GOATS'98.

(b) Simulation

Figure 5-1: At–sea and simulated results of the comparison between the power spectral density measured with no target present versus elastic target. The data window was selected post–detection.

advantageous source/receiver geometries.

Examples of mine classification through PSD and bispectrum analysis are shown in this section using real data collected from the GOATS 1998 [22] and GOATS 2002 experiments, as well as simulated data generated using MIT–MCM. Although the exact experimental conditions cannot be perfectly known, the experimental scenario is reproduced in each case with the highest fidelity possible. The PSD $C_2^z(\omega)$ is estimated by using the Blackman–Tukey technique [74]:

$$\hat{C}_2^z(\omega) = \sum_{\tau=-M+1}^{M-1} \hat{m}_2^z(\tau) w(\tau) e^{-j\omega\tau} \tag{5.1}$$

where $w(\tau)$ is a filtering window, with length $M < N$, $\hat{m}_2^z(\tau) = \frac{1}{N}\sum_{n=\tau+1}^{N-1} z(n)z(n-\tau)$ and $\hat{m}_2^z(-\tau) = \hat{m}_2^z(\tau)$, for $0 \leq \tau \leq N-1$, is the estimated second order moment of the process $z(n)$. The filtering window is an even function, which decays smoothly to zero and is such that $w(0) = 1$ and $w(\tau) = 0$ for $|\tau| \geq M$. The choice of a non parametric method, such as the Blackman–Tukey procedure, is motivated by the fact that there is no a priori knowledge of the spectrum model. Moreover, the Blackman–Tukey method is preferred over the periodogram, because the latter is biased and has a variance which does not decrease with the number of samples. On the contrary, the

Blackman–Tukey estimator, acting like a locally weighted average of the periodogram, reduces the high statistical variations [74].

The bispectrum $C_3^z(\omega_1, \omega_2)$ is estimated as

$$\hat{C}_3^z(\omega_1, \omega_2) = \sum_{\tau_1=-L_3}^{L_3} \sum_{\tau_2=-L_3}^{L_3} \hat{m}_3^z(\tau_1, \tau_2) \cdot w(\tau_1, \tau_2) e^{-j(\omega_1\tau_1+\omega_2\tau_2)} \tag{5.2}$$

where $\hat{m}_3^z(\tau_1, \tau_2)$ is the second order moment estimated with the indirect method described in [56], $L_3$ the region of support of $\hat{m}_3^z(\tau_1, \tau_2)$, and $w(\tau_1, \tau_2)$ is the filtering window. The motivation for using a bispectral approach for classifying the target lies once again in the assumptions that leas to the application of the Van Cittert–Zernike theorem. If there are a large number of independent scatterers in the range–azimuth cell, then the measured reverberation from a given range can be approximated as a Gaussian random variable. The bispectrum of a Gaussian–distributed variable is zero. The bispectrum of a deterministic signal, i.e. the elastic response of the target, is, presumably, non–zero.

After the calculation of the PSD or bispectrum of the total signal and the corresponding reverberation–only signal, a simple classification algorithm computes the gain of the signal with respect to the reverberation and decides for the presence or absence of the elastic response following the specular response. A gain corresponds to a man–made target classification, on the contrary, a unit gain corresponds to a natural object classification. The classification parameters are defined as follows. For the second order statistic the gain $\gamma_2$ is defined as

$$\gamma_2 = \frac{\int_\omega \frac{C_2^z(\omega)}{C_2^r(\omega)} d\omega}{\int_\omega \frac{C_2^r(\omega)}{C_2^r(\omega)} d\omega} = \frac{\int_\omega \frac{C_2^z(\omega)}{C_2^r(\omega)} d\omega}{B} \tag{5.3}$$

where $C_2^r(\omega)$ is the reverberation PSD and $B$ is the bandwidth. The classification parameter computed from the third order statistics is named $\gamma_3$ and is defined as

$$\gamma_3 = \frac{\int_{\omega_1} \int_{\omega_2} \frac{|C_3^z(\omega_1,\omega_2)|}{|C_3^r(\omega_1,\omega_2)|} d\omega_1 d\omega_2}{\int_{\omega_1} \int_{\omega_2} \frac{|C_3^r(\omega_1,\omega_2)|}{|C_3^r(\omega_1,\omega_2)|} d\omega_1 d\omega_2} = \frac{\int_{\omega_1} \int_{\omega_2} \frac{|C_3^z(\omega_1,\omega_2)|}{|C_3^r(\omega_1,\omega_2)|} d\omega_1 d\omega_2}{B_1 B_2} \tag{5.4}$$

where again $C_3^r(\omega_1, \omega_2)$ is the reverberation bispectrum and $B_1$ and $B_2$ are the bandwidths relative to the bidimensional frequency domain. Both performance measures are normalized so that they can be compared with one another.

The results from the PSD and bispectrum estimation using real data collected during the GOATS 1998 and the GOATS 2002 experiments, as well as simulated data, are discussed in Sections 5.1.1–5.1.3. The discrimination of the elastic response from the reverberation requires the estimation of the reverberation spectra. Thus, the spectra of the total signals are compared to the spectra of the reverberation-only signals, relative to the same investigation area. This information is available to the AUV during the first stage of the mine hunting mission, prior to the time that any target detection has occurred. The numerical analysis demonstrates that the bispectrum improves the gain $\gamma$ with respect to the PSD, thus leading to improved classification performance in low signal-to-noise ratio (SNR) scenarios.

In the first subsection, the acoustic simulation tool is used and its strengths and weaknesses briefly discussed. The following two subsections show the numerical results for the GOATS 1998 and GOATS 2002 experimental scenario, respectively. In both cases, the MIT–MCM simulation tool is run as a theoretical baseline for comparison. In all the examples the targets are 1 m diameter buried spheres, with the center of the sphere positioned at 0.5 m below the seabed. The classification is achieved by applying the full CDAC processing on the simulated or experimental time series just as it would be implemented on board the AUV. The adaptive detection algorithm proposed in Section 4.3.4 is first applied to the data to detect the presence and the position of the targets. Once a detection has occurred, the classification algorithm is applied to the data inside the elastic search window. The PSD and the bispectrum of the received signal are then compared to the reverberation-only PSD and bispectrum, respectively. In the numerical examples the filtering windows in Eq. (5.1) and (5.2) are chosen to be the Hamming window.

Table 5.1: Water column and bottom parameter values.

| **Parameter** | **Value** |
|---|---|
| $c_1$ | 1500 m/s |
| $\rho_1$ | 1000 Kg/m$^3$ |
| $c_2$ | 1700 m/s |
| $\rho_2$ | 1800 Kg/m$^3$ |
| $l_0$ | 1 m |
| $\sigma_c$ | 0.01 |
| $\theta_{gr}$ | 30° |

### 5.1.1 MIT–MCM Acoustic Simulated Data

Before comparing the simulation results with the experimental results, the PSD calculated from simulated data is compared with the PSD derived from a theoretical model which considers only surface scattering [8]. The reverberation second order statistics are derived for a linear geometry, assuming that the water column and the lower bottom are homogeneous media with constant density and sound speed. A constant density, but random sound speed profile medium is positioned between the two homogeneous media. The density and the sound speed mean value are equal to those of the homogeneous lower medium. The parameter values used in the examples are reported in Table 5.1. Fig. 5-2 shows the reverberation PSD and corresponding autocorrelation function (ACF) computed for a planar wave impinging on the seabed as described above. A slightly more realistic model, which involves cylindrical geometry consideration, is considered in [46]. However, the most significant omission of the simulations is expected to be that of subbottom volume scattering. This phenomenon indeed appears clearly in the following numerical examples, as will be discussed in the following section.

The PSD shown in Fig. 5-2 is integrated at each frequency over the wave number plane to simulate the source beam, and it is then possible to compare it with the PSD calculated from the time series generated by MIT–MCM. The result in Fig. 5-3 shows a very good agreement between theoretical and simulated results over the full frequency band. The PSD are evaluated in dB re 1 Pa. Having established

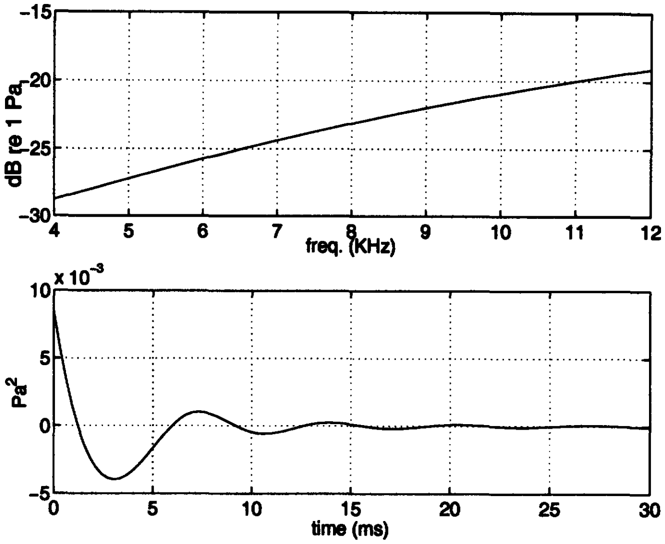

Figure 5-2: Theoretical reverberation power spectral density (PSD) and autocorrelation function (ACF) from an incident plane wave.

the consistency between analytical results and the reverberation signals generated by MIT–MCM, the MIT–MCM–generated results will be used as the theoretical baseline for comparison with GOATS experimental data in the following examples.

### 5.1.2 GOATS 1998 Experimental Data

The plots in Fig. 5-4 show the estimated PSD when the sphere is present in the target field as well as the reverberation–only estimated PSD for the experimental and simulated data, respectively. The data used to estimate the reverberation PSD are collected inside the same temporal window which was established after the specular detection has occurred, in order to process data backscattered from the same spatial field. The reverberation data are collected before the detection, when no target is present in the insonified patch. Fig. 5-4 compares the experimental results with the simulation results, together with the PSD estimated when the target is simulated as a rock. The PSDs are evaluated in dB re 1 Pa and the frequency axis is in kHz. Both experimental and simulated data show that the elastic response is a valuable means to discriminate man–made objects, such as mines, against natural objects, such as rocks. The natural frequency–selectivity of the elastic targets causes the peaks of

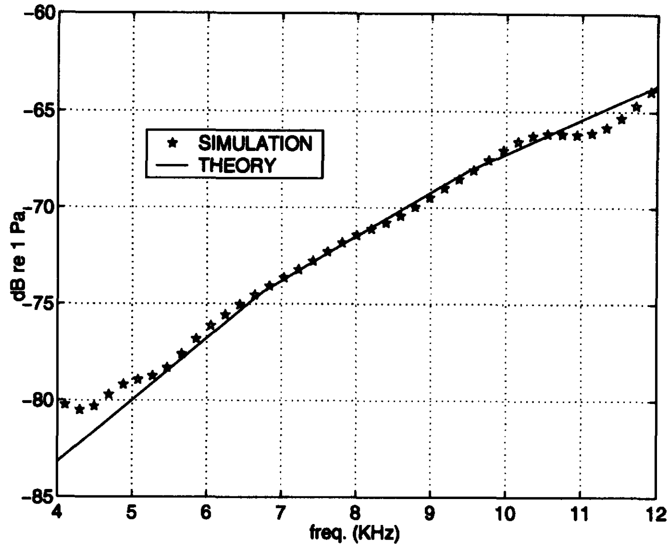

Figure 5-3: Theoretical and simulated reverberation PSD.

the elastic response appear at specific frequencies, thus making the use of spectral analysis a powerful means to discriminate such peaks. As previously pointed out, the simulation tool neglects the volume scattering processing which appears at lower frequencies. This is evident from the plots in Fig. 5-4. Finally, it is worthwhile to note that when the target sphere is a rigid rock there is no elastic response following the specular response and the PSD is the same as the PSD of the reverberation signal, as it is shown in Fig. 5-4.

Fig. 5-5 shows the modulus of the elastic sphere bispectrum normalized to the modulus of the reverberation bispectrum, using the same experimental and simulated data of the previous example. The bispectrum is shown in dB re 1 Pa, and the frequency units in the axis are kHz, as in the previous example. The results obtained applying the third order spectral analysis show the presence of a significant gain when the target is a mine–like object. The same quantities calculated for a rock–like target give rise to a unit gain (i.e. $\gamma = 1$), due to the fact that the signal received inside the elastic window has the same statistical properties of the reverberation.

The gains $\gamma_2$ and $\gamma_3$ computed for this scenario and the corresponding simulated data are shown in Table 5.2 and show that the computation of the bispectrum allows a higher gain than the PSD. The gain appears to be higher for the simulated data,

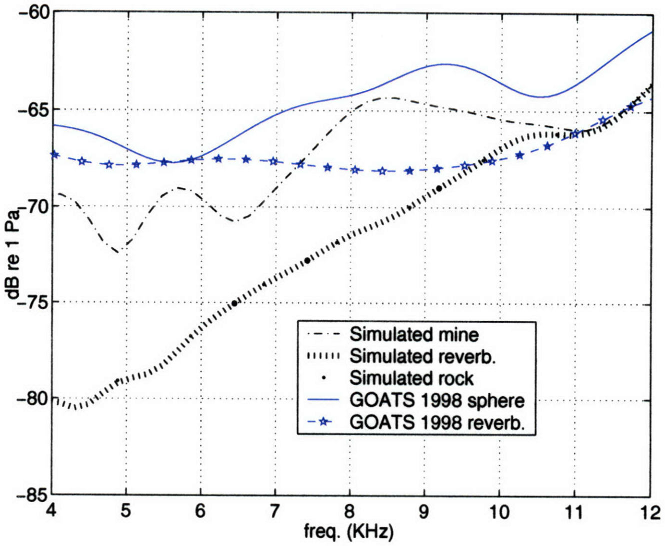

Figure 5-4: Sphere PSD estimation compared to the reverberation and rock spectra, using the GOATS 1998 and simulated data.

Table 5.2: Classification gains for the GOATS 1998 experiment.

| | **Experiment** | **Simulation** |
|---|---|---|
| $\gamma_2$ | 2.0200 | 4.0615 |
| $\gamma_3$ | 2.6956 | 5.6867 |

as can also be inferred from the plots in Fig. 5-4 and Fig. 5-5.

### 5.1.3 GOATS 2002 Experimental Data

The same quantities calculated in the previous subsection are now calculated using the GOATS 2002 experimental data. In contrast to the fixed–source GOATS'98 dataset, the GOATS 2002 data is truly measured by a mobile sonar system. The AUV in this case is monostatic, carrying a source as well as a receiver. Fig. 5-6 shows the estimated PSD of the sphere compared to the estimated reverberation PSD for both experimental and simulated data. As in the previous example, in the case of simulated data, the estimated PSD is plotted when the target sphere is modeled as a rock. In both experimental and simulated data the elastic peaks are clearly distinguishable from the reverberation spectrum, although they appear to be more pronounced in the simulated data. As previously discussed for the GOATS 1998 data, the PSD when

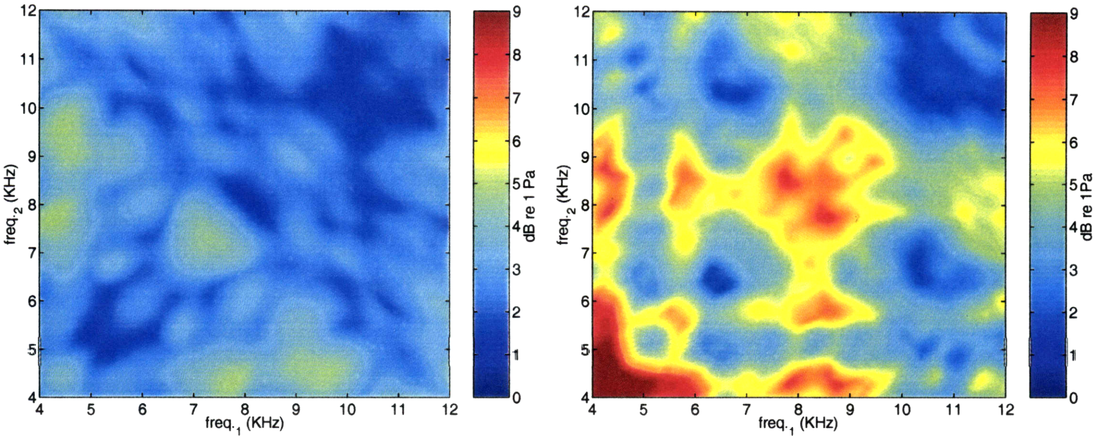

(a) Experimental data

(b) Simulated data

Figure 5-5: Sphere bispectrum gain over reverberation, using the GOATS 1998 and simulated data.

the target is a rock is the same of the reverberation PSD, because the target does not radiate elastic waves into the ocean. Again, it can be inferred from the experimental data that the volume scattering process is dominant over the surface roughness scattering at the lower frequencies. The volume scattering dominance in this case goes up to 15 kHz as opposed to 10 kHz in the previous example. This increased frequency range is probably due to the higher grazing angle in the GOATS 2002 experiment (25 degrees vs. 16.2 degrees), which leads to increased subbottom penetration. The resulting increase in volume scattering follows intuitively, although more rigorous proof of this effect has been demonstrated both theoretically and experimentally [37].

Fig. 5-7 shows the modulus of the mine–like target bispectrum normalized to the modulus of the corresponding reverberation bispectrum, for both experimental and simulated data. In both cases it is possible to classify the mine–like object, because the target bispectrum gains up to 4 dB for the experiment and up to 10 dB for the simulation. This gain is higher at the lower frequencies, in agreement with the plots in Fig. 5-6.

Finally, the gain coefficients $\gamma_2$ and $\gamma_3$ computed for the GOATS 2002 scenario are shown in Table 5.3. As in the previous example, the bispectrum offers improved

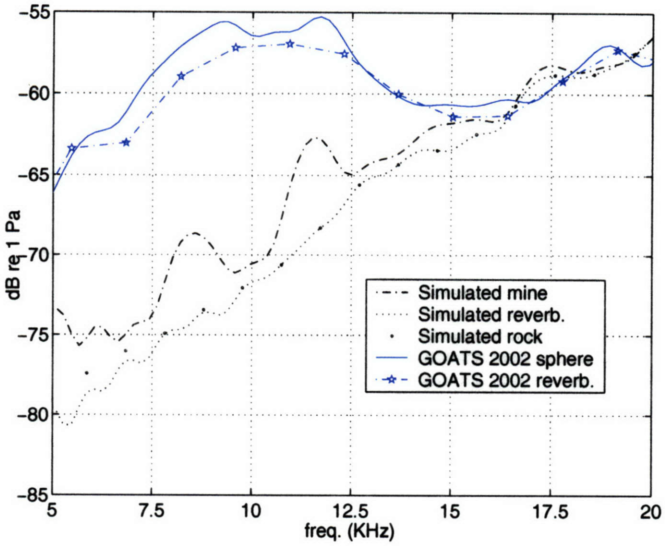

Figure 5-6: Sphere PSD estimation compared to the reverberation and rock spectra, using the GOATS 2002 and simulated data.

Table 5.3: Classification gains for the GOATS 2002 experiment.

| | **Experiment** | **Simulation** |
|---|---|---|
| $\gamma_2$ | 1.2786 | 1.5544 |
| $\gamma_3$ | 1.3113 | 2.0658 |

classification capabilities compared to the PSD, and the improvement is higher for the simulated data. The gains obtained for the GOATS 2002 experiment are lower than the corresponding gains obtained for the GOATS 1998 experiment, due the higher reverberation levels in the GOATS 2002 scenario caused by the wide–beam source. It is expected that the coherent summation of multiple pings may be used to improve the performance.

## 5.2 Shape Classification

Shape classification is the primary goal of high-resolution sonar imaging, whether using side scan or synthetic aperture techniques. In buried target imaging, the AUV is is required to perform synthetic aperture imaging to achieve sufficient resolution due to the relative length scales of the AUV and the acoustic wavelength required

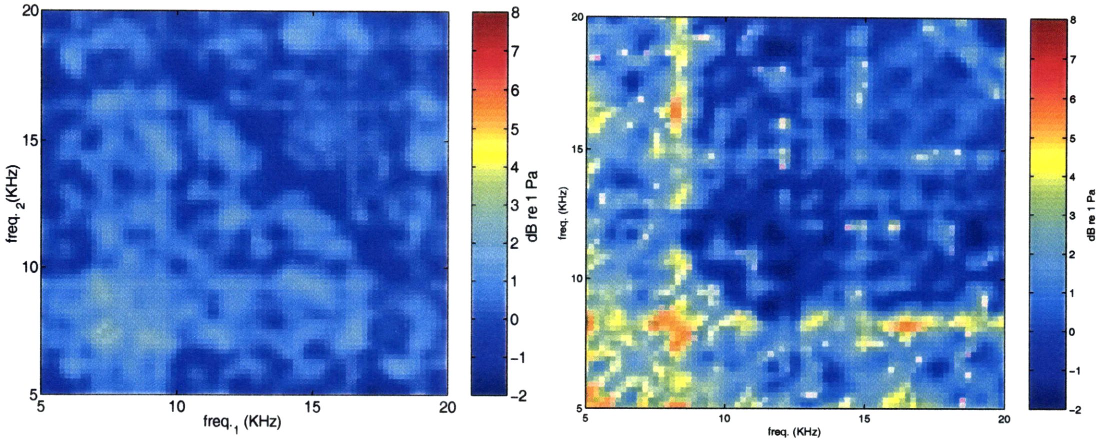

(a) Experimental data

(b) Simulated data

Figure 5-7: Sphere bispectrum gain over reverberation, using the GOATS 2002 and simulated data.

for subbottom penetration. A great deal of progress has been made in overcoming the sub–wavelength navigation accuracy requirements imposed by synthetic aperture imaging, but it remains a difficult challenge, particularly to run robustly on–line. As an alternative method for shape classification, a rough idea of the shape can be determined from its radiation beampattern, which gives an indication of the aspect ratio of the target as well as its overall size. For example, a sphere has a fairly omnidirectional scattered field at low frequency, while a high aspect ratio target such as a cylinder exhibits several lobes in its scattered field. Figure 5-8 illustrates the radiated field from a 2 m long, 0.5 m diameter cylinder both in simulation and in at–sea experiment. In both plots, the source is fixed at the bottom of the figure. Two AUVs fly by the target and simply map the amplitude of the scattered field to the angle of scattering. A strong lobe is clearly shown in both figures, which is consistent with the specular reflection from a cylinder of this size and shape. The slight alteration in direction is due to misalignment of the source and target during the at–sea experiment. Because the vehicles are approximately 50 m away from the target, this method is robust to navigation error, as an error of several meters (or wavelengths) will result in a very small angular error. In addition, the linear paths

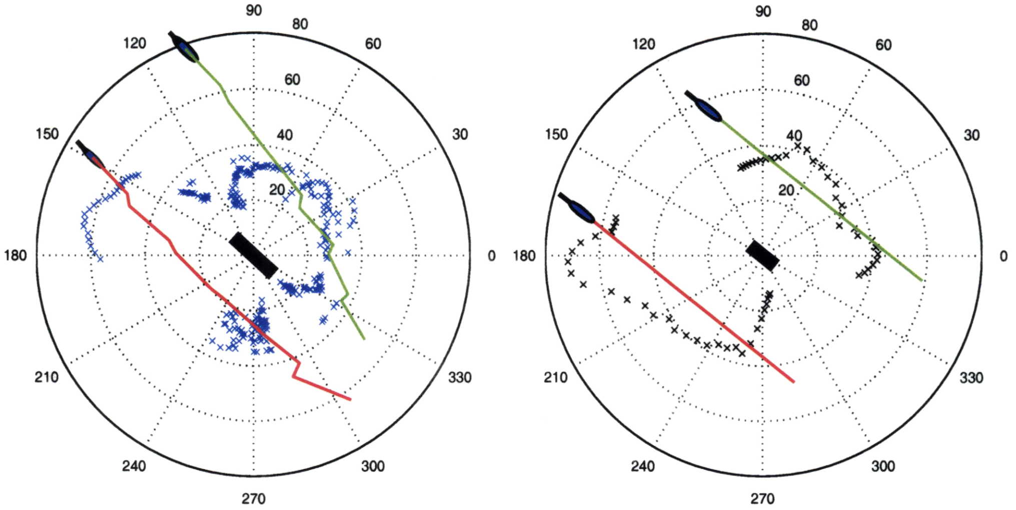

(a) Experimental result. (b) Simulated.

Figure 5-8: (a) At–sea GOATS'98 experimental result. The AUVs move past the target along a line, mapping the target scattered amplitude on the angular map. The approximately 45° aspect angle of the cylinder is consistent with a strong specular return directly to the left. (b) Simulation of a similar experiment. The results closely match the experimental result, demonstrating the highly accurate modeling capability.

of the AUV minimize the navigation error and maximize the area search rate.

Note that this approach exploits the nature of the AUV mission. The high mobility of the sonar platforms combined with the relatively short field of view create a situation where wide angular diversity of the scattered field is exploitable. Configurations with multiple vehicles further enhance this capability.

### 5.2.1 Image–based Shape Extraction

An extensive set of tools for object recognition in high–resolution imagery has been developed for a wide variety of applications, including facial recognition, robotic vision and satellite surveillance. Even at high frequencies, object recognition in sonar imaging presents a challenge due to the high clutter environment. Despite the enhanced resolution available through the SAS processing, the low frequencies required fundamentally limit the resolution such that coarse imaging is all that can be ex-

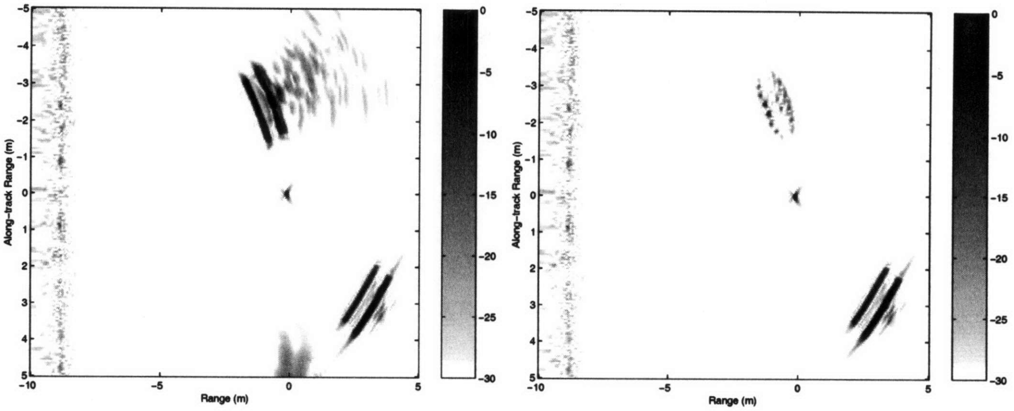

(a) (b)

Figure 5-9: SAS imagery from the simulated mission, at 5 kHz. (a) Two cylinders and a sphere, from Fig. 4-12 (a). (b) SAS image with the cylinder at (-1.0,-2.5) replaced with a spheroid of similar dimension.

pected. For a central frequency of 5 kHz, the maximum resolution of the SAS image is on the order of 10 cm. With this kind of resolution, the difference between a smooth–edged object and a sharp–edged object may be difficult to distinguish. Fig. 5-9 illustrates this fact. The left image is exactly the same as shown in the previous chapter, in Fig. 4-12. On the right, the target at the top of the image is a spheroid rather than a cylinder. The spheroid has radii equal to the radius and length of the cylinder. Note that the overall size of the targets can be well estimated, but the fine detail of the edges cannot be readily extracted from the image. Another interesting feature of the image is the distinction between the top right corners of the images. The spheroid is rigid whereas the cylinder is elastic, resulting in the cloud in the top right corner of the cylinder image only.

### 5.2.2 Pattern Matching

It is clear from the example shown in Fig. 5-8 that the beampattern is exploitable for some level of information extraction. The human viewer may see the difference between two targets, but it remains to reduce this information into a distinct measurable quantity that is representative of the target. The pattern matching method would

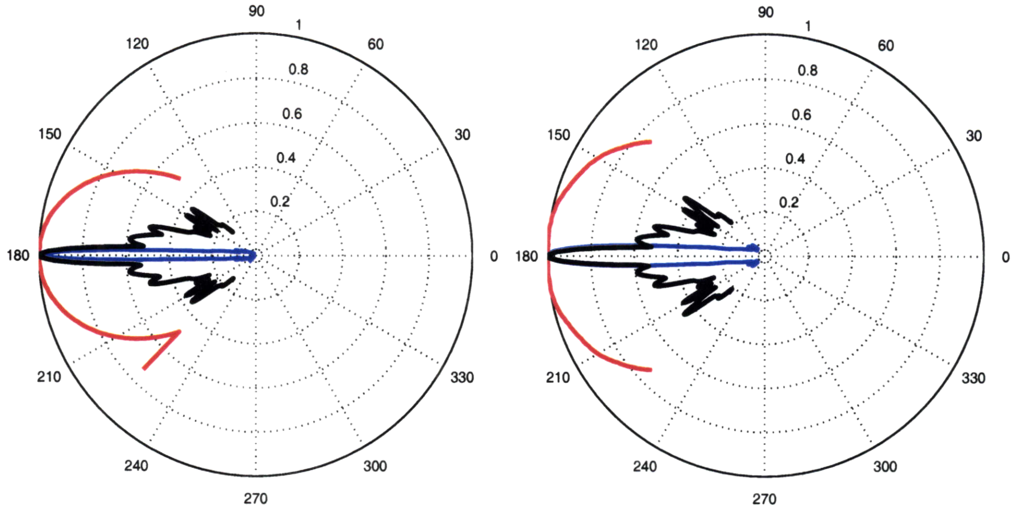

(a) Monostatic

(b) Fixed source

Figure 5-10: Receiver pass of three targets: in red, a 0.5–m radius sphere; in blue, a 2–m long, 0.5–m radius cylinder; in black, a 2–m long, 0.5–m radius spheroid.

reduce the data into a "score" that represents the correlation between a database entry and the measured data.

For benign scenarios, meaning monostatic or fixed–source sonar geometries interrogating proud targets, the pattern matching method can meet with success. Consider for example the scattered field patterns shown in Fig. 5-10. In this example, there are three candidate targets. The red line corresponds to a 0.5–m radius sphere, the blue line corresponds to a 2–m long, 0.5–m radius cylinder and the black line corresponds to a 2–m long, 0.5–m radius spheroid. In both plots, the receiver vehicle passes to the left of the target from the bottom of the plot to the top. The target is located at the center of the polar plots. In the left plot, the vehicle is monostatic. In the right plot, the source is fixed on the left side of the plot.

The obvious problem with pattern matching is the infinite number of patterns required to classify all types of targets from all sonar geometries. In addition, different burial conditions have a significant impact on the sonar returns, and must therefore also be included in the database. Reduction of the database size requires a reduction of the measurements of interest, either by restricting the relative sonar geometry in some way, or by limiting the number of targets in the database.

### 5.2.3 Characteristic Dimensions

Another approach to the shape classification is to reduce the scattered field data to characteristic dimensions of the target. While the rough size of a target may not be sufficient to determine whether it is a target of interest, it may be sufficient to make a better decision on how to proceed with the classification. For example, an aspect–dependent target has strongly preferred specular scattering angles, which may lead to alternative classification strategy from that which would be used for an aspect–independent target.

Consider a target positioned at the center of the reference system axes, at a depth $D$ from the sea surface. In the far field of the target consider a sonar transmitter on board of a single AUV, which insonifies the target, and multiple receivers onboard several vehicles, which move along specific trajectories. Due to the far field assumption, the target radiates in the space a pressure field described by the beampattern $\beta(\theta, \phi)$:

$$P_T(k, R, \theta, \phi) = \frac{e^{jkR}}{R} \beta(\theta, \phi) \tag{5.5}$$

where $k = 2\pi/\lambda$ is the wavenumber, with $\lambda = c/f$ denoting the wavelength, $c$ the sound speed and $f$ the frequency, $R$ is the target–receiver distance and $\beta(\theta, \phi)$ is the beampattern, which depends only on the target–receiver polar and azimuthal angles, respectively $\theta$ and $\phi$. When a planar cut of the beampattern is considered, the dependence on the polar angle $\theta$ is released. Each AUV measures a set of angle–amplitude pairs $(\phi, |P_T(k, R, \phi)|)$ in the backward scattering direction, which represents a sampling of the 3–D planar cut of the beampattern. From this information it is possible to reconstruct the characteristic dimension of the target, which is related to the dimension of the main lobe in the beampattern.

Consider a cylinder of length $L$ and radius $a \ll L$, with the main axis aligned with the vertical axis. The receiving vehicles sample the backscattered signal at the ping rate $pr$ and extract the beampattern amplitude from the complex envelope of the signal. The data are a set of bistatic angle–amplitude pairs. At this processing point, the position of the target has already been estimated, so that the range $R$ is known. In this simple case, the beampattern has a sinc–shaped function:

$$\beta(\phi) = \text{sinc}\left(\frac{L}{\lambda}\sin(\phi)\right) \tag{5.6}$$

where the angle $\phi$ is the azimuth. This expression for the beampattern is valid when the incident wave propagation direction is broadside to the cylinder. When the cylinder is rotated with respect to the propagation direction, or equivalently the propagation direction is $\phi_T \neq 0°$, the beampattern assumes the following form:

$$\beta(\phi) = \text{sinc}\left(\frac{L}{\lambda}\left(\sin(\phi) - \sin(\phi_T)\right)\right) \tag{5.7}$$

where $\phi_T$ denotes the steering direction. Consider the case $\phi_T = 0°$ and denotes with $R(\phi)$ the the distance between the axes origin and the AUV. The received signal amplitude is expressed as

$$s(\phi) = \frac{\beta(\phi)}{R(\phi)} = \frac{\text{sinc}\left(\frac{L}{\lambda}\sin(\phi)\right)}{\sqrt{\frac{D^2}{\cos^2(\phi)} + h^2}} \tag{5.8}$$

where $D$ is the horizontal (i.e. in the $x-y$ plane) distance between the AUV and the target and $h$ is the difference between their $z$–axis components. If the AUV is flying on a straight path, the sampling points are $d = v \cdot pr$ far away, being $v$ the AUV speed. The signal $s(\phi)$ is sampled at the positions

$$\phi_n = \tan^{-1}\left(\frac{D}{-D\frac{\lambda/L}{\sqrt{1-(\lambda/L)^2}} + (\delta+n)d}\right) \tag{5.9}$$

where $n = 0, 1, \ldots, N-1$ and

$$N = \frac{2D}{d\sqrt{(L/\lambda)^2 - 1 + 1}} \tag{5.10}$$

is the maximum number of points inside the beampattern main lobe. In (5.9)

$$-D\frac{\lambda/L}{\sqrt{1-(\lambda/L)^2}} + \delta d \overset{\Delta}{=} y_0 \tag{5.11}$$

is the first sampling point, assuming that the AUV is flying along the positive $y$–axis direction. Here $\delta$ is a random variable with uniform distribution in the range $[0,1]$. Eq. (5.8) and (5.9) give the theoretical relation between the beampattern and the object length. This parameterization is the key to invert the relation in a simple way and estimate $L$ directly.

The complete statistical signal model must account for the reverberation process, so the received signal (after beamforming and filtering) can be written as

$$\mathbf{z} = \mathbf{s}(L) + \mathbf{r} \tag{5.12}$$

where $\mathbf{z} = [z(0)\ z(1)\ \cdots\ z(N-1)]^T$ is the vector comprising the signal samples and $\mathbf{s}, \mathbf{r}$ are defined in the same way. If the reverberation probability density function (pdf) $p_r(\mathbf{r})$ is known, the optimum MLE can be derived as

$$\hat{L}_{ML} = \arg\max_L\{p_r(\mathbf{z} - s(L); L)\}. \tag{5.13}$$

The MLE $\hat{L}_{ML}$ can be easily derived when the reverberation pdf is Gaussian:

$$\hat{L}_{ML} = \arg\min_L ||\mathbf{z} - s(L)||^2 \tag{5.14}$$

where $||\cdot||$ is the vector norm operator. Because the function is non–linear, it is necessary to use numerical technique to find the zero of the derivative of the function itself. A more realistic model of the reverberation process is the K distribution [1]. The estimator cannot be derived in a closed form, but the maximization problem can be solved with numerical algorithm. When the reverberation pdf is not Gaussian, the estimator in (5.14) is not the MLE anymore, but is the least squares estimator (LSE). Of course, when the reverberation is Gaussian distributed the two estimators coincide. A performance degradation is expected when the LSE is used and the reverberation is not Gaussian distributed, causing the estimator to be sub-optimal.

The estimator performance is evaluated in terms of bias $b(\hat{L}/\lambda)$ and mse of the cylinder length normalized to the wavenumber, in order to obtain non-dimensional quantities:

$$b(\hat{L}/\lambda) = E\{\hat{L}/\lambda\} - L/\lambda \tag{5.15}$$

$$mse(\hat{L}/\lambda) = E\{(\hat{L}/\lambda - L/\lambda)^2\} = var\{\hat{L}/\lambda\} + b^2(\hat{L}/\lambda) \tag{5.16}$$

where $E\{\cdot\}$ denotes the statistical expectation and $var\{\hat{L}/\lambda\} = E\{(\hat{L}/\lambda - E\{\hat{L}/\lambda\})^2\}$ is the statistical variance. These quantities can be evaluated numerically through Monte Carlo simulations and the mse compared to the CRLB, which is the lower bound for any unbiased estimator:

$$CRLB(L/\lambda) = \frac{1}{-E\left\{\frac{\partial^2 \ln p_r(\mathbf{z}-\mathbf{s};L/\lambda)}{\partial^2 L/\lambda}\right\}} \tag{5.17}$$

The lower the squared bias, the closer the mse is to the CRLB, which is reported in the simulation plots as a benchmark. When the reverberation is Gaussian distributed with zero mean the CRLB can be expressed as [40]

$$CRLB(L/\lambda) = \frac{1}{\left(\frac{\partial \mathbf{s}(L/\lambda)}{\partial L/\lambda}\right)^T \mathbf{C}^{-1} \left(\frac{\partial \mathbf{s}(L/\lambda)}{\partial L/\lambda}\right)} \tag{5.18}$$

where $\mathbf{C} = E\{\mathbf{r}\mathbf{r}^H\}$ is the covariance matrix of the reverberation process. Usually $\mathbf{C}$ is not known and must be estimated from secondary data, i.e. data collected when there is no target present in the insonified field. The region from which the secondary data are collected must be close to the target field in order to assure the same statistical properties.

### Performance Analysis

To demonstrate the expected performance of length extraction of elongated targets, consider a cylinder in the target field and a single receiver flying along a straight path at a distance $D = 10$ m from the $y$–axis and $h = 10$ m. In the following examples the AUV speed is $v = 1$ m/s, the ping rate is $pr = 1$ sec$^{-1}$ and the sound speed is $c = 1500$ m/s. In this example a narrowband transmission is considered, with central frequency $f_0 = 3$ KHz. The minimum target size is $|L/\lambda|_{min} = 1$, which corresponds to an infinite number of sampling points inside the beampattern main lobe, while the maximum target size is $|L/\lambda|_{max} = \frac{\sqrt{9d^2+4D^2}}{3d}$, which corresponds to the case when there are only 3 sampling points inside the main lobe.

Fig. 5-11 shows how the number of sampling points inside the main lobe in the backward scattering direction decreases for increasing $L/\lambda$. As previously mentioned, when $L/\lambda \to 1$ the number of sampling points tends to infinity, while when $L/\lambda \to |L/\lambda|_{max}$ the number of points is minimized. The mse is expected to increase for increasing $L/\lambda$ because there are less available data to process. This consideration is validated by Fig. 5-12 where the mse of the MLE is plotted together with the CRLB and the best imaging resolution in absence of noise and reverberation. Best imaging resolution in this and the other examples refers to the well–known $\lambda/2$ imaging resolution limit that is theoretically achievable with synthetic aperture processing. The SNR is 10 dB and the reverberation is generated as a white Gaussian process. When $L/\lambda$ is small enough, the MLE can significantly improve the imaging performance.

Fig. 5-13 shows the same quantities as a function of the SNR, when $L/\lambda = 1.667$. When $SNR > 5$ dB the MLE furnishes a substantial improvement with respect to the best imaging techniques. When $SNR < 10$ dB the mse departs from the CRLB due to the non–linearity of the MLE.

Finally, Fig. 5-14 shows the mse of the MLE and the LSE as a function of the SNR, when the reverberation is an exponentially correlated Gaussian process. The correlation function is defined as

$$r(m) = E\{r(n)r(n+m)\} \tag{5.19}$$

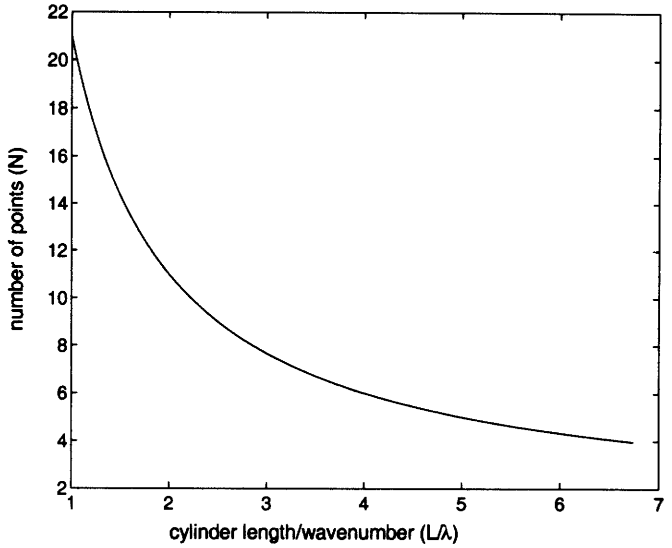

Figure 5-11: Number of sampling points for different values of the normalized cylinder length $L/\lambda$ (decorrelated reverberation).

and the degrees of correlation is defined through the correlation coefficient $\gamma$:

$$\gamma = \frac{r(m)}{r(m+1)}, \tag{5.20}$$

which is chosen to be $\gamma = 3$. When the reverberation is correlated the performance degrades because the degree of innovation between adjacent samples is decreased. The performance continues to decline as the the degree of correlation increases.

### Simulation Results

Turning to the example illustrated in Fig. 5-10, the 3 dB bandwidth is used for the inversion of the target lengths. The determination of zero crossings is prevented by the underlying noise and reverberation. The length estimates of the targets using the monostatic and fixed–source sonars are shown in Tables 5.4 and 5.5, respectively, along with the correct values.

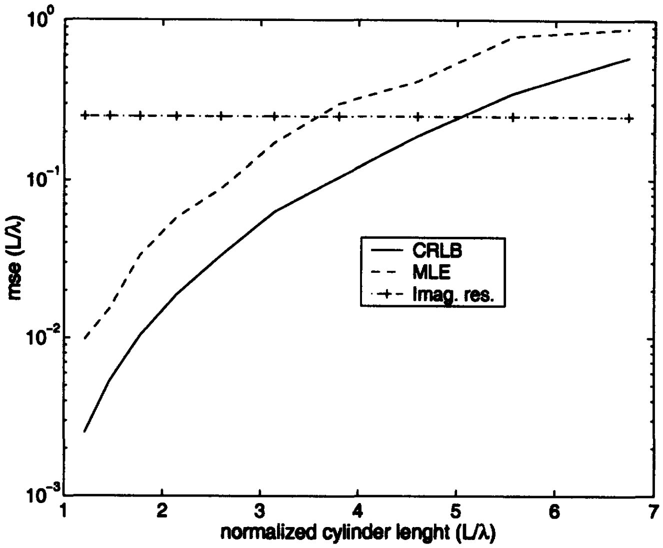

Figure 5-12: MSE of the MLE compared to the CRLB and the imaging resolution for different normalized cylinder length values and $SNR = 10$ dB (decorrelated reverberation).

Table 5.4: Dimension estimates for the monostatic sonar.

| | **Experiment** | **Simulation** |
|---|---|---|
| *sphere* | 1.0 | 0.14 |
| *cylinder* | 2.00 | 2.25 |
| *spheroid* | 2.00 | 1.25 |

## 5.3 SAS Color Imaging

One way to combine spectral and shape characteristics with a concise presentation format is through color imagery. This method has some practical advantages in the low-frequency systems considered in this thesis. In particular, the use of bottom-penetrating sonars was shown in Chapter 3 to present problems for micronavigation. In order to avoid this situation, a high-pass filter may be implemented to separate

Table 5.5: Dimension estimates for the fixed-source sonar.

| | **Experiment** | **Simulation** |
|---|---|---|
| *sphere* | 1.0 | 0.18 |
| *cylinder* | 2.00 | 2.20 |
| *spheroid* | 2.00 | 1.75 |

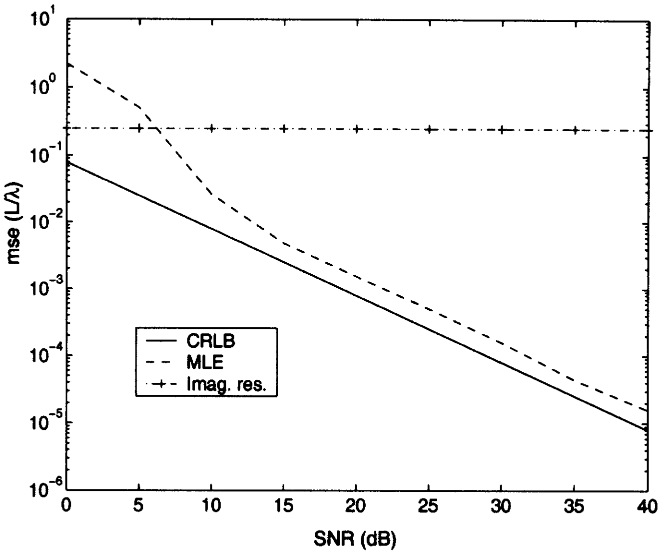

Figure 5-13: MSE of the MLE compared to the CRLB and the imaging resolution for different SNR values and $L/\lambda = 1.667$ (decorrelated reverberation).

out the components of the signal that interact with the seabed only superficially. In addition, it was shown in Chapter 4 that buried targets are easier to detect after low pass filtering the data. This need for a range of filters leads naturally to a parallel processing scheme in which the SAS imagery can be generated in each band. These images can then be combined in different color bands, just like red–green–blue (RGB) image filters used for digital imaging and televisions.

Fig. 5-15 shows two separate AUV missions using the MIT–MCM simulator. In both missions, the AUV follows the same sinusoidal trajectory past a target that lies approximately 50 m away from the point of closest approach. The sonar returns from each ping are stacked and the overall ping-by-time plots are displayed in the figure. On the left plot, the target is a 5 m long, 0.5 m radius rigid cylinder. The first two strong returns are from the prominent corners of the cylinder, while the later two returns are the reflections from the air–water interface. On the right, the target is a 1–m radius steel sphere. In this plot, the first two strong returns consist of the direct and the flexural Lamb wave of the sphere, while the later return is the reflection of the specular return off the air–water interface. The Lamb wave does not appear in this reflection due to the high angular difference between the backscattering and the

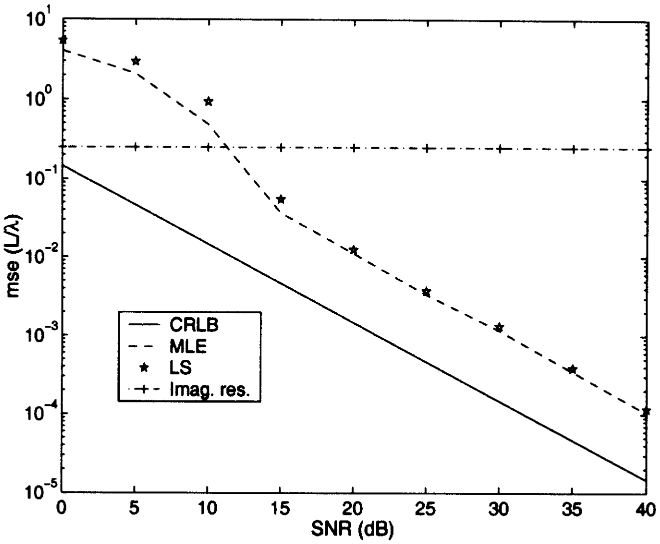

Figure 5-14: MSE's of the MLE and LSE compared to the CRLB and the imaging resolution for different SNR values and $L/\lambda = 1.667$ (correlated reverberation with $\gamma = 3$).

surface reflection. The targets in both cases were chosen to be very prominent for demonstration purposes.

In Fig. 5-16 are shown synthetic aperture sonar (SAS) images that are constructed from the simulated sonar data. These simulations are intended to demonstrate the feasibility of estimating target size from the sonar data, in combination with spectral diversity. In this case only the sharp corners of the cylinder are seen, and these have broadband .

To evaluate the feasibility of recognizing objects based upon their spectral responses, a similar exercise was performed in the simulator. In this example, the AUV takes the same trajectory past two 1 m diameter spheres that differ only in their material of construction. The SAS images of the two spheres are shown in Fig. 5-17. On the left, the rigid sphere shows only a direct backscattered reflection, while the steel sphere on the right exhibits frequency–dependent elastic scattering that is slightly delayed with respect to the direct reflection.

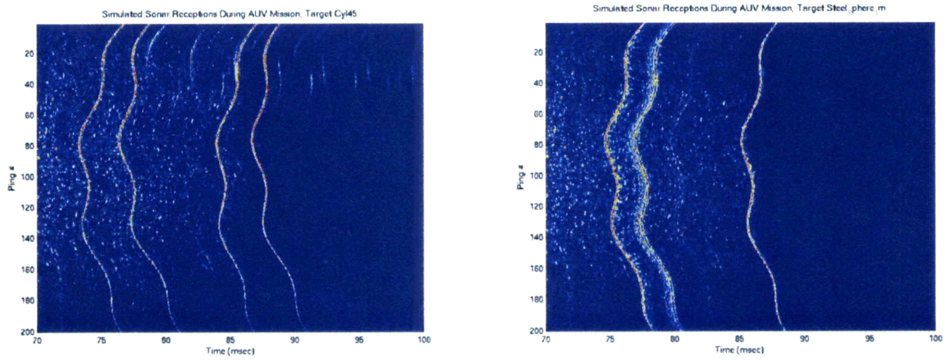

(a) (b)

Figure 5-15: Simulated sonar receptions for an AUV as it traverses a sinusoidal path past (a) a steel sphere of 1 m radius and (b) a 5 m long, 0.5 m radius rigid cylinder.

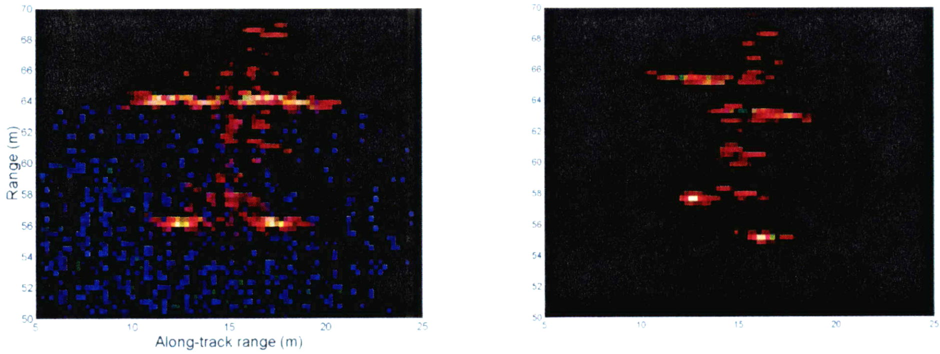

(a) (b)

Figure 5-16: Synthetic aperture sonar images generated from simulated sonar receptions by an AUV passing by a 5 m long cylinder at an aspect angle of (a) 0 degrees, (b) 45 degrees.

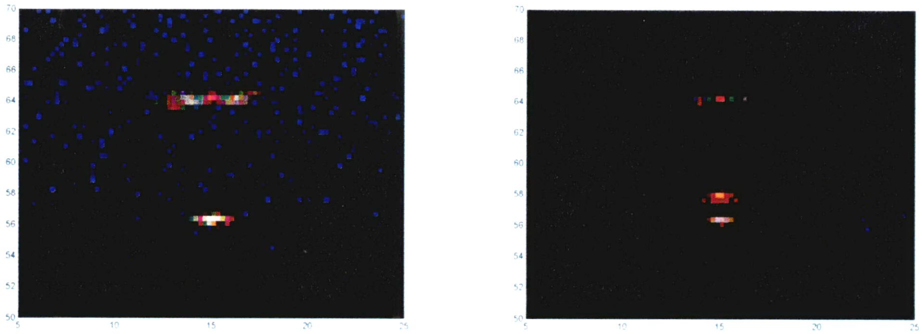

(a) Rigid sphere. (b) Steel sphere.

Figure 5-17: Synthetic aperture sonar images generated from simulated sonar receptions by an AUV passing by a 1 m diameter sphere.

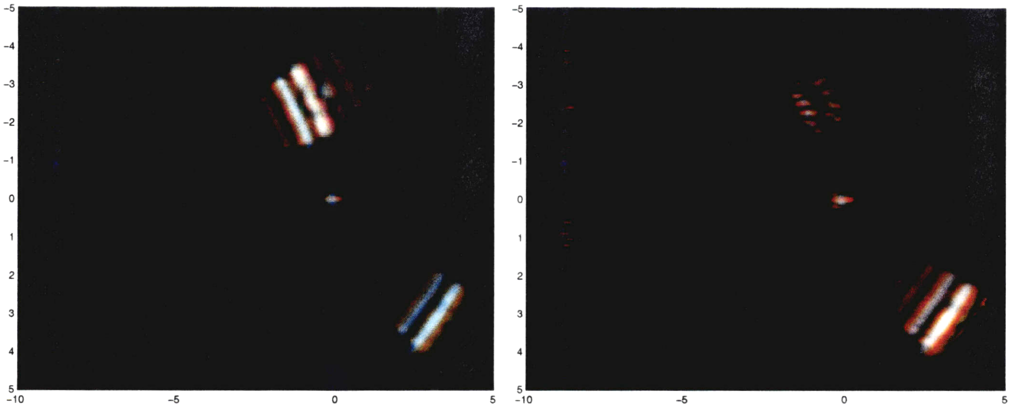

(a) (b)

Figure 5-18: Color SAS imagery of the three–target fields. The target fields are the same as those in Fig. 5-9

.

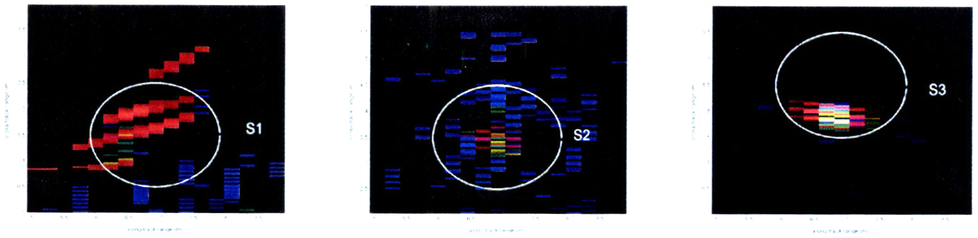

(a) (b) (c)

Figure 5-19: RGB SAS images of three 1–m diameter, air–filled steel spheres of various burial conditions: (a) 1 m deep, (b) flush–buried, (c) half–buried (proud).

### 5.3.1 Application to Experimental Data

The GOATS experimental series provides a rare and valuable source of live AUV–borne sonar receptions from discrete targets in the 1-15 kHz range. Once again, the GOATS'98 dataset is exploited in order to evaluate whether it is realistic to discriminate between targets using color SAS imagery. Fig. 5-19 shows SAS images of the three spherical targets. Note that, although the three targets are exactly the same, their respective images differ in color due to the varying burial conditions. The 1 m deep sphere (S1) appears as a low frequency, red image due to the lowpass filtering behavior of the seabed. The flush–buried sphere (S2) appears in red and green, and the proud sphere appears clearly in all bands. The blue speckle in the two buried sphere images corresponds to the high–frequency seabed scattering that rivals the scattering strength of the faint targets. The proud sphere stands clearly above the scattering, and the roughness scattering is therefore not seen in its image.

Although the RGB SAS images are useful for a human user to visualize the different backscattering characteristics of the three spheres, robust autonomous classification from these images is difficult to achieve.

## 5.4 Near–Interface Effects from GOATS

Buried target classification is of paramount importance in the removal of mines in both land and sea. The challenge lies in the fact that the frequency regimes required for subsurface penetration are typically on the order of the target size, and therefore do not allow sufficient image resolution for classification. Data diversity, in the form of frequency and angular spread, can be used to provide additional classification clues. In recent years, much work has been devoted to exploit frequency and angular diversity in radar applications for landmines [59, 39]. Similar sonar applications have received less attention because of their apparent impracticality.

A primary reason that sonar applications have been deemed impractical is because of the area coverage rate limitation imposed by the critical angle of the seabed. Mines can be located in very shallow water (VSW), typically of less than 30 m depth. Critical grazing angles in the coastal ocean are typically $20 - 30°$, so the range of the sonar is limited to about twice the ocean depth for propagating penetration into the seabed. This limitation places a severe limit on the mapping rate of the mine–hunting sonar.

One response of the sonar community has been to examine whether there is significant energy propagating in the seabed due to alternative coupling methods, e.g., through the seabed roughness scattering or frequency–selective phase matching from the ripple structure [49]. This approach yielded some promising results in modeling and experimental applications for one–way propagation to buried geophones in the mid–frequency regime (1–10 kHz). Traditional sonar applications are monostatic, and as such would require two–way propagation through the alternative coupling mechanism.

The GOATS project was then developed (in part) to evaluate the feasibility of sonar detection and classification of buried targets under sub–critical insonification. In the affiliated experiments, several mine–like objects (MLOs) were placed in a variety of burial conditions and insonified with a parametric, sub–critical source. The scattered fields were measured monostatically and bistatically with a stationary horizontal line array (HLA) and a moving linear array mounted on an AUV. Some observed features of the scattered field were not expected, particularly regarding the coupling between the evanescent field in the seabed and the elastic modes of the targets.

This section documents some of the new findings of the interaction between an elastic target and a sub–critical source, including the empirical and model–based evidence for the strong coupling. The GOATS'98 experiment provided two platforms for a sampling of the scattered field from the buried targets. A 12–m long HLA was fixed either in a bistatic or monostatic position during each test series in addition to the 0.7–m long AUV–borne array. The AUV traversed the test area, sampling the scattered field over a quasi–regular pattern. A bistatic SAS algorithm [22] provides a substantial enhancement to the along–track resolution of the AUV receiver.

### 5.4.1 HLA Results

The HLA consists of 128 neutrally buoyant hydrophones separated by 9 cm, corresponding to $\lambda/2$ spacing for an 8.4 kHz signal. The source exceeds the $\lambda/2$ aliasing condition, as it is an 8 kHz Ricker wavelet. Grating lobes are avoided by limiting the HLA field of view to $\pm 60^\circ$. During the course of the GOATS'98 experiment, the HLA was positioned for each run on 5–m high trellis towers in either a monostatic or a bistatic configuration.

In the monostatic configuration, the backscattering from the various targets is measured. The monostatic HLA receives returns above the critical angle only from S1 over its full aperture, and from the flush–buried cylinders C1 and C2 for parts of its aperture. The flush–buried and half–buried spheres, S2 and S3 respectively, lie below the critical grazing angle over the full HLA aperture. Since we are interested here in the sub–critical insonification with above–critical reception, we investigate only the responses for S1, C1 and C2 with the monostatic HLA.

The buried sphere S1 lies 1–m below the seabed at its center. As such, we expect significant low–pass filtering to be achieved by the seabed even with above–critical insonification. Fig. 5-20 shows the spectrogram of the S1 signal at various insonification angles, generated using the time series created by focusing the HLA on the target. In (a) and (b) it can be seen that the target is readily detectable, although the signal is limited to less than 10 kHz. Several Lamb waves are also possibly detectable. As the source goes below the critical angle, as shown in (c) and (d), there is still signal at the target location but it is nearly indistinguishable from the reverberation.

The flush–buried cylinders demonstrate the angular dependence of non–spherical targets. The cylinder C2 lies at approximately 45° aspect with respect to the source at the midpoint of the rail, and so its specular response is not at its strongest in the direction of the monostatic HLA. However, Fig. 5-21 shows that the specular return is readily detectable at or above critical insonification, while the chirp–like elastic response is prominent over the full range of insonification angles, including the severely sub–critical angle of 17.6°. This reflects the fact that specular returns are a function of the source–target–receiver geometry, while the elastic returns are based solely on the nature of the target and, in the buried target case, the sonic cone.

The cylinder C1, on the other hand, is normal to the source at the same position, and thus has maximum specular response in the backscatter direction. In this case the specular backscatter is prominent both above and below critical grazing insonification due to the backscattering strength in the 90° aspect orientation and the shallow burial depth. In fact, the backscattered signal does not vary significantly with source position. The spectrograms of the target returns at the HLA are shown in Fig. 5-22. The apparent elastic returns appear to be broadband multiples of the specular return.

### 5.4.2 AUV SAS Results

The bistatic SAS generated by autofocusing the bistatic AUV receiver data has been shown to be an effective imaging tool. However, the classification of targets is of much greater interest, particularly for the bistatic geometry. The bistatic data contains diverse frequency and angular responses from the target. Fig. 5-23 shows the time–frequency response of the 1–m deep buried sphere, as measured by the AUV receiver passing slightly forward of the target. The high angle of the source, 30.5°, allows a significant amount of energy to penetrate the seabed and be scattered by the target. Note that the specular response has a distinct low–pass filter quality, as the seabed

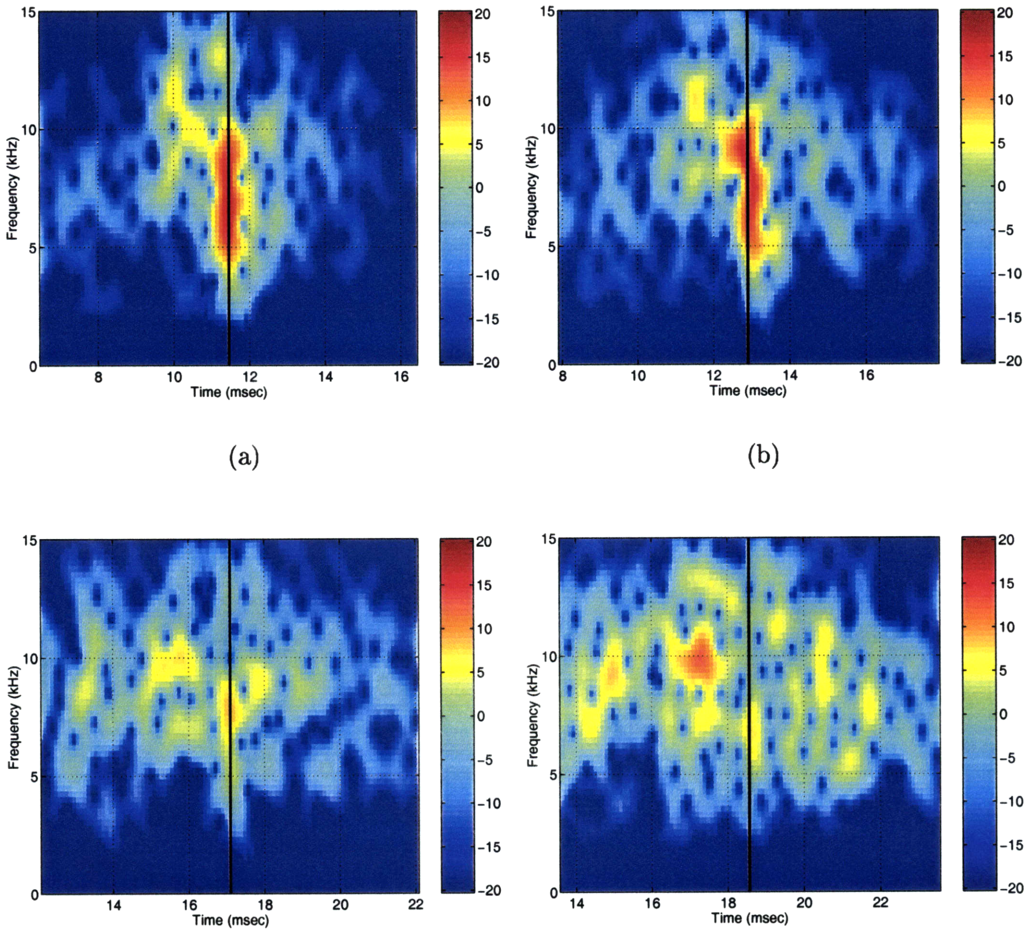

(a) (b)

(c) (d)

Figure 5-20: Spectrogram of the S1 backscattering under varying insonification regimes, using the focused time series over the full monostatic HLA. Receiver grazing angles are above critical, varying from 27.5° to 33.7°. (a) Above critical insonification, 39.8°. (b) Above critical insonification, 33.7°. (c) Critical insonification, 24.0°. (d) Below critical insonification, 21.8°

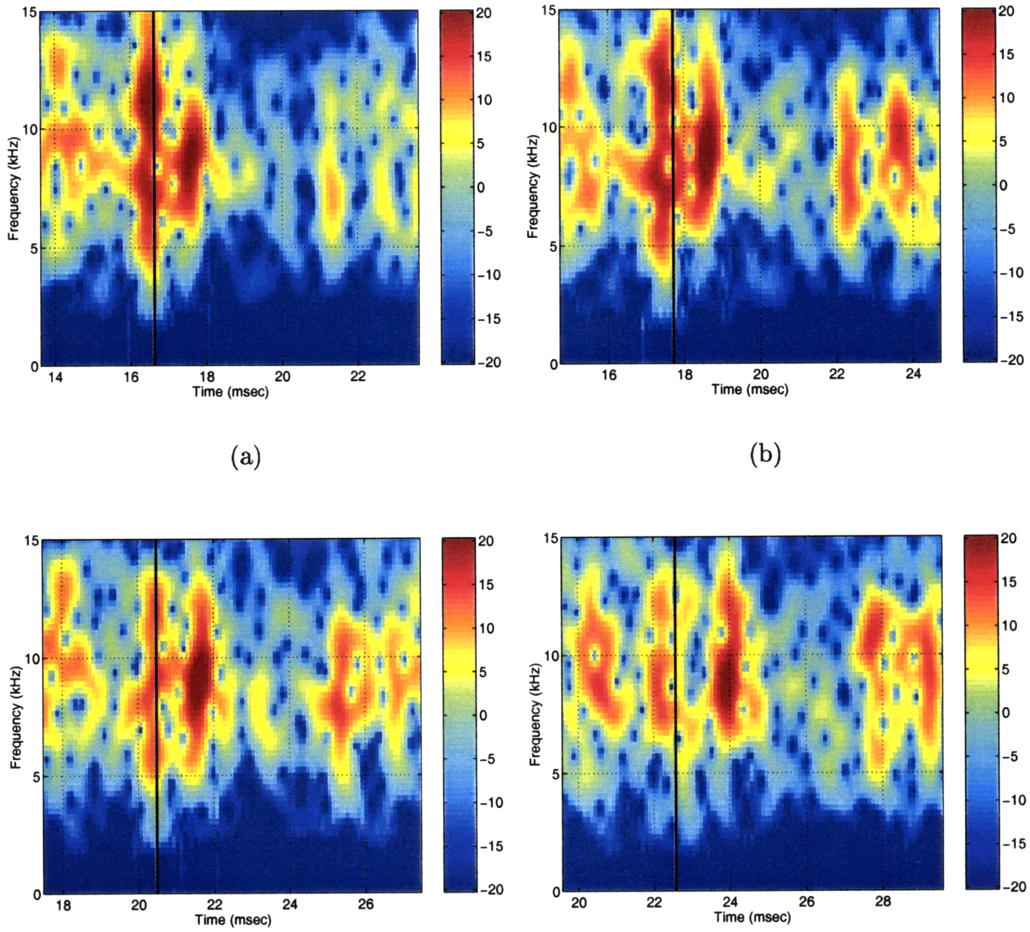

(a) (b)

(c) (d)

Figure 5-21: Spectrogram of the C2 backscattering under varying insonification regimes, using the focused time series over the above critical segment of the monostatic HLA. Receiver grazing angles range from 30.0° down to the critical grazing angle of 24.0°. (a) Above critical insonification, 29.3°. (b) Above critical insonification, 26.9°. (c) Critical insonification, 24.0°. (d) Below critical insonification, 17.6°

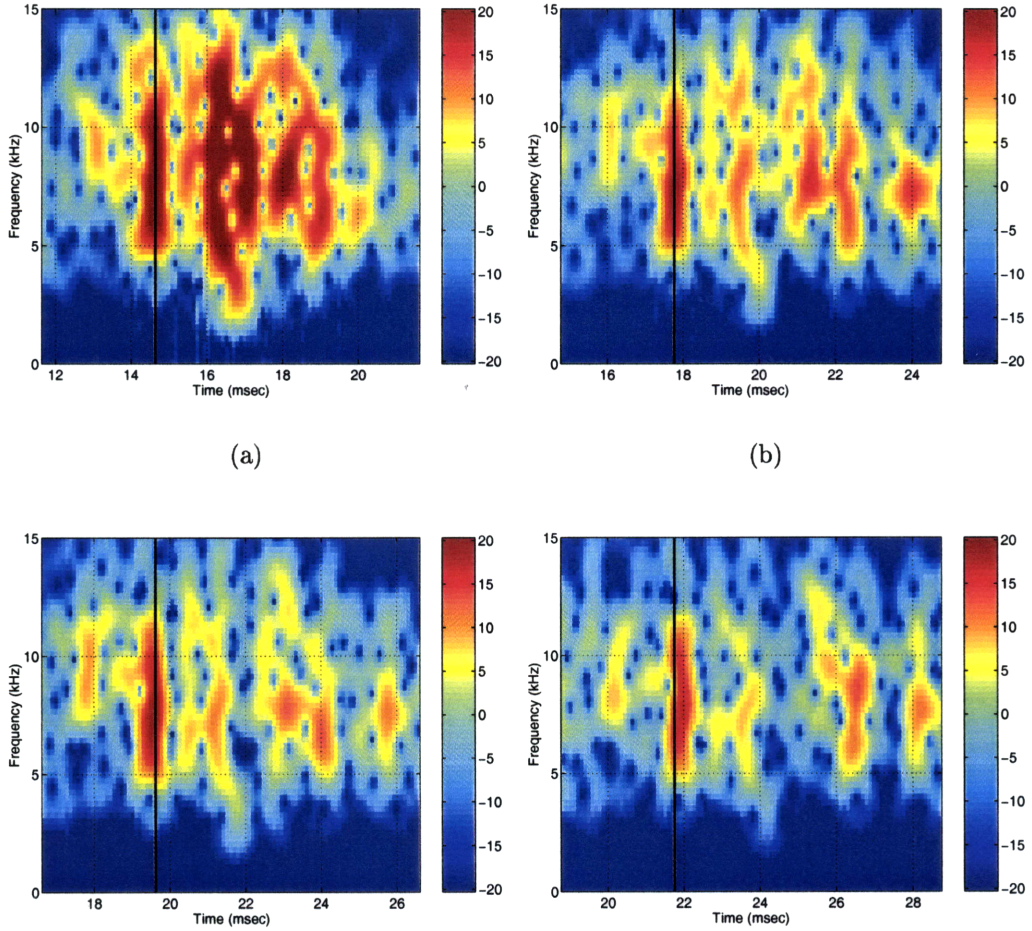

(a) (b) (c) (d)

Figure 5-22: Spectrogram of the C1 backscattering under varying insonification regimes, using the focused time series over the above critical segment of the monostatic HLA. Receiver grazing angles range from 30.0° down to the critical grazing angle of 24.0°. (a) Above critical insonification, 26.9°. (b) Below critical insonification, 21.9°. (c) Below critical insonification, 20.2°. (d) Below critical insonification, 17.6°

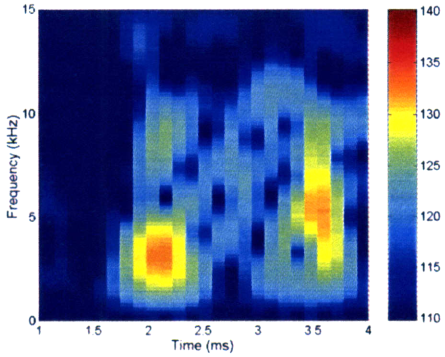

Figure 5-23: Spectrogram of the 1–m deep buried sphere (S1) backscattering from above critical insonification, 30.5°.

attenuation mechanism has removed the high frequency components.

In Fig. 5-24 is shown the focused time–frequency response of the flush–buried sphere. Under sub–critical insonification, the direct return is weak and at very low frequency, as expected by the conventional ray path propagation physics. In fact, the first elastic response is stronger than the direct response, and is at higher frequency, about 10 kHz. There are also additional narrowband elastic responses that are detectable. Under super–critical insonification, the elastic structure is essentially the same, but the specular return is much stronger.

In Fig. 5-25 are shown the same results for the proud sphere. Both of these spectrograms are for sub–critical insonification, but the insonification regime is unimportant because the target is not buried. However, the spectrograms are included for comparison with the buried spheres. In (a), the classical sphere response can be clearly seen. There is a strong specular reflection, followed by several Lamb waves. A preliminary analysis of the target responses is presented in other work [78].

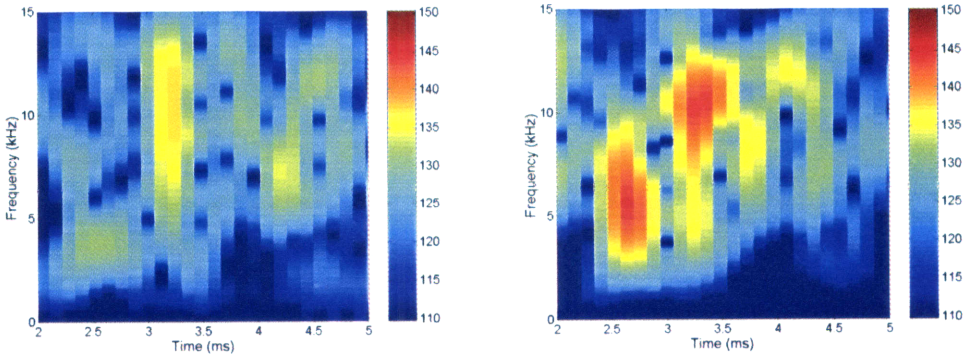

(a) (b)

Figure 5-24: Spectrogram of the flush–buried sphere (S2) backscattering under varying insonification regimes, using the focused time series over a 7 m synthetic aperture created with the AUV–borne array. (a) Source sub–critical, 18.7°. (b) Source above critical, 24.4°

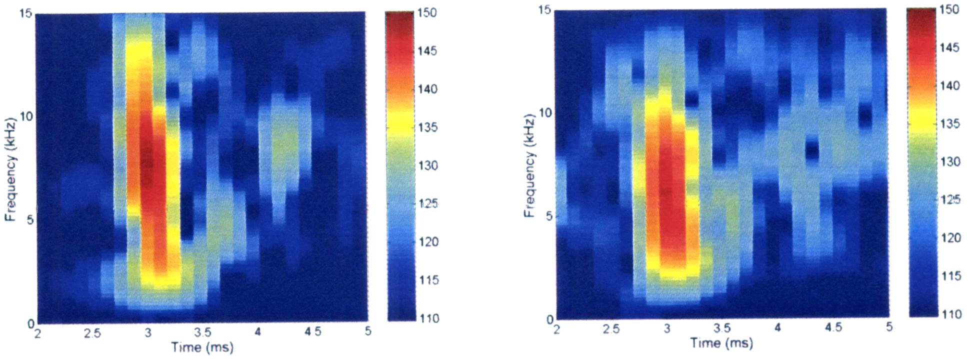

(a) (b)

Figure 5-25: Spectrogram of the proud sphere (S3) backscattering under varying insonification angles, using the focused time series over a 7 m synthetic aperture created with the AUV–borne array. (a) Source sub–critical, 16.2°. (b) Source below critical, 20.3°

# Part III

# Target Classification with Actively Mobile Sonar Platforms

# Chapter 6

# Exploiting Vehicle Autonomy

In this chapter the application of vehicle mobility in the context of an overarching mission is considered. Recall that active mobility has been defined in this thesis as on–the–fly sonar path deviations in response to the content of the sonar receptions. The vehicle generally will have survival tasks to accomplish, such as basic navigation, maintaining depth and altitude, and obstacle avoidance. In addition, the vehicle generally has a preset mission path, designed to allow efficient and complete coverage of a given area. Sonar–adaptive behavior requests must be incorporated into this web of competing mission objectives throughout the mission. The organization and prioritization of tasks is highly dependent upon the goals of a particular mission, and are therefore left to the side in this work. The question at hand is how to detect and classify a target through active sonar–adaptive behavior.

In view of the communications and controls lag inherent in underwater systems, a degree of decision–making must be entrusted to the on–board systems in order to exploit the full power of mobile sonar platforms. Autonomy in terms of completing a CDAC mission means that the interpretation of and reaction to received sonar data are determined at the platform level. The signal processing algorithms and platform motions are the tools that the vehicle can vary during the course of the mission in order to optimize its CDAC performance. In comparison to full autonomy, these tools will be limited in this chapter to provide a small subset of the possibilities of autonomous mobile sonar platforms. In particular, the autonomous behaviors to be investigated consist of simply concatenating the detection and classification tasks described in previous chapters to create sonar–adaptive CDAC missions.

Due to the emphasis on the littoral ocean in this thesis, and to the desire for simplicity of analysis, the depth control of the platform is left to the navigation and safety systems of the vehicle. Depth control is much more sensitive to competing safety concerns in shallow water, because the boundaries of the water column are nearby. A swimming vehicle has relatively little to worry about in terms of avoiding obstacles floating in the water column. Target detection and classification concerns are also not critically impaired by the restriction to heading–only adaptation. In shallow water, relatively little information about the target is to be gleaned through elevation changes when compared to the azimuthal diversity available through heading control. In fact, nearly all of the available signal diversity available through depth control can be achieved through heading control to varying ranges.

## 6.1 Continuous vs. Discrete Path Adaptation

### 6.1.1 Continuous Path Adaptation

The most conceptually pleasing, if impractical, method of employing sonar–adaptive behavior is to give heading control directly to the sonar system, and have the signal processing algorithm make a decision whether to turn left or right at each ping. Within the context of a pre–planned mission, the continuous path adaptation should be initiated with a reliable detection. After the detection, the vehicle is free to follow the sonar information to maximize its mission performance. By ceding the ping–to–ping heading control to the sonar system, the vehicle temporarily abandons its pre–planned mission. Upon completion of the target investigation, the vehicle then returns to its greater mission.

Given an appropriate cost function and decision tree, the continuous path adaptation can lead to optimal results for detection and/or classification of targets. However, there is the outstanding problem of determining when a target has been detected or

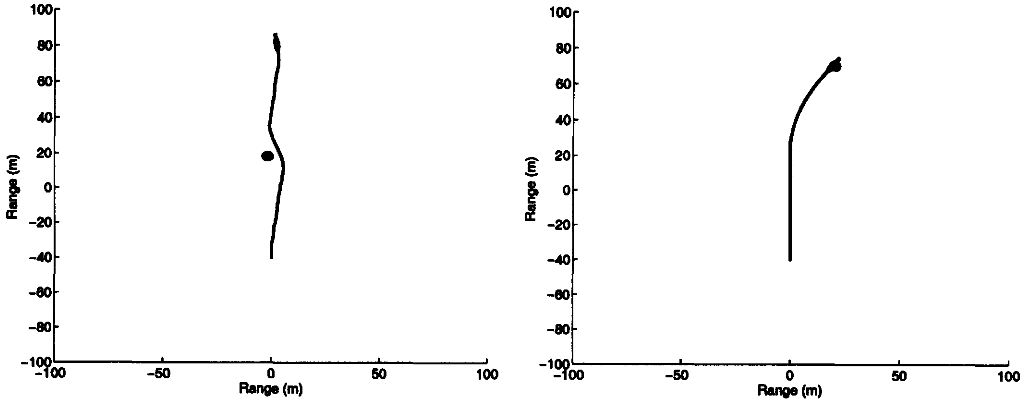

(a) Object avoidance.

(b) Object hunting.

Figure 6-1: Simulation of obstacle avoidance and object hunting missions, where the object of interest is a 1–m diameter sphere.

classified, i.e. when to abort the adaptation and return to the original path. Moreover, there is the issue that the trajectory followed by the vehicle may not lend itself to readily returning to the original mission path. The risk is run of winning the battle and losing the war, i.e. losing sight of the overall mission in the pursuit of some potential target.

While not appropriate for a detection or classification mission, the continuous path adaptation method is the best way to achieve certain mission objectives. Prime examples of missions that are well–suited for continuous path adaptation are vehicle docking, mine disposal and obstacle avoidance. In the first two cases, there is no need to continue the mission after the adaptation event. In the latter case, the mission cannot be completed as planned due to the obstacle. Simulated examples of object hunting (i.e., vehicle docking or mine disposal) and obstacle avoidance missions are shown in Fig. 6-1. In these figures, the sonar–adaptive trajectory is shown in response to receptions from a 1–m diameter spherical target. In Fig. 6-1 (a), the platform moves around the obstacle while maintaining as close to the original path as possible. In Fig. 6-1 (b), the sonar–adapted path finishes at the object, where the mission is declared complete.

### 6.1.2 Discrete Path Adaptation

The obvious problem with continuous cost functions is that they cause the AUV to wander about the target field in an unpredictable manner. In the context of a larger mission, this type of unpredictable behavior is unacceptable. For example, the AUV may successfully localize and classify a target of interest, but spend all of its time in a small portion of its area of responsibility. The AUV may also overreact to anomalies such as biological returns without sufficient multi–ping integration. A way to mitigate this instability is to provide the AUV with a set of prescribed behaviors that are target–centric. With proper planning, these prescribed paths can be completed with the vehicle returning to the original trajectory. The discrete path adaptation strategy involves two steps. First, a target (or targets) must be detected based upon the initial thresholding, as in Sec. 4.3.2. These candidate targets are then tracked over several pings while the sonar platforms continue their pre–planned mission. During this stage, the probability of detection is refined through coherent or incoherent multi–ping integration. The second step is to detect the target with a higher degree of confidence with a higher threshold. A further requirement in this second step is that the target be localized relative to the sonar platforms so that the prescribed path can be implemented properly. In order to kick off the discrete path adaptation, a target, about which the prescribed motion will be performed, should be detected and localized with some degree of certainty. Then the vehicle deviates from its pre–planned path to perform the prescribed subtask, and resumes its mission.

#### Prescribed Behaviors for Monostatic Systems

One significant difference between mechanical mobile sonar platforms and biological systems is that of fine muscular control. In particular, the mechanical system typically steers as a rigid body and achieves deformable sensing through electronic steering at the receiver, while a biological system bends, nods and stretches as needed to evaluate the local environment. Nowhere is this limitation more clear than in the most directly comparable system to the biological sonars, namely the monostatic mobile sonar platform.

While a dolphin adapts its source as it approaches a target [5], both for target recognition purposes and for reverberation suppression, the mobile sonar platform is typically a fixed angle, fixed mode source that is carried aboard the platform, projecting over a wide angle with high power. The result is that the mechanical mobile monostatic system trajectory for optimum available signal is largely dictated by the source position. In order to maintain the source on the target, the vehicle is limited to a circular path around the target at a standoff range that corresponds to the elevation angle of the source. The amount of allowable deviation from the circle depends upon the beamwidth of the source.

### Prescribed Behaviors for Bistatic Systems

The only real limitation upon the prescribed behaviors of bistatic systems is for the source platform, as indicated in the previous section. The receivers are free to move anywhere around the target field without impacting the potential reception from the target. The difficulty is then precisely the opposite of the monostatic case. In the bistatic case, one must determine *apriori* what trajectory will yield the desired and/or required information from an infinity of choices. All this is to be predicted while not knowing anything about the target.

For generalized targets, there are only a few feasible approaches: the continuous heading control approach of Sec. 6.1.1, a circling behavior or a gridded search. The continuous cost function approach, as illustrated previously, can lead to wild behavior even in monostatic systems. In bistatic or multistatic systems, it is even more critical to reduce the degrees of freedom of the system, so the circling or gridded search behaviors are favored.

Another option for prescribing bistatic behaviors is to have a set of possible behaviors designed to exploit the signatures of known targets. In order for this system to work, however, there must be a means to pre–classify the target to select the appropriate path. The radiated field of the target must be known in detail and a strategy determined to ensure that the salient features are measured.

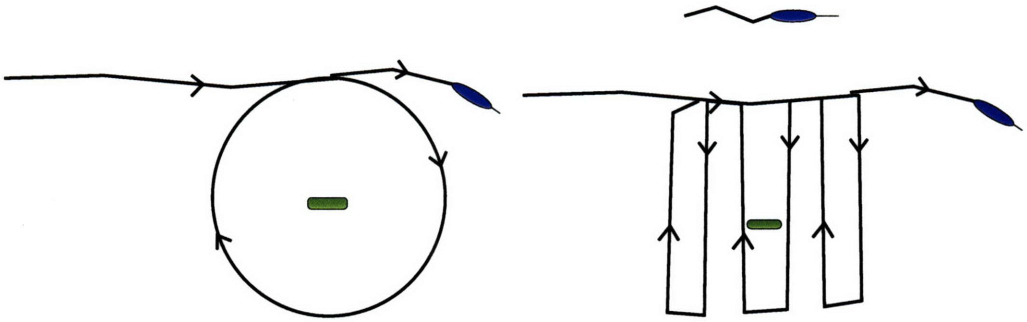

(a) Prescribed circle pattern. (b) Prescribed lawnmower.

Figure 6-2: Illustration of prescribed sonar–adaptive paths for the AUV. On the left, the standard monostatic circling behavior. At right, the receiver vehicle performs a lawnmower search pattern while the source vehicle remains steady.

#### Conclusions Regarding Discrete Path Adaptation

Discrete path adaptation addresses the major problem of continuous path adaptation; namely, that the end state of the vehicle does not necessarily lend itself to returning to the original mission. Therefore a set of preferred adaptive subtasks can be designed so that the detection and classification information can be obtained without jeopardizing the overall mission. Some example prescribed paths that meet these criteria are illustrated in Fig. 6-2. On the left, the circular pattern that is typical for monostatic sonar platforms is shown. On the right, a source vehicle maintains a steady trajectory while the receiver vehicle performs a lawnmower pattern over the detected target.

### 6.1.3 Continuous-Discrete Hybrid Approach

Both the continuous and the discrete path adaptation methods described above have a weakness. The weakness of the continuous adapation was that the path can lead anywhere, thus making it difficult to return to the pre–planned trajectory. The discrete path adaptation method has the weakness that it takes a lot of time about each potential target to perform a circuit or grid over the area. In this section, the use of the continuous path adaptation method to complement the discrete adaptation method is proposed to mitigate the major weakness of both.

In this hybrid approach, the vehicle is allowed to deviate from the path with the continuous heading control in a limited way. Essentially, the pre–planned mission should be devised in such a way that vehicle is provided a lane in which to travel rather than a straight–line path. This is similar to the way a person would search a nondescript area like a field. A lawnmower or other gridded search, while allowing some freedom to deviate from the path to investigate an interesting object. The major difference is that the AUV cannot easily stop or backtrack when needed.

Another way to allow limited continuous path adaptation is to have deformable search grids. If the vehicle deviates from its path in a way that causes it to miss an area of responsibility, then the rest of the later passes can be shifted to compensate.

Some examples of this hybrid sonar–adaptive approach are shown in Fig. 6-3. On the left, a simple pre–planned lawnmower search pattern by a single AUV is shown as a solid line. Upon detection of a target, the vehicle deviates from the pre–planned lawnmower pattern into a finer resolution pattern, as indicated by the dashed line. After completing a segment near the detected target, the pre–planned lawnmower pattern resumes. In the right figure, a cooperative searching pattern is shown. Each vehicle is given a path of responsibility to search for targets. In this example, the vehicles are assumed to have right–looking monostatic sonars. When the vehicle to the left detects a target at the limit of its field of view, it adjusts its path to more clearly interrogate the target. This vehicle also informs its neighbors, as illustrated by the vehicle to the right of the target, and they adjust their paths accordingly to maintain total area coverage.

## 6.2 Sonar–adaptive Detection and Imaging

Considering first the contents of Chapter 4, a degree of vehicle autonomy can be applied to enhance the detection and imaging performance during the course of a mission. In this implementation, the vehicle pre–detects a possible target and deviates from its nominal trajectory in order to confirm or reject the pre–detection. This second phase of detection can use any target detection or imaging method. In the

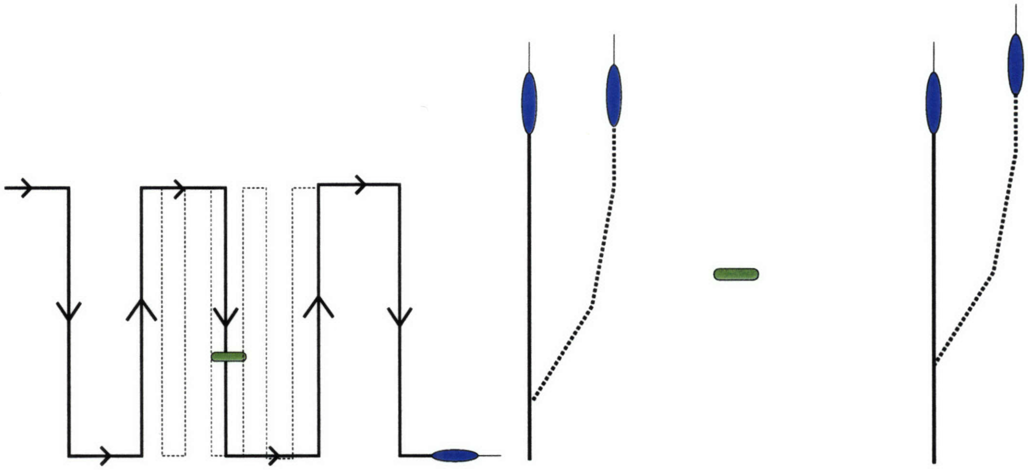

(a) Hybrid lawnmower pattern. (b) Prescribed lawnmower.

Figure 6-3: Illustration of hybrid sonar–adaptive paths for the AUV. On the left, a pre–planned lawnmower path (shown as solid line) is changed to a finer resolution search (dashed line) upon target detection. At right, a cooperative searching method is shown, in which the deviation made by the vehicle on the left is compensated by the vehicle on the right.

case of imaging, the pre–detection allows a cutout or thumbnail image of the target and its local surroundings, reducing the computation requirement and the amount of information that would be transmitted to the manned ship or disposal vehicle.

### 6.2.1 Maximizing SNR

In a continuously adaptive path, the ping–to–ping signal level is maximized for the signal of interest. In the case of detection, the signal power of the output of the matched filter is maximized. For classification the signal of interest may be the narrowband difference between the target return and the expected reverberation return, the image contrast or another measure.

An example of a sonar–adaptive mission for maximizing SNR is shown in Fig. 6-4. On the left panel, a simulation of a sonar–adaptive mission is shown. The red dashed line illustrated the planned trajectory of the vehicle, happening to pass near a target (located at the origin). The solid red line shows the actual path of the vehicle. As the vehicle enters the figure from the bottom left, some random heading errors

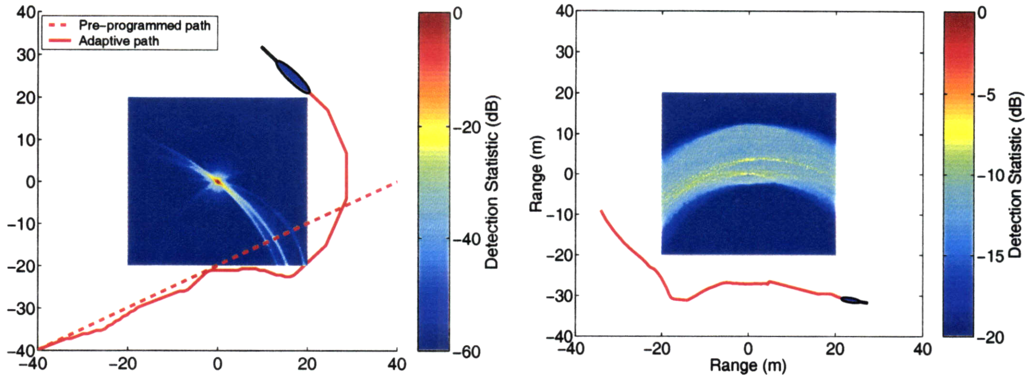

(a) Simulation.

(b) GOATS 2002.

Figure 6-4: Examples of adaptive behavior for detection of a 1–m diameter sphere.

cause it to slightly deviate from the planned path. Finally, upon detection of the target, the vehicle begins to judge whether to turn left or right based on whether the target return is strengthening or weakening. The result is that the vehicle begins to circle the target. The color map indicates the SNR in the vicinity of the target. As can be seen, the target is well detected and localized after the shown trajectory. On the right panel, a similar scenario is shown with real data from the GOATS 2002 experiment. In this case, the vehicle passes near a target and the SNR plot is formed. The trajectory cannot be changed after the fact, but if heading control were available the vehicle would circle the target in this case as well.

### 6.2.2 Prescribed Maneuvers

For discrete adaptation, a pre–planned adaptive behavior may be implemented to maximize the probability of seeing the target. As mentioned previously, a monostatic system is likely to circle the target. Two variations on this theme are circling at the design grazing angle of the source, or choosing the circle radius such that there is supercritical insonification of the seabed. A sonar platform with control over source grazing angle could accomplish both. Customized paths for different targets are possible, but are unlikely to yield significant new information. In Fig. 6-5, optimized monostatic vehicle trajectories are shown for 3 different targets. As can be seen, the

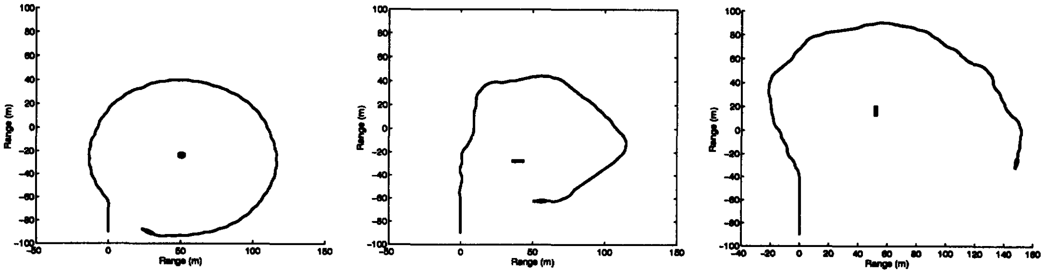

(a) Sphere.

(b) Cylinder at 0 degree aspect.

(c) Cylinder at 90 degree aspect.

Figure 6-5: Examples of adaptive behavior for monostatic detection.

deviation from the circular path is small.

For a bistatic system, the maintenance of the source on the target is desirable, along with a sampling of the scattered field measured at many azimuthal angles. Likely bistatic patterns for a general target would be to hold the source relatively still while the receiver performs a circular or lawnmower path, implementing one of the classification tasks outlined in Chapter 5. It is desirable to also interrogate the target from multiple vantage points, so the receiver motion may be repeated for several source angles to refine the classification result. Again, customization is possible but unlikely to provide a significant advantage worthy of the mission risk.

### 6.2.3 Post–detection Imaging

Generating imagery throughout the mission, such as with a side–scan sonar, is not generally the most efficient use of disk space. The image itself is a transformation from the measured time series into focused pixels. The first problem is that the pixels are selected over a grid and therefore many contain no useful information. Secondly, the image output loses some of the original character of the measured time signals, potentially losing valuable classification clues.

On the other hand, forsaking imagery in favor of a more abstract signal analysis is impractical for many missions. A fundamental reason is for verification of results. In the case of an object hunting mission, the vehicle may make a decision regarding

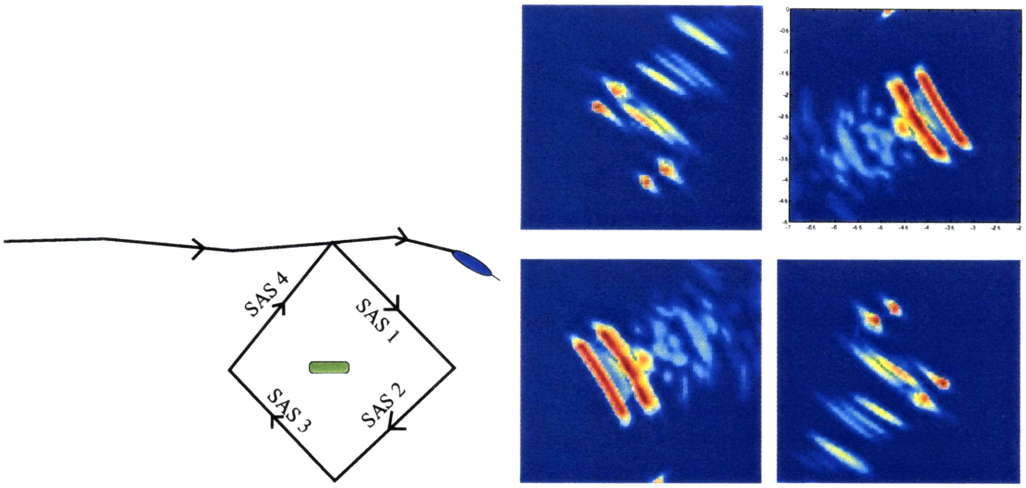

(a) Multi–aspect SAS pattern.

(b) Prescribed lawnmower.

Figure 6-6: Illustration of post–detection SAS processing by an AUV. Once the target is detected, the AUV performs a diamond–shaped path around the target, generating a SAS image from each side of the target.

detection and/or classification of a target based upon a statistical argument, but the human operators would most likely want to double–check this result. A sonar image is the most easily human–readable format to transmit basic information about a target. Therefore it may be advantageous for the mobile sonar platforms to make postcard images of the target of interest and transmit these relatively small images over the acoustic modem.

In Fig. 6-6, the post–detection SAS imagery is shown for a cylinder as the vehicle performs a diamond–shaped trajectory about the target. The diamond shape is a variation of the circular trajectory that is used to optimize the imaging performance. The micornavigation procedure works best on quasi–linear paths, so a new image is formed on each facet of the diamond. As can be seen in the imagery, significant information can be gleaned from the multiple vantage points, and the elastic returns can be seen despite the losses and smearing caused by the imaging process.

## 6.3 Sonar–adaptive Target Classification

The post–detection SAS imagery example described above could be considered a form of sonar–adaptive classification. The common thread among all post–detection processes is that the signal processing and/or the platform motions change based on the sonar data. In Fig. 6-7, an example of shape–based sonar–adaptive classification is shown. In this case, a team of three vehicles — a remote source and two receiver vehicles — traverse an area with a target in it. The receiver vehicles detect a target and then redirect their motions such that one is in front of the target and one behind (with respect to the source). The scattered field is then mapped as previously described. In situations for which platform motion compensation is unreliable this method can be used to estimate the vehicle shape.

All of the other target classification methods described in Chapter 5 can similarly be applied post–detection. Once a target is detected, the sonar platform can move nearer the target and focus its source to enhance its capability to detect the elastic responses. In general, other classification methods could be used once this sonar–adaptivity is employed, up to and including physically retrieving the target and carrying it back for inspection.

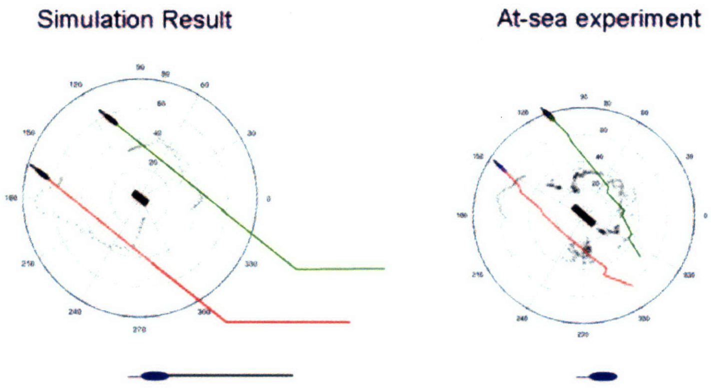

Figure 6-7: Sonar–adaptive mission for scattered field mapping.

# Chapter 7

# Conclusions and Future Work

In this thesis, the application of generally mobile platforms for acoustic classification of targets in shallow water was investigated. This represents a small step into a rapidly expanding world. Synthetic aperture imaging was always kept close at hand, both because it generates an aesthetic result and because it is the closest standardized signal processing algorithm to the mobile sonar system. The thesis began with characterizing the receptions to and from moving sources and receivers in a waveguide, with the targets assumed stationary. From there, the micronavigation technique was explored in the context of a bottom–penetrating sonar, or a lower frequency sonar in general. The result of this synthetic aperture limit was then studied in terms of SAS imagery and adaptive detection. From there, classification methods exploiting the spectral and shape character of targets were investigated. Finally, all of the lessons were combined to sonar–adaptive, active target hunting missions.

It is clear that the possibilities of generally moving sonar platforms are virtually boundless, and that this thesis addresses only a few minor issues in realizing these capabilities. This thesis has attempted to lead toward a system concept that has many decision branches, but where each decision is made as simple as possible.

Regarding the micronavigation work, it would be interesting to document the micronavigation performance versus seabed type, including ripple fields. It is a difficult process, however, as ground truth data are hard to come by, with the best opportunity coming at facilities containing a fixed rail. One discouraging note regarding the use of micronavigation is that it is likely a matter of time before inertial navigation or an improved undersea GPS reduce or eliminate the navigation problem. On the other hand, the inversion for seabed statistics by a roving sonar platform remains of interest for optimized detection and classification.

With regards to target detection, the compromise between single ping methods and multiple–ping methods causes a delicate balance in the processing. Vehicle–mounted sources, particularly narrow–beam sources, introduce inconsistent detections in multiple ping problems. The effects of vehicle dynamics on low–amplitude target detections is of interest. Efficient implementations of the track–before–detect (TBD) method have shown some promise in the AUV application [47]. The detection problem is the focus of a concurrent thesis based on the GOATS project, by Liu, so the reader is referred to that work for state of the art as well as future work.

Target classification is a highly subjective science. The methods shown in this thesis have been demonstrated both in simulation and experiment to effectively distinguish between known targets. It is recommended that future experiments include rocks if possible. The comparison between sonar–adaptive systems and biological systems leads to the obvious conclusion that perhaps the testing methodology should mirror this fact. In particular, blind tests, in which the vehicle must find and detect a target, while neither the vehicle nor the scientists interpreting the data know what or where the target is, would be an appropriate measure of success or failure.

True cooperative behavior is an ongoing topic of concern with respect to robotics, communications and signal processing. Within a limited mission, a planned cooperative effort between two or three AUVs is feasible.

Although enhancement of mission performance with sonar–adaptive motion is highlighted in this work, effective mission pre–planning is not a solved problem. In particular, searches over large, possibly range–dependent areas with teams of vehicles is an academic topic of interest. Anti–submarine searches over large areas have been well studied, but the use of AUVs adds some new facets to the problem. The potential use of dozens or hundreds of vehicles is one new facet that may be introduce interesting academic problems in multi–vehicle coordination as well as high–order search patterns. The capability of the AUVs to perform in very shallow water is also a new dimension to the problem, as the relative range–dependence in very shallow water can be dramatic.

Comprehensive zone–clearing missions would be an exciting demonstration of the sonar–adaptive missions.

Once each of these topics is addressed, experiments in cluttered fields and rocky embankments should be undertaken.

One legacy of this thesis is the MIT–MCM software package, which in reality is a bare–bones simulation of sonar–bearing AUV missions. There are two areas in which the simulation package could be dramatically improved. One of these is in the vehicle dynamics. The system can handle any vehicle dynamics, which is all that is required when replaying a prior experiment. However, there is no physical model restricting or guiding the motion for forward modeling. Hydrodynamic modeling, and even oceanographic modeling, could be applied to make the vehicle motion more realistic. A second means to improve the software package is the inclusion of elastic properties in the generalized target modeling. Related work is currently underway.

In many ways, fully automated detection and classification with sensor–adaptive motion parallels the behavior of biological beings, including humans. During the course of a long–term mission, the AUV may experience a wide range of operational conditions and target types. The reaction of a biological system is to learn from its experience and adapt its behavior to account for the acquired knowledge. This important aspect of mobile sonar target classification has not been addressed at all in this thesis. Rather, the lessons acquired from experiments and theory have been applied to the vehicle. The vehicle itself behaves as instructed, requiring human intervention to "learn." However, it would be an exaggeration to say that the current state of the art is prepared for long–term deployment of learning AUVs for automated target hunting. As the automated detection and classification methods are refined and applied robustly in limited deployments, the learning behavior will become a more practical concern.

# Appendix A

# GOATS'98 Experiment

During the bistatic imaging phase of the GOATS'98 experiment, a stationary source was used to insonify a patch on the seafloor that contained a known target field (Fig. A-1 ). The source used was a Topographic Parametric Sonar (TOPAS), which provides a highly directive beam on a given patch of the seafloor. A receiver array mounted on an autonomous underwater vehicle was used to sample the scattered field. The experiment was performed in an area close to shore with water depth 14 m and a sandy seabed. The sound velocity profile of the water column was a nearly uniform 1520 m/s.

## A.1 Source

The TOPAS sonar is a parametric source with a secondary frequency band of $2 - 16\ kHz$. The source level in the secondary frequency band is 201 $d\beta\ re\ \mu Pa$ @ $m$. This relatively low frequency band was chosen for improved seabed penetration, which in turn enhances the buried target detection capability. Although reduction in frequency obviously increases penetration at super-critical angles, the more interesting regime for rapid mapping is sub-critical insonification, which has been shown to provide significant evanescent wave field penetration in this frequency range [49] . The source transmitted a series of pings at a repetition period of 300 ms, with each ping being a broadband Ricker wavelet with center frequency 8 kHz.

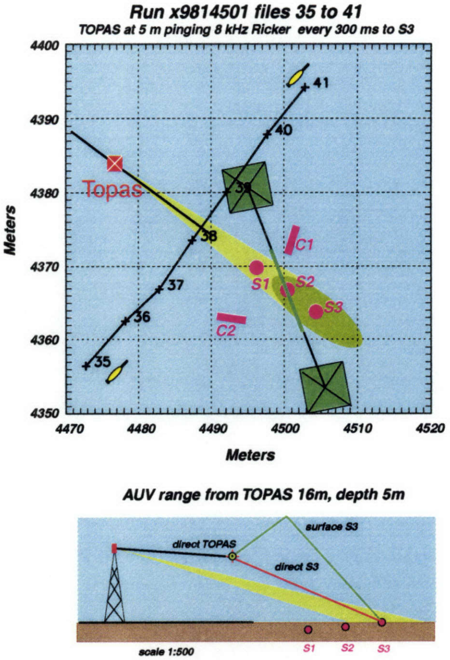

Figure A-1: GOATS'98 experimental geometry. A TOPAS parametric source is mounted on a tower which may be relocated along a horizontal rail to change angles of incidence on the seabed targets. A fixed 128-element horizontal hydrophone array was suspended 5 m over the targets for fixed bistatic measurements, while an AUV equipped with a receiving array and acquisition system was used as a moving receiver platform, creating synthetic apertures at different offsets from the target field.

As illustrated in Fig. A-1 , the parametric projector was mounted on a 10 m tall tower that could be re-positioned along a 20 m long rail on the seabed to allow target insonification at grazing angles below as well as above the critical angle of approximately 24° for penetration into the seabed [49] . During the experiment, both sub- and super-critical insonification angles were tested, but the current work concerns only sub-critical grazing angles.

## A.2 Target Field

Five targets of various geometry and burial conditions were deployed in a relatively smooth portion of sandy seabed, in an area 10 - 20 meters from the end of the TOPAS rail, as shown in Fig. A-2 . The targets included 3 air-filled spherical steel shells with

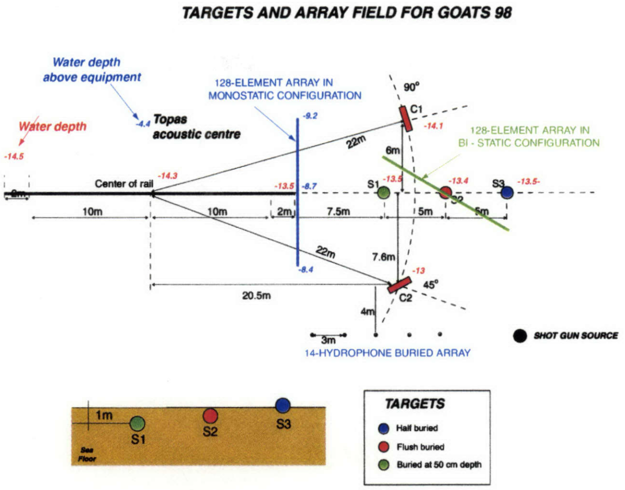

Figure A-2: Layout of the target field for GOATS'98. 5 targets were deployed, three empty spherical shells, half-buried (S3), flush-buried (S2) and completely buried (S1), respectively. In addition two water-filled cylindrical shells were flush buried, at aspects 90° (C1), and 45° (C2), respectively. The targets were deployed such that they could be insonified at angles above and below the critical grazing angle of approximately 24° [49] . Here the horizontal line array is shown in a quasi-monostatic configuration.

diameter 1 m and wall thickness 3 cm. One was half-buried (S3), one flush-buried (S2), and one was buried 0.9 m below the surface (S1) at its center. In addition 2 steel cylinders were flush-buried at aspect angles of $90^o$ (C1) and $45^o$ (C2) respectively. The 2 m long and 50 cm diameter cylinders were both water-filled and had a shell thickness of 6 mm.

## A.3 Autonomous Underwater Vehicle

The AUV used as a receiver platform was an Odyssey II AUV equipped with a linear acoustic array in a 'swordfish' configuration, as can be seen in Fig. A-3 . The array consisted of 8 omnidirectional hydrophones linearly spaced with $\Delta x = 0.1\ m$, which corresponds to the $\lambda/2$ sampling at 7.5 kHz. The apparent undersampling is mitigated by the fact that the array is not required to steer over the full 180 degree half-space.

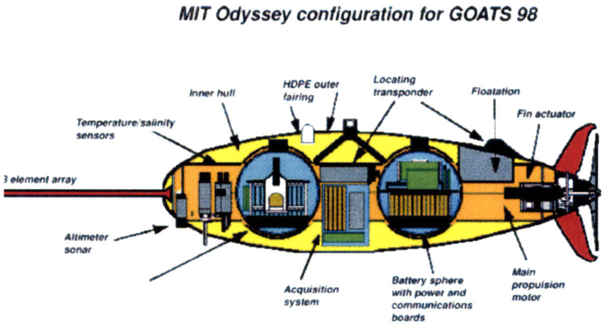

Figure A-3: Odyssey II AUV equipped with an 8-element array in a 'swordfish' configuration. The element spacing is 10 cm. A dedicated acquisition system is mounted in the center bay of the vehicle, with data stored on disk for post-processing.

The AUV was programmed to perform a 'lawn-mower' survey over the target field, with the actual AUV track indicated by the the lines crossing the target field in Fig. A-4 . The AUV was navigated using a 8-12 kHz long baseline (LBL) acoustic navigation system to travel between way-points alternating between the two sides of the target field. It used the LBL to update its position and adjust the trajectory every 10 seconds. The numbers on the AUV track indicate the vehicle position when the LBL navigation cycle was initiated. The navigation cycle was interleaved with the TOPAS transmissions to avoid mutual interference. To synchronize the transmissions with the navigation cycle, the LBL interrogation pulse was detected by the TOPAS receiver electronics, triggering a 7 second ping sequence after a 3 second delay. Thus, only 7 seconds of data were available for SAS processing in each navigation cycle, corresponding to a 7 m synthetic aperture.

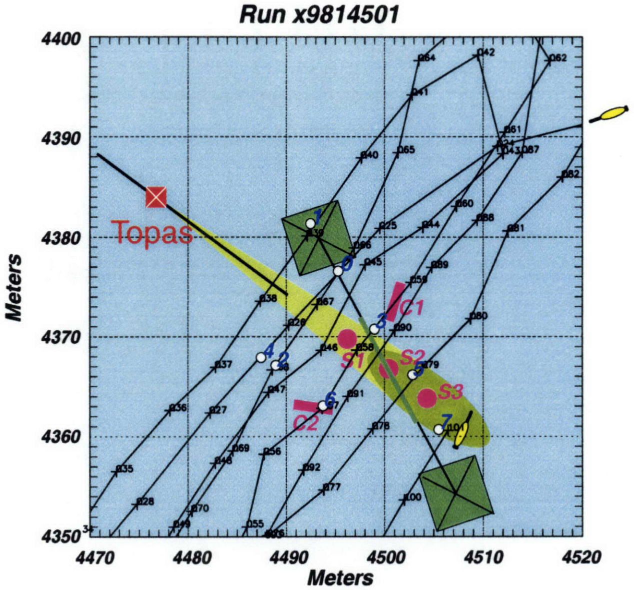

Figure A-4: AUV track over the target field.

# Appendix B

# User's Manual for MIT–MCM Version 1.0

## B.1 Acoustic Simulation

The bulk of the acoustic simulations included in this thesis were carried out using a modified version of SEALAB–MCM by VASA Associates, Inc. While the standard version provided accurate bi-static measurements using ray propagation theory and high frequency target models, modifications to the code were necessary to improve the speed of computation, as well as the following additional features:

1. expanding the available variety of targets
2. the capability to dynamically plan the vehicle path in "real-time" mode
3. provide for reflections from the seabed and sea surface
4. the capability to run missions with multiple sources, receivers and targets

### B.1.1 Simulation Philosophy

The MIT–MCM package is designed to resemble the experimental process as closely as possible, and to include as much of the relevant physics as possible. In order to achieve this level of realism, the missions are first organized as experimental missions.

This organization is implemented by creating a directory in which to hold all the data files, and maintaining data logs that record the position of the sources and receivers at each ping.

The represented physical phenomena include reverberation realizations, multipath, propagation modeling and target scattering. The representation of each of these physical processes is described in the following section.

### B.1.2 Propagation Models

Propagation modeling is used to represent the travel of the acoustic signals from source to the target (or receiver) and the target to the receiver. Several types of models are available, although all of the simulation effort for this thesis were performed using a simple ray model.

#### Ray Model

The basic propagation model utilized in most of the simulations is a ray path model, implemented in such a way that it includes all refractive paths that contain at most one reflection. With this model, there are three possible paths from source to target: direct, surface-reflected and seabed-reflected. The same three paths are possible from target to receiver, resulting in 9 round-trip propagation paths for each scatterer. The paths to a typical target are illustrated in Fig. B-1.

#### Normal Modes Model

For longer–range simulations, a normal mode propagation model could be used. At this time, normal modes is not included.

#### Wavenumber Integration

Full wave–theoretic solutions are possible with OASES wavenumber integration solutions, but again this is not implemented to date.

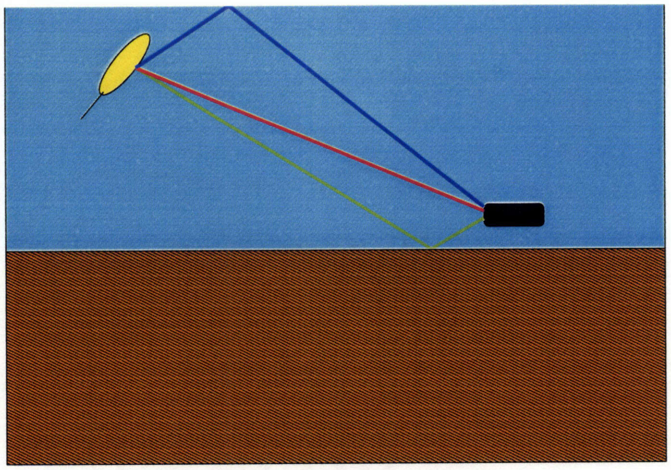

Figure B-1: Modeled propagation paths between source and target. Red is the direct path, green is the bottom-reflected path, and blue is the surface-reflected path.

### B.1.3 Target Scattering Models

#### Sphere and Cylinder Models

Exact analytic solutions exist for scattering from spherical or cylindrical targets. The available boundary conditions are rigid, pressure–release, void shell or fluid–filled shell. The sphere solution is valid for all frequencies, while the cylindrical shell model is limited to relatively high frequency. Both solutions are limited by the memory size at the high frequency end.

#### Virtual Source Models

The method of virtual sources provides the capability to include all geometric effects of scattering, including multiple scattering, from arbitrarily shaped targets. The limitation to this method is that it does not inherently include the elastic response of the target. Rigid and pressure release boundary conditions are implemented in MIT–MCM. Impedance boundary conditions are easily implementable but have not been included to date. An extension is needed to mesh stiffness matrices from finite element solvers to truly claim a capability of arbitrarily shaped, arbitrarily constructed target models.

### B.1.4 Seabed Scattering Models

The seabed scattering is based on the paper by D.C. Ricks [66]. The seabed is divided into small sections, and random realizations are generated by applying a Goff–Jordan power spectrum. The random seed is maintained so that the realizations are consistent from ping to ping.

### B.1.5 Handling Adaptive Missions

Adaptive missions are generally handled through Matlab or shell scripting. Set the number of pings in the *.msrc* file to one, and execute the mission. Once the output files are written, the data can be processed with whatever processing code is under test, and the next desired position computed. The input files for the sources and receivers can then be modified, and the simulation can then be executed for the following ping appended to the current mission.

### B.1.6 Mission Visualization

Included in MIT–MCM is a visualization tool using Plotmtv. The purpose of this visualization is to see the state of the vehicles and targets at each ping. However, the Plotmtv drawing freezes execution until the user closes the figure, so it is more commonly useful just to check the setup positions of the targets and vehicles. An example of the Plotmtv visualization is shown in Fig. B-2. In this example, there is a source vehicle, shown in green, that also has a receiver. There are two other receiver vehicles, shown in orange. Five targets of various shapes and sizes are shown in red, distributed throughout the target field. The blue border shows the computation range of the reverberation. The purple box shows the sonar footprint of the source, and the green line from the source ends at the intersection of the beam axis with the seabed.

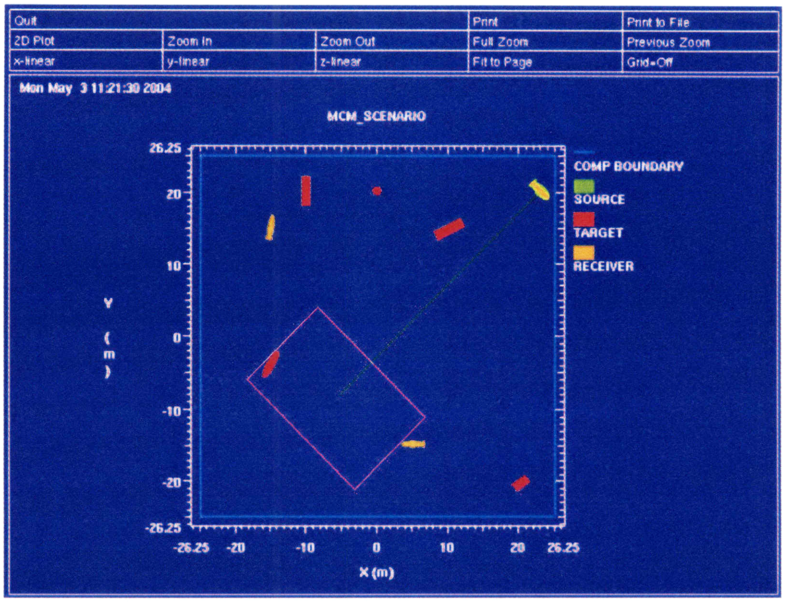

Figure B-2: Visualization of the MIT–MCM mission at a given ping. In this scenario there is one source and three receivers, with five targets of various shapes in the target field.

## B.2 Usage

First, the environment variable MASTER must be defined, pointing to the directory and root of the input file names. For example, for input files named *Test_MCM.** located in the directory */home/mit_mcm*, the environmental variable would be set with the following command:

```
setenv MASTER /home/mit_mcm/Test_MCM
```

Then, the executable *mcm_mission* is called from the command line with a choice of options. Use *mcm_mission --help* for current descriptions of command line options. At the time of this printing, the usage is as follows:

```
Usage:  mcm_mission -[sprila] --debug --help
-s to view scenario on each ping.
-i<#> to assign a mission number.
-p to view each data series as it is computed.
-r to include the reverberation computation.
```

```
-l<name> to use trajectory from log files of base <name>
-a<#> to append to the previous mission as ping number <#>
--debug to print debugger information.
--help to view this help information.
```

### B.2.1 Replay Mode

The *-l* option is effectively a replay mode. Using this option, the vehicle positions at each ping are given with an existing set of log files. Note that the *-l* option requires a log file base. For a given base name *fileroot*, the log files will be named

```
fileroot_s%.3d_r%.3d.log
```

where the numbers represented by %.3d are left zero–padded, three–digits source and receiver identification numbers. For example, the second source and third receiver will share a log file named

```
fileroot_s002_r003.log
```

Inside this file are the positions of the specified source and the specified receiver at the time of each ping made by the specified source. The log files are ASCII format, and each line contains, in the following order:

1. the ping number
2. the mission time (in sec)
3. the x position of the source (in m)
4. the y position of the source (in m)
5. the z position of the source (in m)
6. the heading of the source (in deg)
7. the pitch of the source (in deg)

8. the roll of the source (in deg)
9. the yaw of the source (in deg)
10. the x position of the receiver (in m)
11. the y position of the receiver (in m)
12. the z position of the receiver (in m)
13. the heading of the receiver (in deg)
14. the pitch of the receiver (in deg)
15. the roll of the receiver (in deg)
16. the yaw of the receiver (in deg)

### B.2.2 Sonar–Adaptive Missions

The *-a* option is intended to enable sonar–adaptive missions. In this case, the number of pings by the source is set to one, and *mcm_mission* is called for each ping. When the code exits, the data are processed by an external program, and the source and receiver states are updated in the input files. The executable *mcm_mission* is then called again with the *-a* option. The external program maintains the ping number and appends the current ping to the existing mission. The data files and the log files are maintained exactly as in the pre–planned mission, allowing the resulting mission to be replayed or reviewed in the same way.

During development, it is recommended to use Matlab for sonar–adaptive missions. When calling *mcm_mission* from Matlab, the exclamation point (!) is needed to revert to a system shell. The MASTER variable must be set each time that *mcm_mission* is called. In Matlab, the calls of the file might look like the following:

```
cmd=sprintf(...
'!setenv MASTER %s/SAS_Test;mcm_mission -i%d -a%d --debug',...
master_directory,...
```

```
mission_id, ...
current_ping);
eval(cmd);
```

## B.3 Input Files

The environmental, source, receiver and target information is all maintained in ASCII input files. These files are purposely intended to be readable by a casual user to allow common–sense checks of the input parameters. It also allows easy access to the files so that they can be edited automatically in sonar–adaptive simulations.

In order to create input files, a set of interactive Perl programs are included with MIT–MCM. These files are named *make_menv_file*, *make_msrc_file*, *make_mrcv_file* and *make_mtrg_file*. The central four letters indicate the relevant file type – environment, source, receiver and target, respectively.

### B.3.1 Environment File

The environment file contains all of the relevant parameters of the water column. An example environment file is shown below:

```
1    !Number of water column layers
1    !Number of sediment layers
2    !Upper half space type (1=vacuum, 2=fluid)
1500.0    !UHS cp (m/s)
0.1    !UHS alphap (m/s)
1.0    !UHS rho (m/s)
30.0    !Depth of water layer #1 (m)
1    !Isovelocity? (1=y,0=n)
1500.0    !Cp of water layer #1 (m/s)
30.0    !Depth of sed. layer #1 (m)
1    !Elastic? (1=y,0=n)
1    !Isovelocity? (1=y,0=n)
1800.0    !Cp of sed. layer #1 (m/s)
0.3    !Alphap of sed. layer #1 (dB/m)
600.0    !Cs of sed. layer #1 (m/s)
0.1    !Alphas of sed. layer #1 (dB/m)
1.8    !Density of sed. layer #1 (g/cm^3)
0.01    !rms height of sed. layer #1 (m)
0.3    !Correlation length of sed. layer #1 (m)
30.0    !Max. X range from origin (m)
30.0    !Max. Y range from origin (m)
*****End of sector.*****
*****End of file.*****
```

Note that there is only one sector. The current version of MIT–MCM does not allow range–dependent propagation. Therefore, as will be seen, the input file deviates slightly from the format of the other input files in that it does not ask the number of sectors in the first line. The comments in each line are intended to be detailed enough to provide a clear idea of each entry. In the example file, there is only one layer in the water column and one layer in the seabed.

### B.3.2 Source File

All of the sources in the mission, which can be an arbitrary number, are included in the source input file, denoted by an extension of *.msrc*. An example of a source input file is shown below:

```
1      !Number of sources
0.000000 !x position (m)
-10.000000 !y_position
29.0    !z position (m)
90.000000 !heading (deg)
L  !source direction
1.0    !Velocity (m/s)
5000.0    !Center frequency (Hz)
3000.0    !Bandwidth (Hz)
0.0003    !Pulse width (sec)
2    !Pulse shape
0.25    !Ping rate (sec)
1    !Number of pings
0.0    !Vertical steering angle (deg)
180.0    !Vertical beamwidth (deg)
0.0    !Horizontal steering angle (deg)
360.0    !Horizontal beamwidth (deg)
1    !shading type
180.0  !source level (dB)
*****End of source.*****
*****End of file.*****
```

This file contains a single source that points to the left of the vehicle. The source is omnidirectional, centered at 5 kHz and emits a Gaussian pulse.

### B.3.3 Receiver File

All of the receivers are included in the receiver input file, denoted by the file extension *.mrcv*. An example receiver input file is shown below:

```
1       !Number of receivers
0.0     !x position (m)
-10.0     !y position (m)
29.0     !z position (m)
90.0     !Heading (deg)
1.0     !Velocity (m/s)
0.0     !x offset (m)
0.025     !x spacing (m)
1     !Number of sensors in x direction
0.0     !z offset (m)
1.0     !z spacing (m)
1     !Number of sensors in z direction
2048    !NData
80000     !Sampling frequency (Hz)
*****End of receiver.*****
*****End of file.*****
```

This file contains only a single receiver with one hydrophone. It samples at 80 kHz for 2048 data points. The initial time of the reception is determined by the direct path from source to receiver.

### B.3.4 Target File

All of the information about the targets in the target field are included in the target input file, denoted by the extension *.mtrg*. An example target input file is shown below:

```
3       !Number of targets
0.0     !x position (m)
0.0     !y position (m)
29.0     !z position (m)
2   !target type
0.0     !cyl. aspect (deg)
2.0     !cyl. length (m)
0.5     !cyl. radius (m)
0.1     !cyl. shell thickness (m)
5200.0    !compressional wavespeed (m/s)
7.3     !cyl. density (g/cm^3)
3000.0    !cyl. shear speed (m/s)
0.3     !cyl. Poisson ratio
*****End of target.*****
-3.0     !x position (m)
2.0     !y position (m)
29.0     !z position (m)
1   !target type
1    !boundary condition type
0.5     !sphere radius (m)
*****End of target.*****
5.0     !x position (m)
0.0     !y position (m)
29.0     !z position (m)
5   !target type
```

```
1   !boundary condition type
20   !number of virtual sources
90.0  !aspect angle (deg)
90.0  !pitch angle (deg)
0.5   !radius (m)
4  !aspect ratio
*****End of target.*****
*****End of file.*****
```

This target input file includes three targets: a cylinder, a sphere and a spheroid. The cylinder is a Rumerman–type cylinder, and the sphere uses the analytic solution for its scattering. The spheroid is represented with virtual sources.

## B.4 Output Files

All of the output files of a given MIT–MCM mission are included inside of the mission directory *Mission_#*, where the number is either assigned by the user using the *-i* option, or assigned by the program itself, as the process ID of the run. Inside of this directory are the data files, distinguishable by their names. If the input files are named *fileroot.** then the signals from source to target to receiver are of the format:

`fileroot_s%.3d_r%.3d_t%.3d_p%.3d.mat`

where the *%.3d* terms are the 3–digit source number, receiver number, target number and ping number, respectively. For example, the first source, second receiver, third target and 123rd ping would be indicated by:

`fileroot_s001_r002_t003_p123.mat`

Direct signals from source to receiver are saved in files named:

`fileroot_s%.3d_r%.3d_p%.3d.mat`

Reverberation signals are saved in files named:

```
fileroot_rvb_s%.3d_r%.3d_p%.3d.mat
```

In addition to the data files, a record is created for the deconstruction of the mission. The positions of all sources and receivers at each ping are written in pairwise position logs. These files are given the extension *.log.* The file names are of the form:

```
fileroot_%d_s%.3d_r%.3d.log
```

where the first number (indicated by %d) is the mission ID number. The other numbers are left zero–padded, three–digit source and receiver numbers.

Finally, the original input files are copied into the mission directory. These are in the state that the mission was initiated. Any changes to the input files during the course of the mission, notably the positions of the vehicles, are not reflected in these files.

*Note*: A desirable extension would be a text mission log, commenting each time a parameter is changed. This would allow more general dynamics of the sonar platforms, including source pulse changes, steering of the source, change of speeds, etc.

## B.5 Addendum

The simulation suite was developed with a view toward combining high fidelity acoustic models with real–time AUV operating system software in a two-step process. The reason for making a two–step process is because the acoustic simulation of a complex reverberant field cannot be implemented in real–time, whereas the adaptive signal processing algorithms must be tested in real–time prior to implementation. In the acoustic simulation phase, the target field is created with buried or proud cylinders and spheres, along with a rough seabed, prior to execution. The simulation is performed using a high–fidelity acoustic model, to include complex acoustical processes such as evanescent waves, rough surface scattering, volume inhomogeneities, elastic seabeds and resonant targets. The source and receiver vehicle initial positions and velocities are given, and the field is simulated at the receiver. The system waits for the acoustic simulation, and then the adaptive signal processing algorithm is executed and the source and receiver are moved according to the recommendation of the particular algorithm. The whole process is repeated for a complete mission. Given a successful algorithm the vehicle will travel along its pre–programmed path until detecting the target, and then deviate from that path in order to optimize the detection or classification statistic as appropriate.

The second stage of the simulation suite is to test the algorithm inside a real-time system. In this stage, the approximate source and receiver paths are known from the first stage, so the data files generated in the first stage can be streamed into the system as “received” data, without further computation. The algorithms are then tested in real-time inside the actual vehicle mission oriented operating system (MOOS) [53] , in which all of the other vehicle processes are running, including navigation and dynamic control systems. This stage of simulation can also be used with experimental data, although such a procedure is limited to real–time detection, since the AUV trajectory obviously cannot be altered after the fact.

# Bibliography

[1] D.A. Abraham and A.P. Lyons. Novel physical interpretations of K–distributed reverberation. *IEEE Journal of Oceanic Engineering*, 27(4):800–13, 2002.

[2] M. Abramowitz and I.A. Stegun. *Handbook of Mathematical Functions.* Dover Publications, Inc., 9th edition, 1972.

[3] A.E. Adams, M.A. Lawlor, V.S. Riyait, O.R. Hinton, and B.S. Sharif. Real–time synthetic aperture processing system. *IEE Proceedings on Radar, Sonar and Navigation*, 143(3):169–76, 1996.

[4] P.W. Ankerman and R.A. Rubega. Bistatic scattering from totally reflecting flat plates. *Journal of the Acoustical Society of America*, 32(4):478–81, 1960.

[5] W.L. Au. Dolphin sonar detection and discrimination capabilities. *Journal of the Acoustical Society of America*, 115:2614, 2004.

[6] A.B. Baggeroer. *Applications of digital signal processing*, pages 331–437. Prentice Hall, 1978.

[7] A.B. Baggeroer, W.A. Kuperman, and H. Schmidt. Matched field processing: source localization in correlated noise as an optimum parameter estimation problem. *Journal of the Acoustical Society of America*, 83(2), February 1988.

[8] F.G. Bass and I.M. Fuks. *Wave scattering from randomly rough surfaces.* Pergamon Press, Oxford, 1979.

[9] D.R. Begault. *3-D sound for virtual reality and multimedia.* MIT Press, 1994.

[10] A. Bellettini, S. Fioravanti, and M. Pinto. Preliminary experimental investigation of synthetic aperture sonar micronavigation. Technical report, NATO SACLANT Undersea Research Centre, La Spezia, Italy, 1999.

[11] M. Benjamin, T. Viana, K. Corbett, and A. Silva. Satisfying multiple rated–contraints in a knowledge based decision aid. In *Proceedings of the Ninth IEEE Conference on Artificial Intelligence for Applications*, volume 2, pages 277–83, Orlando, FL, 1993. IEEE.

[12] M.R. Benjamin. Multi–objective autonomous vehicle navigation in the presence of cooperative and adversarial moving contacts. In *MTS/IEEE Oceans'02*, volume 3, pages 1878–85. IEEE, 2002.

[13] J. Blauert. *Spatial hearing.* MIT Press, 1983.

[14] M. Born and E. Wolf. *Principles of optics: Electromagnetic theory of propagation, interference and diffraction of light.* Pergamon Press, Oxford, 1975.

[15] L.M. Brekhovskikh and Y.P. Lysanov. *Fundamentals of ocean acoustics.* AIP Press, New York, 1982.

[16] V. Clark. Projecting decisive joint capabilities. *Sea Power*, Oct 2002.

[17] J.C. Curlander and R.N. McDonough. *Synthetic aperture radar: Systems and signal processing.* Wiley, 1991.

[18] P.N. Denbigh. A design study for a correlation log to measure speed at sea. *J. Navigation*, 35:160–184, 1982.

[19] Y. Doisy. General motion estimation from correlation sonar. *IEEE Journal of Oceanic Engineering*, 23(2):127–140, April 1998.

[20] D. Doolittle. The payoff is in the payload: Using AUVs in scientific research. *Underwater Magazine*, 11(2), 2003.

[21] G.L. D'Spain, E. Terrill, C.D. Chadwell, J.A. Smith, and R. Zimmerman. Passive acoustic localization with an AUV-mounted hydrophone array. *Journal of the Acoustical Society of America*, 115(5):2615, 2004.

[22] J.R. Edwards, H. Schmidt, and K. LePage. Bistatic synthetic aperture target detection and imaging with an AUV. *IEEE Journal of Oceanic Engineering*, 26(4):690–699, October 2001.

[23] J.C. Evans, J.S. Smith, P. Martin, and Y.S. Wong. Beach and near-shore crawling UUV for oceanographic measurements. *MTS/IEEE Oceans '99: Riding the Crest into the 21st Century*, 3:1300–6, September 1999.

[24] J.A. Fawcett and B.H. Maranda. A hybrid target motion analysis/matched–field processing localization method. *Journal of the Acoustical Society of America*, 94(3):1363–71, 1993.

[25] K. Gade and B. Jalving. An aided navigation post–processing filter for detailed seabed mapping UUVs. In *Proceedings of the 1998 Workshop on Autonomous Underwater Vehicles*, pages 19–25, 1998.

[26] T. Gaiffe. Ixsea's AUV navigation system. *Underwater Magazine*, 10(1), 2002.

[27] G.C. Gaunard and H.Überall. RST analysis of monostatic and bistatic echoes from an elastic sphere. *Journal of the Acoustical Society of America*, 73(1):1–12, 1983.

[28] P.T. Gough and D.W. Hawkins. A short history of synthetic aperture sonar. *International Geoscience and Remote Sensing Symposium IGARSS'98*, 2:618–20, 1998.

[29] D. Gouré. Sea–mine threat can no longer be ignored. *National Defense Magazine*, Aug 2002.

[30] A.N. Guthrie, R.M. Fitzgerald, D.A. Nutile, and J.D. Schaffer. Long–range low–frequency CW propagation in the deep ocean: Antigua–Newfoundland. *Journal of the Acoustical Society of America*, 56(1):58–69, 1974.

[31] P.E. Hagen. AUV/UUV mission planning and real time control with the HUGIN operator system. *MTS/IEEE Oceans 2001*, 1:468–73, November 2001.

[32] K.E. Hawker. A normal mode theory of acoustic Doppler effects in the oceanic waveguide. *Journal of the Acoustical Society of America*, 65(3):675–81, 1979.

[33] M.P. Hayes and P.T. Gough. Broad-band synthetic aperture sonar. *IEEE Journal of Oceanic Engineering*, 17(1):80–94, 1992.

[34] E.v. Hinuber. New approaches in high–performace navigation solutions for AUVs and ROVs. *iMAR company website - http://www.imar-navigation.de/download/underwater_imar.pdf*, 2003.

[35] P. Hursky, M.B. Porter, B.D. Cornuelle, W.S. Hodgkiss, and W.A. Kuperman. Adjoint modeling for acoustic inversion. *Journal of the Acoustical Society of America*, 115:2824–33, 2004.

[36] F. Ingenito. Scattering from an object in a stratified medium. *Journal of the Acoustical Society of America*, 82(6):2051–9, 1987.

[37] D.R. Jackson and K.B. Briggs. High-frequency bottom backscattering: Roughness versus sediment volume scattering. *Journal of the Acoustical Society of America*, 92(2):962–977, August 1992.

[38] R.L. Eigel Jr. and A.J. Terzouli Jr. Bistatic scattering characterization of a complex object. *IEEE International Symposium of the Antennas and Propagation Society*, 3:1784–7, 1999.

[39] W.R. Scott Jr., J.S. Martin, and G.D. Larson. Investigation of a technique that uses elastic waves to detect buried land mines. In *Proceedings of the IEEE 2000 International Geoscience and Remote Sensing Symposium*, volume 4, pages 1640–2, Piscataway, NJ, 2000.

[40] S.M. Kay. *Fundamentals of statistical signal processing volume II: Detection theory*. Prentice Hall, New Jersey, 1998.

[41] J.J. Kovaly. Radar techniques for planetary mapping with orbiting vehicle. *Annals of the New York Academy of Sciences*, 187:154–76, 1972.

[42] Y. Lai and N.C. Makris. Spectral and modal formulations for the doppler–shifted field scattered by an object moving in a stratified medium. *Journal of the Acoustical Society of America*, 113(1):223–44, 2003.

[43] S.G. Lemon. Towed–array history 1917–2003. *IEEE Journal of Oceanic Engineering*, 29(2):365–73, 2004.

[44] J.J. Leonard, A.A. Bennett, C.M. Smith, and H.J.S. Feder. Autonomous underwater vehicle navigation. *MIT Marine Robotics Laboratory Technical Memorandum 98-1*, 1998.

[45] A. Leonessa, J. Mandello, Y. Morel, and M. Vidal. Design of a small, multipurpose, autonomous surface vessel. *MTS/IEEE Oceans 2003*, 1:544–50, September 2003.

[46] K.D. LePage and H. Schmidt. Spectral integral representations of monostatic back scattering from three–dimensional distributions of sediment volume inhomogeneities. *J. Acoust. Soc. Am.*, 113(1), January 2003.

[47] T.C. Liu and H. Schmidt. Concurrent detection and localization of buried targets using track-before-detect processing. *J. Acoust. Soc. Am.*, 2002.

[48] E.F. MacKrell. Network–centric intelligence works. *Sea Power*, Jul 2003.

[49] A. Maguer, W.L.J. Fox, H. Schmidt, E. Pouliquen, and E. Bovio. Mechanisms for subcritical penetration into a sandy bottom: Experimental and modeling results. *Journal of the Acoustical Society of America*, 107(3), March 2000.

[50] A. Matos, N. Cruz, A. Martins, and F.L. Pereira. Development and implementation of a low–cost LBL navigation system for an AUV. *MTS/IEEE OCEANS '99. Riding the Crest into the 21st Century*, 2:774–9, 1999.

[51] T.R. Michel and K.A. O'Donnell. Angular correlation functions of amplitudes scattered from a one-dimensional, perfectly conducting rough surface. *J. Opt. Soc. Amer.*, 9(8):1374–84, 1992.

[52] E. Millett. AUV lab history. *MIT AUV laboratory website - http://auvlab.mit.edu/history.html*, 2004.

[53] P. Newman. MOOS home page oe.mit.edu/p̃newman/moos.

[54] P.M. Newman and J.J. Leonard. Pure range–only subsea SLAM. In *Proceedings of the 2003 IEEE International Conference on Robotics and Automation*, volume 2, pages 1921–6, Taipei, Taiwan, 2003. IEEE.

[55] M. Tran Van Nhieu and F. Ywanne. Sound scattering by slender bodies of arbitrary shape. *Journal of the Acoustical Society of America*, 95(4):1726–33, 1994.

[56] C.L. Nikias and A.P. Petropulu. *Higher–Order Spectra Analysis*. Signal Processing Series. Prentice Hall, 1993.

[57] I.R. Nourbakhsh. The failures of a self–reliant tour robot with no planner. *SAGE project: http://www-2.cs.cmu.edu/ illah/SAGE/sagefailures.pdf*, 1998.

[58] V.V. Ol'Shevskii. *Characteristics of Sea Reverberation*. Consultants Bureau, New York, 1967.

[59] K. O'Neill. Broadband bistatic coherent and incoherent detection of buried objects beneath randomly rough surfaces. *IEEE Transactions on Geoscience and Remote Sensing*, 38(2):891–8, March 2000.

[60] M. Pinto, S. Fioravanti, and E. Bovio. Accuracy of synthetic aperture sonar micronavigation using a displaced phase center antenna. Technical report, NATO SACLANT Undersea Research Centre, La Spezia, Italy, 1998.

[61] M.A. Pinto, A. Bellettini, S. Fioravanti, S. Chapman, D.R. Bugler, Y. Perrot, and A. Hetet. Experimental investigations into high resolution sonar systems.

In *MTS/IEEE Oceans'99 Conference Proceedings: Riding the Crest into the 21st Century*, volume 2, pages 916–22, Piscataway, NJ, 1999.

[62] J.E. Piper, K.W. Commander, E.I. Thorsos, and K.L. Williams. Detection of buried objects using a synthetic aperture sonar. *IEEE Journal of Oceanic Engineering*, 27(3):495–504, 2002.

[63] C. Plante, T. Frieden, and N. Peckenham. Yemeni president calls USS Cole attack 'very well planned'. *CNN website: http://www.cnn.com/2000/US/10/18/cole.investigation/index.html*, October 2004.

[64] S. Proshkin. Russian sea mines. *Military Parade JSC*, 1998.

[65] A. Quazi. An overview on the time delay estimate in active and passive systems for target localization. *IEEE Transactions on Acoustics, Speech and Signal Processing*, 29(3):527–533, June 1981.

[66] D.C. Ricks. Pseudorandom realization of transient acoustic waves scattered from randomly rough patches. *IEEE Journal of Oceanic Engineering*, 22(4):332–341, April 1997.

[67] K.D. Rolt and H. Schmidt. Azimuthal ambiguities in synthetic aperture sonar and synthetic aperture radar imagery. *IEEE Journal of Oceanic Engineering*, 17(1):73–9, 1992.

[68] P.J. Ryan. Mine countermeasures a success. *Sea Power*, May 2003.

[69] K. Scarbrough, R. Tremblay, and G. Carter. Performance predictions for coherent and incoherent processing techniques of time delay estimation. *IEEE Transactions on Acoustics, Speech, and Signal Processing*, 31(5):1191–1196, 1983.

[70] H. Schmidt and W.A. Kuperman. Spectral and modal representations of the doppler–shifted field in ocean waveguides. *Journal of the Acoustical Society of America*, 96(1):386–95, 1994.

[71] H. Schmidt and J. Lee. Physics of 3-D scattering from rippled seabeds and buried targets in shallow water. *Journal of the Acoustical Society of America*, 105(3):1605–1617, 1999.

[72] R. Singer and R. Sea. New results in optimizing surveillance system tracking and data correlation performance in dense multitarget environments. *IEEE Transactions on Automatic Control*, 18(6):571–582, 1973.

[73] T.K. Stanton and C.S. Clay. Sonar echo statistics as a remote–sensing tool: Volume and seafloor. *IEEE Journal of Oceanic Engineering*, 11(1):79–83, 1986.

[74] P. Stoica and R. Moses. *Introduction to Spectral Analysis.* Prentice Hall, 1997.

[75] R. Stolt. Migration by fourier transform. *Geophysics*, 43(1), 1978.

[76] D. Tang and G.V. Frisk. Spatial correlation of acoustic waves scattered from a random ocean bottom. *Journal of the Acoustical Society of America*, 97(5):2783–2803, May 1995.

[77] Dajun Tang. *Acoustic wave scattering from a random ocean bottom.* PhD thesis, MIT/WHOI, Cambridge, MA 02139, June 1991.

[78] A. Tesei, A. Maguer, W.L. Fox, R. Lim, and H. Schmidt. Measurements and modeling of acoustic scattering from partially and completely buried spherical shells. *Journal of the Acoustical Society of America*, 112(5):1817–1830, 2002.

[79] TheFreeDictionary.com. Naval mine. *http://encyclopedia.thefreedictionary.com/naval%20mine*, 2004.

[80] S. Thrun, J. Schulte, and C. Rosenberg. Interaction with robots in public places. *IEEE Journal of Intelligent Systems*, 22:7–11, 2000.

[81] N. Toumelin and J. Lemaire. New capabilities of the REDERMOR unmanned underwater vehicle. *MTS/IEEE Oceans 2001*, 2:1032–5, November 2001.

[82] B.H. Tracey and H. Schmidt. Seismo-acoustic field statistics in shallow water. *IEEE Journal of Oceanic Engineering*, 22(2):317–331, April 1997.

[83] H.L. Van Trees. *Detection, estimation, and modulation theory. Part 1, Detection, estimation, and linear modulation theory.* Wiley, New York, 1968.

[84] G. Veruggio and F.Grassia. ROMEO: a versatile unmanned underwater vehicle for marine research. *MTS/IEEE Oceans '95: Challenges of our changing global environment*, 3:2003–7, October 1995.

[85] J.M. Walton and R.W. Uhrich. 114 untethered UUV dives: lessons learned. *MTS/IEEE Oceans '95: Challenges of our changing global environment*, 1:594–9, October 1995.

[86] M.F. Werby, H.Überall, A. Nagl, S.H. Brown, and J.W. Dickey. Bistatic scattering and identification of the resonances of elastic spheroids. *Journal of the Acoustical Society of America*, 84(4):1425–36, 1988.

[87] X. Yu, T. Dickey, J. Bellingham, D. Manov, and K. Streitlien. The application of autonomous underwater vehicles for interdisciplinary measurements in Massachusetts and Cape Cod bays. *Continental Shelf Research*, 22:2225–45, 2002.

[88] G. Zhang, L. Tsang, and Y. Kuga. Studies of angular correlation functions of scattering by random rough surfaces with and without the buried object. *IEEE Trans. Geosci. Remote Sensing*, 35:444–52, 1997.

[89] M. Zwolski. Naval mine history. *Airborne mine countermeasures website: http://members.aol.com/helmineron/minehist.htm*, 2004.